Dissertation

Universität Bremen

Fachbereich für Physik und Elektrotechnik
Institut für Umweltphysik

The temporal variability of the OH* airglow layer: A study based on Fourier Transform Spectroscopy and mesospheric models

---

Zur Erlangung des akademischen Grades Dr. rer. nat.

vorgelegt von

Dipl.-Phys. Stefan Kowalewski

1. Gutachter: Prof. Dr. Justus Notholt
2. Gutachter: Prof. Dr. Christian von Savigny

Eingereicht am: 23.12.2014
Promotionskolloquium: 18.03.2015

Für meine Familie

Abstract

The mesospheric fraction of the atmosphere has been proposed by previous studies as a highly sensitive indicator of climate change. In contrast to the lower atmosphere, the build-up of greenhouse gases, in particular CO_2, is expected to lead to a more pronounced radiative cooling. While the lower and middle mesospheric regions show strong evidence of long term cooling trends, the upper mesospheric trend is rather uncertain. Simultaneously, the upper mesosphere exhibits a large dynamic variability, in particular over the polar regions, such that mesospheric air is strongly departing from its radiative equilibrium. Improving our understanding of the driving processes of the dynamic variability is therefore crucial for understanding the climate response of the upper mesospheric and mesopause region. In this connection, the emission from the hydroxyl (OH*) airglow layer at mesopause altitudes is one important source of information, which is extensively used in the present work to study the temporal variability of this region by means of Fourier transform spectroscopy and mesospheric models. The main contributions of this work are divided into two parts:

Part 1: Spectroscopic observations of the OH* emission were performed during the polar winter seasons at the high latitudinal AWIPEV station in Ny-Ålesund, Spitsbergen. Based on the observed OH(3-1), OH(4-2), and OH(8-5) Meinel emission bands, rotational temperature estimates are derived and serve as a close approximation of ambient kinetic temperatures. A temperature time series is created for the periods from 2007-12 and 2013-14. A comparison with temperature estimates from the AURA/MLS satellite reveals that ground-based temperature estimates are lower for most of the time. The smallest offset is found for the OH(3-1) temperature estimates, which reduces to a few Kelvin or even less during some periods. In contrast, the offsets of OH(4-2) and OH(8-5) temperature estimates to MLS remain quite substantial for most of the time and can reach values as large as a few tens of Kelvin. While a sensitivity test shows a critical dependency of the temperature retrieval on the simulated atmospheric transmission for both emission bands, in particular the exceptionally low OH(8-5) temperature estimates are a surprising result compared to previous studies.

In addition to the intercomparison of different temperature estimates, NCEP1 re–analysis data were used to study the impact of sudden stratospheric warmings on the dynamic variability of the upper mesosphere that is reflected in the associated temperature estimates. Evidence of mesospheric feedbacks to changes in the stratospheric conditions was found in a number of cases. An interesting case example was found in January 2011 where changes in upper mesospheric temperatures appear to precede changes in the stratospheric dynamic conditions, which seems to contradict an upward propagating disturbance explanation.

Finally, harmonic perturbations in the observed OH* emission brightness and associated temperature estimates are a common feature at hourly time scales in the derived time series of this work. Following previous theoretical considerations on the impact of vertically propagating waves on the OH* airglow layer, phase shifts between brightness and temperature perturbations were identified and discussed in the time series. The observed brightness/temperature relations are supposed to be dependent on vertical wave properties, implying a valuable application of the OH* measurements for future studies.

Part 2: Previous studies revealed systematic vertical shifts between different vibrational populations of OH*. The thermalisation at different altitudes induces differences between rotational temperatures from different OH* Meinel bands. With the aim of improving our understanding of the driving processes that modulate the vertical shifts in the OH* Meinel emission, this work performs gas-kinetic simulations by means of a collisional quenching model driven by SD–WACCM4 model runs. This work finds that the combined effect of collisional quenching with atomic and molecular oxygen is crucial to understand seasonal changes in the vertical shifts between different OH* emission bands, whereas previous studies were mainly focusing on the impact of atomic oxygen only. At diurnal time scales the model results suggest that changes in the source gases of OH* become another important factor. A similar investigation of vertical shifts between different OH* emission bands based on spaceborne observations by SABER reveals a qualitative agreement with the model results, while the quantitative deviations imply that further improvements in our theoretical understanding are necessary.

Contents

1. Introduction

The Earth's atmosphere is a crucial life supporting medium of this planet and has been subject to substantial changes during the Earth's evolution. It nowadays provides the conditions for a manifold of lifeforms, which in turn significantly affect its chemical composition and the Earth's albedo. This again has important implications for the total energy budget in response to the incident solar radiation, and through this inducing momentum to the Earth's atmosphere. It appears that the conditions we experience on this planet are the result of a complex interaction within the entire Earth system that is responding to the incoming solar radiation. From prehistoric climate records we find evidence of drastic variability in the atmospheric state, having severe implications for the life supporting conditions on this planet. Due to the pronounced world wide growth in economies and agricultural land use over the past decades, the associated accelerated anthropogenic release of gases that can potentially influence the Earth's energy budget is leading to a rising concern among societies and policy makers. The Montreal protocol is a prominent example of an intergovernmental treaty that regulates the anthropogenic release of ozone depleting halogenated substances into the atmosphere. It entered into force in 1989 with the aim of preventing the destruction of the stratospheric ozone layer, which is protecting life from harmful solar ultraviolet (UV) radiation. More recently, Garcia et al. [2012] have confirmed within model projections from the Whole Atmosphere Community Climate Model (WACCM) that a world without the successful ratification of the Montreal protocol would have experienced a collapse of the entire ozone layer by the mid-21st century.

The release of greenhouse gases as a result of the strong increase in fossil fuel combustion and agricultural land use, in particular carbon dioxide (CO_2) and methane (CH_4), is another important issue from the anthropogenic altering of the atmospheric composition. According to the recently published 5^{th} assessment report of the Intergovernmental Panel on Climate Change (IPPC, 2013), the anthropogenic impact on global warming since the 1950s is considered to be highly significant, while CO_2 concentrations have increased by 40 % since pre-industrial times. However, the scientific debate on global warming is still subject to large uncertainties, which certainly must be attributed to the complexity of this topic. In this context, it is important to note that climate change is not constrained to the tropospheric layer, but ranging from the oceanic bottoms to the land ecosystems to the atmospheric edge of space. Hence, a thorough understanding of the response and interaction between different components of the entire Earth system is mandatory to allow reliable future climate projections.

The middle atmosphere, ranging from the tropopause to the homopause at about 100 km altitude [Brasseur and Solomon, 2005], is one part of this puzzle, which has attracted the attention of an increasing number of research groups over the past decade. However, in particular the mesospheric fraction, starting at about 50 km altitude, is one of the still least understood components of the Earth's atmosphere for mainly two reasons. Firstly, in-situ sensing of this region is technically very challenging and practically limited to cost expensive rocket campaigns; and secondly, in many cases remote sensing of this region requires the consideration of non local thermal equilibrium (non-LTE) conditions, posing a non-trivial problem to the data evaluation.

Despite these problems, there is a growing scientific consensus on the importance in understanding the climate response of this atmospheric region, which, among others, is manifesting by the growing Network of the Detection of Mesospheric Change (NDMC). One reason for that is the high sensitivity of this region to dynamical and chemical perturbations, which makes it a favourable early indicator of climate change. In this context, the climate response can be quite different in comparison with the tropospheric layer below. For instance, CO_2 warming of air occurs in the tropospheric layer due to the absorption of infrared (IR) emission from the Earth's surface. In contrast, CO_2 at mesospheric altitudes acts as a cooling IR-radiator into space, therefore a global cooling of this atmospheric region is expected. Indeed, evidence of a mesospheric cooling has already been found by various authors as summarised in the review papers on mesospheric temperature trends by Beig et al. [2003] and Beig [2006]. Following these papers, they deduce a cooling trend of about 2-3 K per decade at the lower and middle fractions of the mesosphere from the bulk of observations. This appears to be quite substantial compared to the globally averaged combined land and ocean surface temperature rise of 0.85 K that is estimated from multiple independent datasets between 1880 to 2012 in the frame of the 5^{th} IPPC report. Vice versa, a growing number of studies report zero-trends for the upper mesospheric boundary, the mesopause, (among others, see Dyrland and Sigernes [2007] and Holmen et al. [2014]) but also a few exceptions exist that report negative trends as large as -10 K per decade [Beig et al., 2003]. The dynamic variability of this region, its sensitive response to changes in the solar forcing, as well as the scarcity of long term measurements (i.e. at least one decade as supposed by Beig et al. [2003] or even two decades as supposed by Khomich et al. [2008]) and their limitation to a fixed geolocation make trend analyses a challenging task, hence, improving our understanding of the driving processes of the dynamic variability will lead to a better understanding of climate change in the mesopause region.

Many observational studies on the mesopause region rely on a special feature, which is commonly referred to as airglow. It results from the emission of electronically excited atoms as well as rotationally-vibrationally (ro-vibrationally) excited molecules, which offers a valuable source of information on the ambient air by means of remote sensing techniques. In particular the Meinel bands, first identified by Meinel [1950a,b] as the emission from the ro-vibrationally excited hydroxyl (OH^*) radical, are a prominent

source of airglow at mesopause altitudes. Fortunately, some of the OH* Meinel bands can be easily observed from the ground during nighttime. Spectroscopic observations of the OH* Meinel bands allow us to determine the OH* rotational temperatures, which are extensively used to study temperature changes at mesopause altitudes. In addition, the OH* brightness is another important parameter, which is responding to changes in the chemical composition of the ambient air. Both parameters, rotational temperature and emission brightness, appear to be highly sensitive to dynamical perturbations, while theoretical models suggest that dynamical properties are directly contained in the combined set of parameters, as we will discuss later in more detail.

In this work, a strong emphasis is given to the OH* Meinel emission (abbreviated as "OH* emission" in the following), which is used as a tool to study mesopause dynamics and temperatures. To provide new insights into the mesopause region, this work pursues two approaches. First of all, ground-based observations by means of Fourier Transform Spectroscopy in the IR wavelength region (FTIR) were performed at the high latitudinal AWIPEV station, which is located in the Arctic village of Ny-Ålesund, Spitsbergen at 78°55'N. Following the preliminary OH* emission measurements prior to this work between 2007-09, a further refinement of the measurements was applied in 2010 to improve the OH* signal strength. Since then, ongoing measurements throughout the polar night have been performed. From selected OH* Meinel bands, rotational OH* temperatures are retrieved and compared with additional temperature measurements from spaceborne platforms. The temporal variability of the temperature time series is further compared to the stratospheric dynamic conditions below, which this work deduces from reanalysis data to study the vertical dynamic coupling between both atmospheric regions. In addition, we also address the variability of the solar forcing and its potential impact on the results of this work. Besides the comparison of the OH* temperature time series with other datasets, we exploit the above mentioned relation between temperature/brightness perturbations based on selected case examples at the end of the first main part of this work.

For the second approach, this work performs gas-kinetic simulations to investigate processes that lead to systematic vertical shifts between the emission profiles of different OH* Meinel bands. While previous studies suggest that the process of collisional relaxation of the excited OH* radicals is primarily determining these vertical shifts, this work investigates the role of the collisional quenching process on the temporal modulation of these shifts. For this task, the gas-kinetic simulations are driven by model runs from the WACCM4 model version extended with specified dynamics. The simulated OH* profiles are further compared with spaceborne measurements of vertical shifts between different OH* Meinel bands. The motivation for the two approaches of this work is summarised in the following.

1.1. Motivation of this work

The climate response at mesopause altitudes is subject to ongoing research. In this connection, the driving processes of the dynamic variability at these altitudes appear to play a significant role. This in particular applies to the polar mesospheric regions, which are largely disturbed due to dynamic perturbations that have their origin mainly in the lower atmospheric layers. Vice versa, high latitudinal ground-based observations are very sparse, but also spaceborne instruments are typically limited in their latitudinal range due to their prescribed orbits. In addition, local small-scale perturbations that play a fundamental role in driving the large-scale circulation, as we will soon discuss, are not fully resolved by spaceborne observations due to their large observational footprints and limited number of orbits per day. In turn, the parametrisation of these small-scale perturbations remains a challenging task in numerical simulations of the middle atmospheric general circulation.

Ground-based observations of the OH* emission can be performed throughout the polar night during clear night-sky conditions at time increments in the order of a few minutes. This significantly broadens the sensitivity to dynamical perturbations compared to spaceborne observations. The establishing of high-latitudinal ground-based observations of the OH* emission is therefore an important contribution to the investigation of the driving processes of the dynamic variability at mesopause altitudes. In addition, ground-based instruments are an important validation source for spaceborne missions, which can be affected by degradation effects over time that, if not considered, would lead to artificial trends in long-term observations.

The motivation for the model part of this study relies on the importance of the vertical profile structure of the OH* emission for the intercomparison of ground-based measurements that consider different OH* Meinel bands. Previous studies have shown that systematic differences exist in the vertical distributions of OH* concentrations with respect to their vibrational level of excitation. This again induces systematic differences in the rotational temperatures based on Meinel bands originating from different vibrational OH* populations. Hence, the precise intercomparison of OH* rotational temperature records based on different Meinel bands requires a profound knowledge about the vertical structure of the OH* profiles. Apparently, this complicates the intercomparison between ground-based observations of the OH* emission, which are usually measuring the integrated emission along the line-of-sight and therefore lack the information about the OH* profile shape and altitude. Hence, a better understanding of systematic processes that modulate the vertical displacements between different Meinel bands will help us to understand associated systematic difference that occur in the comparison between different ground-based long-term datasets.

1.2. Structure of thesis

A review of the physical background of this study is provided in Chap. 2. It introduces the basic concept of the classification of atmospheric layers. This is followed by a general discussion about the global circulation with a special focus on the mesospheric fraction. This discussion summarises the most important dynamical processes that are driving or perturbing the mesosphere with the aim of providing a general background on the natural variability of the OH* emission. The following sections summarise the formation process of OH* radicals and explain how their emission spectrum is related to the ambient temperature.

Chapter 3 provides a background on the instrumentation and measurement principles. It begins with a summary on the principles of Fourier transform spectroscopy and introduces the method of this work to derive rotational temperatures from the measured OH* emission spectra. This is supplemented by a review of important issues in the measurements; namely, the impact of the atmospheric transmission on the OH* emission signal, the instrumental sensitivity and its thermal stability during operation. In addition, this chapter investigates the impact of the new viewing direction that is applied to the measurements since 2010. Finally, a brief summary is given on the instrumentation of the AURA/MLS satellite. It provides independent temperature measurements, which are compared with the ground-based temperatures measurements in the next chapter.

Chapter 4 discusses the temperature time series above Ny-Ålesund. It begins with an introduction on the quality criteria that are applied in the data filtering of this work. This is followed by a brief overview on the developed data processing scheme. The temperature time series from different OH* Meinel bands and spaceborne measurements from MLS are then discussed and related to the solar as well as stratospheric dynamic conditions as noted earlier. The final section of this chapter addresses the observed small-scale perturbations in the OH* emission and discusses the related implications from current theoretical models.

Chapter 5 addresses the model part of this work. It introduces the updated quenching model that was established in this work and summarises the key features of the extended WACCM model, which is used to drive the gas-kinetic simulations of OH*. In addition, it provides a brief overview on the TIMED/SABER satellite, which is used for comparison of the model results. Based on a sensitivity study, this chapter addresses the diurnal and seasonal impacts of the collisional quenching process on the vertical shifts between the OH* Meinel bands.

Chapter 6, the final chapter, summarises the main aspects of the experimental and model parts of this work and outlines their implications for the mesospheric region. Potential future applications to the ongoing OH* observations in Ny-Ålesund and the model approach of this work are discussed in the outlook at the end of this chapter.

2. Scientific Background

2.1. The vertical layers of the atmosphere

The Earth's atmosphere is classified according to different layers that have distinct characteristics. One criterion for classifying atmospheric layers is the associated vertical temperature gradient, as illustrated by the schematic vertical thermal profile in Fig. 2.1. This profile can be split up into layers where temperatures either decrease with altitude (i.e. troposphere and mesosphere) or increase with altitude (i.e. stratosphere and thermosphere). Between these layers, intermediate layers exist where temperatures remain rather constant with altitude. We denote these intermediate layers with the term "pause" instead of "sphere" in the end of their names. Depending on the geographic position, the seasonal and local time, the altitudes of the intermediate layers and the temperature gradients of the surrounding layers will differ. Furthermore, conditions can occur where the vertical thermal structure inside a layer can be locally reversed, leading to a more complex structure.

The thermal structure of the atmosphere results from different factors that favour the warming or cooling of air. For instance, the large abundances of stratospheric ozone, a very effective absorber of UV radiation, lead to a strong radiative heating, which is the main driver of the positive temperature gradient with height in this region. In contrast, radiative IR cooling into space starts to dominate in the mesospheric layer via vibrational relaxation of CO_2, H_2O and O_3 [Brasseur and Solomon, 2005]. At mesopause altitudes the dominant radiative cooling mechanism is provided by CO_2, which is largely driven by transfer of energy due to collisions with atomic oxygen [Beig et al., 2003]. For the thermospheric region, radiative heating due to the increasing amount of highly energetic solar radiation starts to dominate again. In this context, heating is primarily due to the deposition of kinetic energy of air molecules and atoms because of the rarefied thermospheric air.

Another classification of atmospheric layers is given by the chemical composition and driving dynamic processes of air. Based on this criterion, air below 100 km is dominated by turbulent mixing processes and mainly consists of N_2 and O_2. Its molecular weight is therefore rather constant with altitude. Above 100 km, the atmospheric composition becomes very heterogeneous with altitude. Because highly energetic solar radiation is significantly increasing with height at this fraction of the atmosphere, photo dissociative processes become more important. In addition, transport of air is dominated by molecular diffusion rather than turbulent mixing. Both processes lead to a weight dependent

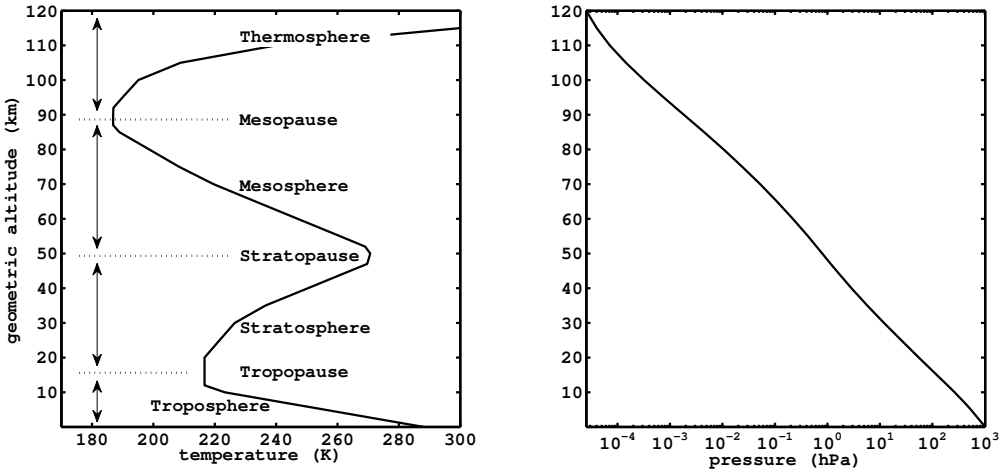

Figure 2.1.: Vertical thermal structure (left panel) and pressure/altitude relation (right panel) based on the U.S. Standard Atmosphere 1976.

distribution of species in the vertical direction. According to these characteristics, the region below 100 km is referred to as the homosphere and the region above 100 km is referred to as the heterosphere. The intermediate layer where molecular diffusion and turbulent mixing compete with each other is referred to as either the homopause or turbopause.

In summary, we find systematic structures in the atmosphere, which are categorised by different atmospheric layers. In the next section, we expand this one-dimensional picture to the meridional direction and review some of the fundamental processes which are driving the mesospheric dynamics.

2.2. Middle atmospheric dynamics

The global circulation of air is an important dynamical process, which is significantly affecting the thermal structure of the mesopause region. A schematic view of the zonally averaged global circulation is presented in Fig. 2.2 where the thermal contrast between different regions is indicated by the coloured background, i.e. "warmer" temperatures are denoted with red colours and "colder" temperatures are denoted with blue colours. At first glance, it might appear surprising that the winter mesopause is warmer than the summer mesopause, in particular above the poles, as illustrated in Fig. 2.2. In fact, the mesopause at the summer pole is the coldest naturally existing place in the Earth's atmosphere [Smith, 2012a]. To understand the thermal contrast between the summer and winter pole, the transport of air, which is denoted by the yellow arrows in Fig. 2.2, must be taken into account. As illustrated, a pole-to-pole meridional circulation exists at the mesopause with upwelling air above the summer pole and downwelling air above the

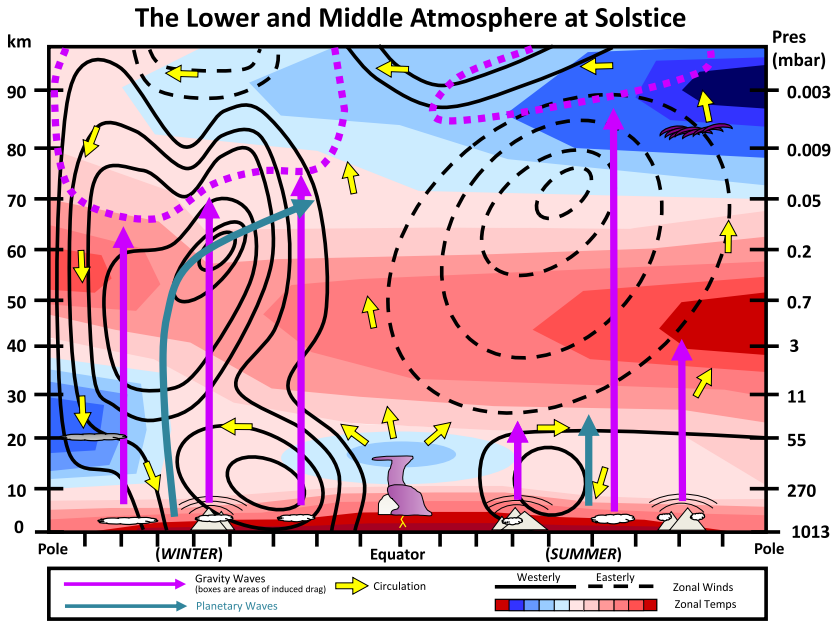

Figure 2.2.: Schematic representation of middle atmospheric ciculation and thermal contrasts during solstice conditions. The propagation of gravity waves and planetary waves is denoted by arrows (see legend). Taken from Meriwether and Gerrard [2004]

winter pole. Due to the adiabatic vertical motion, up-/down welling air parcels depart from their radiative equilibrium because of the associated adiabatic cooling/warming. A fundamental process, which is driving the meridional circulation between both poles, is given by the dissipation of breaking internal gravity waves in the mesosphere. In general, wavelike perturbations are a crucial dynamical feature of the atmosphere in the altitude range between 10 km and 110 km [Fritts and Alexander, 2003]. To provide an overview on the physical background of these features and their implications for the dynamical and thermal state of the mesospheric region, different mechanisms producing these features are reviewed in the following.

2.2.1. Gravity waves

Internal gravity waves are an essential driver of mesospheric dynamics. They can be generated by orographic disturbances (e.g. air flow over mountains) as well as non-orographic disturbances (e.g. frontal systems, thunderstorms, velocity jets) in the lower atmosphere. These disturbances lead to wavelike perturbations due to the *fluid buoyancy* of ambient air [Nappo, 2002]. An additional restoring force is given by the Coriolis force which becomes significantly important, if horizontal wavelengths are greater than about 300 km [Brasseur and Solomon, 2005]. Typical horizontal wavelengths of gravity waves range between 10 to 1000 km, while observed vertical wavelengths range between

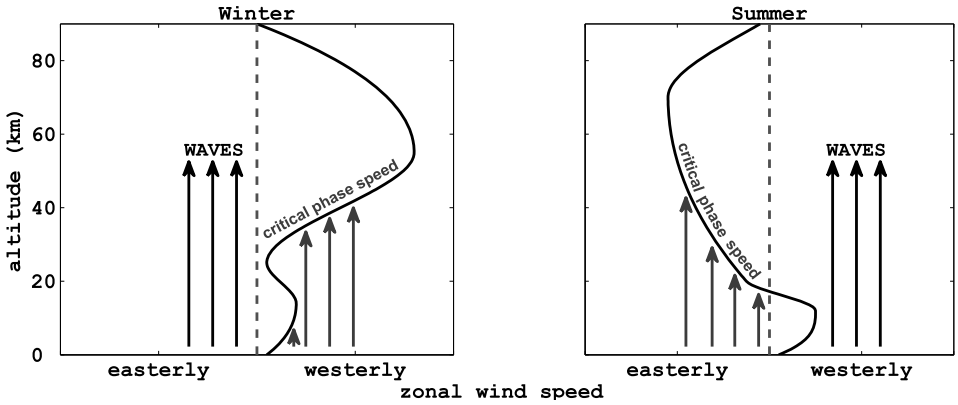

Figure 2.3.: Schematic vertical distribution of mid-latitudinal zonal winds and its impact on the vertical propagation of gravity waves. Filtering of gravity waves occurs where phase speeds approach zonal wind speeds. Adapted from Lindzen [1981].

10 to 30 km near the mesopause [Fritts and Alexander, 2003].

An important property of gravity waves is that they can propagate from the lower atmosphere to the mesosphere as indicated by the pink arrows in Fig. 2.2. By doing this, they provide a source of transport of energy to the mesosphere, which can be released via wave dissipation, in particular due to wave breaking, as will be discussed soon. The process of gravity wave propagation and energy transfer can be described by means of the fundamental equations of fluid dynamics, i.e. the momentum equation that results from Newton's laws of motion, the conservation of thermal energy and the continuity of mass. Different methods exist to find (approximate) solutions for these non-linear differential equations, as described in more detail, among others, in the textbooks of Andrews [1987] and Nappo [2002]. The reader who is interested in a more detailed discussion of mathematical solutions to these equations is referred to these books. Here, we limit the discussion to some of the crucial implications for mesospheric dynamics that result from corresponding wave solutions.

Typically, the generation of gravity waves results from the excitation of a spectrum of monochromatic waves. This leads to the formation of wave packets that propagate through the atmosphere with a corresponding group velocity u_g and transport the energy of disturbance in the same direction. Air parcels oscillate with a corresponding phase speed u_p along wave fronts perpendicular to the propagating wave packets. By assuming that the atmosphere is a stratified fluid medium, it can be shown that a gravity wave is completely absorbed, if its phase speed is equal to the zonal wind speed of the atmosphere. Vice versa, if the gravity wave phase speeds sufficiently differ from the zonal background flow, these waves propagate nearly undamped through the atmosphere [Andrews, 1987]. It follows that the vertical propagation of gravity waves is largely controlled by the vertical distribution of zonal wind fields, as illustrated in Fig. 2.3. This

figure shows an exemplary vertical profile of zonal wind speeds at mid-latitudes during the winter season (left panel) and during the summer season (right panel). As illustrated, the phase spectrum of gravity waves results in dominant westward propagating gravity waves in the winter mesosphere and dominant eastward propagating gravity waves in the summer hemisphere. In this connection, the westerly (/eastward) stratospheric winter jet acts as an effective filter to the mesospheric gravity wave spectrum, as indicated by the solid black contour lines in Fig. 2.2. The same, but not as pronounced, also applies for the easterly (/westward) stratospheric summer jet, as indicated by the dashed black contour lines in Fig. 2.2. This shows an interesting connection between the mesosphere and the lower atmospheric layers, because changes in the zonal wind fields below the mesosphere, e.g. due to the stratospheric wind reversal during the equinox, are affecting the mesospheric gravity wave spectrum. Vice versa, gravity waves can also affect the zonal background flow via wave dissipation [Fritts, 1984].

As gravity waves propagate in the vertical direction, the density ρ_0 of the atmosphere decreases, as illustrated in the right panel of Fig. 2.1. It can be shown that the gravity wave amplitude increases as the inverse square root of density, $\rho_0^{-1/2}$, if we assume that no wave dissipation takes place [Andrews, 1987]. However, at some critical altitude gravity wave amplitudes have grown so large that they start to break due to convective overturning or shear instability. This in turn leads to turbulent mixing of the atmosphere, but it also induces a zonal force that either accelerates or decelerates the zonal mean flow depending on the sign of the horizontal phase propagation relative to the zonal mean flow. Because of the stratospheric filtering effect on gravity wave phase directions, as discussed above, the induced momentum from gravity wave breaking will typically decelerate the zonal mean winds at wave breaking altitudes. Because gravity waves do not necessarily completely dissipate when they first start to break at a critical altitude, they can further propagate upwards and release their energy by subsequent wave breaking at higher altitudes [Nappo, 2002]. In the mesopause and lower thermosphere region (MLT) the predominant breaking of westward propagating gravity waves finally leads to a reversal of the westerly to an easterly wind direction [Smith, 2012a]. Because of the increasingly viscous character of the thermosphere, the further vertical propagation of gravity waves is effectively limited by their associated strong dissipation [Fritts and Alexander, 2003].

The decelerating zonal force of breaking gravity waves in the mesosphere, also referred to as gravity wave drag, is balanced by a meridional wind from the summer to the winter pole, which leads to the up-/downwelling of air above the summer/winter pole because of continuity of mass [Andrews, 1987]. Apparently, a profound knowledge of the gravity wave interaction with the zonal mean flow is essential to understand the dynamical and thermal state of the mesopause region, in particular above the poles. Because of their relatively small wavelengths, general circulation models typically rely on parametrisation schemes of gravity wave forcing. Specialised high resolution gravity wave models (e.g. Zülicke and Becker [2013]) and the progress in observations are steadily

improving these parametrisations. Of course, gravity waves cannot be directly observed, but their perturbation can be seen, among others, in the response of the hydroxyl airglow layer, which therefore offers an important tool to study gravity waves in the mesopause region.

2.2.2. Rossby waves

Planetary scale Rossby waves result from the meridional gradient in potential vorticity (PV), where PV is a measure of the vertical component of the angular momentum of fluid elements [Brasseur and Solomon, 2005]. By assuming that dissipative processes are negligible, the PV is a conserved quantity between isentropic surfaces[1]. Simply speaking, if we think of a rotating column of air that is enclosed by a lower and upper isentropic surface, any squashing or stretching of the column must be compensated by changes in its rotation, i.e. stretching leads to an acceleration and squashing leads to a deceleration of rotational motion. Furthermore, if the column of air is deflected towards either the North or the South, e.g. by a large scale orographic obstacle, the Coriolis force will affect the angular momentum of the (rotating) column of air. Hence, to conserve the PV a restoring force results from this deflection and because of the inertia of the column of air a wavelike oscillation is establishing.

Planetary scale Rossby waves are westward propagating relative to the mean flow [Brasseur and Solomon, 2005]. It can be shown that upward propagating Rossby wave modes only exist in the stratosphere below a critical velocity (e.g. see Eq (12.16) in Holton [2004]) and during westerly wind conditions. As illustrated in Fig. 2.2, this condition mainly limits the vertical propagation of planetary scale Rossby waves to the winter stratosphere, where they are ducted equatorward [Meriwether and Gerrard, 2004]. Similar to the vertical propagation of gravity waves, the amplitude increases with altitude until breaking of Rossby waves occurs in the winter stratosphere. This again leads to a deceleration of the mean flow and through this inducing a downward circulation in the stratosphere. On some occasions, a large amplification of Rossby wave generation is establishing in the troposphere, which leads to a dramatic Sudden Stratospheric Warming (SSW) event because of the pronounced adiabatic heating of stratospheric air in response to the induced downward circulation, as initially proposed by Matsuno [1971].

As per definition, a stratospheric warming is said to be an SSW event, if the zonal mean temperature at 10 mbar or below increases poleward from 60° latitude [Labitzke, 1981]. In addition, the deceleration of the zonal flow further improves the conditions for vertical propagation of Rossby wave into the stratosphere, which eventually can even lead to a large scale reversal of stratospheric zonal winds that is accompanied by a splitting of the polar night vortex. In this case, an SSW event is said to be major. If no split of the polar vortex occurs, it is said to be a minor SSW event.

[1] Isentropic surfaces refer to as surfaces of constant temperature acquired by an air parcel that would be lowered adiabatically to a reference pressure level (usually ground pressure).

Apparently, SSW events will also affect the stratospheric filtering of the gravity wave spectrum due to the induced changes in zonal wind fields. This in turn will alter the gravity wave forcing in the MLT region. According to Liu and Roble [2002], who studied the impact of SSW events on the mesospheric region based on a coupled general circulation model, they found a pronounced deceleration and reversal of the easterly winds in the MLT region. In response to the wind reversal, an equatorward/upward circulation is induced in the MLT, which leads to a strong adiabatic cooling of up to 50 K according to the study of Liu and Roble [2002]. With the reestablishing of the polar vortex, the gravity wave filtering is again altered such that an enhanced dissipation of gravity waves establishes at the mesopause due to the weak planetary wave activity [Hoffmann et al., 2007]. As a consequence, the induced reestablishing of the dynamic conditions prior to the SSW warming leads to a subsequent mesopause warming.

The recent model study by Zülicke and Becker [2013], which investigates the SSW effect to the MLT region by explicitly simulating the gravity wave effect, shows that MLT cooling events are very likely to occur during major but also minor SSW events. This also appears to be consistent with observations that frequently show MLT cooling events prior to the peak of SSW events (e.g. Walterscheid et al. [2000], Sigernes et al. [2003], Siskind et al. [2005], Kurihara et al. [2010], Holmen et al. [2013].) However, while the response between SSW events and mesopause cooling appears to be a robust feature in model simulations and observations, the response to mesospheric zonal winds remains uncertain, as shown in Zülicke and Becker [2013]. This illustrates, among others, that the SSW impact on the MLT region remains subject of ongoing investigations. As outlined by Zülicke and Becker [2013], this also applies to the general preconditioning of SSW events.

2.2.3. Tides

Atmospheric tides are largely driven by the periodic solar forcing which results from the rotation of Earth. As stated in Andrews [1987], the gravitational forcing by the moon and sun is much less important, hence, the following discussion is limited to thermal atmospheric tides. These tides can be categorised into two types; migrating and non-migrating tides.

Migrating tides are mainly forced by the absorption of UV radiation by O_3 in the middle atmosphere and absorption of visible and IR light by water vapour in the troposphere [Becker, 2012, Brasseur and Solomon, 2005]. Accordingly, these tides are sun-synchronous tides and therefore westward propagating relative to the ground. Owing to the daily rotation of the Earth, temperature oscillations are induced with periods that are harmonics of a solar day.

In contrast, non-migrating tides are non-sun-synchronous tides, i.e. they can either propagate westward or eastward, or they can be stationary to the ground. This is because these tides are mainly forced by the release of latent heat from the precipitation of tropospheric water vapour, thus, these tides are related to the meteorological conditions in the lower atmosphere [Brasseur and Solomon, 2005]. In addition, other geographically fixed tropospheric heat sources may also induce non-migrating tides [Andrews, 1987].

By analogy with gravity and Rossby waves, tidal wave amplitudes increase with height, which can lead to temperature oscillations at the mesopause by as much as 20 K for the diurnal migrating tide [Smith, 2004]. This tide is particularly important for the equatorial region, where the tidal amplitude reaches its maximum value until it decays to its minimum value around $\pm 30^\circ$ latitudes because of destructive self-interference (see Andrews [1987]). This in turn leads to temperature contrasts, which induce thermal winds such that horizontal wind components show a largest amplitude at $\pm 30^\circ$ latitudes Brasseur and Solomon [2005]. According to Smith [2004] horizontal wind amplitudes can exceed 50 m/s, which can be quite significant compared to gravity wave phase speeds that are typically less than 100 m/s [Fritts, 1984]. Therefore, tidal thermal winds can potentially affect the gravity wave breaking in the MLT region through phase filtering, which gives another interesting example of the coupling between two different dynamically driving processes in this region.

2.2.4. Solar disturbances

In addition to the periodic solar forcing due to Earth's rotation, the solar variability itself is also affecting the mesospheric region. While the total solar flux is rather constant in time, fluctuations can be quite substantial in the UV wavelength region. Two distinct features of the variability of the UV solar irradiance are the 11-year solar sunspot cycle and, with a smaller magnitude, the 27-day solar rotation cycle. As discussed in Beig et al. [2008], the fluctuation of the UV irradiance is affecting the energy budget of the mesospheric region by solar heating (mainly due to UV absorption of O_2, O_3 and CO_2) and chemical heating via energy release from exothermic reactions that are driven by photochemistry. For instance, von Savigny et al. [2012a] reported the presence of a 27-day signature in the mesopause temperatures at equatorial latitudes from spaceborne observations. Further studies on the impact of the 11-year solar sunspot cycle on mesospheric temperatures are reviewed by Beig et al. [2008], Beig [2011]. These studies are of great importance for the analysis of mesospheric long-term temperature trends, which are significantly affected by the variability of solar forcing.

Another source of solar disturbances affecting the mesospheric region are energetic particle precipitation (EPP) events. These include so-called energetic electron precipitation (EEP) events that arise from the Earth's radiation belt during geomagnetic storms as well as solar proton events (SPE) that arise from coronal mass ejections or solar flares, which produce large fluxes of highly energetic protons [Sinnhuber et al., 2012]. Due to

the terrestrial magnetic field, the energetic particles precipitate above the polar regions where they disturb the dynamic conditions by altering the heating and cooling rates according to different processes, as summarised in Sinnhuber et al. [2012].

In short, these processes include:

- Joule heating from the energy dissipation of charged particles moving in an electric field
- particle heating
- chemical heating from induced exothermic reactions
- altering the heating/cooling rates via the catalytic destruction of O_3 from odd hydrogen ($HOx = H, OH, HO_2$) species that are produced in response to the SPE.

In particular the latter process can have a strong impact on the mesospheric dynamics. Following Becker and von Savigny [2010], catalytic ozone losses of up to 70 % between 50 km and 70 km can occur during an SPE, which leads to a reduced diabatic heating of this region during sunlit conditions. Based on a mechanistic general circulation model, they show a positive response in the zonal winds of the summer mesosphere, which has also been confirmed by MF/meteor radar observations from Singer et al. [2013]. Due to the altered gravity wave filtering, Becker and von Savigny [2010] find a positive temperature anomaly at summer mesopause altitudes.

2.3. Airglow at the mesopause: The hydroxyl airglow layer

It was mentioned in the beginning that airglow observations are a valuable tool to study the mesopause region. While the OH* airglow layer is one of the most prominent emission sources, about 25 atmospheric components actually exist (ionised species, molecules and atoms) that mainly contribute to the overall airglow of the MLT and upper atmosphere [Khomich et al., 2008]. It is worth noting that airglow should not be confused with the aurora, as both shown in Fig. 2.4, because they rely on different excitation processes. The aurora is formed by the collision between air and highly energetic charged particles that arise from the Earth's magnetosphere[2]. As a consequence, auroras are constrained to the auroral belts that are usually located at high latitudes around the geomagnetic poles.

[2]The magnetosphere represents the Earth's magnetic field, which interacts with the continuous plasma flow from the solar corona (solar wind) [Khomich et al., 2008].

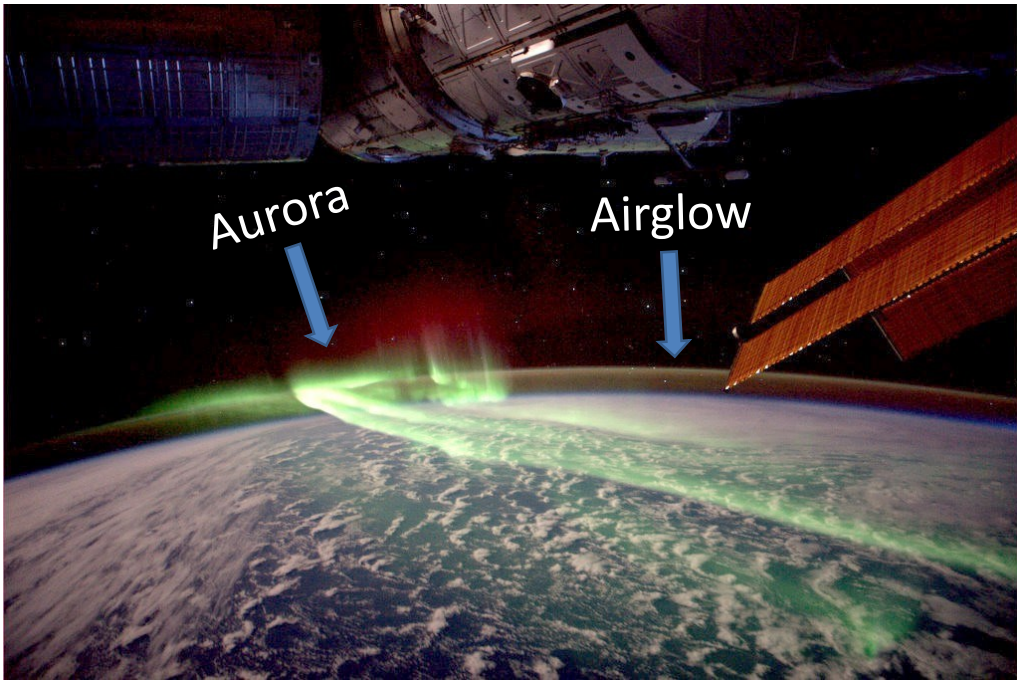

Figure 2.4.: Picture of the aurora and airglow taken from ESA astronaut André Kuipers onboard of the ISS. Photo credit: ESA/NASA

In contrast, airglow is a globally present phenomenon, which can be attributed to the following processes:

- Photolysis reactions
- Fluorescence (re-emitting of absorbed photons)
- Chemiluminescence (excitation via chemical reactions)

Each of these processes give rise to electronic and/or ro-vibrational excitation of a species, which emits light through radiative deexcitation. Depending on the excitation/production process of a specific airglow species, its formation is constrained to a typical altitude region, thus, forming an airglow layer. For instance, the greenish airglow layer visible in Fig. 2.4 results from the electronic transition of $O(^1S_0) \rightarrow O(^1D_2) + h\nu(5577\text{Å})$ where the metastable $O(^1S_0)$ is mainly formed via the Barth mechanism (see Bates [1988]). The associated 5577Å emission is centred at an altitude of about 96 km and has a vertical extent of 8 km in terms of its Full Width at Half Maximum (FWHM) [Snively et al., 2010]. By comparison, the hydroxyl airglow layer is typically centred at about 87 km and has a FWHM of about 8 km (see Baker and Stair Jr [1988] and She and Lowe [1998]). The existence of different airglow layers has an important implication for their observation, because each layer is typically responding to a different altitude region. As we already know from early rocket campaigns (see [Baker and Stair Jr, 1988]), not only do vertical shifts exist between different airglow layers, but also different bands of the

OH* Meinel emission show systematic vertical shifts in their profiles, which we discuss more thoroughly in Chap. 4 and 5.

In the following section, we review the production mechanism of OH* and the associated emission. This review provides a basis for the derivation of rotational temperatures, which this work uses to study the mesopause dynamics above Ny-Ålesund.

Hydroxyl emission

It is nowadays generally accepted that the OH* radical is mainly produced by the exothermic reaction between ozone and atomic hydrogen, as initially proposed by Bates and Nicolet [1950]:

$$H + O_3 \rightarrow OH^*(+3.3eV) + O_2 \tag{R1}$$

In addition, as proposed by Krassovsky [1963], the recombination of the perhydroxyl radical (HO_2) with atomic oxygen provides another mechanism to produce OH*, i.e.:

$$HO_2 + O \rightarrow OH^*(+2.3eV) + O_2 \tag{R2}$$

The excess energy of both reactions leads to ro-vibrationally excited OH* (denoted with *) in its $X^2\Pi$ ground state with vibrational quantum numbers between $\{6 \leq \nu \leq 9\}$ for reaction (R1) and $\{\nu \leq 6\}$ for reaction (R2) [Le Texier et al., 1987]. Different opinions exist on the importance of reaction (R2) to the overall formation of OH* at the mesopause, as summarised by Xu et al. [2012]. However, their study implicates that the contribution of reaction (R2) is rather negligible for vibrational excitation levels greater than $\nu = 3$.

The ro-vibrationally excited OH* radicals relaxate to lower vibrational states via radiative deexcitation or collisional quenching with other species. Because of the highly rarefied air at the mesopause, the probability of radiative deexcitation is large enough to contribute to a substantial emission of OH* during the nighttime. In fact, if the total intensity of the OH* nighttime emission were to be converted to the green 5577Å emission, this would lead to a spectacular airglow as intense as the brightest class of auroras all over the sky [Khomich et al., 2008]. On the other hand, the daytime OH* emission suffers from the pronounced photo dissociation of O_3 because it directly impacts the production of OH* via reaction (R1). In addition, the presence of the strong Rayleigh scattering background from the sun further complicates OH* dayglow observations, because the associated photon noise is proportional to the square root of the background intensity [Davis et al., 2001]. It is for these reasons why ground-based OH* observation are typically limited to the OH* nightglow.

The actual transition between different vibrational states of the excited OH* radical can be described in terms of quantum mechanical selection rules for a diatomic molecule as described by Herzberg [1950]. Because of the departure from the ideal harmonic

oscillator, overtone transitions (i.e. $\Delta\nu = \pm 2, \pm 3, ...$) are possible in addition to the fundamental transition (i.e. $\Delta\nu = \pm 1$). Without consideration of the electronic orbital angular momentum only changes in the rotational level by $\Delta J = \pm 1$ would be allowed. However, spectroscopic observations of the OH* emission reveal strong lines that must be associated with vibrational transitions that possess the same rotational state. Based on these selection rules, three different branches, the P ($J' - J'' = -1$), Q ($J' - J'' = 0$) and R ($J' - J'' = +1$) branch, exist with J' denoting the upper and J'' denoting the lower rotational state. A schematic view of the P,Q,R branches is presented in Fig. 2.5.

It should be noted that purely rotational transitions, i.e. $\Delta\nu = 0$, are also possible. In general, the total energy of a diatomic molecule is to a very good approximation given by the sum of its electronic, vibrational and rotational energies:

$$\mathrm{E_{tot}} = \mathrm{E_{e^-}} + \mathrm{E_{vib}} + \mathrm{E_{rot}} \tag{2.1}$$

As indicated in Fig. 2.5 the differences between adjacent rotational energy levels are small compared to vibrational energy levels. The largest energies result from electronic transitions, thus:

$$\Delta\mathrm{E_{e^-}} > \Delta\mathrm{E_{vib}} > \Delta\mathrm{E_{rot}} \tag{2.2}$$

Because the wavelength λ of an emitted photon is related to the energy of transition in terms of the Planck relation,

$$\lambda = hc/\Delta\mathrm{E} \tag{2.3}$$

with the Planck constant h and speed of light c, it is evident that emissions due to electronic transitions have typically shorter wavelengths and emissions due to rotational transitions have typically longer wavelengths. The emission from the ro-vibrational transitions of OH* is located in the visible and near infrared (NIR) region.

Following Herzberg [1950], it is convenient to express the energies in Eq. (2.1) as functions of wavenumbers $\sigma = 1/\lambda$ by dividing each energy term by (hc). Given the resulting term values, the wavenumber σ can be calculated from the difference between the sum of term values before (denoted with $'$) and after (denoted with $''$) the transition:

$$\sigma = T' - T'' = (T'_{e^-} - T''_{e^-}) + (G' - G'') + (F' - F'') \tag{2.4}$$

where T_{e^-} is the term value of electronic energy, G is the term value of vibrational energy and F is the term value of rotational energy.

Because the electronic spin of the unpaired OH* electron can be oriented either "up" or "down" along the internuclear axis, the $\mathrm{X^2\Pi}$ ground state is split into the $\mathrm{X^2\Pi_{3/2}}$ and $\mathrm{X^2\Pi_{1/2}}$ substates. Here, the subscript denotes the quantum number of the total angular momentum of electrons $\Omega = |\Delta - \Sigma|$, where Δ $(= 1)$ is the quantum number of the electronic orbital angular momentum and Σ $(= \pm 1/2)$ is the quantum number of electronic spin. The $\mathrm{X^2\Pi_{3/2}}$ and $\mathrm{X^2\Pi_{1/2}}$ substates correspond to the electronic ground state and the first excited state, respectively. The quantum number J, which designates

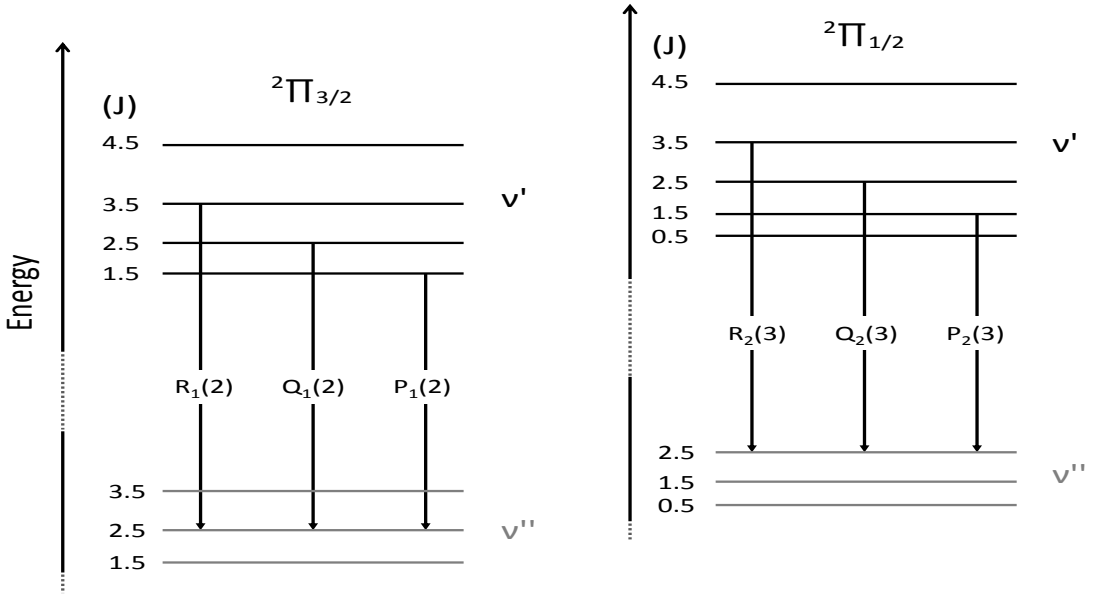

Figure 2.5.: P,Q, and R branches of the ro-vibrational transitions of the $X^2\Pi_{3/2}$ ground and $X^2\Pi_{1/2}$ first excited electronic state. The larger energetic separation of the illustrated vibrational states ν compared to rotational states J is indicated by the dotted line on the energy axis. The nomenclature of ro-vibrational transitions is adapted from French et al. [2000].

the total rotational angular momentum of the molecule, can be any integral value of Ω [French et al., 2000]. Both substates lead to doublet splitting of rotational lines, as illustrated in Fig. 2.5.

Following the nomenclature of French et al. [2000], the lower index of a ro-vibrational transition, as used in Fig. 2.5, designates the $X^2\Pi$ substate. The number inside the brackets denotes the $(J'' - 0.5)$ value for the $X^2\Pi_{3/2}$ state and the $(J'' + 0.5)$ value for the $X^2\Pi_{1/2}$ state. In addition to the transitions shown in Fig. 2.5, the further narrow Λ- and hyperfine splitting of rotational lines (see Herzberg [1950]) is not considered in this study due to the limited spectral resolution of the performed ground-based measurements.

The intensity of a rotational emission line depends on the probability of the ro-vibrational transition, which is expressed by the Einstein coefficient A and the absolute concentration N of molecules in the initial state. It is a common approach to assume a Boltzmann distribution of rotational states within a vibrational band. However, as outlined by Sivjee [1992], reaction (R1) produces highly excited rotational states such that the initial rotational distribution is significantly departing from a Boltzmann distribution. Therefore, the rotational population of the created OH* radicals must first be thermalised through collisions with the ambient mesopause air. This of course requires

that the radiative lifetime τ_i of the corresponding vibrational state ν_i is large enough to allow for a sufficient number of collisions. As stated by Perminov [2009] at least 10 collisions are needed to thermalise the lower rotational states. Estimates of radiative lifetimes show that τ is decreasing with increasing vibrational level ν_i. However, the absolute values can differ substantially within the literature. For instance, a comparison of different estimates of radiative lifetimes can be found in Turnbull and Lowe [1989]. To estimate the number of collisions of OH* in its excited state, we may use the shortest radiative lifetimes listed therein, i.e. $\tau_{(\nu=1)} = 44.0$ ms for the lowest vibrational state and $\tau_{(\nu=9)} = 3.34$ ms for the highest vibrational state. In addition, we may assume that the rate of collisions at about 90 km altitude is $2 \cdot 10^4(\mathrm{s}^{-1})$ according to Khomich et al. [2008]. If we use these numbers as a conservative estimate, the number of collisions would range between about 70 ($\nu = 9$) and 880 ($\nu = 1$), which is still above the required 10 collisions. It should be noted, though, that the actual vibrational lifetime is smaller because of the additional possibility of vibrational relaxation through collisions with the mesopause air. In particular higher rotational levels can show significant departures from a Boltzmann distribution, as observed by Pendleton et al. [1993] for various ro-vibrational Meinel bands of OH*. Still, the lower rotational levels of the $X^2\Pi$ system usually match the Boltzmann distribution quite well, in particular up to the 5^{th} rotational level of the P branch [Khomich et al., 2008]. Because of the longer radiative lifetimes, transitions from lower vibrational states allow for an improved thermalisation of OH* (see also Bittner et al. [2002] and references therein).

Another factor which can introduce a departure from the Boltzmann distribution of observed rotational lines arises from the finite thickness of the OH* airglow layer. Depending on the line-of-sight, the observed line intensities refer to a profile weighted average. Accordingly, if the emission stems from a non-isothermal profile, the observed rotational lines from this emission will be, strictly speaking, non-Boltzmann. However, according to Offermann and Gerndt [1990] the associated temperature gradient should be small during undisturbed conditions, while Bittner et al. [2000] note that disturbances (e.g. due to gravity waves) at scales comparable or even smaller than the layer thickness can lead to some distortion of the observed rotational lines from a Boltzmann distribution.

Based on the assumption of thermalised rotational states, the intensity of a rotational line can be expressed in units of (photons/sec cm^2) as follows:

$$\begin{aligned} I_{(i',\nu',J'\to i'',\nu'',J'')} =& N_{\nu'} A_{(i',\nu',J'\to i'',\nu'',J'')} \\ & \cdot \frac{2(2J'+1)}{Q_{\nu'}} \exp\left[-\frac{F_{J'} hc}{k_B T_{rot}}\right] . \end{aligned} \tag{2.5}$$

Here, $N_{\nu'}$ is the concentration of molecules in the upper vibrational state ν', A is the Einstein coefficient, $Q_{\nu'}$ is the rotational partitioning function of the upper vibrational state (see Herzberg [1950]), $F_{J'}$ is the rotational energy term, T_{rot} is the rotational temperature and the index $i \in [1, 2]$ denotes the $X^2\Pi_{i-1/2}$ substate. Because of the thermalisation of

the rotational population, T_{rot} is representing to a very good approximation the kinetic temperature of ambient air. Rearranging the above equation and taking the logarithm of it leads to the following expression:

$$\ln\left[\frac{I_{(i',\nu',J'\to i'',\nu'',J'')}}{2(2J'+1)A_{(i',\nu',J'\to i'',\nu'',J'')}}\right] = \ln\left[\underbrace{N_{\nu'}/Q_{\nu'}}_{\text{constant}}\right] - \frac{F_{J'}hc}{k_B T_{rot}} \tag{2.6}$$

Apparently, this is a linear equation with a slope parameter that is determined by the rotational temperature T_{rot} and other known constants. This implies that T_{rot} can be estimated from the relative differences in rotational line intensities by means of a linear regression analysis. As noted earlier, selected rotational lines should arise from thermalised rotational populations, otherwise the line intensities would not follow the linear expression above. In principle, we may already use Eq. (2.6) to determine a rotational temperature directly from a measured spectrum. Instead, this work uses an iterative forward modelling approach, which also accounts for the wavelength depended instrumental sensitivity and atmospheric transmission, as discussed in the next chapter.

As part of the forward modelling, a theoretical calculation of the OH* emission lines is done by a Fortran procedure. This procedure was written by E. J. Llewellyn, Institute of Space and Atmospheric Studies, University of Saskatchewan, Saskatoon, Canada and further improved by H. Winkler, IUP Bremen. The theoretical calculation is based on the principles discussed above and uses expressions for energy term values and line intensities given in the textbook of Kovács [1969]. For the calculation of line intensities, corresponding Einstein coefficients are determined from calculations of the matrix elements $R_{(i',\nu',J'\to i'',\nu'',J'')}$ of the dipole moment of the diatomic molecule as explained in Sect. (3.1-2) in Kovács [1969]. In addition, further correction terms are added to Eq. (2.1) to account for energy shifts due to the centrifugal forcing of the molecule as well as the interaction between spin and rotation (i.e. Eq. (10) and Eq. (13) in Sect. (2.1.3) of Kovács [1969]). This work uses the revised molecular constants published in Bernath and Colin [2009]. The spectral line widths are considered in the next steps of the forward modelling approach.

Some important processes, which contribute to the line broadening, are:

- **Natural broadening**: Results from the Heisenberg time-energy uncertainty relation $\Delta E \Delta \tau \geqq \frac{h}{4\pi}$, thus, shorter radiative lifetimes increase the uncertainty of energy states.
- **Doppler broadening**: Emitted frequencies are Doppler shifted by the translational motion of OH* radicals
- **Pressure/Temperature broadening**: The effect of collisions impact the statistical radiative lifetime, which again increases the uncertainty of energy similar to the natural broadening.
- **Instrumental line shape (ILS)**: Diffraction of light at finite instrumental components (slits, apertures, optical components) produces a further line broadening (see later instrumental discussion).

Different line shapes exist that are suitable to describe the above listed processes. The actual line shape is given by the convolution integral of contributing line shapes (see also Sect. 3.2). While the ILS-broadening is determined by the instrumental setup, the other processes listed above are controlled by the molecular properties of the emitting species as well as the altitude region. Apparently, pressure broadening is particularly important at lower altitudes, but plays a minor role in the rarefied mesopause region. The natural broadening of OH* is also considerably small, hence, Doppler broadening is the most important atmospheric process in determining the line shape of the OH* emission. According to Andrews [1987] the FWHM of Doppler broadening is given by:

$$\Theta_{\mathrm{D,FWHM}} = 2\frac{\sigma}{c}\sqrt{\frac{\ln(2) k_B T}{M_a}} \tag{2.7}$$

with the Boltzmann constant k_B, the molecular mass M_a, which in terms of unified atomic mass units is about 17 u for OH, and other parameters as previously defined. To give an impression of the effect of Doppler broadening, let us assume a mesopause temperature of 220 K and a spectral line at $\sigma = 8500$ cm^{-1}. As discussed in the following chapters, these values may serve as an upper boundary with regard to the spectral sensitivity of the instrument and mesopause temperatures. Accordingly, the FWHM of the Doppler broadening based on these values is about 0.02 cm^{-1}.

3. Instrumentation and measurement principles

In this work the OH* emission is measured with an FTIR spectrometer, which is located at the scientific village of Ny-Ålesund, Spitsbergen. As shown in Fig. 3.1, Ny-Ålesund lies slightly below 80° latitude. It is one of the very few permanent outposts at these high Arctic latitudes where several atmospheric measurements are conducted throughout the year. Since 1992, regular FTIR absorption spectroscopy measurements were performed by using either the sun or the moon as a light source [Notholt et al., 1997]. From the observed spectral absorption features several stratospheric as well as tropospheric trace gases are inferred above Spitsbergen. Due to the absence of sunlight during the polar night, these measurements are limited to a period of about 4 to 5 days around each full moon. The remaining operational time is freely available for airglow measurements, which have been performed since 2007 during the polar night. The next section discusses the principle of the FTIR spectrometer. This is followed by a brief overview on the MLS instrument onboard the Aura satellite, which is used for comparison with the ground-based measurements.

3.1. Bruker HR120/125 Fourier Transform Spectrometer

The spectrometer used in this work is a HR120/125[1] FTIR spectrometer from Bruker Optics. This instrument relies on the principle of a Michelson interferometer, which is illustrated in the left panel of Fig. 3.2. According to this schematic picture a collimated beam from a light source is split into two paths by the beamsplitter B. The splitting results from a thin coating layer (highlighted in yellow) upon a substrate with high transmissivity in the wavelength region of interest. Ideally, half of the incident light is either transmitted or reflected by the coating. Each light path follows a mirror arm where the light is reflected back to the beamsplitter as shown in this figure. The back reflecting mirror of the one arm is located at a fixed position. The mirror of the other arm can be moved back and forth along the optical axis such that the optical path length inside this arm can be changed continuously. If the optical path lengths of both mirror

[1] The original spectrometer version HR120 received an upgrade of its electronic components during autumn 2012. This upgrade turned it into version HR125, but the optical elements as well as the detector used for the OH* measurements remained unchanged. Therefore, this upgrade should not affect the actual OH* measurements.

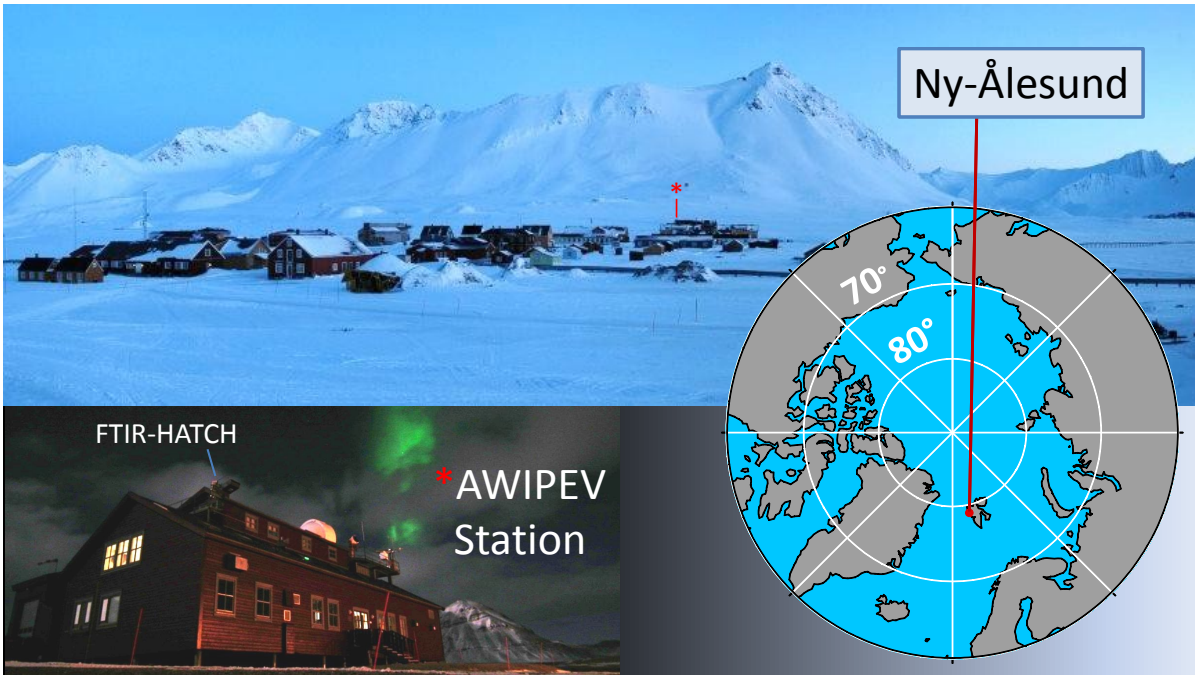

Figure 3.1.: The village of Ny-Ålesund and the AWIPEV research station, which is housing the FTIR spectrometer used in this work.

arms are equal, their back reflected beams interfere constructively with each other at the beamsplitter. The plate C in Fig. 3.2 compensates the additional optical path length due to the light travelling through the substrate medium of the beamsplitter coating. Accordingly, the plate C must have the same size, orientation and refractive index of the carrier substrate of B. In addition, the optical path length of the coating is also affecting the phase of penetrating light. For a monochromatic light source a layer thickness of $\lambda/4$ would result in a complete destructive interference of light towards the emission source, hence, the complete intensity of light arrives at the detector D in this case. Vice versa, if the optical path difference x between both mirror arms is $\lambda/2$, the mixed light towards the detector interferes completely destructively. Usually, polychromatic light sources are investigated. Therefore, only at $x = 0$ all harmonic components will interfere constructively at the beamsplitter, else, the intensity of light at the detector is modulating as a function of the optical path difference. By *scanning* the movable mirror along the optical axis, the measured modulated intensity versus x is called interferogram. As we will soon discuss, the interferogram can be converted to a spectrum by means of Fourier transformation.

The light source in this work is the OH* emission. Because of the long travelling distance, the incident light can already be assumed to be collimated. It is guided inside the laboratory by movable mirrors, which are located inside a hatch on top of the roof of the AWIPEV building (Fig. 3.3, left panel). To protect these mirrors during bad weather conditions the station engineer can manually close the hatch. However, because

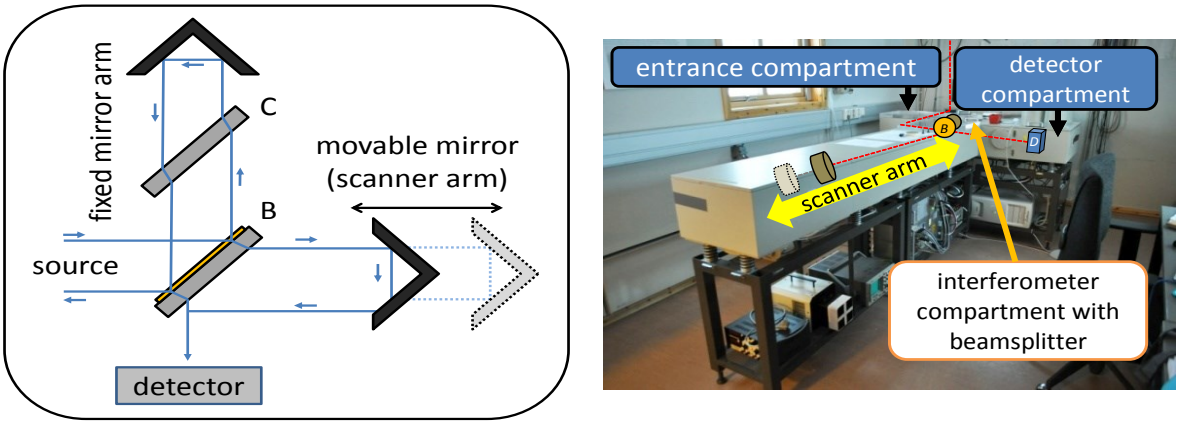

Figure 3.2.: Left panel: Principle of a Michelson interferometer. Right panel: Bruker HR120/125 spectrometer used in this work.

of the permanent operation of OH* measurements during the polar night, additional windows were mounted to the hatch, such that it can remain closed during the period of OH* measurements as shown in the right panel of Fig. 3.3. To prevent the icing of the window glasses due to the upwelling warm laboratory air, the hatch is connected with a ventilated tube to the laboratory. Below this tube, the atmospheric light is further guided by a plane mirror into the first compartment of the spectrometer where the collimated beam is focused on an aperture wheel, before it is collimated again on the beamsplitter according to the schematic picture above. The actual spectrometer is shown in the right panel of Fig. 3.2 where all compartments are denoted correspondingly.

This type of a spectrometer has certain advantages as frequently outlined in the literature (e.g. see Herres and Gronholz [1984]):

- **Connes advantage**: A high spectral accuracy is achieved from the precise measurement of the optical path difference x. This is usually done by coupling an additional laser beam into the light path of the instrument. From the self-interference of this beam x can be sensed by the precision of the laser wavelength.

- **Multiplex- or Fellget advantage**: All frequencies emanating from the light source impinge simultaneously on the detector.

- **Jacquinot advantage**: The simultaneous observation of an entire frequency range allows for a higher throughput of radiation.

It should be noted, though, that the multiplex advantage is limited by the optical properties of the instrument and the responsiveness of the selected detector. Optical components (i.e. window glasses, beamsplitter and mirrors) will always suffer from transmission

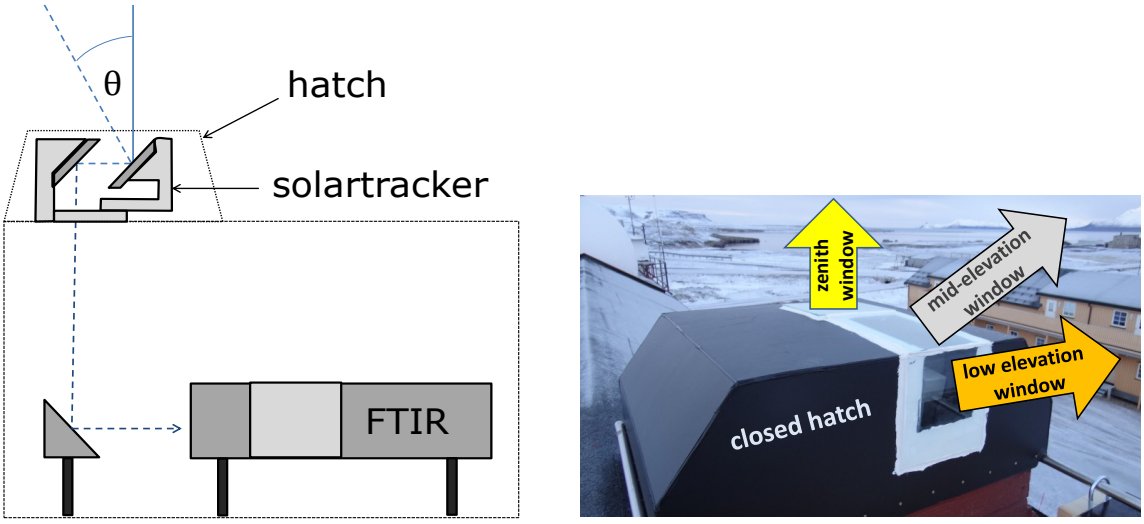

Figure 3.3.: Left panel: Schematic lightpath from the solartracker to the FTIR spectrometer. Right panel: Closed hatch with windows.

losses and have a limited spectral bandwidth. The same also applies for the responsiveness of the detector. Optical properties of different beamsplitters and detectors are shown in Fig. 3.4.

Depending on the spectral region of interest, an optimal combination of detector and beamsplitter should be used. This work uses an Indium Gallium Arsenide (InGaAs) detector together with a coated calciumfloride (CaF_2) beamsplitter, which are both suited to the spectral region between about 5500 and 8000 cm^{-1} wavenumbers[2].

The InGaAs detector belongs to the class of photodetectors, which are commonly used for the infrared spectral region. According to the theory of the electronic band structure of a semiconducting material, incident photons can move bound electrons from their valence band to a higher energetic conducting band where they freely propagate. This requires that the photonic energy is sufficient to overcome the bandgap between both bands. From the Planck relation Eq. (2.3) it follows that wavelengths of incident photons must be below a certain cut-off wavelength, which corresponds to the bandgap of the material. Again, the bandgap depends on the lattice parameters by determining the strength of the potential seen by the electrons. Accordingly, the energy gap becomes smaller when the interatomic distances increase. This can be achieved by changes in the relative composition of the InGaAs compounds or by thermal expansion of the material. On the downside, a smaller bandgap also increases the probability of electronic band transitions due to the thermal energy distribution of vibrating lattice atoms. The

[2]In the field of Fourier transform spectroscopy wavenumbers are commonly used as a spectral unit.

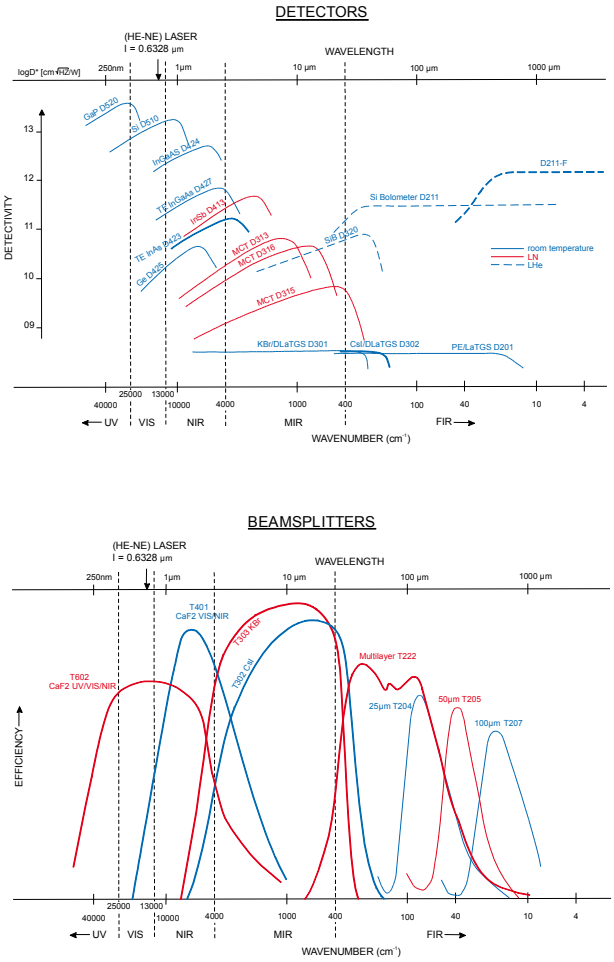

Figure 3.4.: Upper panel: Responsiveness curves of different detectors. Lower panel: Sensitivity curves of different beamsplitters. Taken from Bruker [2011]

resultant induced dark current obscures the measured voltage at the semiconductor in response to the incident light and should be minimised correspondingly.

3.2. Rotational temperature retrieval

Based on the provided Fortran tool to calculate theoretical OH* emission lines, Fig. 3.5 shows several lines within the spectral sensitivity range of the instrumental setup. Each transition band ($\nu' \rightarrow \nu''$) is colour coded. In addition, the upper panel shows the atmospheric transmission based on a radiative transport calculation from the SFIT2 algorithm [Hase et al., 2004]. This calculation assumes a standard atmospheric profile with the line-of-sight in zenith direction. In particular the strong absorption features due to water vapour in the region between about 6700 and 7500 cm^{-1} complicate the ground-

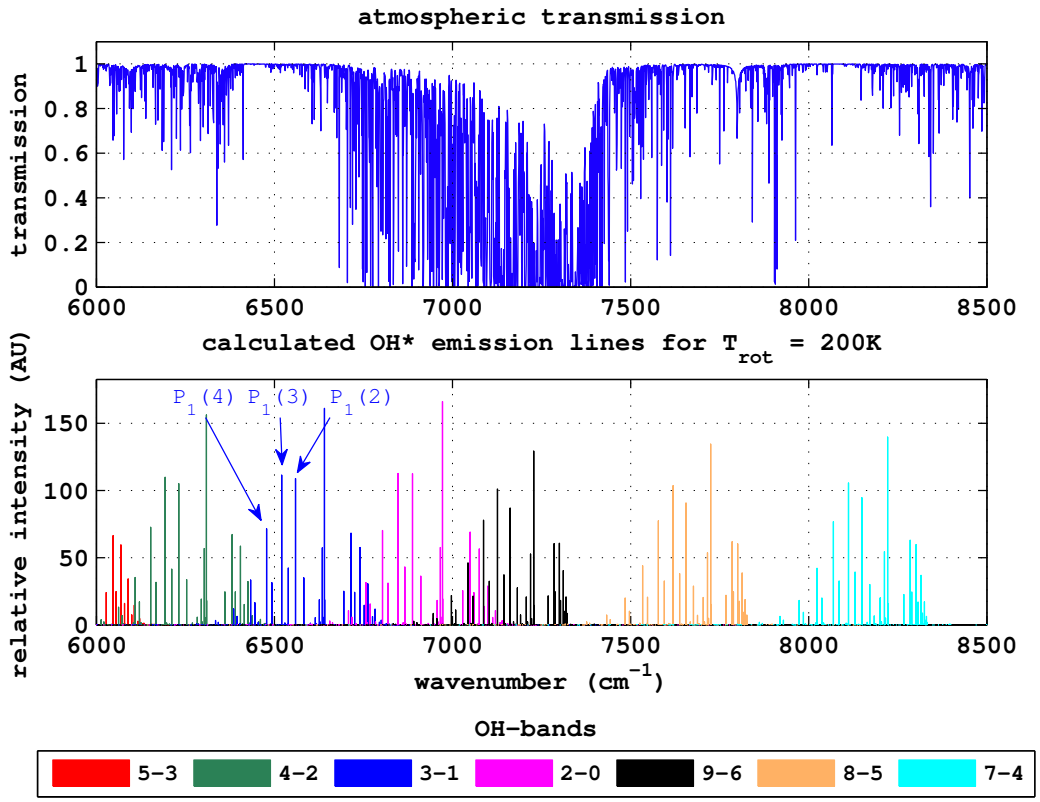

Figure 3.5.: Theoretical OH* line calculations and atmospheric transmission in zenith direction.

based observation of some emission bands. By comparison of the observed OH* Meinel bands above Ny-Ålesund, the OH(3-1) band appears to be a favourable ro-vibrational transition for the derivation of rotational temperatures for mainly two reasons:

- The emission lines lie in a region of high and rather constant atmospheric transmission.
- The initial excited state has a relatively long radiative lifetime, which favours the thermalisation of the rotational population.

The first point in particular applies for the emission lines of the $P_1(2)$, $P_1(3)$, $P_1(4)$ as well as the $P_2(2)$, $P_2(3)$, $P_2(4)$ transitions of the $X^2\Pi$ state. According to the previous chapter, these emission lines should result from a well thermalised rotational population, therefore, T_{rot} should be a good approximation of the ambient kinetic temperature.

Following up the previous section, the measured interferogram $I(x)$ of the OH* emission must be converted to a spectrum first, before further mathematical techniques can be applied to derive T_{rot}. The theory of this conversion is based on the Fourier analysis. A brief discussion of its principle idea is given as follows.

3.2.1. Fourier analysis

In a mathematical sense, $I(x)$ can be expressed as a superposition of sine and cosine functions as follows:

$$I(x) = \int_{-\infty}^{+\infty} E(\sigma) \exp(+i2\pi\sigma x) d\sigma \equiv \mathscr{F}\{E(\sigma)\}. \tag{3.1}$$

This expression already contains the spectrum E we are interested in. The operation $\mathscr{F}$ is called the Fourier transform of the function $I(x)$. Vice versa, the inverse Fourier transform $\mathscr{F}^{-1}$ is given by[3]:

$$E(\sigma) = \int_{-\infty}^{+\infty} I(x) \exp(-i2\pi\sigma x) dx \equiv \mathscr{F}^{-1}\{I(x)\}. \tag{3.2}$$

Physically, the integration over negative wavenumbers does not appear meaningful, but it plays an important role in the symmetric transformation between the spatial and wavenumber domain [Davis et al., 2001]. In addition, the infinite limits in the integration of optical path differences x in Eq. (3.2) is not achievable by a real physical measurement, but also the sampling of the interferogram $I(x)$ takes place at discrete rather than continuous steps. Replacing the continuous integration by a finite summation,

$$\int_{-\infty}^{+\infty} dx \rightarrow \Delta x \sum_{-N}^{N-1} \quad ,$$

turns Eq. (3.2) into its discrete form:

$$E_L(\sigma) = \Delta x \sum_{j=-N}^{N-1} I(x_j) \exp(-i2\pi\sigma x_j) \quad ; \quad x_j = j\Delta x. \tag{3.3}$$

This corresponds to the discrete sampling of $2N$ points in the spatial domain from $x = -L$ to $x = L$ at equally spaced intervals Δx with $L = N\Delta x$. Accordingly, the spectrum itself consists of $2N$ points in the spectral domain with a resolution width of:

$$\Delta\sigma = 1/2L. \tag{3.4}$$

The effect of the finite path difference can be expressed by an infinitely long interferogram multiplied with a finite boxcar function:

$$\Pi_{2L}(x) = \begin{cases} 1, & |x| \leq L \\ 0, & |x| \geq L \end{cases} \quad . \tag{3.5}$$

[3]It should be noted that other definitions of $\mathscr{F}$ and $\mathscr{F}^{-1}$ exist in the literature, where the sign of each exponential function is reversed. However, for symmetric functions both operations are the same, thus, in this case the selection of the sign has no scientific meaning. The definition used here is adapted from Kauppinen and Partanen [2001].

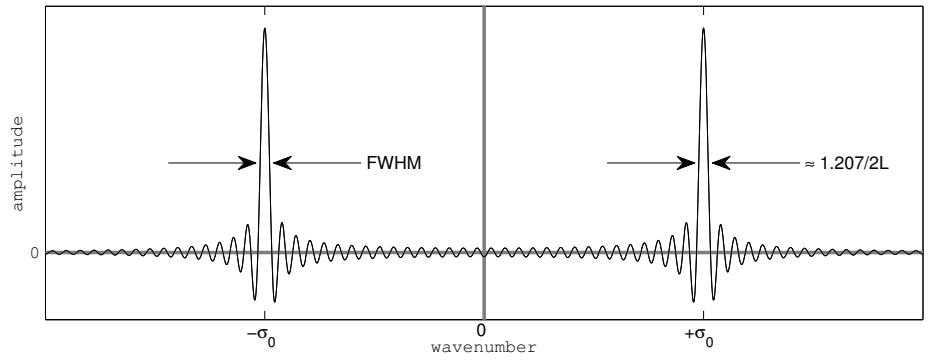

Figure 3.6.: Sinc function in the spectral domain due to the finite instrumental optical path length L. The mirror image at negative wavenumbers results from the inverse Fourier transform of the interferogram.

According to the convolution theorem of Fourier analysis, the inverse Fourier transform of a product of two functions is equivalent to the convolution of the inverse Fourier transforms of each function:

$$\mathscr{F}^{-1}\{f \cdot g\} = \mathscr{F}^{-1}\{f\} * \mathscr{F}^{-1}\{g\} \tag{3.6}$$

with

$$f * g \equiv \int_{-\infty}^{+\infty} f(u)g(x-u)du. \tag{3.7}$$

The inverse Fourier transform of a boxcar function is given by

$$\mathscr{F}^{-1}\{\Pi_{2L}(x)\} = \int_{-L}^{+L} \exp -i2\pi\sigma x dx = 2L\mathrm{sinc}(2\pi\sigma L) \tag{3.8}$$

with the sinc function

$$\mathrm{sinc}(x) = \frac{\sin(x)}{x}. \tag{3.9}$$

Let us now assume a spectral line that is represented by a Dirac delta function $\delta(\sigma)$, i.e. it has a zero line width and its area is normalised to 1. In this special case the convolution of the Dirac delta function with an ordinary function $f(x)$ will reproduce the same function:

$$\int_{-\infty}^{+\infty} \delta(u)f(x-u)du = f(x) \tag{3.10}$$

When replacing $f(x)$ with the sinc function according to Eq. (3.8), it is evident that even given a spectral line of infinitesimal width the resolved spectral line width has a finite value of at least FWHM $\approx 1.207/(2L)$ due to the finite optical path length of the instrument as shown in Fig. 3.6. Therefore, Eq. (3.8) is also referred to as the *instrumental function*.

The finite size of the entrance aperture introduces another instrumental effect on the spectral line shape. This effect can be understood by consideration of different path lengths of light from the finite aperture to the detector, which produce a fringing pattern around the focal plane of the detector. These fringes can be described by the multiplication of the interferogram with a sinc function. By analogy with Eq. (3.8) the inverse Fourier transform of a sinc function is represented by a boxcar function. According to the convolution theorem (3.6) it follows that a boxcar shape *aperture broadening* is introduced in the spectral domain correspondingly. This type of line broadening increases with the size of the entrance aperture. On the other hand, a maximum optical throughput should be achieved for the measurements of the OH* emission, therefore the effect of aperture broadening should not conflict with the desired spectral resolution. According to the manufacturer of the spectrometer, the instrumental entrance aperture size leads to a spectral line broadening of[4]:

$$\Delta\sigma_{\mathrm{apt}} \geq \frac{d^2}{8f^2}\sigma \tag{3.11}$$

where d is the diameter of the aperture and $f = 418$ mm is the focal length of the HR120/125 spectrometer. If we use this equation to estimate the effect of aperture broadening in the spectral range between 6000 and 8500 cm^{-1} according to Fig. 3.5, the broadening should range between 0.61 and 0.8 cm^{-1} when choosing the maximum aperture setting of $d = 12$ mm. By comparison, the spectral resolution for the OH* measurements as a function of maximum optical path difference (OPD) is set to $\mathrm{RES}_\sigma = 1$ cm^{-1} in this work, which is generally greater than the estimated aperture broadening above. As shown by Kauppinen and Partanen [2001], the sinc distortion of the signal due to the finite scanning path (see Eq. 3.8) will dominate in this case, therefore the effect of aperture broadening is neglected in this work.

Recalling the estimated Doppler broadening of OH* emission lines of about 0.02 cm^{-1} in Sect. 2.3, the selected instrumental resolution of 1 cm^{-1} is still considerably larger. Therefore, the side lobes of spectral lines due to the introduced sinc functions will be noticeable. As outlined by Herres and Gronholz [1984] the intensity from the main lobe of a spectral line leaks into the side lobes, which therefore represents an artefact in the spectral domain. This effect is also referred to as *spectral leakaging* in the literature. In addition to the spectral leakaging of a single emission line, the side lobes of neighbouring emission lines can distort the line intensities of the main lobes. Again, recalling that the rotational temperature is represented by the relative spectral line intensities (see Eq. 2.6), the spectral leakaging could also affect the temperature retrieval. As shown by Davis et al. [2001], increasing the instrumental resolution, such that the instrumental function is of equal or smaller width compared to the actual width of the emission line, would be one possibility to reduce the effect of spectral leakaging. However, this would also be for the cost of additional sampling time. Another possibility is given by the so-called *apodization* of the spectrum. Instead of using a boxcar *window function*

[4]Formula taken from the OPUS 6.5 software manual.

to account for the truncated infinite interferogram in a real measurement, a decaying window function to zero with its centre around the point of maximum constructive interference, the so-called centre burst, is multiplied with the interferogram before it is Fourier transformed to the spectral domain. For instance, this function could be of triangular shape. The inverse Fourier transform of this product will have significantly reduced side lobes, but also the spectral line width has increased by more than one third compared to the case when multiplying the interferogram with a boxcar window [Herres and Gronholz, 1984]. Other, more complex functions exist with specific damping and line broadening properties and can be selected according to the individual preferences. This work uses the Blackman Harris 4-term window as an apodization function, which is given by Harris [1978]:

$$\begin{aligned} W_{\mathrm{BH4}} &= a_0 - a_1 \cos\left(\frac{2\pi}{N}n\right) + a_2 \cos\left(\frac{2\pi}{N}2n\right) - a_3 \cos\left(\frac{2\pi}{N}3n\right), \\ n &= 0, 1, 2, ..., N-1, \\ a_0 &= 0.35875,\ a_1 = 0.48829,\ a_2 = 0.14128,\ a_3 = 0.01168\ . \end{aligned} \tag{3.12}$$

The coefficients above correspond to the maximum side lobe reduction to a -92 dB level (found by Harris [1978]) and are also used by the OPUS spectral processing software of the spectrometer. According to Herres and Gronholz [1984] the W_{BH4} function is one of the best side lobe damping functions, even though the linewidth is somewhat similar to the triangular function.

Another issue that arises from the discrete sampling of the interferogram is the so-called *picket-fence effect*. In the worst case, a frequency component in the interferogram domain may lie exactly between two sampling points, which according to Herres and Gronholz [1984] can lead to an erroneous signal reduction of 36 %. Therefore, the picket-fence effect can also potentially distort the ratio of OH* emission lines, which again would impact the rotational temperature retrieval. Similar to the problem of spectral leakaging, we may overcome this effect by choosing a sufficient instrumental resolution, but again for the cost of additional sampling time. Another possibility to compensate for the picket-fence effect without increasing the instrumental resolution is by extending the discrete interferogram with zero points before performing the Fourier transform. This so-called *zero filling* or *zero padding* is equivalent to an interpolation in the spectral domain, which helps to reduce the picket-fence effect.

Not only does the discrete sampling distort individual emission lines, as discussed above. According to the sampling theorem (see Kauppinen and Partanen [2001]), a broad spectral band of periodic signals must be sampled at least with twice the wavenumber of the highest wavenumber component of the spectral band. The corresponding sampling interval is the so-called Nyquist frequency:

$$(\Delta x)_{\mathrm{Nyquist}} = 1/2\sigma_{\mathrm{max}}. \tag{3.13}$$

Any spectral components above this critical frequency are folded back in the spectral domain, which leads to a distortion of the spectrum due to aliasing. To avoid this, the sampling interval should not be greater than the interval according to Eq. (3.13).

The phase correction is another important aspect in terms of the Fourier transform, and briefly mentioned here. It becomes important when considering the measurement of a real interferogram. In the ideal case, the interferogram might be represented by a symmetric function. In this case, the complex part of the spectrum would vanish after the Fourier transform. However, this does not apply for the real case where the interferogram always contains some asymmetry. For instance, dispersive effects of the optical components lead to differences in the optical path lengths of different wavelength components, which induce an asymmetry to the interferogram that will distort the spectrum, if not considered by a specific phase correction method (e.g. see Davis et al. [2001]).

The actual computation of the inverse Fourier transform based on Eq. (3.3) would be a computational expensive task due to the usually large number of sampling points. Sophisticated algorithms exist that can efficiently reduce the computational load. These Fast Fourier Transform (FFT) algorithms are usually implemented in common spectroscopic software tools.

3.2.2. Iterative retrieval method

The method of determining the rotational temperature from a measured spectrum[5] follows a forward modelling approach as illustrated in Fig. 3.7. It begins with an initial guess of a rotational temperature, which is fed into the provided Fortran procedure to calculate a theoretical OH* emission spectrum. In the next step, the theoretical emission spectrum is corrected for the effect of atmospheric transmission and the spectral sensitivity of the instrument. With the help of the convolution theorem according to Eq. (3.6) the instrumental function is modelled by truncating the corresponding interferogram and by multiplying it with the W_{BH4} function given in Eq. (3.12). In addition, zero filling is applied to the interferogram before it is Fourier transformed back to the spectral domain. At this point, a first synthetic spectrum is generated and can be compared with the measured spectrum. Both spectra may probably differ and the goal is to adjust the synthetic spectrum by subsequent iterations according to Fig. 3.7 to minimise the associated residuum. This poses a non-linear least squares problem:

$$\sum_{i=1}^{k}(f(\sigma_i) - y(\sigma_i))^2 \rightarrow \min \tag{3.14}$$

with the synthetic spectrum $f(\sigma)$ and the measured spectrum $y(\sigma)$, both sampled at k points. The function $f(\sigma)$ is determined by a set of independent parameters, which

[5]The term "measured spectrum" will be used synonymously with "Fourier transformed measured interferogram" in the following.

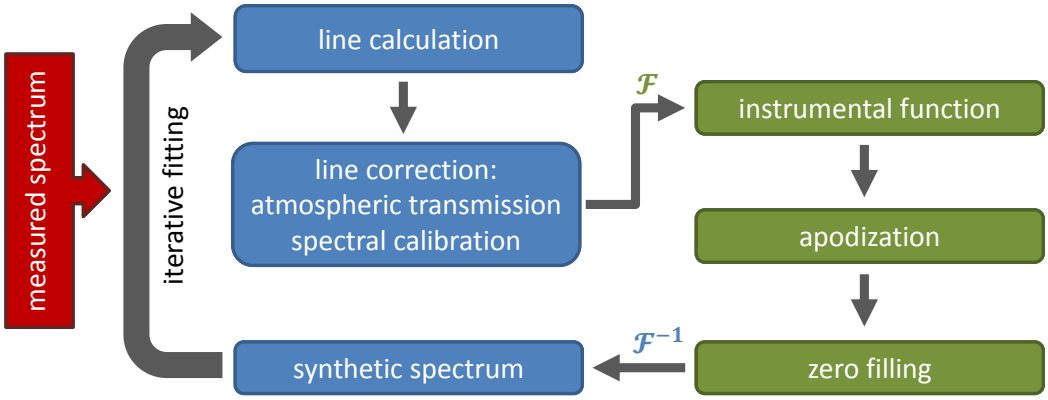

Figure 3.7.: Iterative spectral fitting of OH* emission lines to retrieve the rotational temperature.

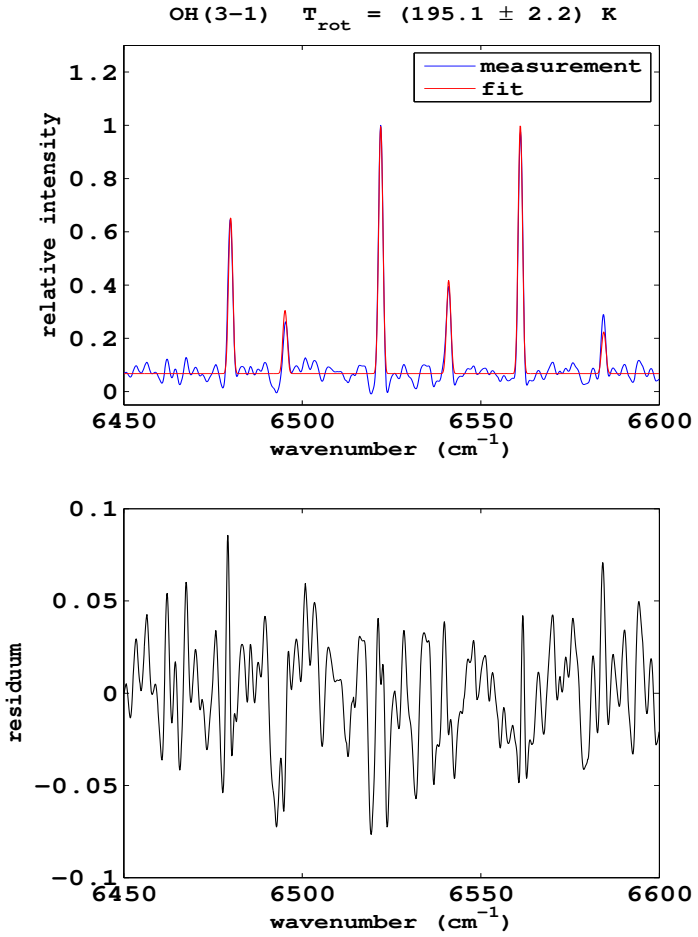

Figure 3.8.: Exemplary fit of an hourly averaged spectrum during 01-Jan-2011, 09:00 (UTC). Upper panel: Fit of OH(3-1) emission lines. Lower panel: Corresponding residuum

includes the rotational temperature T_{rot}. In addition, a scaling parameter as well as two offset parameters are included, i.e. one that accounts for a general frequency shift and one that accounts for an offset to the spectral intensity baseline level. It is important to note that the relative intensities of the emission spectrum are solely determined by the rotational temperature T_{rot} by analogy with Eq. (2.6). The minimisation according to Eq. (3.14) is then achieved by searching the optimum values for the set of parameters. Different mathematical methods exist to perform this task in an iterative fashion. This work uses the Gauß-Newton algorithm as a standard tool for the spectral fitting.

An example of a spectral fit is given in Fig. 3.8. This fit uses a spectral window from 6450 cm^{-1} to 6600 cm^{-1}, which encloses the first 3 rotational lines of the P_1 and P_2 branches of the OH(3-1) Meinel emission band. Both spectra are apodized with the same W_{BH4} window and contain the same number of grid points, which can be achieved by zero filling. The initial temperature guess for this fit is set to $T_{rot} = 200$ K, while the synthetic spectrum converged at $T_{rot} = 195.1$ K. By assuming that the errors of the individual parameters are independent from each other, we can relate the uncertainty of these parameters to the diagonal elements of the corresponding error covariance matrix, which in turn depends on the residuum between the measured and fitted spectrum. Based on this approach, a temperature uncertainty of ± 2.2 K is estimated for the spectral fit in Fig. 3.8. Different factors are influencing the amount of uncertainty and will be discussed in the next section.

3.3. Measurement uncertainty and noise

As mentioned above, the uncertainty of the retrieved temperature according to Fig. 3.8 is related to the residuum between the measured and fitted synthetic spectrum. Apparently, systematic errors will always be present on either side. For the synthetic spectrum, this includes imperfections of the spectroscopic line calculation, line correction, and the simulated instrumental function. Vice versa, instrumental errors are also introduced by various factors such as the misalignment of optical components, mechanical jitter of the mirrors, electronic noise of the spectrometer components, etc. Even given a perfectly operating spectrometer together with a perfect theoretical line calculation of the OH* emission, any persisting background photon flux, which is superimposing the OH* emission, will add noise to the spectrum. In the literature this situation is also referred to as the *background-noise limited case* (e.g. Birk and Brault [1988]), which in particular becomes significant for the OH* emission during twilight and daylight conditions, as already mentioned in Sect. 2.3. During the absence of sunlit conditions, other light sources such as the moon or street lamps may also produce a noticeable interfering background. But one may even think of an ideal case, where any light source other than the OH* emission would have been completely filtered out. Still, this ideal case would contain some residual fluctuation between the measured and fitted spectrum, because the impinging number of photons on the detector is subject of statistical fluctuations, which introduce *signal quantum noise*. Therefore, this represents the most preferable situation for the

observer, but in practice it is usually limited to faint emission sources that require the detection via cooled photomultiplier detectors with cooled amplifier stages [Leigh, 1996]. In contrast, the InGaAs detector used in this work operates at room temperatures. As discussed in Sect. 3.1 this leads to an increased probability of inducing thermal dark (noise) currents, but also the thermal noise inside other electronic components, such as the amplifier stages, is contributing to the instrumental noise level.

By reducing the measurement noise as much as possible, this will improve the measured spectrum with regard to its signal-to-noise ratio (SNR) and, therefore, it should also improve the goodness of the spectral fitting. Of course, this does not prevent from inefficiencies in the spectroscopy, but for the following let us assume that these are relatively small and that non-LTE conditions apply to a very good approximation for the observed OH* emission lines. In a quantitative sense, Birk and Brault [1988] proposed the following equation to estimate the SNR of a measured signal under the assumption of a negligible background photon flux:

$$\mathrm{SNR}_\sigma = \eta_M \sqrt{\frac{A_B \eta_F \eta_O \eta_q M(T_{\mathrm{source}}, \sigma)}{2(\Delta_{\mathrm{MOPD}})^3 \sigma_{max}} \frac{t_s}{\sigma_{\max} - \sigma_{\min}}} \tag{3.15}$$

with

$$\begin{aligned}
A_B &= \text{area of the parallel beam,} \\
\eta_M &= \text{modulation efficiency,} \\
\eta_F &= \text{transmittance of optical filters,} \\
\eta_O &= \text{optical efficiency of the instrument, including:} \\
&\quad \text{beamsplitter efficiency,} \\
&\quad \text{reflectance of mirrors,} \\
\eta_q &= \text{quantum efficiency of the detector,} \\
t_s &= \text{sampling time,} \\
\Delta_{\mathrm{MOPD}} &= \text{maximum optical path difference in the interferogram,} \\
\sigma_{\max} - \sigma_{\min} &= \text{spectral range,} \\
M(T_{\mathrm{source}}, \sigma) &= 2\pi c \sigma^2 / (\exp(hc\sigma / k_B T) - 1) \rightarrow \text{photon exitance}
\end{aligned}$$

The modulation efficiency η_M describes how well the information of the modulated signal in the interferogram domain is maintained by the real instrument compared to an ideal interferometer (see also Hase [2012]). It is in particular suffering from the misalignment of the optical components and therefore a precise realignment of the spectrometer should be performed at regular time intervals (i.e. once a year for the HR120/125). However, there are always certain limitations to the alignment procedure, e.g. the scanner arm might be bended to a small amount, such that the mirror sledge is moving in more than one direction during one scan, or mechanical jittering of the reflecting mirrors is caused

by the rapid change in direction at the point of maximum OPD. Therefore, the modulation efficiency will always be smaller than unity, if expressed as the ratio between the real and ideal modulation.

Optical filters help to minimise the background noise, but they will always lead to transmission losses, even around the spectral region of maximum transmission. As long as the background noise is not critical, which appears to be a plausible assumption for the nighttime observation of the OH* emission, one may exclude any optical filters in the light path to improve the SNR. However, another issue arises from the internal helium-neon (HeNe) laser signal of the FTIR, which is used to sense the OPD with high precision. Because this signal is coupled into the optical path of the instrument, it will also interfere with the InGaAs detector and heavily distort the OH* emission signal. To prevent this distortion an optical laser block filter was used in front of the InGaAs detector prior to 2010. Because of difficulties with the OH* signal strength in combination with the same filter in 2010, it was then replaced by a "paper block", which directly shades most of the laser reflexes but without blocking most of the source light beam.

The quantum efficiency of the detector corresponds to the ratio between detected and incident photons expressed in terms of their number Φ per second per wavenumber:

$$\eta_q(\sigma) = \frac{\Phi_{\text{detected}}(\sigma)}{\Phi_{\text{incident}}(\sigma)}. \tag{3.16}$$

It is worth noting that another measure of the detector efficiency exists, namely the detectivity D^*, which is preferably used by manufacturers as a figure of merit in their product descriptions. It is defined as:

$$D^*(\sigma) = \frac{A_D \Delta f}{\text{NEP}(\sigma)} \tag{3.17}$$

with the detector area A_D, the frequency bandwidth $\Delta f = 1/(2\pi t_s)$, and the noise equivalent power NEP, which corresponds to the signal power needed to yield an SNR value of 1. Despite its common usage as a figure of merit, Birk and Brault [1988] argue that this quantity can be quite misleading, because its values are obtained for the background-noise limited case, therefore any direct SNR estimates from this quantity must assume the same case. With respect to the OH* emission it appears that η_q is a more reliable quantity to classify the efficiency of the detector, therefore one should be cautious when comparing different detectors based on Fig. 3.4.

According to Eq. (3.15), narrowing the spectral range will improve the SNR in the spectral domain. This can be understood in terms of a *multiplex disadvantage*, as the simultaneous detection of photons will contribute to the *photon noise current*. Furthermore, a lower resolution width, which is contained in Δ_{MOPD} (see Eq. 3.4), will also improve the SNR.

Another method of increasing the SNR is to reduce random white noise by coadding several scans. Since the Fourier transform of white noise is again white noise [Davis et al., 2001], this may be done either in the interferogram or spectral domain. Because of the random variability of error signs, coadding of N scans will help to improve the SNR by a factor of $\sqrt{N}$ [Smith, 1995]. It is interesting to note that this operation is equivalent to the selection of a longer integration time according to Eq. (3.15). However, too slow sampling can result in some disadvantages, such as periodic $(1/f)$ noise from periodic fluctuations of the source or digitising noise due to the discrete sensing of intensity units, as described both in Davis et al. [2001]. In this case *rapid sampling* helps to reduce the associated noise so that coadding several scans will improve the SNR for the same sampling time t_s.

In summary, to gain a good SNR one should use a narrow band detector, avoid any higher resolution setting than needed for the spectral line discrimination and use a high sampling frequency. A further optimisation can be achieved by improving the overall efficiency of the instrument according to the η-parameters in Eq. (3.15). Apart from the goal of measuring with a sufficient SNR, any systematic changes of the wavelength dependent instrumental sensitivity should be accounted for the line correction according to Fig. 3.7. This is done by means of a spectral calibration with a blackbody source and will be discussed in the next section. In addition, the transmission of the hatch window is also systematically affecting the OH* signal and will be discussed in Sect. 3.5.

3.4. Determination of instrumental sensitivity

A blackbody radiation source was purchased to characterise the wavelength dependent instrumental sensitivity. The source consists of a blackbody cavity, which can be heated to a temperature of up to 1050°C with a precision of ±0.1°C. To produce a collimated beam of light, which can be coupled into the entrance compartment of the FTIR, a gold-coated off-axis parabolic mirror with a high and fairly constant transmissivity in the IR region is used in front of the blackbody cavity. In the frame of this work, both parts were mounted on a plate such that the parabolic mirror is completely covered by the field of view of the blackbody cavity. From the known temperature of the blackbody its spectrum can be estimated by a Planck curve. The blackbody spectrum is then altered by the wavelength dependent instrumental sensitivity function. Accordingly, the relative changes in the instrumental sensitivity can be estimated by dividing the measured blackbody signal with the calculated Planck curve from theory. Ideally, one should also account for the transmission losses of the gold-coated mirror in front of the blackbody, but also the blackbody will slightly depart from an ideal blackbody source. However, based on the manufacturer's classification sheets of both components it is assumed in this work that any wavelength dependent effects due to these departures are negligible in the spectral region of interest compared to the instrumental sensitivity function of the FTIR. Furthermore, since the rotational temperatures are retrieved from the relative intensities of OH* emission lines, an absolute calibration is not required for this task.

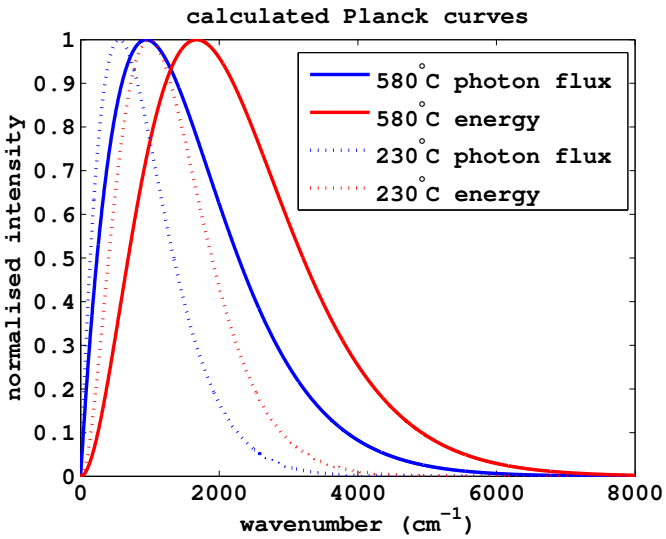

Figure 3.9.: Normalised Planck curves based on different units and temperatures (see legend).

Before calculating the Planck curve for a given blackbody temperature, one has to consider which units are the most appropriate for the detector in use. For instance, the output signal of a thermal detector, such as a bolometer, is proportional to the incident energy flux. In this case, the Planck curve should be expressed in terms of energy flux as a function of wavenumber, which according to Davis et al. [2001] is given by:

$$B_e(\sigma, T) = \frac{2hc\sigma^3}{\exp\left(\frac{hc\sigma}{k_B T}\right) - 1} \quad (\mathrm{Wm^{-2}sr^{-1}/cm^{-1}}). \tag{3.18}$$

Note that the equation above assumes that c is expressed in units of cm/s instead of m/s, otherwise we would have to multiply $\sigma(\mathrm{cm^{-1}})$ by a factor of 100. In contrast to the expression above, the output signal of a photomultiplier detector is proportional to the number of impinging photons, but does not depend on the photonic energies. Therefore, the Planck curve should be represented in units of photon flux:

$$B_p(\sigma, T) = \frac{2\pi c\sigma^2}{\exp\left(\frac{hc\sigma}{k_B T}\right) - 1} \quad (\text{photons m}^{-2}\mathrm{sr^{-1}/cm^{-1}}). \tag{3.19}$$

As illustrated in Fig. 3.9, the shape of the Planck curve does not only depend on the blackbody temperature, but also on the selected units. Despite the slightly smaller quantum efficiency η_q of the InGaAs detector compared to a photomultiplier detector, its response should be rather similar. Therefore, the calculation of the Planck curve is performed in photon flux units for the InGaAs detector used in this work.

Two examples of measured Planck curves and the inferred instrumental sensitivity are shown in Fig. 3.10. Here, the left panels are based on a selected blackbody temperature of 230°C and the right panels are based on a selected blackbody temperature

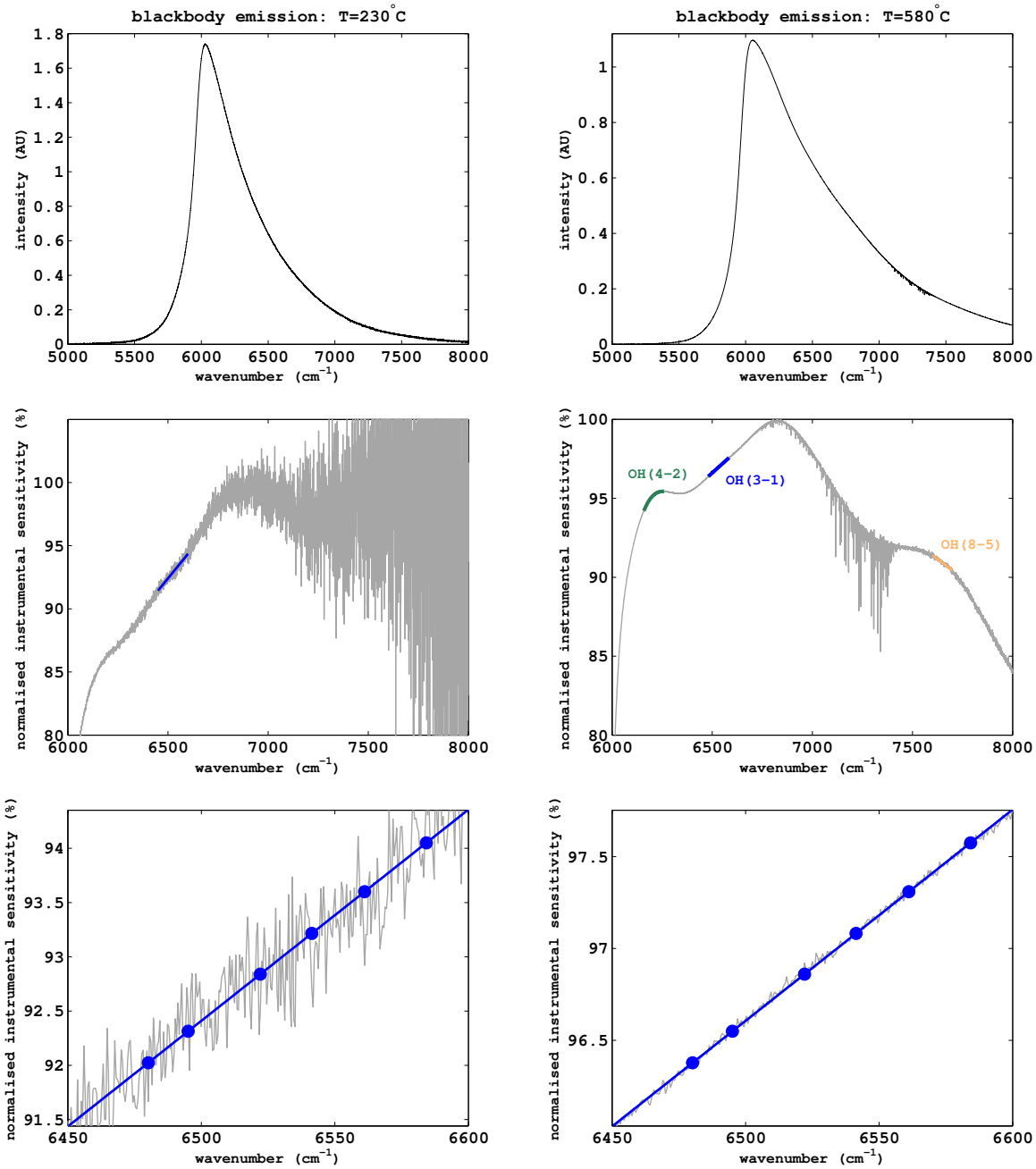

Figure 3.10.: Instrumental sensitivity from measured Planck curve (using InGaAs detector and 12.5 mm entrance aperture) of a 580°C (right panels) and 230°C (left panels) blackbody source signal: The upper panels show the measured blackbody signal for each temperature. Calculated instrumental sensitivity plots for each temperature are shown below. The fitted spectral ranges of the first 3 main emission lines of the P_1 and P_2 branch of different OH* Meinel emission bands are highlighted in the middle panels. The position of the OH(3-1) emission lines is denoted by the circles in the close-up view in the lower panels.

ΔT :	min	max	mean
OH(3-1)	0.71 K	1.83 K	1.16 K
OH(4-2)	0.44 K	1.38 K	0.81 K
OH(8-5)	-1.13 K	-0.45 K	-0.76 K

Table 3.1.: Impact of the instrumental sensitivity correction functions on the hourly rotational temperatures from 2008 to 2012 shown in Sect. 4.3. The first/second value in each row indicates the minimum/maximum temperature change $\Delta T = T(\text{with correction}) - T(\text{without correction})$ found in the 2008–12 time range due to the applied correction function. The third value indicates the average change of all temperature results due to the correction function.

of 580°C. The measurement of the 230°C blackbody signal was performed with the same instrumental settings as used for the OH* emission measurements. By increasing the blackbody temperature to 580°C, the detected interferogram signal already starts to clip. To avoid any clipping of the signal, a lower pre-amplifier stage of the InGaAs detector was selected for the measurements. By doing this, we have to assume that the change in the signal pre-amplification does not affect the shape of the instrumental sensitivity function.

The determined instrumental sensitivity from both measurements is shown in the second row of Fig. 3.10. By comparison with the measured Planck curve shown in the first row of Fig. 3.10, we notice that the apparent noise level is now increasing with wavenumber in contrast to the measured spectrum[6]. Apparently, we have to bear in mind that by dividing the measured blackbody signal with the theoretical Planck curve, we are also scaling the apparent noise level in the spectral domain according to the shape of the Planck curve. This in particular becomes visible for the 230°C measurement, where the determined instrumental sensitivity becomes barely visible above 7200 cm^{-1} according to Fig. 3.10. The situation improves for the 580°C measurement, as the Planck curve is shifting towards the spectral range, where the instrument becomes more sensitive (see Fig.3.9). In this case, the shape of the instrumental sensitivity curve is still nicely resolved for the spectral range of the OH(8-5) Meinel band (generally abbreviated "OH($\nu' - \nu''$) band" in the following). Vice versa, for lower wavenumbers, which enclose the OH(3-1) and OH(4-2) bands, the instrumental sensitivity still appears to be sufficiently resolved for both blackbody temperature settings, so that we can estimate the relative change in the instrumental sensitivity by a linear fit for the OH(3-1) and by a polynomial fit for the OH(4-2) and OH(8-5) bands as shown in Fig. 3.10.

Let us now compare the relative change in the linearly fitted instrumental sensitivity in the OH(3-1) wavelength region of the $P_1(4)$ and $P_2(2)$ transition, i.e. the outermost rotational lines used for temperature retrieval (see lower panels of Fig. 3.10). For the

[6]If we suppose mainly stationary white noise in the measured interferogram domain, this equally transforms to the spectral domain as stated in Sect. 3.3.

230°C based measurement the sensitivity drops by 2.2 ± 0.1 % towards lower wavenumbers. Here, the uncertainty is estimated from the calculated standard error of the slope parameter (see A.1). For the 580°C based measurement the drop in the instrumental sensitivity is about 1.22 % with an uncertainty smaller than 0.03 %. Accordingly, the uncertainty in the fitting plays a negligible role compared to the deviation of about 1 % between both measurements. A list of further blackbody calibration results can be found in the appendix (A.1) where different settings (blackbody temperature, aperture size, pre-amp stage) have been tested for the measurements. This list also includes separate results for the forward and backward-scan mode[7] of the scanner arm, but the overall deviation between both scanning modes is smaller than 0.1 % in most cases and therefore negligible for the rotational temperature retrieval. In general, the decrease of the instrumental response towards lower wavenumbers in the OH(3-1) fitting region ranges between 1 % and 2 %. This also shows that the different blackbody settings did not result in a major difference in the determined (relative) instrumental sensitivity in the spectral fitting region of the OH$(3-1)$ band. The same situation also applies for the OH$(4-2)$ band.

If we expanded the spectral fitting region, the correction for the instrumental response would become more important. However, as previously discussed, the inclusion of emission lines from higher non-thermalised rotational states can introduce non-LTE conditions, which would complicate the theoretical line calculation. Furthermore, if we expanded the spectral region across multiple OH* Meinel bands, these would require the consideration of individual rotational temperatures in the theoretical line calculation. This is because the emission from different OH* Meinel bands typically arises from different altitude regions with different ambient temperatures, as we will discuss in the chapters 4 and 5. It is for these reasons that this work only accounts for a single OH* Meinel band in the derivation of a rotational temperature and limits the spectral fitting to the spectral region of the corresponding first three main lines of the P_1 and P_2 transitions.

Based on the listed blackbody calibration measurements in the appendix A.1, an average instrumental response function was estimated for the OH(3-1) and OH(4-2) bands and taken into account for the whole time series. For the OH(8-5) band, the instrumental response function was estimated from the 580° C blackbody measurement in Fig. 3.10 to make sure that it is sufficiently resolved in the measurement. With respect to the later analysis of the temperature time series above Ny-Ålesund, the impact on the hourly rotational temperature estimates is rather small for all emission bands as summarised in Tab. 3.1.

[7] The interferogram can be recorded either while the scanner arm is moving away from the centre-burst (forward-scan) or towards the centre-burst (backward-scan).

3.5. Window transmittance

The method of determining the transmittance of the hatch windows is similar to the previously discussed blackbody calibration. Again, the collimated beam of the blackbody radiation source is coupled into the FTIR. Then, two measurements are taken, i.e. one measurement where the collimated blackbody beam has to penetrate through the window glass and one measurement without any window glass in the optical path. The latter measurement serves as a background radiation measurement. By dividing the first measurement with the background radiation measurement we get the transmittance of the window.

Due to the size of the hatch and limited space inside the FTIR laboratory, a detachment of the glued hatch windows would have been necessary to conduct the measurements inside the laboratory. Instead, the measurements were performed directly on the roof of the building as shown in Fig. 3.11. For the measurements of the front window transmittance, the blackbody was placed in front of the so-called solar tracker mirrors, which guide the collimated beam into the FTIR laboratory (see left panel of Fig. 3.11). Both measurements that are required to characterise the window transmittance are then performed when the hatch is either opened or closed. This makes the situation more challenging for the zenith window, because it would require a platform that can safely carry the blackbody setup with a total weight of more than 10 kg above the solar tracker while the hatch is either opened or closed. Instead, a more simple carrying plate was mounted on the blackbody setup, which allowed to point the blackbody beam through the zenith window as shown in the right panel of Fig. 3.11. On the downside of this approach, we have to relocate the blackbody setup for the background measurements. In this case, we simply use the same background measurements that were taken for the front window setup and assume that any impacts due to misalignments are negligible.

The determined transmittances curves for the front and zenith windows are shown in Fig. 3.12. In each case, the transmittance curve can be approximated by a two-order polynomial function. If we use the data points between 6000 and 7000 cm^{-1} (highlighted in green), the polynomial fits agree quite well in this spectral region for both hatch windows. We therefore use the associated fitting parameters for the later correction of the OH(4-2) and OH(3-1) line calculation. For the spectral range of the OH(8-5) emission lines, the noise level has noticeably increased due to the decreasing instrumental sensitivity and blackbody radiance. With regard to the front window, the transmittance appears to be rather constant according to Fig. 3.12, implying that the impact on the rotational temperature retrieval should be small. For the zenith window, the transmittance seems to drop further within the OH(8-5) spectral range, but the noise level makes an estimate difficult. It is for these reasons that at this stage the impact of the window transmittance is only considered for the OH(3-1) and OH(4-2) bands in the following.

Within the spectral range of the $P_1(4)$ and $P_2(2)$ transition of the OH(3-1) band the

Figure 3.11.: Blackbody setup to measure the transmittance of hatch windows. The parallel blackbody beam is guided by the movable mirrors (solar tracker) inside the FTIR laboratory. Left panel: Setup for background signal (open hatch). Right panel: Setup to measure the transmittance of the zenith window (closed hatch).

relative change in transmittance is about 1 % for the zenith window and less than 0.4 % for the front window. Because the window transmittance is decreasing with increasing wavenumbers in both cases, these results suggest that the window transmittance is also partially compensating the impact of the instrumental sensitivity function in the same spectral range. With regard to the OH(4-2) band, the relative change in the window transmittance is even less compared to the OH(3-1) band, as we can see in Fig. 3.12.

In addition to the relative changes in the window transmittance, which are critical for the rotational temperature retrieval, it is also interesting to look at the overall change in the emission signal amplitude. For the front window the signal amplitude of the measured interferogram dropped by about 13 % once the hatch was closed. In comparison, the loss is quite striking for the zenith window, where the signal amplitude dropped by a factor of 4, implying a significant signal loss at the zenith window. In this context, two difficulties in the measurements should be noted.

As mentioned above, both measurements that are required for the determination of the zenith window transmittance were performed with different blackbody positions. Each position required a new manual alignment of the blackbody setup together with the solar tracker mirrors. Hence, the large drop in intensity could be due to the difficult manual alignment of the experimental setup. In contrast, the front window measurements were performed with the same instrumental alignment, because no change of the blackbody position was required.

Another important issue is an existing misalignment of the FTIR during these measurements, which were shortly performed after the instrumental upgrade of the spectrometer to version HR125. Unfortunately, this misalignment was also severely distorting the

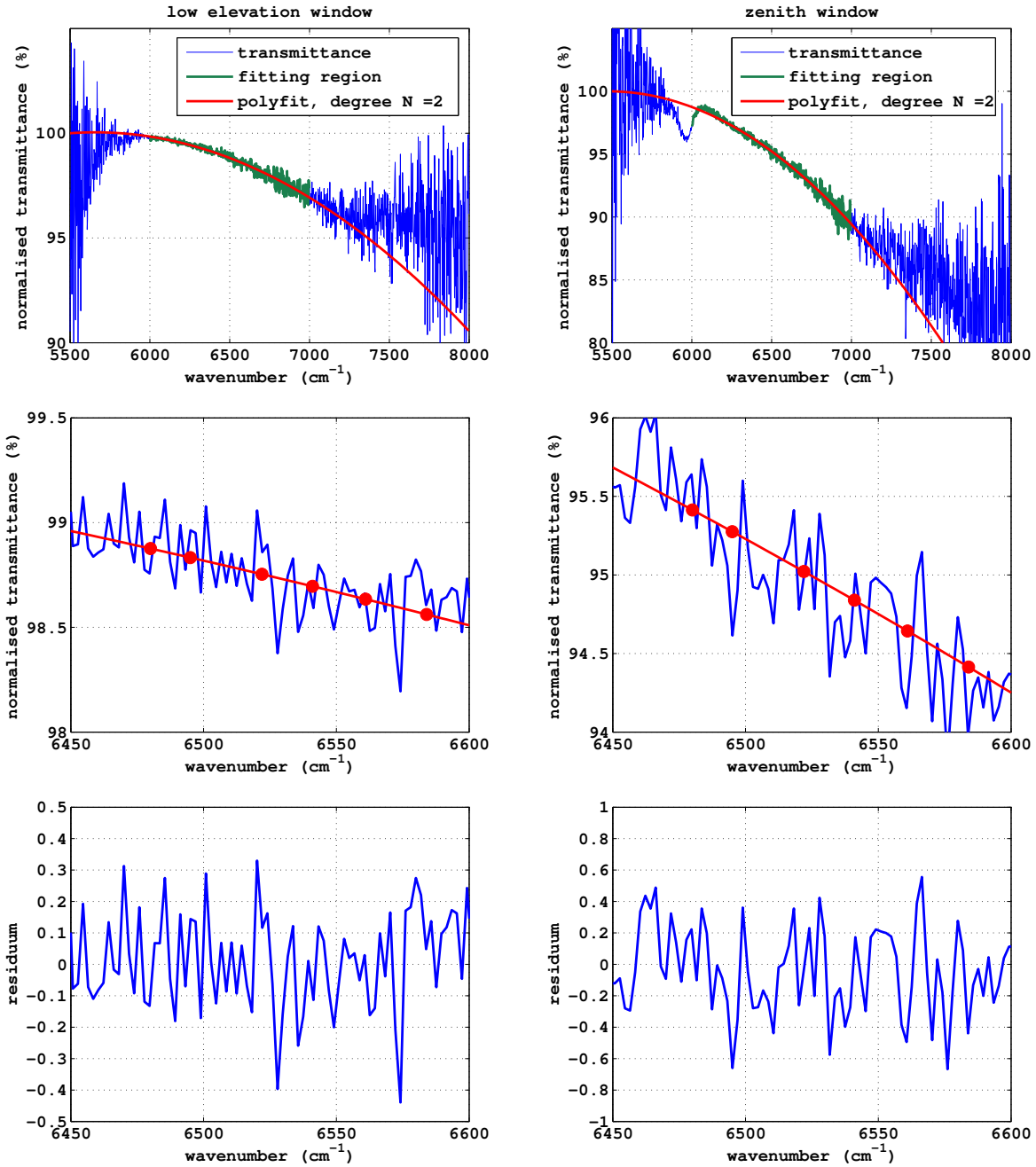

Figure 3.12.: Measured transmittance of low elevation hatch window (left panels) and zenith hatch window (right panels). A quadratic polynomial is used as a fit function (red line), while the fitting region is highlighted in green. The middle panels show a close-up view of the spectral region, which encloses the first 3 main lines of the P_1 and P_2 branches of the OH(3-1) emission (denoted by circles). The lower panels show the residuum between the measured and fitted transmittance.

ΔT :	min	max	mean
OH(3-1)	0.17 K	1.38 K	0.81 K
OH(4-2)	0.33 K	1.53 K	0.87 K

Table 3.2.: Impact of combined correction for the instrumental sensitivity and window transmittance (low elevation and zenith) on the rotational temperature results from 2008 to 2012 by analogy with Tab.3.1

OH* measurements during the polar night in 2012–13. In a following routine realignment of the instrument in February 2013, a problem in the positioning of the scanner arm was identified and solved by the IUP engineer. This also led to a significant improvement of the OH* signal.

Despite the identified instrumental misalignment, this issue may be less critical for the measurements of the windows transmittance, because any systematic impacts on the instrumental sensitivity should cancel out when dividing the transmitted signal by the measured background.

Due to the small relative changes in the determined window transmittance within the spectral windows of the OH(3-1) and OH(4-2) bands, the impact on the temperature retrieval remains small. Table 3.2 shows the impact on the temperature results when accounting for the combined effect of the instrumental sensitivity and window transmission in the emission line calculation. Accordingly, the impact of the line correction is in the order of 1 K or less than 1.6 K at maximum for the considered time range from 2008 to 2012.

3.6. Thermal stability of uncooled InGaAs detector

The previous two sections were concerned with the classification of the instrumental sensitivity, including the transmittance of the hatch windows. This classification was based on a limited number of measurements of a blackbody calibration source, hence, we have to assume that the instrumental drift between these measurements does not have any significant impact on the continuous measurements of the OH* emission during the polar night. In addition, we should also keep in mind that the blackbody source is heating up the spectrometer including the detector, which are both not temperature controlled. Even though, the change in the instrumental sensitivity appears to be rather small based on different calibration measurements with different blackbody temperatures, the implementation of an uncooled InGaAs detector led to some concerns with regard to its thermal stability and the associated impact on the instrumental sensitivity. Typically, airglow detector systems, such as the GRIPS (Ground based Infrared P-branch Spectrometer) instruments as part of the NDMC network, employ cooling techniques to the detector design. Not only does this improve the thermal stability of the detector system,

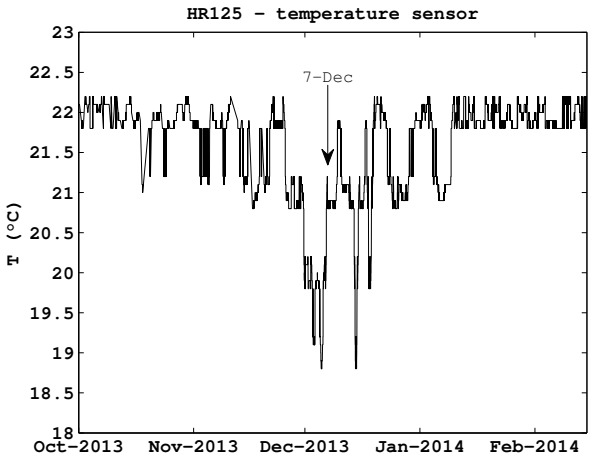

Figure 3.13.: Recorded temperature inside the interferometer compartment of the HR125.

but it also reduces the thermal noise.

With regard to our existing concerns, a potential validation method of the thermal stability of our detector was suggested to us by Prof. Dr. P. J. Espy, Norwegian University of Science and Technology, Trondheim. This method has the advantage to be completely independent from any "artificial" calibration source. Instead, this method can be directly applied to the measured OH* spectra and was implemented in this work to validate the temporal stability of our detector response.

The principle of this method relies on the observation of OH* emission lines, which we suppose to have a constant ratio in their intensities with time. To find these lines, let us assume a Boltzmann distribution of rotational states within a vibrational band according to Eq. (2.5) of Sect. 2.3. Furthermore, let us consider two different rotational transitions of the same vibrational band, which originate from the same initial rotational state J'. In this case the ratio between both intensities simplifies to the following equation:

$$\frac{I_{(i',\nu',J' \rightarrow i'',\nu'',J'')}}{I_{(i',\nu',J' \rightarrow i'',\nu'',J''')}} = \frac{A_{(i',\nu',J' \rightarrow i'',\nu'',J'')}}{A_{(i',\nu',J' \rightarrow i'',\nu'',J''')}}. \tag{3.20}$$

Despite the previously mentioned ongoing discussion on the appropriate values for the Einstein coefficients A, these should be, to a very good approximation, constant in time. Therefore, we may relate any temporal changes in the ratio above to changes in the instrumental sensitivity, which arise from the thermal instability of the detector response or from any other instrumental drifts.

With the instrumental upgrade of the HR120 to version HR125 in autumn 2012, the spectrometer received a temperature sensor inside the interferometer compartment.

Temperature values are synchronously recorded with the spectra, so that we can directly compare time invariant OH* emission intensity ratios with the instrumental temperature records. By doing this, we assume that the temperature contrast between the interferometer and detector compartment, which are directly connected with each other, is negligible. A time series of instrumental temperatures is shown in Fig. 3.13. Temperatures were ranging between 19° C to 22° C. Unfortunately, a software bug inside the spectrometer caused an output error of the first fractional digit, which caused the jumps between $\Delta T = 0.3°$ C and 0.7° C in Fig. 3.13. However, after consultation with the spectrometer manufacturer Bruker, it should be reasonable to assume a precision of $\pm 0.5°$ C for the recorded temperatures.

A selection of three time invariant intensity ratios for the OH(3-1) and OH(4-2) bands is plotted against instrumental temperatures in Fig. 3.14. The initial rotational state J' and the wavenumbers of emission lines are denoted in the lower table of Fig. 3.14.

Each point in the scatter plots represents a single intensity ratio between two emission lines from a single spectrum that was integrated over an approximate time of 13 min. Corrections from the spectral calibration, window transmission, atmospheric transmission, and the zero offset to the spectral baseline have been considered in the determination of intensity ratios. As we can see, for most intensity ratios a significant correlation to the changes in the instrumental temperatures is missing. Only the $R_1(1)/P_1(3)$ intensity ratio of the OH(3-1) band shows a weak anti-correlation that is already statistically significant with respect to a 99% confidence level. In comparison with the other selected emission lines of the same emission band, the offset to the considered spectral range in the temperature retrieval is largest for the $R_1(1)$ transition, so the actual impact on the retrieval may be still insignificant, as also suggested by the other line ratios. We get back to this point again in Sect. 4.3 where we compare the time series of rotational and instrumental temperatures in 2013–14 with each other.

As a side aspect of the measured intensity ratios it is worth comparing the experimental values with those predicted from theory. French et al. [2000] did such a comparison for their experimental observations of the OH(6-2) emission with a Czerny-Turner scanning spectrophotometer at Davis, Antarctica. Similarly to this publication, Tab. 3.3 compares the measured intensity ratios by the HR125 with the same set of theoretical studies, but now referring to the OH(3-1) and OH(4-2) bands. The experimental values refer to the mean of all samples and the uncertainty is indicated by the standard deviation of all sample points. We find that all theoretical intensity ratios lie in the uncertainty ranges of the experimental values, apart from the $Q_1(2)/P_1(3)$ intensity ratio of the OH(4-2) band, which is slightly above the upper boundary of uncertainty. Interestingly, the experimental results of French et al. [2000] are generally below the theoretically predicted values, even when taking their uncertainty estimates into account. Instead, we also find that the $Q_1(2)/P_1(2)$ mean value of the HR125 nicely matches the theoretical values for the OH(3-1) band and appears to be even higher for the OH$(4-2)$ emission band,

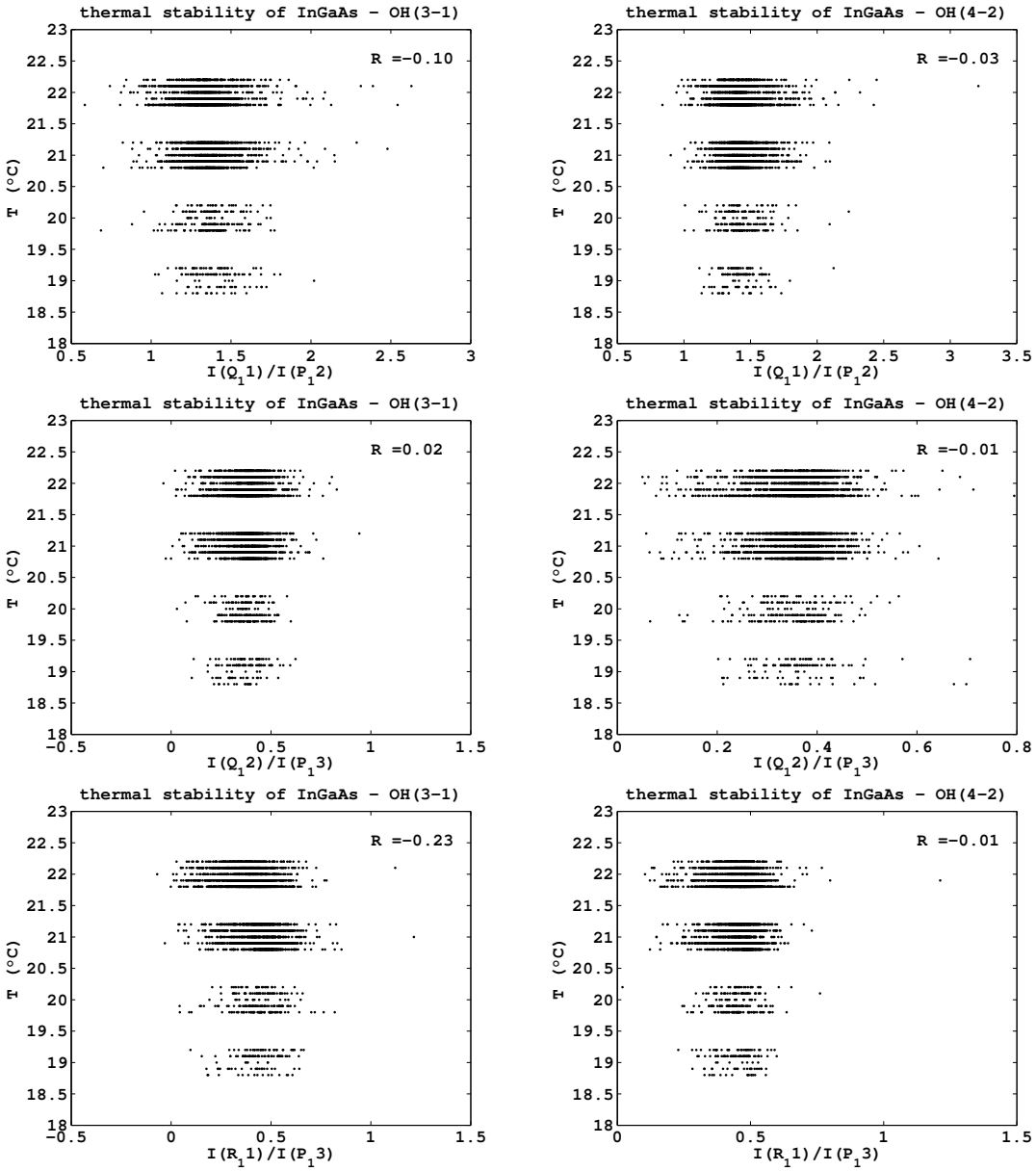

J'	Ratio	OH(3-1), v (cm^{-1})	OH(4-2), v (cm^{-1})
1.5	$Q_1(1)/P_1(2)$	6642/6561	6316/6238
2.5	$Q_1(2)/P_1(3)$	6636/6522	6310/6200
2.5	$R_1(1)/P_1(3)$	6717/6522	6388/6200

Figure 3.14.: OH* Meinel intensity ratios from single measurements ($\approx$ 13 min measurement time each) against HR125 temperatures. Correlation coefficient denoted by R value. Equal initial rotational state and wavenumbers of emission lines listed in the lower table.

Ratio	T&L	Mies	LWR	HR125
OH(3-1): $Q_1(1)/P_1(2)$	1.36	1.35	1.33	1.36 ± 0.15
OH(3-1): $Q_1(2)/P_1(3)$	0.46	0.45	0.44	0.379 ± 0.090
OH(3-1): $R_1(1)/P_1(3)$	0.49	0.48	0.46	0.41 ± 0.10
OH(4-2): $Q_1(1)/P_1(2)$	1.36	1.35	1.34	1.42 ± 0.14
OH(4-2): $Q_1(2)/P_1(3)$	0.46	0.45	0.44	0.357 ± 0.073
OH(4-2): $R_1(1)/P_1(3)$	0.49	0.48	0.46	0.452 ± 0.079

Table 3.3.: Time invariant intensity ratios of the OH(3-1) and OH(4-2) bands. Theoretical values inferred from Turnbull and Lowe [1989], Mies [1974], Langhoff et al. [1986], and experimental results from HR125 measurements.

but still with the theoretical values in the range of uncertainty. It should be briefly mentioned that French et al. [2000] determined their ratios from a single coadded spectrum of the entire measurement period. While the time invariant line ratios should be retained during the spectral coadding, their uncertainty estimates refer to individual error sources in the coadded spectrum. By comparison, their uncertainty estimates are about one order smaller compared to the standard deviations in Tab. 3.3 so that the theoretical values remain outside of their estimated uncertainty ranges.

3.7. Intercomparison between cooled and uncooled InGaAs detectors

In addition to the uncooled InGaAs detector, the FTIR instrument received a second InGaAs detector in 2012, which is equipped with thermoelectric cooling stages. This technique provides a cooling of the InGaAs diode to $-40°C$. Even though this detector was purchased in the frame of another IUP project, which aims at lunar absorption spectroscopy measurements, it would be freely available for the remaining operational time during the polar night. However, despite its advantages in terms of thermal noise and stability, further aspects play an important role for its feasibility to measure the OH* emission.

First of all, the InGaAs diodes of both detectors differ in their lattice constants, which again is impacting the detector response according to our discussion in Sect. 3.1. In contrast to the narrow band InGaAs diode of the uncooled detector, the cooled detector is equipped with an extended InGaAs diode, which has a larger spectral sensitivity range. Recalling Sect. 3.3, a narrow band sensitive range improves the SNR of the measured signal, thus, favouring the use of the narrow band InGaAs diode.

With regard to the cooling of the InGaAs diode another important aspect arises. In this case, the internuclear distances of lattice atoms will decrease, which leads to an increase of the semiconductor bandgap. Accordingly, the minimum photonic energies

required to raise electrons from the valence to the conduction band will increase, thus, the associated cut-off frequency of the detector will shift towards higher frequencies. In the worst case the cut-off frequency may be shifted close or even beyond the spectral windows that are used for the rotational temperature retrieval.

This gives rise to the question as to whether the thermal-noise-improvement of the cooled extended InGaAs diode is compensated by the above discussed aspects. In order to shed light on this question, let us consider two exemplary spectra that are shown in Fig. 3.15. Both spectra were recorded during excellent weather conditions on the same night, while the measurement settings only differ in the used detectors. For better comparison, both spectra were normalised and shifted to the same zero baseline level. In the upper panel of Fig. 3.15 the normalisation refers to the highest emission peak intensity of each spectrum. In this case, the noise level appears to be more pronounced for the cooled detector.

To get a more quantitative sense of the difference in the SNR between both measurements, we can estimate the SNR of the P_1 rotational lines of the OH(3-1) band by taking the ratio between the line amplitudes and the standard deviation of noise. The latter can be estimated from nearby spectral regions that do not contain any obvious emission signals. From this estimate we find that, on average, the linear SNR of the OH(3-1) $P_1(2)$,$P_1(3)$, and $P_1(4)$ rotational lines improves by about 34 % for the uncooled InGaAs detector according to this example. Similarly, the improvement for the same set of OH(4-2) P_1 rotational lines is about 29 %.

Interestingly, the situation is different for the lower wavenumbers where the performance of the cooled InGaAs turns out to be superior to the uncooled InGaAs. In comparison, the $P_1(4)$ line of the OH(5-3) band at about 5840 cm^{-1} is only slightly above the noise level for the uncooled detector (see lower panel of Fig. 3.15). In contrast, the cooled InGaAs detector is even sensitive to the P_1 branch of the OH(6-4) band up to about 5550 cm^{-1}. This shows us that the upward shift of the cut-off frequency of the cooled InGaAs diode is not seriously impacting the OH* measurements. Instead, the cooled InGaAs diode benefits from its extended sensitivity range towards lower wavenumbers that enclose the OH(5-3) and OH(6-4) bands.

Nonetheless, the best SNR is still achieved for the measurements of the OH(3-1) emission with the uncooled InGaAs detector. In addition, the longer radiative lifetimes make the OH(3-1) band the preferable choice for the temperature retrieval. Still, the coverage of several OH* emission bands is interesting because it provides additional information on the thermal gradient inside the OH* layer as noted earlier (see also later discussion in Sect. 4.3). In principle, the new instrumental upgrade to version HR125 allows for simultaneous measurements with two detectors, so that we may benefit from the broadened spectral bandwidth of both InGaAs detectors. However, such measurements would require the splitting of the modulated source light inside the spectrometer by a dichroic

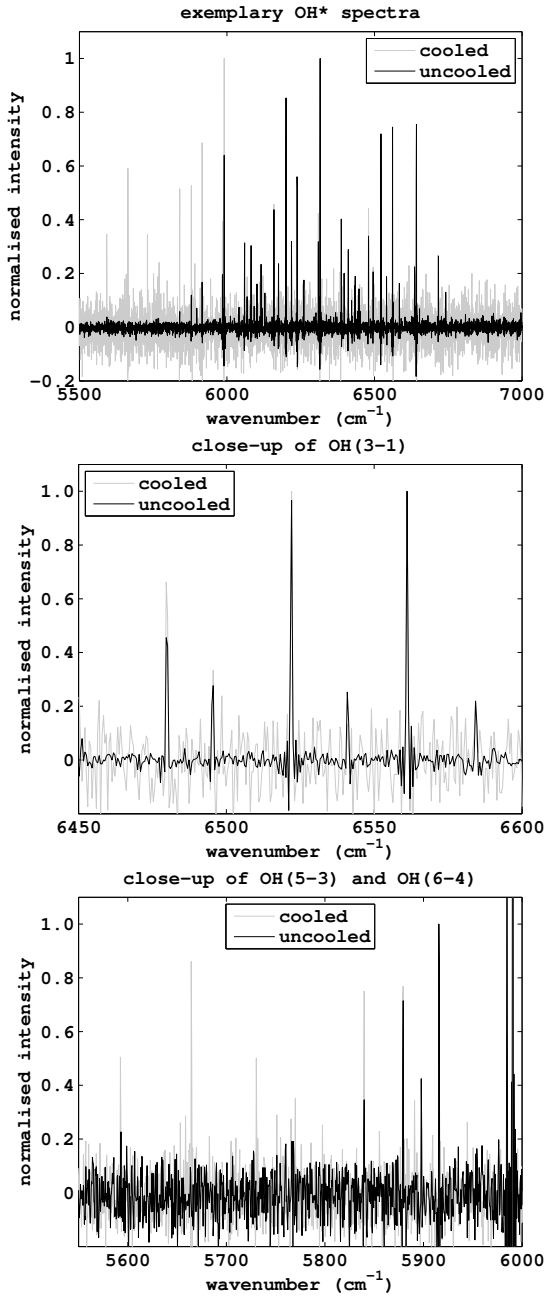

Figure 3.15.: Two OH* spectra measured during 13-Oct.2013 with the uncooled/cooled InGaAs detector. Both measurements use the same settings, including the same spectral integration time of about 13 minutes. Upper panel: Normalised to highest intensity between 5500 and 7000 cm^{-1}. Middle panel: Normalised with respect to the $P_1(2)$ rotational line of the OH(3-1) band at about 6561 cm^{-1} . Lower panel: Normalised with respect to the $P_1(2)$ rotational line of the OH(5-3) band at about 5916 cm^{-1}.

mirror, hence, only half of the signal intensity would be available for each detector in the ideal case. It is for these reasons that it was decided in this work to proceed the ongoing measurements with the uncooled InGaAs detector.

3.8. Impact of line-of-sight

Apart from the instrumental setup, the line-of-sight (LOS) plays another important role for the signal strength of the OH* emission. This is because the apparent OH* layer thickness, i.e. the path length of the LOS inside the OH* layer, depends on the zenith angle of the LOS. Accordingly, a larger zenith angle leads to a larger path length of the LOS inside the OH* layer. As long as the effect of self-absorption inside the OH* layer is negligible, the photon flux towards the observer will enhance due to the increased OH* layer thickness along the oblique LOS. According to Khomich et al. [2008] the atmosphere is optically thin at altitudes above 80 km for wavelengths between 0.35 μm and 2.0 μm. This wavelength region is equivalent to wavenumbers ranging from 5000 cm^{-1}

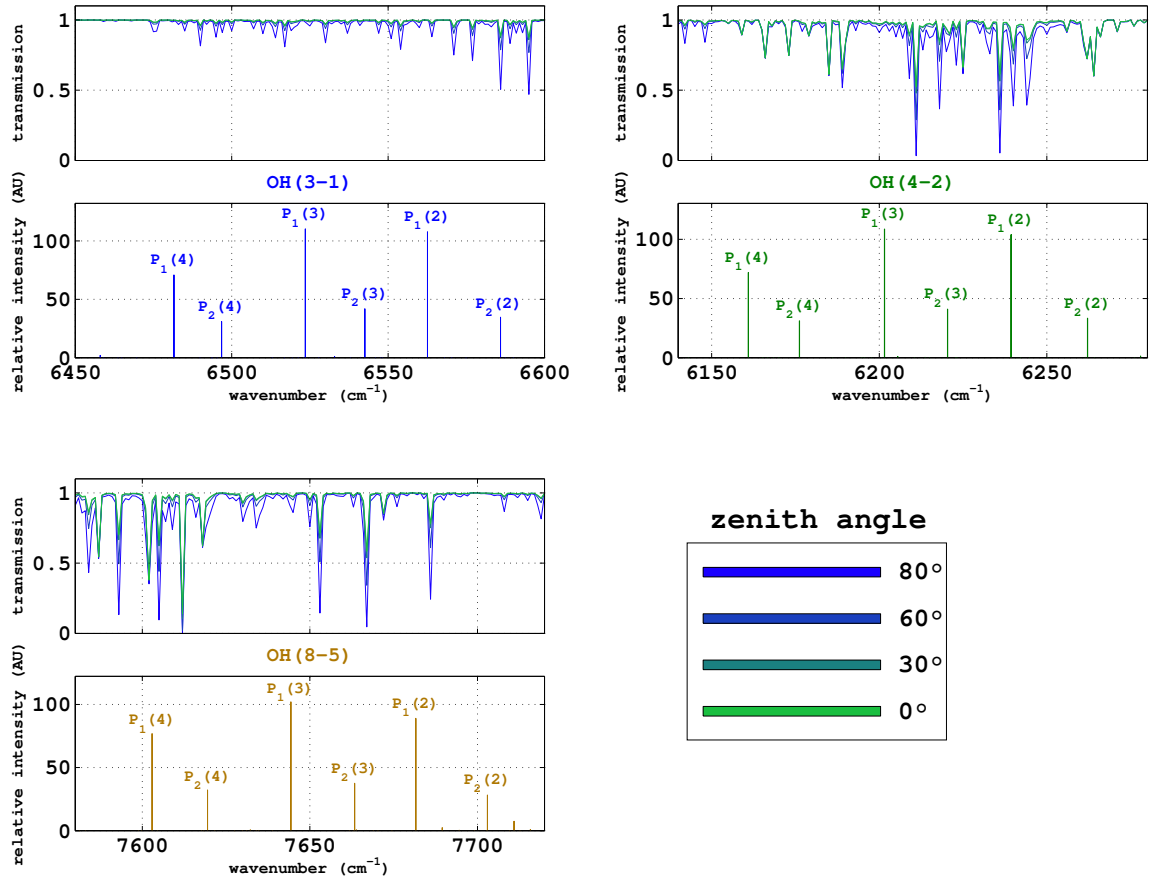

Figure 3.16.: Impact of viewing angle on simulated atmospheric transmission in the spectral regions of the observed OH* emission above Ny-Ålesund.

$\overline{\Delta T}$:	2007-10	2010-12
OH(3-1)	1.1 K	5.9 K
OH(4-2)	-9.4 K	-45.6 K
OH(8-5)	8.4 K	31.4 K

Table 3.4.: Average temperature change due to the applied correction for the atmospheric transmission in the hourly rotational temperatures retrieval between 2007-10 (zenith LOS) and 2010-12 (low elevation LOS).

to about 28500 cm^{-1}, which is also enclosing the spectral region of the observed OH* emission. It is therefore plausible to assume that the effect of self-absorption is negligible for the observed OH* emission. However, we have to take into account that the atmospheric transmission is also depending on the zenith angle of the LOS and may compensate the gain in signal strength from the larger apparent OH* layer thickness.

Let us recall the simulated atmospheric transmission according to Fig. 3.5 of Sect. 3.2. We can do the same modelling of radiative transport for different zenith angles. Figure 3.16 shows spectral windows that enclose the first three OH* emission lines of the P_1 and P_2 branches of the OH(3-1), OH(4-2), and OH(8-5) bands, which lie in the sensitivity range of the instrument. While changes in atmospheric transmission are rather small for the considered emission lines of the OH(3-1) band, the impact on the $P_1(2)$ rotational line of the OH(4-2) band is much more pronounced. Similarly, the $P_1(4)$ rotational line of the OH(8-5) band is suffering from the reduced atmospheric transmission, but changes due to the varying viewing angles are less pronounced. In contrast to the correction for the instrumental sensitivity and hatch window transmission, the impact of the atmospheric transmission on the iterative temperature retrieval is quite substantial as summarised in Tab. 3.4. We will get back to these values in our later discussion in Sect. 4.3.2. Let us now consider to what extent the intensity of the OH* emission enhances, if we increase the zenith angle of our LOS. To get a sense of this enhancement, we can derive the relationship between the zenith angle Θ and the path length d of the LOS inside the OH* layer by means of trigonometric considerations (see appendix A.2):

$$d = \sqrt{a^2 - \left(R_\mathrm{E} \sin\left(\Theta\right)\right)^2} - \sqrt{b^2 - \left(R_\mathrm{E} \sin\left(\Theta\right)\right)^2} \ , \tag{3.21}$$

with

$$\begin{aligned} a &= R_\mathrm{E} + h_1 + h_2 \ , \\ b &= R_\mathrm{E} + h_1 \ , \end{aligned}$$

where R_E is the radius of the Earth, h_1 is the altitude of the layer, and h_2 is the layer thickness. Based on this equation, Fig. 3.17 shows the relation between the path length d and zenith angle Θ for a layer with an assumed thickness of 8 km and which is centred

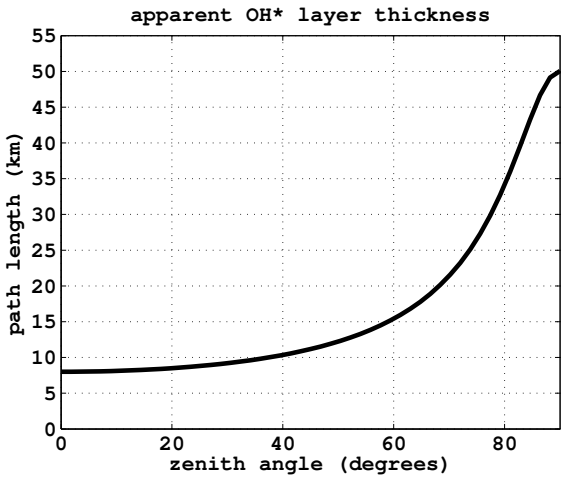

Figure 3.17.: Apparent layer thickness depending on the zenith angle of the line-of-sight for a spherical layer at 87 km altitude with a layer thickness of 8 km.

at an altitude of 87 km. As we can see, the change in the path length with increasing zenith angle is relatively small at the beginning. At about 60°, where the path length has almost increased by a factor of two, the relative changes are significantly improving. A further increase of the zenith angle to 80° leads to an apparent OH* layer thickness of 35 km, which corresponds to a factor of 4.4 with respect to the zenith direction.

Because of the negligible effect of self-absorption in the OH* layer and the moderate change in atmospheric transmission losses for most rotational lines, these results indicate a potential improvement of the OH* emission signal strength by using a high zenith (i.e. low elevation) angle. With the installation of new hatch windows in the frame of this work in autumn 2010, continuous measurements at high zenith angles became possible. Beforehand, test measurements were performed at different zenith angles (open hatch) to validate the actual improvement of the signal strength.

Figure 3.18 shows three exemplary spectra that are superimposed and normalised to the same $P_1(3)$ rotational line of the OH(3-1) band to allow for a better visual comparison of noise levels. Apart from the viewing direction, all measurements were performed with the same settings and the same 13 min spectral integration time. We can nicely see that the higher zenith angle is improving the OH* signal strength. With respect to the $P_1(3)$, OH(3-1) rotational line, the linear SNR improves by a factor of 1.6 between the zenith angles of 70° and 80°. It further improves according to a factor of 3.3, if we consider the change of the zenith angle from 50° to 80°. The measurement at zenith direction is excluded in this example, because the emission lines were already barely visible during this sequence of measurements.

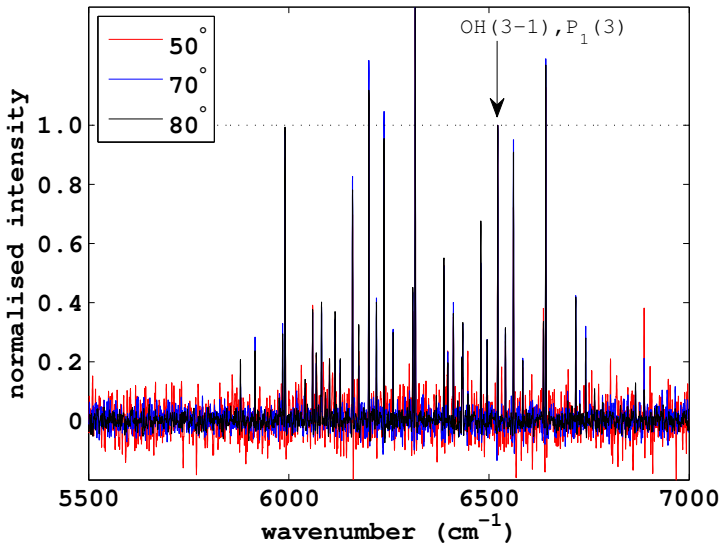

Figure 3.18.: Three subsequent spectra based on three different zenith angles, taken on 01-Nov 2010.

The observed improvements in the SNR confirm the expected signal strengthening due to the larger apparent OH* layer thickness at high zenith angles. Of course, we have to bear in mind that the OH* emission intensity is also fluctuating with time, as we will discuss more in depth in the later chapters. We therefore have to assume that the impact of the intrinsic variability of the OH* emission signal is small with regard to the exemplary spectra in Fig. 3.18. Repeated test measurements at different zenith angles give further support to the SNR improvement at high zenith angles. Due to the position of the hatch windows, a final zenith angle of 83° was selected and applied to the ongoing measurements since November 2010. In a statistical sense we can evaluate the impact of the viewing direction to the signal intensity from the distribution of recognised SNRs of the OH(3-1) emission spectra during both periods. For this task, let us consider again the $P_1(3)$ rotational line of the OH(3-1) band. To estimate the SNR of this line, we look for the highest signal amplitude within the spectral range of ± 4 cm^{-1} around the expected line position at 6522 cm^{-1}.

Because of the large range of recognised SNR values, logarithmic SNR values are determined in addition:

$$\mathrm{SNR(dB)} = 10 \cdot \log \frac{I_a}{\mathrm{STD_{noise}}} \tag{3.22}$$

with the signal amplitude I_a and the standard deviation of noise $\mathrm{STD_{noise}}$. Given the total number of 98000 spectra in the period from 2007 to 2012, the distribution of recognised SNR values of the OH(3-1)/$P_1(3)$ line is illustrated in Fig. 3.19 at linear and logarithmic scales. The period where the LOS is pointing to the zenith direction is indicated by the grey bars and the period where the LOS is pointing to a zenith angle

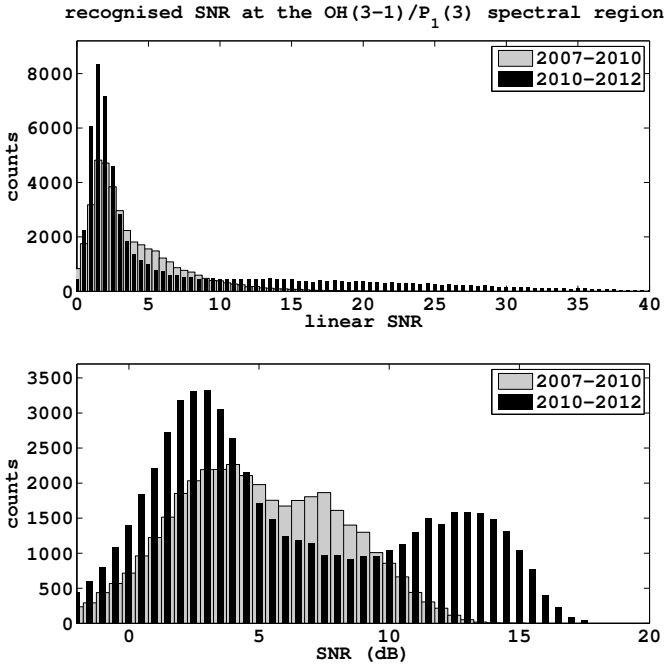

Figure 3.19.: Histogram of detected SNRs in the spectral region of the $P_1(3)$ rotational lines of the OH(3-1) band prior to 2010 (zenith viewing direction) and after 2010 (low elevation viewing direction). Upper/Lower panel: linear/logarithmic SNRs.

of 83° is indicated by the black bars. Here, no filter is applied to the spectra yet, so that the counted spectra with low SNR values refer to pure noise spectra. For the higher SNR values we can clearly see an improvement after the change in the viewing direction in 2010, in particular when looking at the logarithmic scale in the lower panel of Fig. 3.19.

3.9. Aura Microwave Limb Sounder (MLS)

In addition to the retrieved mesopause temperatures from our ground-based FTIR measurements of the OH* emission, this work also includes temperature measurements from the MLS instrument onboard the Aura (NASA) satellite [Waters et al., 2006]. This instrument is equipped with radiometers, which sense the thermal microwave emission of different molecules at different spectral ranges. Temperatures are retrieved from the thermal emission of the 118-GHz O_2 spectral line and the isotopic 234-GHz $O^{18}O$ spectral line. The temperature data product is available via open access through the data archive system[8] of the Goddard Earth Science Data and Information Center. This work uses the Level 2 Data Version 3.3, which according to the provided MLS quality document uses retrieval algorithms that are largely unchanged from those of V2.2. By comparison between both versions, the vertical resolution at the mesopause and thermosphere region

[8]follow http://mls.jpl.nasa.gov/products/

is further improved in V3.3. A comprehensive discussion of V2.2 temperatures is given in Schwartz et al. [2008].

In summary, MLS performs atmospheric limb scans of the above stated oxygen radiance. By means of optimal estimation techniques vertical temperature profiles are retrieved from the radiance profiles. The spatial coverage of MLS profiles reaches up to 82°N in latitude. According to the V3.3 quality document the vertical resolution of temperature profiles at the 0.001 hPa pressure level ranges between 10 km to 13 km with an along-track horizontal resolution of about 220 km and a cross-track resolution of about 12 km. The estimated V3.3 temperature precision at this pressure level is ± 2.5 K. It is further mentioned that any values above this pressure level (i.e. < 0.001 hPa) are not recommended for scientific use. If we consider the altitude/pressure relation based on the U.S. Standard Atmosphere (1976) shown in Fig. 2.1, the OH* layer altitudes are already close to this limit. To exclude non-recommended temperature results from the MLS retrieval, data points that contain bad quality flags, as described in Schwartz et al. [2008], are discarded from the analysis of this work.

3.10. Summary

This chapter discussed the principles of Fourier transform spectroscopy and instrumental characteristics of the employed FTIR spectrometer in this work. In addition, the impact of the LOS on the measurements was reviewed and a summary on the spaceborne MLS instrument was given. The key aspects with regard to the measurements of the OH* emission are summarised as follows:

- The combined impact of the hatch window transmission and instrumental sensitivity on the iterative temperature retrieval is found to be less than 1.6 K , while the largest impact is found for the atmospheric transmission, reaching a few tens of Kelvin for the OH(4-2) and OH(8-5) bands for low viewing angles.
- The thermal stability of the uncooled detector was tested based on time invariant intensity ratios from the OH* emission. A comparison with instrumental temperature changes indicated no significant impact in most cases. Only one ratio indicated a weak but already significant correlation to the instrumental temperature.
- The comparison between a new detector with a cooled extended InGaAs diode and the default uncooled detector with a narrow band InGaAs diode revealed a better performance of the latter detector for the OH* emission measurements. Only at lower wavenumbers the new detector's performance is superior, allowing for the detection of emission lines from the OH(5-3) and OH(6-4) bands but with low SNRs. It was therefore decided to proceed the measurements with the uncooled detector.
- An overall improvement of the OH* emission strength was shown for oblique viewing directions.

4. Mesospheric temperatures above Spitsbergen

After our discussion of the fundamentals of the remote sensing of mesopause temperatures from the OH* emission, we now establish a data processing scheme to create a temperature time series based on the recorded emission spectra in Ny-Ålesund. Because of the continuous operation during the polar night, this processing scheme must include a quality assessment of the recorded spectra, which discards noisy as well as contaminated spectra from the subsequent processing. We discuss critical quality criteria in the next section and how these are implemented in the automated selection of good spectra. Once we have established the data processing scheme in Sect. 4.2, we discuss the temporal variability of the created temperature time series at daily and hourly scales in the subsequent sections.

4.1. Data selection

As noted above, the FTIR operates continuously during the polar night regardless the current weather conditions that may affect the measurements of the OH* emission. To account for the weather conditions during the measurements this would require either a manual 24 h operation or an automated consideration of real–time weather information from local sensors. However, in the latter case any gaps in the operation of these local sensors could potentially interrupt the measurements of the OH* emission with the FTIR. Continuous measurements regardless the current weather conditions avoid such interruptions, but require a later rejection of contaminated spectra. Preferably, this rejection is implemented in an automated data processing scheme to prevent any biasing of the results due to a visual identification of contaminated spectra.

Because the OH* emission requires clear night-sky conditions, continuous measurements during the polar night will lead to a substantial number of recorded spectra that contain nothing but noise. Despite the large number of pure noise spectra the file size of recorded spectra is not a critical issue owing to the relatively coarse spectral resolution setting of 1 cm^{-1}. However, it should be noted that a continuous operation leads to a more pronounced mechanical wearing of the scanner arm, in particular with regard to the mirror sledge runners. To reduce the mechanical wearing, this work implemented an automated validation of nighttime conditions by recognising the amplitude of the centre burst in the interferogram domain. With the onset of sunlit conditions the signal amplitude is significantly increasing due to the Rayleigh scattering background. Vice

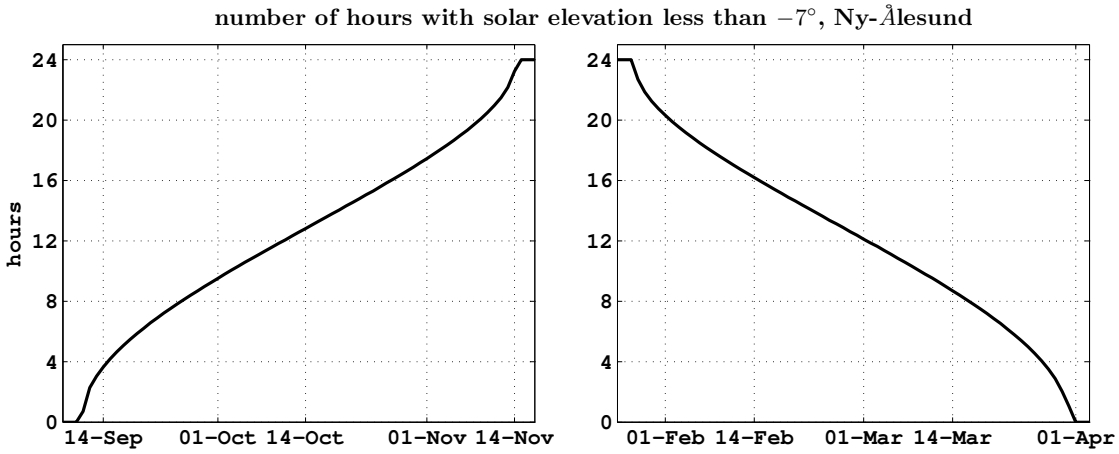

Figure 4.1.: Calculated number of hours per day with a solar elevation angle smaller than −7° at the geolocation of the FTIR (78°55′N, 11°56′O, 21 MAMSL) based on the *sun_position* algorithm by Vincent Roy (last update 22/08/2005). This algorithm is further based on Reda and Andreas [2004] and can be accessed through the file-exchange repository of mathworks.com.

versa, the SNR of the OH* emission rapidly decreases as discussed before. Therefore, we can avoid the inclusion of daytime spectra before and after the period of 24 h darkness during the polar night by setting a threshold for the recognised signal amplitude.

To illustrate the available period of night-sky conditions at our measurement site Fig. 4.1 shows the number of hours per day where the elevation angle of the sun is below −7°. Based on this threshold value the period of 24 h darkness ranges from mid-November to the end of January. The intermediate periods, where this threshold value is only satisfied during a fraction of a day, are about two months each.

The exclusion of daylight contaminated spectra is a simple computational task[1]. In contrast, the identification of contaminated spectra due to partial cloud cover or haze layers is more challenging. Cloud or haze layers can lead to a damping or complete absorption of the OH* emission signal. In addition, depending on their micro-physical properties they can also reflect light from other sources such as the moon or artificial sources from the ground, which can disturb the measurements. In the following, we discuss the impact of artificial light sources on the OH* emission measurements, which may also serve as a measure of cloud cover. In addition, local sensors of the Baseline Surface Radiation Network (BSRN) can be utilised to estimate the current cloud coverage as discussed in the subsequent section.

[1]Because of the specific OPUS software environment the easiest approach to identify sunlit conditions during the operation is to look at the amplitude of the centre burst in the interferogram domain. In the later data processing the *sun_position* algorithm, which is applied in Fig. 4.1, can be used in addition to filter out spectra that exceed a determined threshold value for the solar zenith angle.

4.1.1. Reflected mercury lines from village lights

Artificial light sources, in particular street lamps, can emit distinct mercury (Hg) lines, which may interfere with the observed OH* emission [Bittner et al., 2002]. Strong Hg I emission lines exist at wavelengths of 13673.51, 15295.82, and 17072.79 Å [Humphreys, 1953], which correspond to wavenumbers of 7313 cm^{-1}, 6536.7 cm^{-1}, and 5857.3 cm^{-1}. The 15295.82 Å Hg I line appears to be the most promising line to be utilised as a cloud cover proxy, because it lies in the spectral region where the instrumental setup for the OH* measurements is highly responsive. In addition, it lies between the $P_1(2)$ and $P_1(3)$ rotational lines of the OH(3-1) band and could therefore severely impact the measurements of the OH(3-1) emission. Accordingly, any contaminated spectra due to the reflected Hg emission from village (street) lights should be discarded from the later analysis.

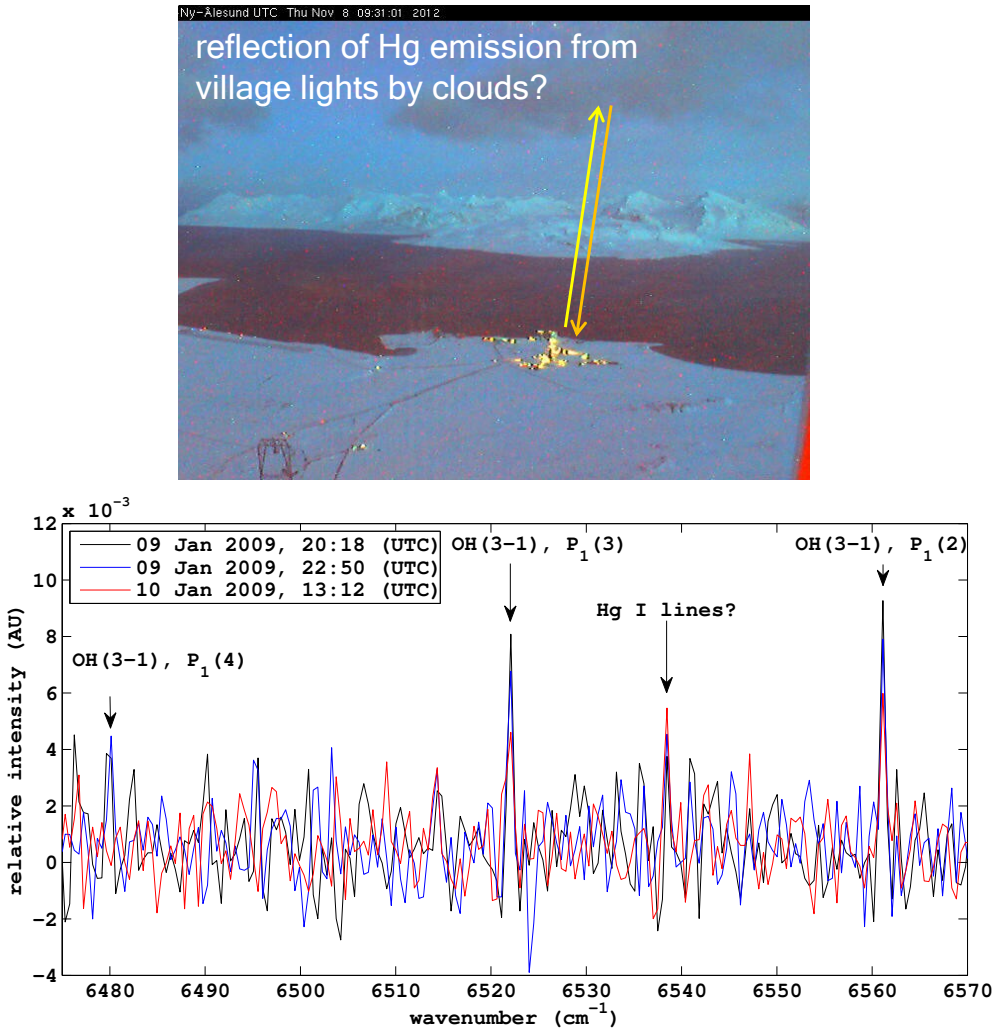

Figure 4.2.: Upper panel: View of illuminated village of Ny-Ålesund (Photo Credit:Kings Bay A.S.). Lower panel: Selected spectra with suggested Hg emission lines.

While the presence of the artificial Hg emission can significantly affect the OH* emission over densely populated areas, the question remains as to whether the street lamps of the remote village of Ny-Ålesund have a recognisable impact on the recorded spectra. To check this, a manual investigation of spectra was performed for periods where the weather conditions should favour the reflection of the Hg emission into the field of view of the instrument. As shown in Fig. 4.2, only on rare occasions some faint Hg emission signals might be visible in the spectra, but these signals are very close to the existing noise level. This indicates that the intensity of village lights is rather negligible and should therefore not significantly impact the observed OH* emission lines. Vice versa, the lack of a clear Hg line during overcast conditions makes this feature less feasible to serve as a proxy for cloud contamination of recorded spectra.

4.1.2. Backscattered light from the moon

In contrast to the backscattered light from the village lamps in Ny-Ålesund, the moon can have a noticeable impact on the OH* emission spectra. An example of three subsequent spectra (approx. 13 min integration time each) is shown in Fig. 4.3, where the moon is passing nearby the field of view of the instrument. The impact of the Rayleigh scattering background is clearly visible around 09:24 UTC where the moon reached its closest distance to the LOS of the instrument. One could account for the spectral background in the iterative rotational temperature retrieval, e.g. by fitting the background in the spectral domain or by filtering out the associated low frequency components in the interferogram domain. However, other studies such as Bittner et al. [2002] or Dyrland et al. [2010] explicitly discard OH* spectra from their analysis, if these are contaminated by moonlight. Therefore, an automated script was written, which detects the relative change of the mean intensity of two different spectral intervals. The first interval ranges from 6000 to 6623 cm^{-1} and it is divided into further subintervals to exclude any emission lines. The second interval ranges from 7100 to 7350 cm^{-1}, which is dominated by strong atmospheric absorption (see also Fig. 3.5) and therefore serves as a reference baseline. Based on this approach, the middle and upper panels in Fig. 4.3 are flagged as contaminated spectra and discarded from the analysis.

4.1.3. Baseline Surface Radiation Network (BSRN)

Local BSRN sensors are located nearby the AWIPEV station. Among others, these include two separate pyrgeometers, which are sensing the up- and downwelling infrared radiation in units of Wm^{-2} [McArthur, 2005]. As we know from our regular experience, cloud free nighttime conditions are associated with a pronounced radiative cooling into space. On the other hand, during overcast conditions the cloud layer acts like a blanket by reflecting the upwelling longwave radiation back to the ground. Accordingly, the amount of up- and downwelling longwave radiation is balanced towards similar values, which we can use as an indicator of cloud coverage.

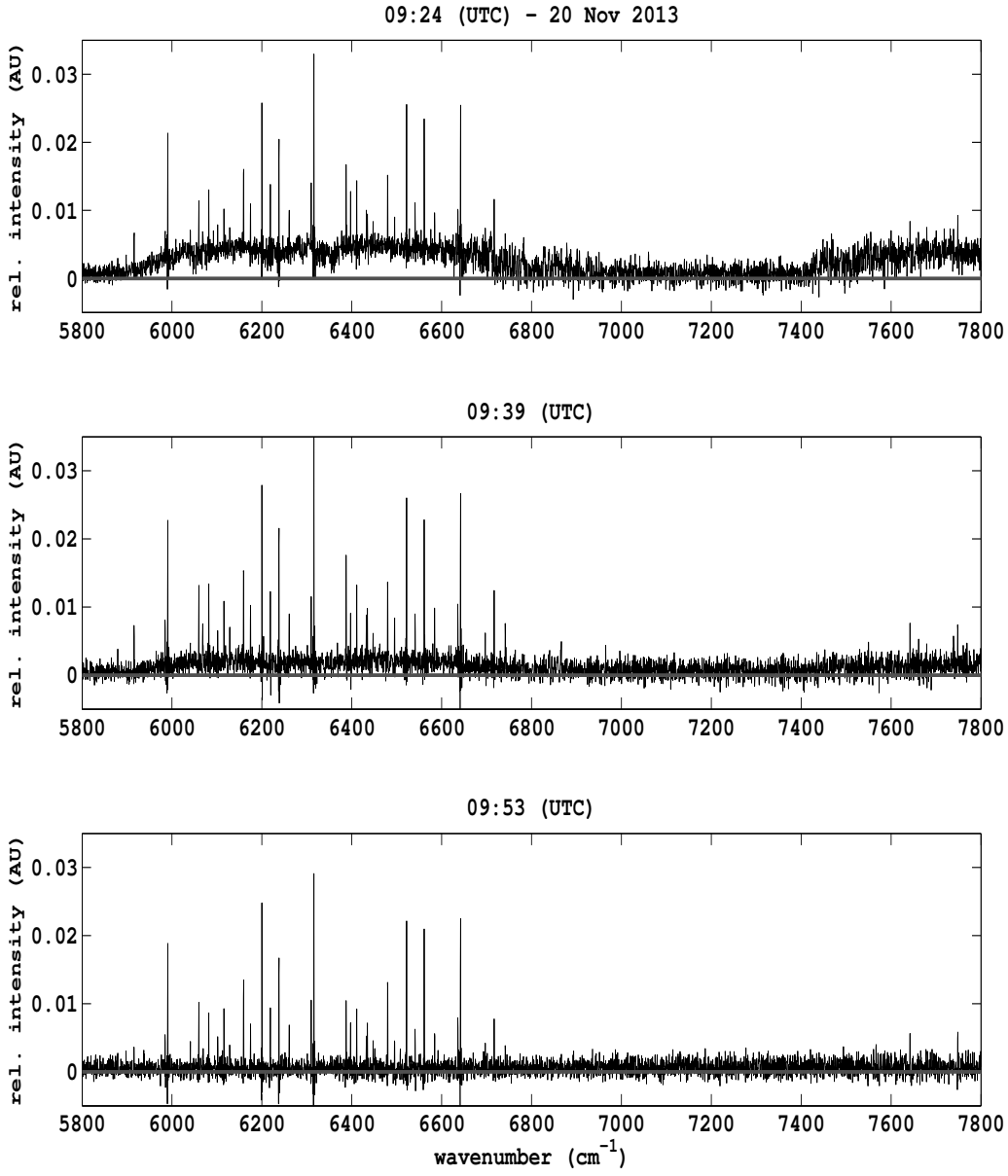

Figure 4.3.: Exemplary sequence of increasing Rayleigh scattering background from the moon.

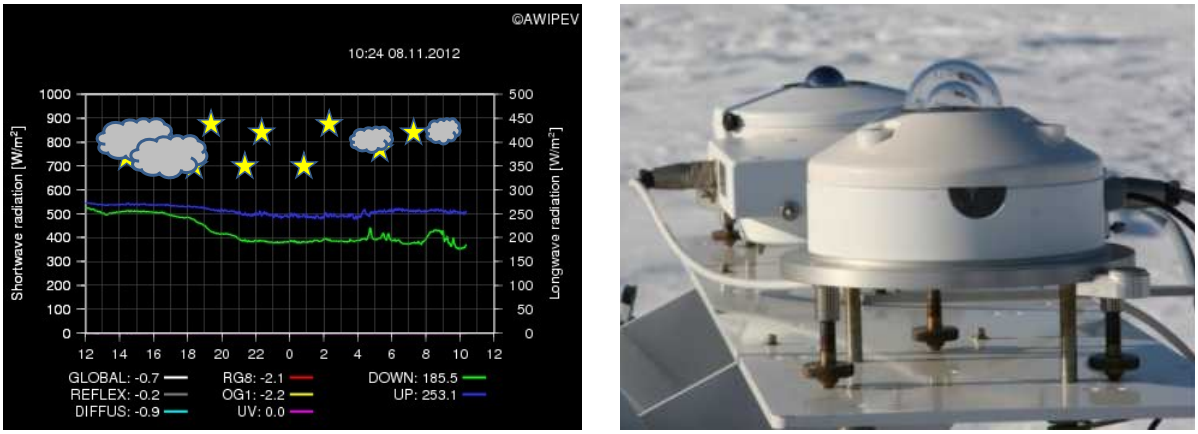

Figure 4.4.: Up- and downwelling longwave radiation detected from BSRN pyrgeometers. Left panel: Exemplary time series with added illustration of associated cloud cover. Right panel: Picture of pyrgeometers at the BSRN site at Ny-Ålesund. Photo Credit: AWIPEV.

An example of the transition from cloudy to clear night-sky conditions is illustrated in the left panel of Fig. 4.4. By determining a certain threshold between the up- and downwelling longwave radiation, we can use this as a criterion in the spectral data filtering to discriminate between cloudy and clear sky conditions at our measurement site.

4.1.4. Auroral contamination

Apart from the Hg I emission lines, auroral emission lines could also interfere with the OH* emission lines. According to Gattinger and Vallance Jones [1981] aural emission lines from the (1-2) Meinel band system of N_2^+ could affect the relative line intensities of the OH* emission bands, which we observe with the FTIR. Two pronounced lines from the (1-2) band system of the N_2^+ Meinel emission exist at wavelengths of 15748 Å and 15114 Å according to Lofthus and Krupenie [1977]. The corresponding wavenumbers of both lines are 6616.4 and 6537.2 cm^{-1}. Interestingly, the N_2^+ Meinel line at 6537.2 cm^{-1} only differs by 0.5 cm^{-1} from the Hg I emission line, which was tested as a proxy of cloud coverage in Sect. 4.1.1.

Further prominent emission lines from atomic nitrogen and oxygen are located between 7363 and 9886 cm^{-1}, but with intensities smaller than one to two orders in magnitude compared to the N_2^+ (1-2) band system [Gattinger and Vallance Jones, 1981].

To exclude contaminated OH* spectra from the analysis, an automated peak search was performed to identify auroral lines in the OH* spectra. Assuming a line peak threshold of four times the standard deviation of the spectral noise level for the identification

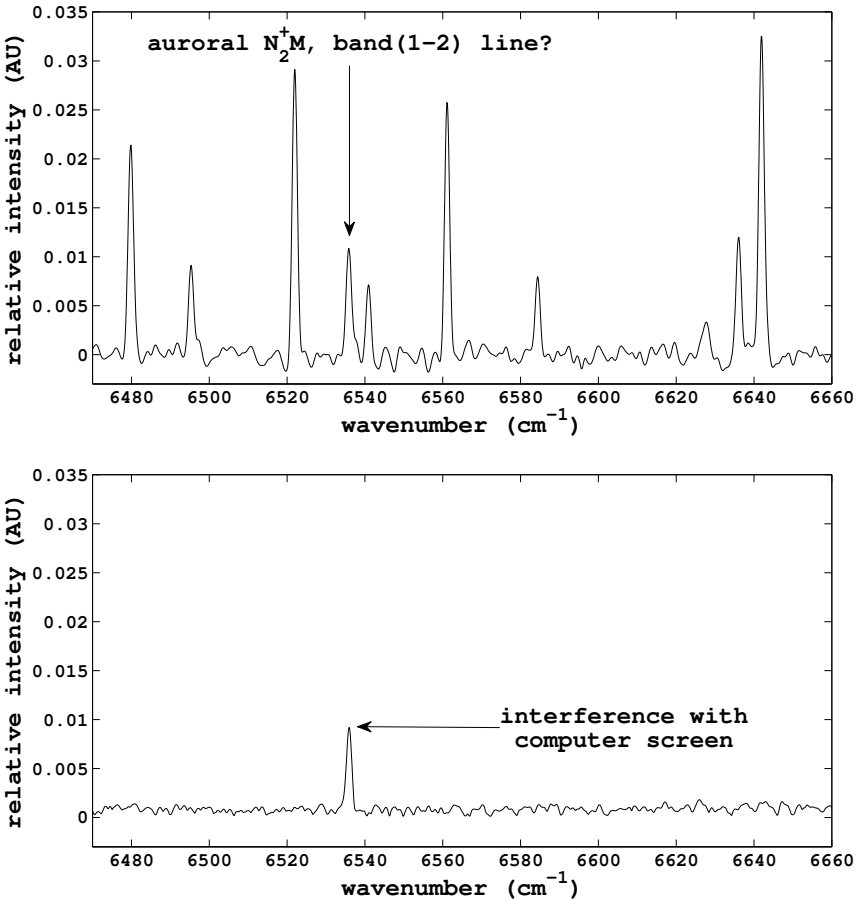

Figure 4.5.: BH4 apodized spectra with arbitrary relative intensity units. Upper panel: OH* emission spectrum with spurious spike between the $P_1(3)$ and $P_2(3)$ rotational lines of the OH(3-1) band, 26 Jan 2011, 12:21 (UTC). Lower panel: Similar spike during overcast conditions, which was identified as an interference with the computer screen, 30 Jan 2014.

of an auroral line, only 67 out of 20000 spectra with visible OH* emission features between 2007 and 2012 were found with an emission line close to 6537 cm^{-1}. An example of such a spectrum is shown in the upper panel of Fig. 4.5. However, none of these spectra contain a pronounced second emission line close to 6616 cm^{-1}, which we would expect due to the (1-2) band system of the N_2^+ Meinel emission. On the other hand, if we attributed this spectral feature to the reflected Hg I emission from the village lights, the number of identified spectra should be significantly larger.

Interestingly, a similar spike in the recorded spectra was found on occasion during overcast conditions, as shown in the lower panel of Fig. 4.5. Indeed, the occurrence of this spike could be clearly related to an interference with the computer screen inside the FTIR laboratory. As soon as the screen is either switched off or shaded, the emission

line disappears in the spectrum. Hence, it is very likely that these occasional spectral features indicate short periods where the computer screen was switched on during the measurements, which also gives an explanation for the missing auroral line feature around 6616 cm^{-1} and the rare occurrence of this emission line.

We can conclude that:

- the station engineers did a good job of switching off the computer screen for most of the time,
- the auroral impact on the OH* emission does not play a critical role at our measurement site.

With regard to the latter point we have to keep in mind that the auroral observations by Gattinger and Vallance Jones [1981] were performed at 58° N. Following Carlson and Egeland [1995] the auroral-particle precipitation is dominated by *high-energy* particles around 60° latitudes, whereas at latitudes around 80° the precipitation is more dominated by *medium-energy* particles. Again, the high energetic particles (i.e. electrons) penetrate deeper into the atmosphere where the auroral spectrum is then dominated by molecular emissions [Lanchester et al., 2009]. This also gives an explanation why the N_2^+ Meinel bands are not recognisable in our OH* spectra.

4.1.5. Further quality control parameters

To determine the quality of individual spectra an automated procedure evaluates the following additional points:

- OH* emission lines exceed a minimum SNR value,
- retrieval error of rotational temperature below a threshold value,
- no spurious spikes located in the spectrum.

The first point assures that the signal is of reasonable strength, the second point accounts for distorted or non-thermalised spectra, and the third point accounts for the spectral line feature, which was identified as the interference with the computer screen. In addition, three additional spectral windows are assigned to identify any spurious spikes, which may arise from not yet identified contaminating light sources or any interference with the electronics. Two windows are located in the spectral region from 5000 to 5600 cm^{-1} and 7900 to 8000 cm^{-1} where the instrumental sensitivity should be rather low. The third window is located between 7180 to 7500 cm^{-1} where the OH* emission should be largely absorbed by the water vapour bands (see Fig. 3.5). Any spectrum which contains a spike inside one of these windows is flagged and discarded from the later analysis.

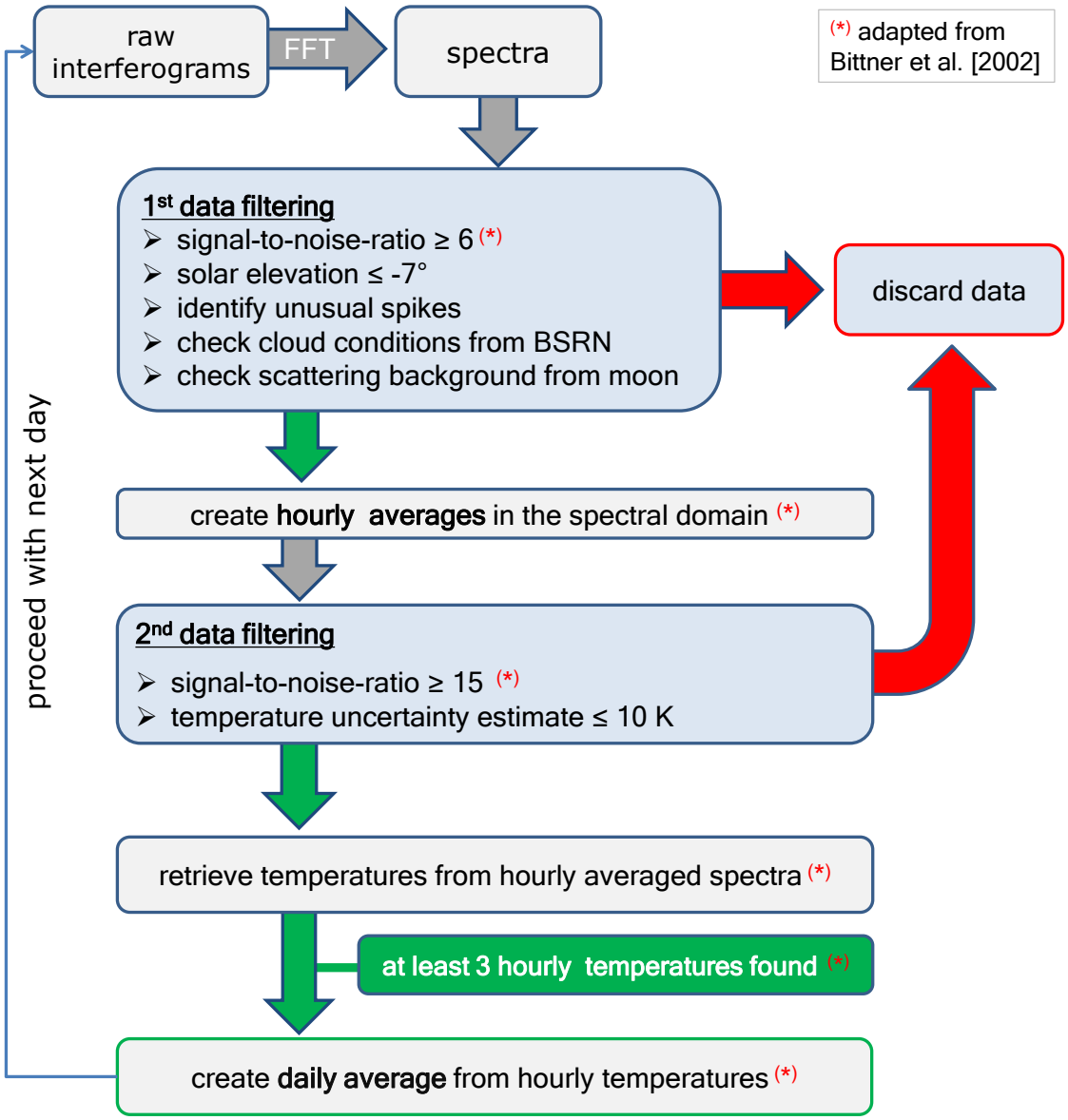

Figure 4.6.: Data processing scheme for the derivation of a time series of rotational temperatures from the OH* emission.

4.2. Data processing scheme

The data processing scheme, which was established in the frame of this work to create a time series of rotational temperatures, is presented in Fig. 4.6. Based on this scheme hourly and daily temperature estimates are calculated from the recorded OH* emission spectra.

In the first step of this scheme all spectra are reprocessed by applying a zero filling and BH4 apodization in the interferogram domain to minimise the picket–fence effect and spectral leakaging (see discussion in Sect. 3.2.1). Each spectrum refers to 100 scans, which have been integrated over a sampling time of approximately 13 min. Based on the quality criteria discussed above, bad spectra are flagged and discarded from the analysis.

We could use the retrieved temperatures from each recorded spectrum to calculate hourly and daily means. However, according to Bittner et al. [2002] this would inevitably introduce an error because of the more pronounced spectral noise and the non-linear dependency of temperatures on intensities. To reduce this error, they suggest creating hourly spectral averages first and then determining the rotational temperatures from these spectra. If at least three hourly temperatures are found within one day, they calculate the daily temperature from the mean of retrieved hourly temperatures. The same criteria for the calculation of hourly and daily temperatures are also applied in other studies (e.g. Sigernes et al. [2003], Dyrland et al. [2010], Holmen et al. [2013]) and therefore implemented in the data processing scheme of this work.

With regard to the weaker OH(8-5) emission lines, very few spectra satisfy the SNR threshold values according to Fig. 4.6. Accordingly, almost all daily OH(8-5) temperature estimates would be rejected due to the selected SNR threshold values. To get at least a few daily OH(8-5) temperature estimates in the time series the quality criteria are relaxed such that the SNR threshold is only tested for the simultaneous OH(3-1) emission in this case.

4.3. Time series of mesopause temperatures above Ny-Ålesund

A temperature time series was created based on the above explained data processing scheme. For the discussion of this time series we address the following aspects in the next sections:

- impact of the data filtering on the results
- intercomparison of temperature estimates from different OH* Meinel bands and MLS
- thermal stability of default uncooled InGaAs detector
- dynamical coupling between the stratospheric and upper mesospheric/mesopause region

These sections mainly address the observed day-to-day variability in the time series. In terms of the dynamical coupling, the main emphasis is therefore on the large scale dynamic control of the upper mesospheric/mesopause region. In addition, the final

section of this chapter addresses the temporal variability at hourly scales, hence, the main emphasis of the final section is on the intrinsic response of the OH* airglow layer to gravity and tidal wave perturbations.

4.3.1. Impact of data filtering

season	net-operating time (days)	remaining fraction after filtering	number of daily temperature estimates*	viewing direction
2007-08	34	25%	9	zenith (open hatch)
2008-09	81	7%	22	zenith window
2009-10	67	8%	13	”
2010-11	100	29%	66	low elevation
2011-12	94	34%	77	”
2013-14	124	31%	84	”

Table 4.1.: Net-operating time and remaining data after filtering of OH(3 − 1) spectra. *The number of daily estimates refers to the convention of Bittner et al. [2002], i.e. three hourly estimates are sufficient to create one daily estimate.

The time series of this work covers six polar winter seasons between 2007 to 2014. A data gap exists for the winter season 2012–13 because of the misalignment issue after the instrumental upgrade (Sect. 3.5) and an identified interference with a wind-lidar system that was accidentally placed nearby the hatch window. Table 4.1 summarises the total net-operating time of the instrument per season, the remaining fraction of observational time after applying the data filtering procedure for the OH(3-1) band, and the number of daily estimates according to the convention of Bittner et al. [2002]. With regard to the latter number, we have to keep in mind that already three hourly estimates are sufficient to create one daily estimate, hence, the number of daily estimates in Tab. 4.1 must not be confused with the fractional observing time after data filtering.

According to Tab. 4.1 we find that the fraction of remaining data after filtering has improved by more than a factor of three between 2008-10 and 2010-14. This again confirms the beneficial impact of the new LOS on the measurements since 2010. With regard to the first season in 2007-08, the absence of hatch windows during that time required the manual operation of the hatch by the station engineer, hence, the operation during unsuitable weather conditions was further reduced.

4.3.2. Intercomparison of temperatures

The temperature time series of this work contains rotational temperature estimates from the emission of three different OH* Meinel bands, i.e. the OH(3-1), OH(4-2), and OH(8 − 5) bands. Before we discuss the temperature differences between the observed OH* Meinel bands as well as their differences to temperature estimates from MLS and other data sets, let us summarise some important aspects with regard to the OH* Meinel bands:

The OH(3-1) band appears to be the best candidate to estimate ambient kinetic temperatures due to the strong thermalisation of the ro-vibrationally excited OH* radicals (Sect. 2.3), the small loss due to the atmospheric transmission (Sect. 3.2), and the high instrumental response at the corresponding wavelength region (Sect. 3.4). In addition, it belongs to the $\Delta\nu = 2$ emission bands, which are the brightest bands of the vibrationally excited OH* radical [French et al., 2000]. The OH(4-2) band has similar good characteristics but the spectral region is close to the instrumental cut-off frequency (see Fig. 3.10) so that measurements of this emission could be more vulnerable to drifts in the instrumental response. Furthermore, it is much more affected by changes in atmospheric transmission (Sect. 3.8). The less efficient thermalisation of the high $\nu = 8$ vibrational state, the smaller sensitivity of the instrument at the corresponding wavelength region, and the smaller intensity due to the larger vibrational deexcitation of $\Delta\nu = 3$ make the OH(8-5) the least favourable candidate for the remote sensing of ambient kinetic temperatures.

Despite the advantages of the OH(3-1) band for the remote sensing of ambient kinetic temperatures, the consideration of multiple OH* Meinel bands is still of particular interest for the following reasons: As mentioned earlier in Sect. 2.3, systematic vertical shifts exist between different Meinel bands of the OH* airglow layer, i.e. the higher the initial vibrational state of the OH* emission, the higher the corresponding altitude region. Based on observations from the SCIAMACHY (Scanning Imaging Absorption spectroMeter for Atmospheric CHartrographY) instrument onboard the ENVISAT satellite, von Savigny et al. [2012b] give a rough estimate for the vertical shifts between the profile peak altitudes of adjacent vibrational states of about 500 m. Accordingly, depending on the initial vibrational state the thermalisation of the excited OH* radicals takes place at a slightly different altitude region. In turn, we are sensing ambient kinetic temperatures at different altitude regions depending on the selected Meinel band of the OH* emission. In principle, this allows us to study temperature differences inside the OH* airglow layer, as also proposed in Perminov et al. [2007].

Figures 4.10 to 4.16 show the temperature time series[2] for the covered winter seasons between 2007 and 2014 (see **pp.81–87**). This section addresses the upper and middle panels of Fig. 4.10 to 4.16, which are explained as follows:

[2]Further supplementary plot included in Fig. 4.12

The upper panel displays hourly as well as daily temperatures, which are derived from the emission of the OH(3-1) band. The uncertainty estimates of derived hourly rotational temperatures (Sect. 3.2.2) are denoted by the error bars. In addition, daily temperature averages derived from measurements of MLS (Sect. 3.9) are displayed for three different mesopause height levels[3] within a collocation radius of 500 km around Ny-Ålesund. The 87 km geometric height level (black solid line) refers to the nominal altitude of the OH* airglow layer. Due to the missing observations of the OH* emission from MLS, we lack the information of the vertical OH* profile shape and its emission peak altitude. Hence, the other two height levels are included to account for vertical shifts of the OH* airglow layer during disturbed conditions. For instance, Winick et al. [2009] reported OH* emission peak altitudes of 80 km and even lower from SABER observations at polar latitudes, which they relate to the unusually enhanced vertical downward motion during particular years. Similarly, Mulligan et al. [2009] reported that the OH* emission peak altitude extended from 76 km to 90 km at polar latitudes between 2002 and 2008.

The middle panel displays daily temperature averages, which are calculated from the hourly OH(3-1), OH(4-2), and the OH(8-5) rotational temperatures (generally abbreviated as "OH($\nu' - \nu''$) temperatures" in the following). Here, the error bars denote the standard deviation of the hourly temperature samples. In addition, the MLS temperature estimates for the nominal 87 km height level are included in this panel for comparison.

Discussion of results: OH(3-1) temperatures

We begin the discussion of results with the intercomparison between OH(3-1) and MLS temperature estimates according to the upper panels of Fig. 4.10 to 4.16. First of all, we notice that the scattering of hourly OH(3-1) temperatures is considerably larger compared to the day-to-day variability of OH(3-1) and MLS temperature estimates. If we compare the daily standard deviation of hourly temperature samples with the mean fitting error of the same day, we find that, on average, the scattering of hourly samples is about 3.3 times larger compared to the mean fitting errors. This implies that the scattering of hourly OH(3-1) temperature estimates is largely reflecting the intrinsic variability of the OH* airglow layer, which we focus more closely in Sect. 4.4.

With respect to the daily OH(3-1) and MLS temperature estimates, we notice that OH(3-1) temperatures tend to be lower than MLS temperatures for most of the time. This is also reflected in Tab. 4.2, which shows the average temperature offsets between our ground-based and MLS estimates per season. More importantly, even when considering the adjacent MLS height levels, the majority of OH(3-1) temperatures have lower

[3]The provided geopotential height levels are transformed to geometric heights, which are then interpolated at the selected height levels.

	offset to MLS(80km)		offset to MLS(87km)		offset to MLS(91km)	
season	OH(3-1)	OH(4-2)	OH(3-1)	OH(4-2)	OH(3-1)	OH(4-2)
2007-08	-12.2 K	-16.8 K	-10.5 K	-15.1 K	-4.1 K	-8.6 K
2008-09	-27.5 K	-26.0 K	-20.9 K	-19.4 K	-12.5 K	-11.0 K
2009-10	-26.0 K	-22.1 K	-19.2 K	-15.3 K	-12.1 K	-8.3 K
2010-11	-7.4 K	-30.1 K	-11.4 K	-34.6 K	-8.1 K	-31.5 K
2011-12	-10.7 K	-26.7 K	-11.8 K	-27.9 K	-6.8 K	-22.9 K
2013-14	-11.8 K	-37.2 K	-11.0 K	-36.5 K	-5.7 K	-31.1 K

Table 4.2.: Average offsets between daily OH(3-1), OH(4-2), and MLS temperatures.

values compared to MLS. This implies some considerable offset between both data sets. Moreover, the temperature offset can be quite variable with time, which to some extent must be attributed to the comparison between fixed reference height levels from MLS and the perturbed OH* airglow layer. For each season displayed in Fig. 4.10 to 4.16 we also find occasions where daily OH(3-1) temperatures lie in the range of adjacent MLS temperature estimates and match the MLS estimates for the 87 km nominal height within a few Kelvin or even less. We further find three short OH(3-1) temperature peaks during 26-Jan 2011, 27-Nov and 23-Dec 2013 that even exceed the range of MLS temperature estimates. In general, we notice that the dynamic range of daily temperatures is larger for the OH(3-1) than for the MLS estimates.

The question remains why most of the daily OH(3-1) temperature estimates are lower compared to those from MLS. We therefore include published results from two additional observational sets and compare them with the MLS and OH(3-1) temperature estimates. The first set is taken from spaceborne measurements by SABER during 2008-09 and was published by Gao et al. [2011]. Their published temperature results refer to the interpolated 85 km height level and the 80°N zonal average. Despite the differences[4] with regard to the local MLS measurements above Spitsbergen, both time series show a very similar temperature range between the cold anomaly around 22-Jan 2009 and the subsequent warming phase, i.e. ranging from about 180 K to 240 K according to Fig. 4.11 and 4.12. Hence, the offset between OH(3-1) and SABER temperature estimates is rather similar in comparison with the independent measurements from MLS.

The second set of temperatures is taken from ground-based measurements of the OH(6-2) band, which are published in Holmen et al. [2013]. These measurements are performed in Longyearbyen, which is located about 110 km South-East of Ny-Ålesund. Interestingly, their published temperatures increase from about 180 K to 210 K during the warming phase after 22-Jan 2009. In comparison with the OH(3-1) temperatures

[4]SABER temperatures are retrieved from the 15 μm and 4.3 μm CO_2 emission. The vertical resolution is about 2 km [Mertens et al., 2009], which is significantly higher compared to MLS. On the downside, SABER observations close to Ny-Ålesund are limited to the period after mid of January due to the transition from southward to northward viewing directions [Mulligan et al., 2009].

in Fig. 4.11, the OH(6-2) temperature range is very similar, hence, both independent ground-based OH* temperature estimates show a similar negative offset to the spaceborne SABER and MLS temperature estimates.

The temperature offset between the independent sets of ground-based and spaceborne observations may be related to differences in their vertical sensitivity and covered altitude regions. With regard to the vertical extent of the OH* airglow layer of about 8 Km, the agreement between the "true" temperature at the profile peak altitude and the observed rotational temperature should be in the order of 1 K during undisturbed conditions according to Offermann and Gerndt [1990]. By comparison, the cold bias during the six consecutive daily OH$(3-1)$ temperature estimates after 5-Feb 2009 is in the order of -20 K, thus, considerably larger compared to the above stated uncertainty that is related to the layer thickness. Vice versa, the rather coarse vertical resolution of about 10 km to 13 km of MLS at mesopause altitudes could give one explanation for the observed temperature offset. However, if the vertical resolution is the main cause for the temperature offset between ground-based and spaceborne observations, we would also expect a similar temperature bias between MLS and SABER because of its higher vertical resolution of about 2 km, whereas the similar dynamic temperature range from both spaceborne instruments does not indicate a temperature bias of similar magnitude.

Another potential reason for the observed temperature offset can result from the departure of the OH* airglow layer from its nominal altitude. In this connection, SABER channels that are sensitive to the OH* emission allow us to sense changes in the OH* emission profile altitudes (see also Sect. 5.3). The corresponding emission profiles from Gao et al. [2011] show a descend of the OH* emission peak altitude to about 80-82 km during the warming phase after 22-Jan 2009 (see upper panel in Fig. 4.12). However, the cold bias of OH(3-1) and OH(6-2) temperatures to the MLS temperature estimates at the nearby 80 km reference level is even more pronounced. Thus, the above suggested impact of the vertical sensitivity and covered altitude region is not evident from the comparison of the considered different data sets.

Interestingly, the cold bias to the MLS temperature estimates after 2010 appears to be less pronounced for the published values by Holmen et al. [2013] in comparison with the OH(3-1) temperatures of this work. On the one hand side, this coincides with the new LOS setting of the FTIR in Ny-Ålesund and may therefore be related to it. On the other hand, this would also imply that the negative offset of OH(3-1) temperatures to MLS is mainly caused by the change of the LOS, which, however, we cannot say for the above discussed warming phase during January 2009.

Discussion of results: OH(4-2) and OH(8-5) temperatures

We proceed our discussion with the additional consideration of OH(4-2) and OH(8-5) temperature estimates according to the middle panels of Fig. 4.10 to 4.16. In general, we find for most daily temperatures that:

$$T_{\mathrm{OH}(3-1)} > T_{\mathrm{OH}(4-2)} > T_{\mathrm{OH}(8-5)},$$

which is also reflected in Tab. 4.2 for the OH(3-1) and OH(4-2) temperatures. Interestingly, one exception exists for the period that followed the cold anomaly in 22-Jan 2009 (4.10) where daily OH(4-2) temperatures are higher in most cases. This period also coincides with the enhanced downwelling of the OH* airglow layer according to 4.12, which could indicate that the inversion between OH(3-1) and OH(4-2) temperatures is related to the special dynamic conditions during that time.

Another striking feature in the time series is the significant change in the offset between OH(3-1) and OH(4-2) temperatures after 2010. While both temperature estimates typically differ by a few Kelvin beforehand (see Tab. 4.2), the average offset is in the order of 10 K during 2011-12 and even reaches the order of 20 K during 2010-11 and 2013-14. Interestingly, the measurement season 2011-12 also contains a persistent feature during 11-Nov to 31-Dec 2011 where the temperature offset reduces to 8.3 K on average. By comparison, the average offset value for the remaining temperature estimates of the same season already reaches 24.4 K.

With regard to the hypothesis that systematics shifts in the rotational temperatures are induced by the vertical shifts between different OH* Meinel bands, the observed offsets between OH(3-1) and OH(4-2) temperatures after 2010 are quite substantial. For instance, von Savigny et al. [2012b] estimate a mean difference of 0.65 K between profile weighted temperatures of two adjacent (initial) vibrational states, which is clearly below the observed offset between OH(3-1) and OH(4-2) temperatures. Of course, we should note that the estimate of von Savigny et al. [2012b] is based on a single month from the MSIS climatology at the equatorial latitude, hence, we have to take into account that the situation can be different depending on the season and latitude. As another example, the presented results from Perminov et al. [2007], which are based on the mid-latitudinal observations from Bakanas et al. [2003], indicate a maximum offset of about 5.5 K between rotational temperatures from the $\nu' = 4$ and $\nu' = 3$ vibrational population of OH* during November. Even though, this is more closely in agreement with our results prior to 2010 as well as the period from 11-Nov to 31-Dec 2011, the offset of the remaining periods is quite unusual, i.e. about three to four times larger compared to Perminov et al. [2007].

If we recall Sect. 3.8, changes in the atmospheric transmission are particularly affecting the OH(4-2) temperature estimates. According to the sensitivity test in Sect. 3.8 (see Tab. 3.4), the correction for the atmospheric transmission at the low elevation viewing angle leads to an average temperature shift in the order of 45 K in the iterative

retrieval. Accordingly, if we didn't apply any correction for the atmospheric transmission at all, OH(4-2) temperature estimates would generally exceed the OH(3-1) and OH(8 − 5) temperature estimates after 2010. Vice versa, the impact of the correction for the instrumental sensitivity and hatch window transmission is in the order of less than one Kelvin on average (Tab. 3.2), thus, negligible. This shows a large potential of the applied correction for the atmospheric transmission to affect the offset between OH(3-1) and OH(4-2) temperature estimates. The significantly larger offsets compared to the literature values should therefore be considered with caution, as these may be the result of deviations from the real atmospheric transmission spectrum.

We expand our discussion to the OH(8-5) temperatures and notice two general striking features in the time series:

- less OH(8-5) temperatures exist [49 versus 271 OH(3-1) daily T estimates],
- OH(8-5) temperatures are exceptionally low [164 K on average].

The first point results from the low SNR of the OH(8-5) band, thus, despite the relaxed data filtering criteria most OH(8-5) temperature estimates are discarded from the analysis due to their large fitting errors. The second point is a surprising result in comparison with previously published results:

Among others, early observations of Shefov [1961] indicate that "*the temperature averaged over the night is sometimes much higher for high vibrational levels than for lower levels*", as stated in Perminov et al. [2007]. Furthermore, Cosby and Slanger [2007] investigated different OH* Meinel bands based on spectroscopic observations from the Keck II telescope on Mauna Kea. They found that temperatures derived from transitions of the $\nu = 8$ vibrational state are generally higher compared to the $\nu = 3$ and $\nu = 4$ state, i.e. between about 6 K and 15 K depending on the season and local time. The seasonal dependency of rotational temperatures from different OH* Meinel bands is also discussed in Perminov et al. [2007]. Based on earlier observations at the mid-latitudinal Zvenigorod observatory (56°N, 37°E) from Bakanas et al. [2003], they present a seasonal evolution of rotational temperatures as a function of initial vibrational excitation state ν'. Interestingly, their presented seasonality also contains rotational temperatures from higher vibrational states that are lower compared to rotational temperatures from lower vibrational states. Following their seasonality, the January temperatures based on the transition from the $\nu = 8$ state are about 10 K lower compared to the $\nu = 3$ state.

Despite the above reported evidence of lower temperatures from the higher vibrational states, the difference between the OH(3-1) and OH(8-5) bands from our observations is still exceptionally high, i.e. about 48 K on average for the entire time series. A persistent thermal contrast inside the OH* airglow layer of this magnitude appears to be rather unlikely to serve as an explanation only. Similarly to the OH(4-2) temperature estimates, we have to take into account the substantial impact of the correction for the

atmospheric transmission on the retrieved OH(8-5) temperatures (Tab. 3.4). In contrast to the OH(4-2) temperature estimates, the correction for the atmospheric transmission has a positive impact on the OH(8-5) temperatures, but still leading to a cold bias with respect to the OH(3-1) temperatures. Furthermore, the temperature estimates before and after 2010 lie in a similar range. This may indicate a consistent correction for the atmospheric transmission in the retrieval, but the limitation to two remaining daily estimates makes a comparison rather difficult.

We further test as to whether the relaxed data filtering criteria for the OH(8 - 5) temperatures affect the results by selecting all hourly OH(8−5) spectra that pass the non-relaxed SNR threshold value according to Fig. 4.6. In this case, the average temperature of 166 K is still exceptionally low. So far, the exceptionally low OH(8-5) temperatures are surprising, even when considering the impact of the correction for the atmospheric transmission.

4.3.3. Thermal stability of measurements during 2013-14

In addition to the investigation of the thermal stability of the uncooled InGaAs detector in Sect. 3.6, we directly compare the fluctuations of the instrumental temperature with the OH(3-1) temperature estimates during 2013-14. According to Fig. 4.16 (see p. 87) we notice two strong temperature peaks around 27-Nov and 23-Dec 2013, which are not as pronounced for the MLS reference temperatures. Furthermore, we notice a drop in the instrumental temperature between 30-Nov and 5-Dec 2013 from about 22°C to 19°C (Fig. 3.13, p. 47). This roughly coincides with the dropping OH(3-1) temperatures between 27-Nov and 9-Dec 2013. On the other hand, the instrumental temperature already reached about 21°C on 7-Dec 2013 where OH(3-1) temperatures are still quite low. This indicates that the above mentioned match between dropping OH(3-1) and

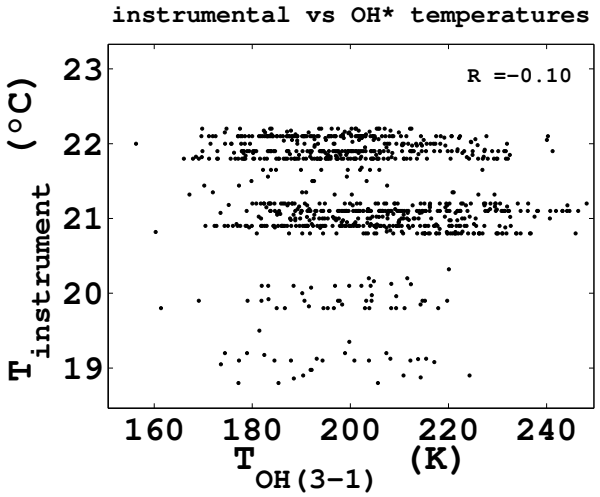

Figure 4.7.: HR125 versus OH(3-1) temperatures; R denotes the correlation coefficient.

instrumental temperatures is most likely due to coincidence. Furthermore, if we look at the scattering plot of OH(3-1) and instrumental temperatures in Fig. 4.7, we find no significant correlation between both quantities, which is also agreement with the studied correlation of time invariant intensity ratios in Sect. 3.6.

4.3.4. Large scale dynamic response

Despite the surprisingly large temperature offsets between different data sets according to Sect. 4.3.2, the temporal variability between these data sets appears to be highly correlated. This implies that the dynamic response is consistently reflected in the OH(3-1), OH(4-2), and MLS temperatures. In the following, we relate the response (i.e. relative temperature changes) to the stratospheric dynamic conditions according to the lower panel of Fig. 4.10 - 4.16, which is explained as follows:

The lower panel of Fig. 4.10 - 4.16 serves as a proxy for the stratospheric dynamic conditions, which according to our discussion in Sect. 2.2.2 can significantly affect the dynamic conditions at mesopause altitudes, in particular in response to an SSW event. If we recall the definition of an SSW event, the zonal mean temperatures increase poleward from 60° latitude at the 10 mbar pressure level or below and in the event of a major SSW event a reversal of zonal winds is manifesting at the same pressure level. By analogy with other studies (e.g. Gao et al. [2011]), the lower panel of Fig. 4.10 - 4.16 shows the difference between the temperature at the pole and the zonal mean temperature at 60°N and 10 mbar pressure level (black line, left axis). In addition, the zonal mean winds at the 60°N latitudinal circle and 10 mbar pressure level are denoted by the blue line (right axis). Temperatures and zonal winds are taken from the NCEP/NCAR reanalysis 1 [Kalnay et al., 1996], which is provided by NOAA/OAR/ESRL PSD, Boulder, Colorado, USA, at http://www.esrl.noaa.gov/psd/.

Based on the description of the stratospheric dynamic conditions according to the lower panel of Fig. 4.10 - 4.16, we find several occasions that meet the criteria for minor and major SSW events. Here, we limit the discussion to the three most relevant SSW events with respect to the temperature time series above Ny-Ålesund.

Major SSW 2009: The major SSW event of 2009 is the most intense within the decade of 2000–10. It is a prominent example of a strong coupling between the stratospheric and MLT region and has been extensively discussed by various studies (e.g. Manney et al. [2009], Labitzke and Kunze [2009], Gao et al. [2011], Hoffmann et al. [2011], Kuttippurath and Nikulin [2012]). According to the lower panel of Fig. 4.11, we find a clear signature of a long lasting reversal of zonal winds to easterlies between 23-Jan and 21-Feb. It is accompanied by a large increase of poleward temperatures at the 10 mbar pressure level, which peaks around 23-Jan. Vice versa, a pronounced dip is present in the MLS temperatures around 22-Jan that is followed by a strong warming, which peaks around 19-Feb. Following the published results of Gao et al. [2011] the

vertical (adiabatic) up- and downwelling of the OH* airglow layer in phase with the temperature changes is clearly visible in Fig. 4.12. Unfortunately, the period during the upwelling/cooling of the OH* airglow layer is not covered by the OH* measurements. Nonetheless, the response in the MLS temperatures nicely matches the proposed coupling from theoretical models as discussed in Sect. 2.2.2 and therefore serves as a good example for the comparison of the other two observed SSW events.

Minor SSW 2011: Another drop in mesopause temperatures is evident in 2011 with its onset on 14-Jan and reaching its peak value two days later. The drop in mesopause temperatures is followed by a warming phase until 26-Feb. Stratospheric zonal winds from the NCEP reanalysis decrease from 22-Jan to 2-Feb, but westerly wind directions are maintained during this period. The poleward temperature difference shows a pronounced peak that coincides with the maximum deceleration of stratospheric winds on 2-Feb, marking a minor SSW event. During the same day mesopause temperatures have just reached their nominal values after the preceding mesospheric warming phase.

In contrast to the major SSW event in 2009, we cannot find a clear correspondence between the drop in mesopause temperatures after 14-Jan and the deceleration of stratospheric zonal winds, as the mesospheric cold temperature anomaly is preceding the onset of stratospheric zonal wind deceleration by about eight days. By comparison, the response between the stratospheric wind/temperature anomalies and the mesospheric cooling anomaly occurred almost instantaneously during the major SSW event in 2009. A similar response between the stratospheric and mesospheric anomalies during SSW events was also shown by the model study of Zülicke and Becker [2013], which suggests a mesospheric response that is slightly delayed (about 1–2 days). However, they also draw the attention to the study of Hoffmann et al. [2007], who found evidence of a reversal of zonal local mesospheric winds from MF/meteor radar observations well in advance before the onset of an SSW event. Interestingly, the presented example by Hoffmann et al. [2007] of the SSW event in 1999 shows an anomaly in the zonal mesospheric winds that is preceding the coinciding stratospheric temperature/wind anomaly by six days, which marks a roughly similar delay in comparison with the eight days delay between the cold mesopause anomaly and stratospheric wind deceleration in 2011.

Following Zülicke and Becker [2013], the observed leading mesospheric anomaly in the zonal winds still appears to be not fully understood. Since the mesopause temperatures are very sensitive to the dynamic conditions, this could imply a similar situation for the observed preceding mesopause response in 2011.

Another potential mechanism to disturb the mesospheric region are solar perturbations (see Sect. 2.2.4). Despite the absence of sunlit conditions during the polar night, a temperature response to changes in the solar forcing can occur with a time lag of about 65 days at high latitudes according to Holmen et al. [2014]. One commonly used indicator of the solar forcing is the F10.7 solar radio flux. However, the provided F10.7

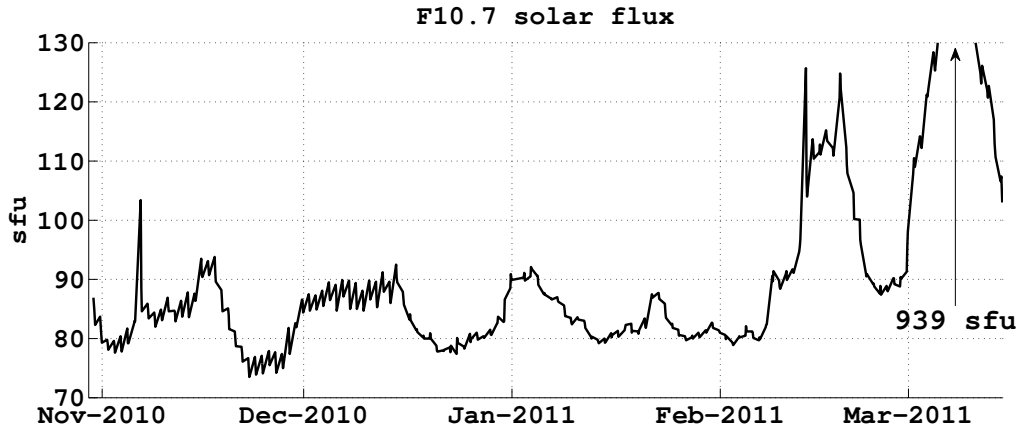

Figure 4.8.: F10.7 solar flux observed from Dominion Radio Astrophysical Observatory, Penticton, Canada; data provided by National Research Council Canada.

flux values from NOAA indicate a rather low fluctuation in the solar activity during the 65 days period prior to the mesospheric temperature anomaly, as shown in Fig. 4.8. Furthermore, the geomagnetic activity was quiet during the minor SSW event and no EPP events were reported for this period of time. Thus, it is unlikely that the mesospheric temperature anomaly during the minor SSW event in 2011 was caused by solar perturbations, yet the driving mechanism remains subject to future investigations.

Minor SSW 2012: A short minor SSW occurred around 31-Dec 2011 that is followed by a more long lasting SSW between 11-Jan and 2-Feb 2012. In comparison with the mesopause temperatures, we find a cold dip in the MLS temperatures that coincides with the peak of the minor SSW according to the NCEP reanalysis data. In contrast to the major SSW event in 2009, the magnitude of the temperature drop is not as pronounced, but a subsequent mesospheric warming after the peak time of the 2012 minor SSW event is clearly visible, in particular when considering the OH* temperature estimates. Between 19 and 25-Jan, OH(3-1) and OH(4-2) temperatures increase by about 25 K, 22 K, respectively. Unfortunately, OH* measurements were disrupted after 25-Jan 2012 for the rest of the winter season due to a short circuit at the AWIPEV station caused by melting water and a required maintenance of the FTIR after the power cut.

Nonetheless, the covered time period appears to be quite interesting, because eruptions of solar flares led to two pronounced SPEs on 23-Jan and 28-Jan, as shown in Fig. 4.9. According to Jackman et al. [2014], this period of SPEs together with another period in March 2012 can be counted as the two largest SPE periods during the current solar cycle. If we consider the solar proton flux displayed in Fig. 4.9, OH* emission measurements were at least performed until the peak of the first SPE starting in 23-Jan.

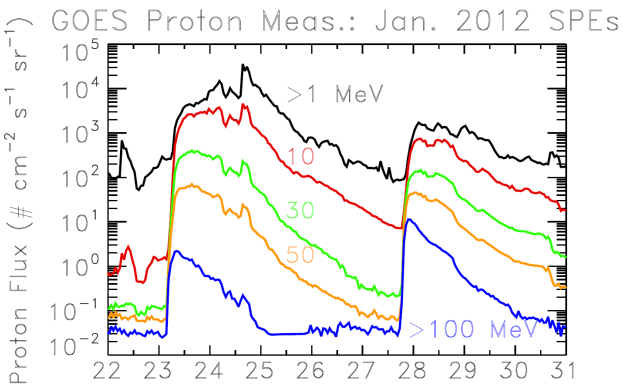

Figure 4.9.: Published GOES 13 proton flux measurements by Jackman et al. [2014], figure taken from the same publication. Different colours denote different energy levels.

The 2012 SPE had a strong impact on the mesospheric chemistry (Sect.2.2.4), resulting in a catalytic destruction of O_3 by up to 60 % in the upper mesospheric region on 25-Jan according to the study of Jackman et al. [2014]. As noted by von Clarmann et al. [2013], "*the temporal coincidence of the warming events with the SPEs makes the assignment of the atmospheric response to the SPE versus dynamical effects convoluted.*" This also applies to our observed mesopause temperatures, which are affected by different processes. Therefore, separating the contributing processes from the SPE and SSW event (see Sect. 2.2.4) is a challenging task, in particular with regard to our local measurements. For instance, heating rates from Joule heating during SPEs are strongly depending on the spatial distribution of the electric fields according to Roble et al. [1987]. Thus, despite the rather negligible zonal net heating due to Joule heating, as reported by Jackman et al. [2007], local heating rates can reach several Kelvin per day (e.g. about 7 K at 87 Km according to the example of Roble et al. [1987]), and therefore may have potentially affected our observed temperatures. Accordingly, further studies on the local conditions will be required to extrapolate the impact of the SPE on our temperatures.

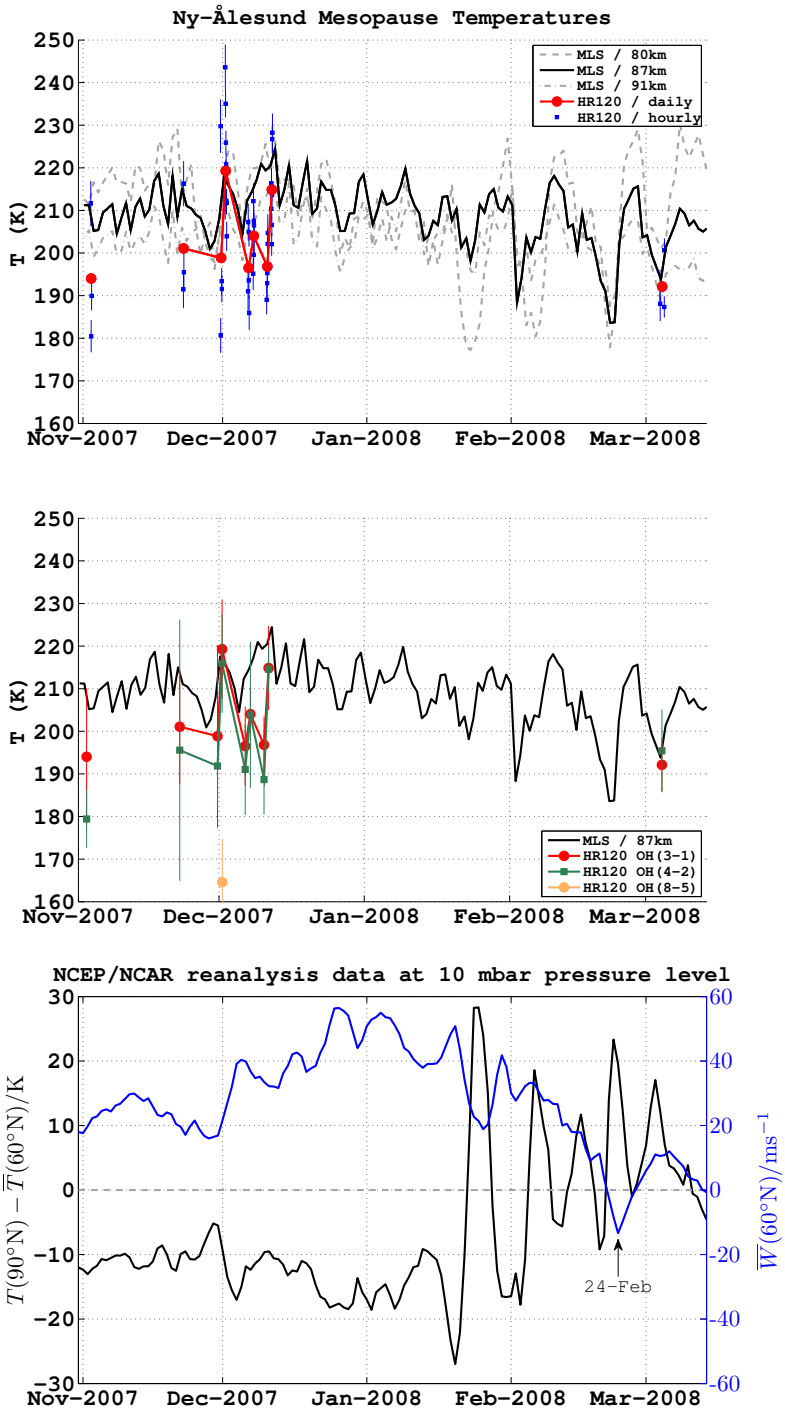

Figure 4.10.: Time series: 2007-08. **Upper panel**: OH(3-1) temperature estimates from HR120. Hourly temperature estimates are denoted by blue squares. The fitting error is indicated by the error bars. Daily temperatures are denoted by red circles. For guidance, closely spaced daily temperatures are connected with a red solid line. Daily averaged MLS temperatures are denoted by the black&grey lines for three height levels. **Middle panel**: Daily temperature estimates from three different OH* emission bands. The standard deviation from the hourly temperatures is indicated by the error bars. MLS temperatures at the 87 km height level are included for comparison. **Lower panel** (NCEP reanalysis): Zonal temperature difference between 60°N and 90°N at 10 mBar level (black line). Zonal wind at 10 mBar level averaged over the 60°N lat. circle (blue line).

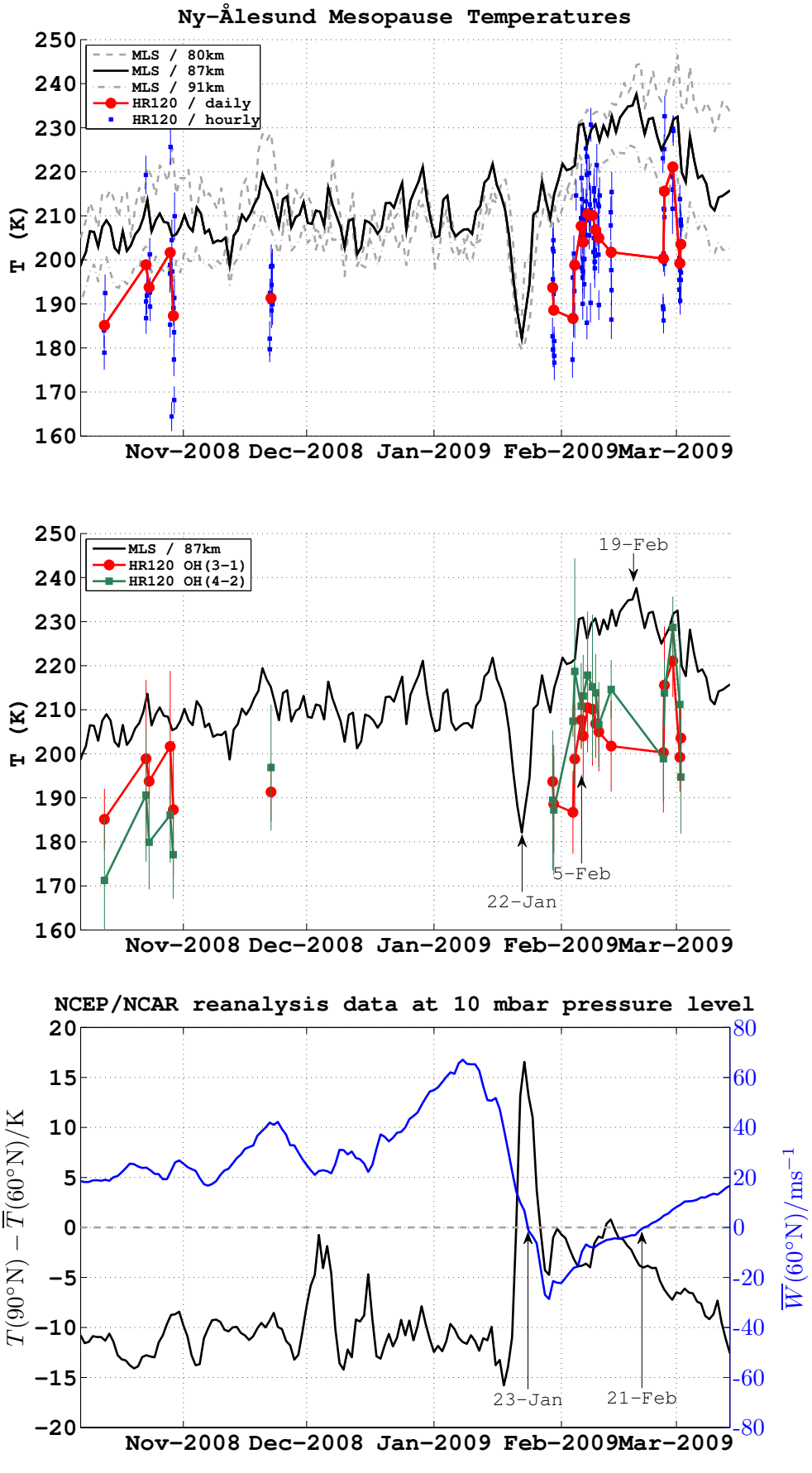

Figure 4.11.: Time series from 2008 to 2009: Same designations apply as for Fig. 4.10.

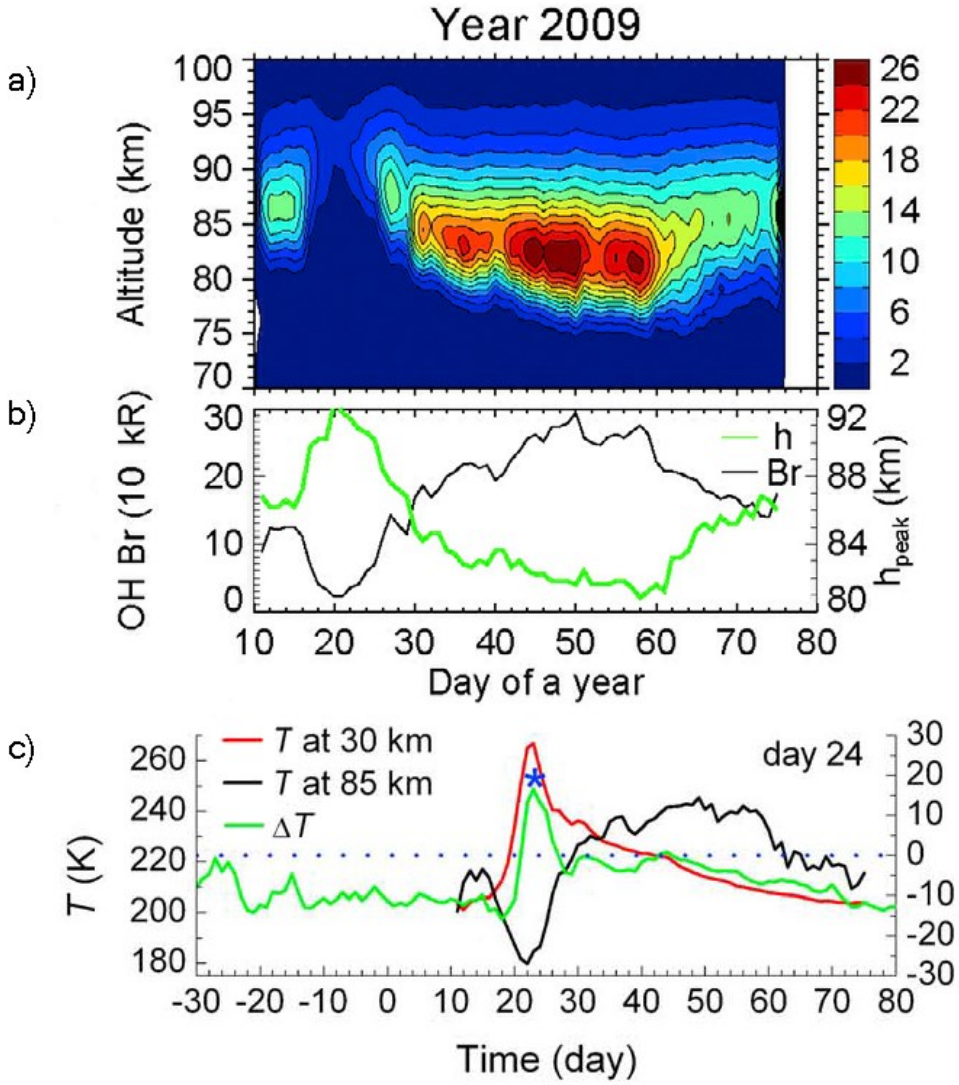

Figure 4.12.: Published SABER results by Gao et al. [2011], figure taken from the same publication. (a-b): OH* emission brightness at 80°N in 10^4photons/cm^3/s; (c): SABER temperatures at 35 km and 85 km altitude level and $\Delta T = T(90°\mathrm{N}) - \bar{T}(60°\mathrm{N})$ by analogy with the lower panel of Fig. 4.10.

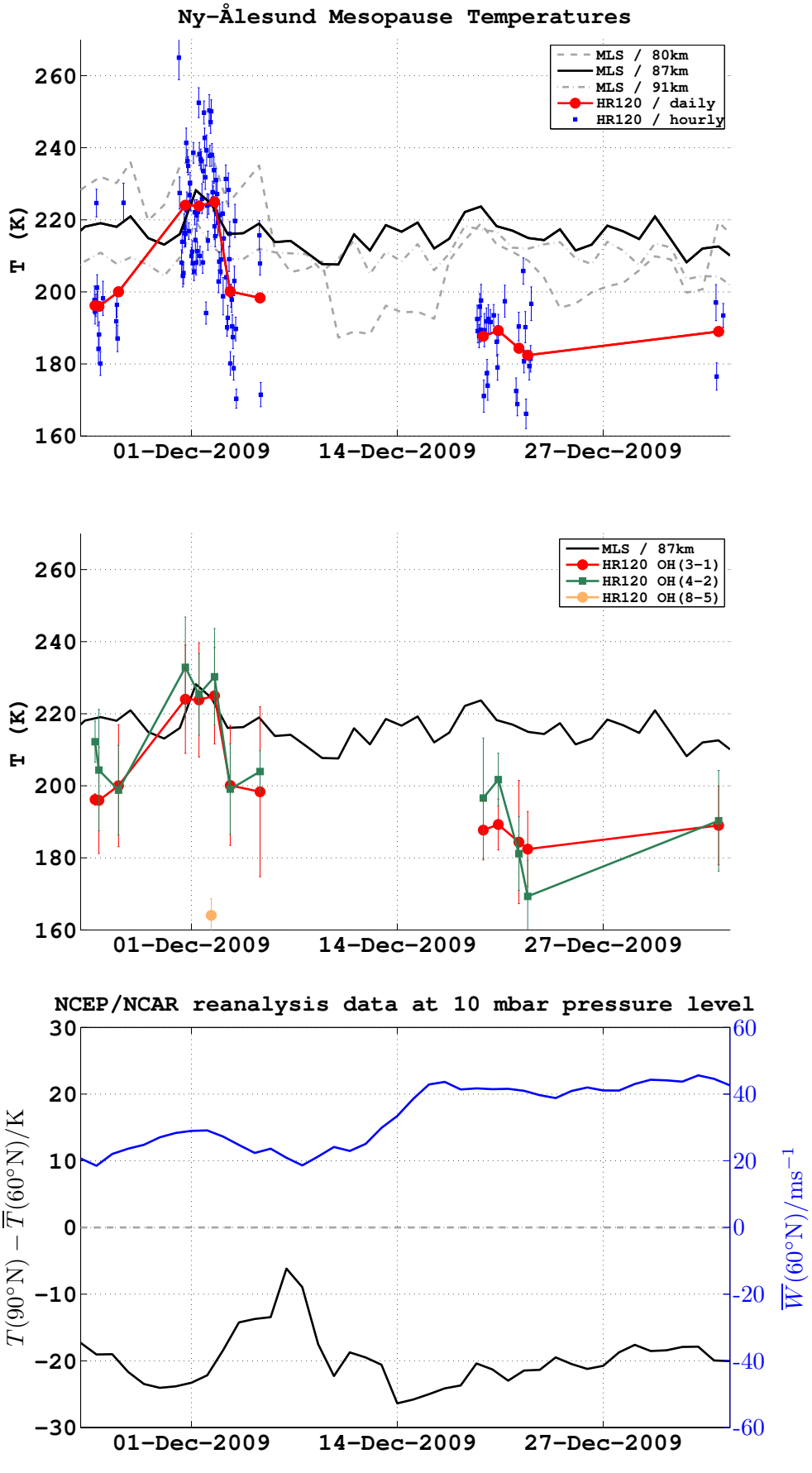

Figure 4.13.: Time series from 2009 to 2010: Same designations apply as for Fig. 4.10.

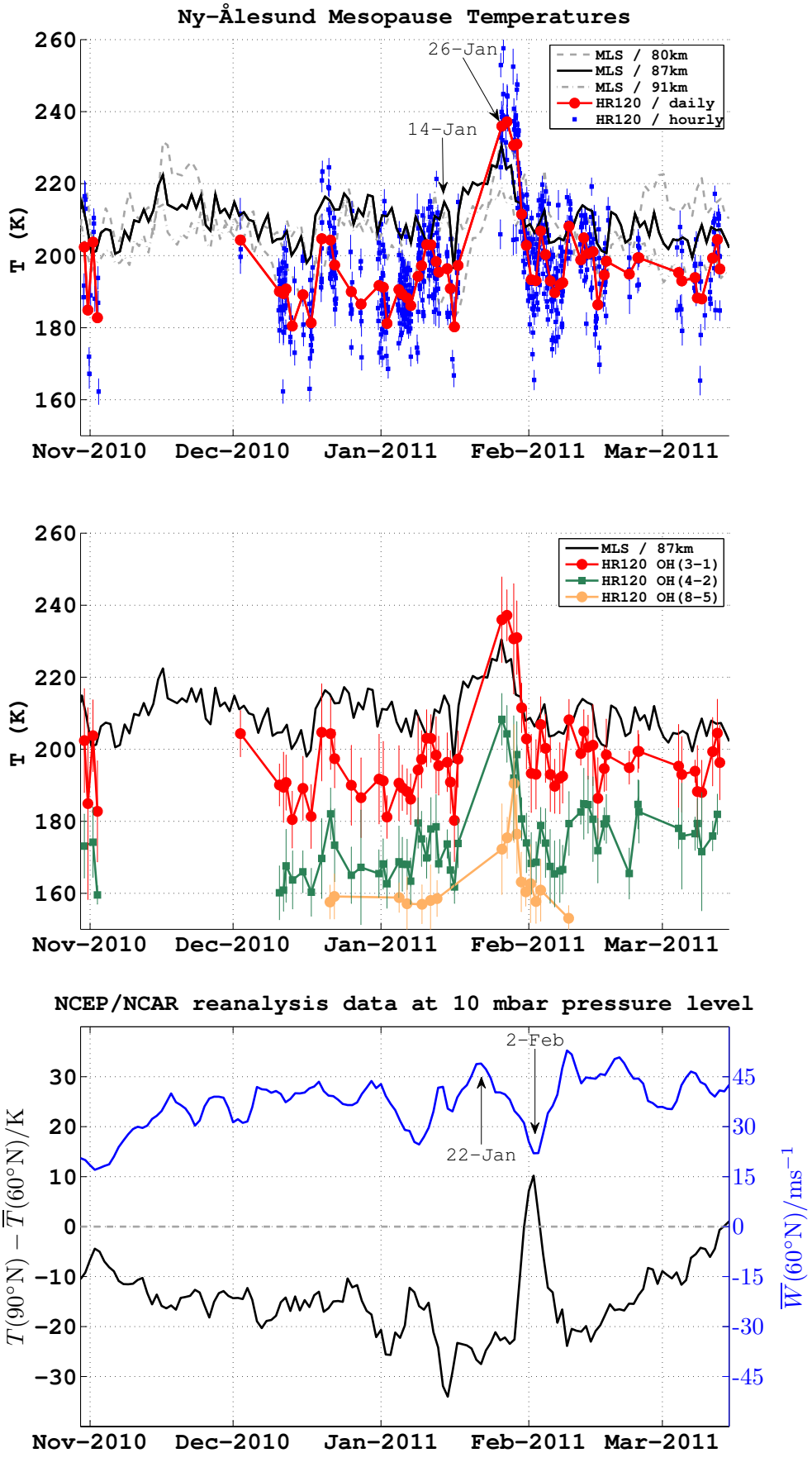

Figure 4.14.: Time series from 2010 to 2011: Same designations apply as for Fig. 4.10.

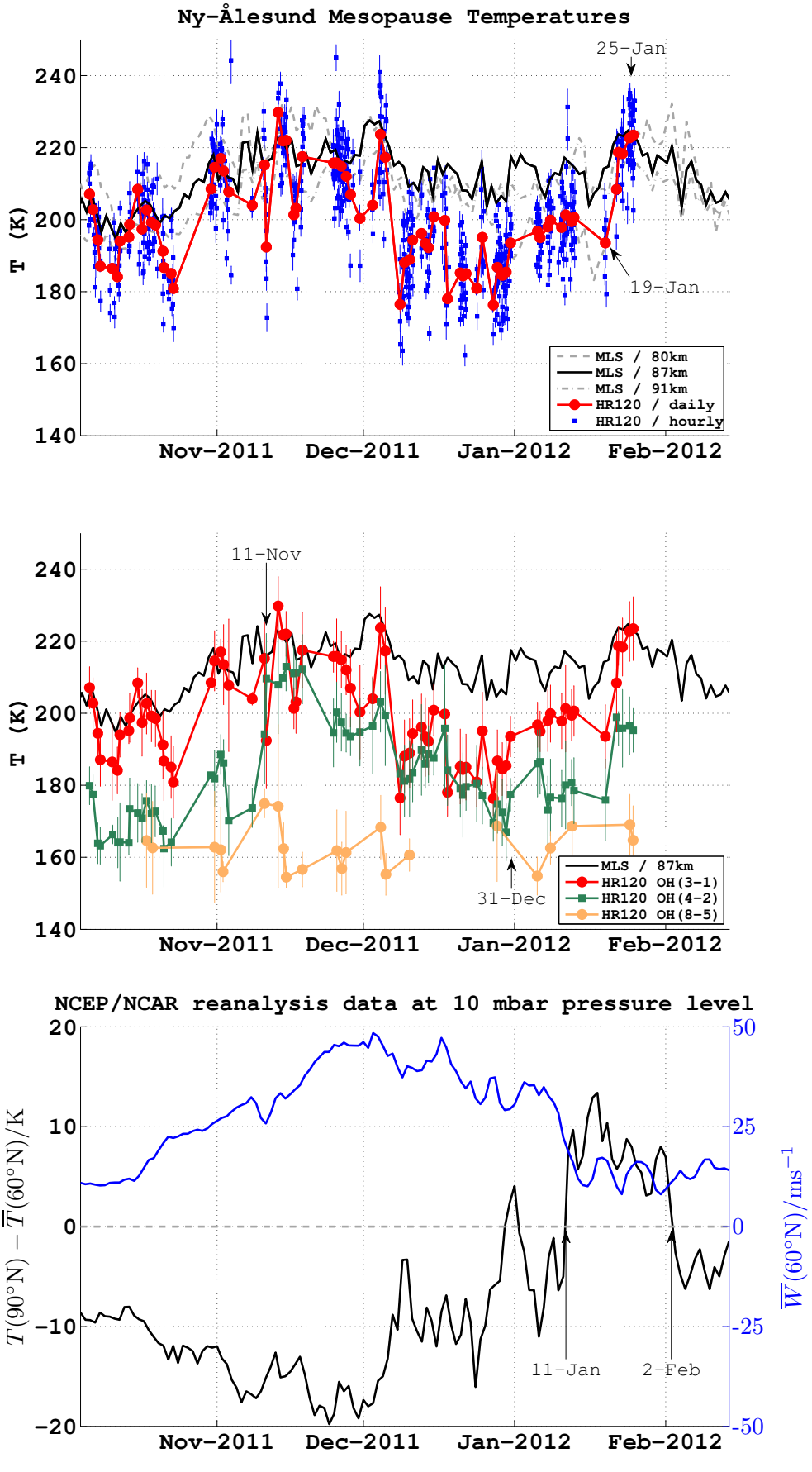

Figure 4.15.: Time series from 2011 to 2012: Same designations apply as for Fig. 4.10.

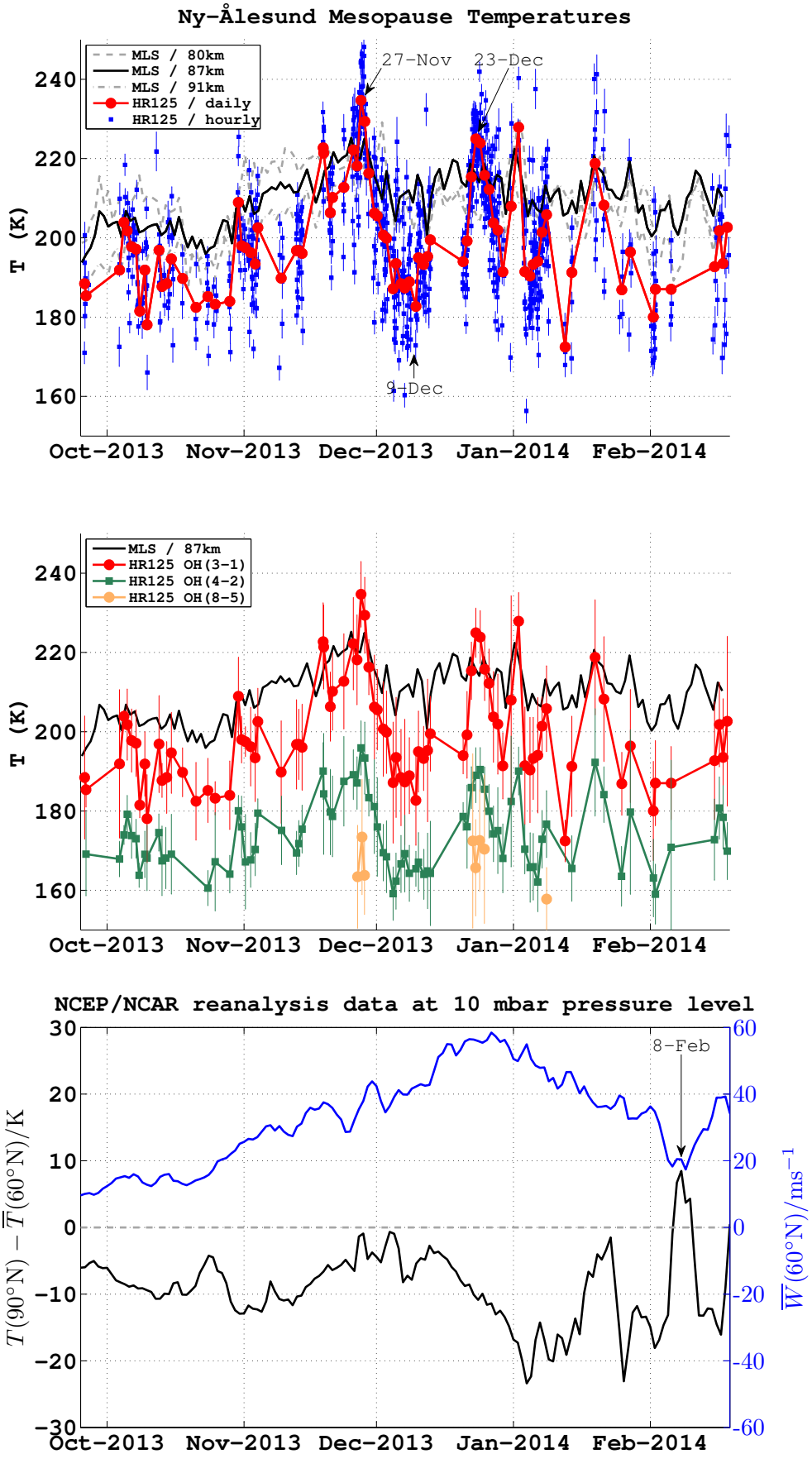

Figure 4.16.: Time series from 2013 to 2014: Same designations apply as for Fig. 4.10.

4.4. Harmonic temperature and brightness perturbations

After the consideration of the day-to-day variability of mesopause temperatures as a proxy for large scale dynamics at corresponding altitudes, we now focus on the hourly variability of OH(3-1) and OH(4-2) temperatures and consider simultaneous measurements of brightness fluctuations of the OH* emission. Fluctuations in both parameters can be of secular (i.e. aperiodic) nature [Huang and Hickey, 2008], but also periodic signatures can by induced by the passage of vertically propagating waves. Referring back to Sect. 2.2, tidal and gravity waves are predominant types of waves that disturb the MLT region and therefore play an important role for the dynamics of this region. Hence, the airglow response provides valuable information on these waves. It is therefore worth reviewing some fundamentals of wave disturbances in the OH* airglow layer at this place, before we discuss these disturbances with respect to the measured temperature/brightness time series of this work.

In an early attempt to quantify the airglow response to harmonic perturbations, Krassovsky [1972] introduced the *Krassovsky's ratio*, which nowadays is typically extended to the complex quantity:

$$\eta = |\eta| \exp\left(i\Phi_K\right) \tag{4.1}$$

with

$$|\eta| = \frac{\Delta B/B_0}{\Delta T/T_0} \tag{4.2}$$

where ΔB is the relative brightness fluctuation to the steady state brightness B_0 of the airglow layer, ΔT is the temperature fluctuation of ambient air to the steady state temperature T_0, and Φ_K is the relative phase between brightness and temperature fluctuations. There has been considerable effort by various theoretical studies to describe the airglow response to monochromatic disturbances by means of Krassovsky's ratio (Hines and Tarasick [1987], Walterscheid et al. [1987], Walterscheid and Schubert [1987], Tarasick and Shepherd [1992], Makhlouf et al. [1995], Swenson and Gardner [1998], among others), but predicted values can substantially differ between competing theories and in some cases even contradict the airglow response in η from observations (e.g. Reisin and Scheer [1996], Oznovich et al. [1997]). This certainly reflects the complex nature of the airglow response, which depends on various factors such as chemical lifetimes of reactive species versus wave period (e.g. Tarasick and Shepherd [1992], Swenson and Gardner [1998]), the impact of collisional quenching with ambient molecules [Makhlouf et al., 1995], the temperature profile of the airglow layer, wave characteristics (e.g. freely propagating versus ducted or evanescent wave type [Liu and Swenson, 2003]), viewing geometry [Tarasick and Hines, 1990]. Despite the complexity in the airglow response to wave perturbations, a growing consensus between the theoretical model of Hines, Tarasick and Shepherd (HTS theory) as well as the model of Swenson and Gardner (SG theory; see references above) and observational studies exist that η is directly reflecting vertical wave properties. Following Reisin and Scheer [1996], they deduce a formula

from the HTS theory, which directly relates the vertical wavelength to the amplitude and phase of η for zenith looking observations. Due to the universality of the HTS theory to various airglow layers, it appears that the dynamical response in terms of the theoretically predicted η is decoupled from the chemistry, as outlined in the not yet published "mini-review[5]" by Jürgen Scheer, Instituto de Astronomía y Física del Espacio.

In addition to the vertical wavelength, the direction of wave propagation, i.e. upward or downward, can be inferred from the sign of phase Φ_K. Following the SG theory, the temperature and brightness response inside the airglow layer to a vertically propagating wave is largest at different altitudes. The SG theory predicts largest temperature fluctuations to manifest near the peak of the OH* airglow layer, while largest brightness fluctuations are predicted to manifest at the bottom side of the OH* airglow layer. An initial estimate of about 3.75 km was made for the vertical separation of maximising fluctuations by Swenson and Gardner [1998] and was further refined to 3.1 km in the follow-up study by Liu and Swenson [2003]. The experimental study by Nikoukar et al. [2007] based on SABER observations revealed a slightly smaller vertical separation of about 2.8 ± 0.7 km but with the theoretical value still in the range of uncertainty. Given the vertical separation in the maximising responses, it is evident that either the observed temperature or brightness is responding first to the perturbing wave depending on the direction of vertical wave propagation. Accordingly, a wave with upward propagating phase (i.e. downward energy propagation) is seen in the brightness response first and a wave with downward propagating phase (upward energy propagation) is seen in the temperature response first. As per definition, this corresponds to either a positive or negative phase value Φ_K.

To make use of η in terms of a quantitative diagnostic tool for vertical wave properties at the mesopause region, a cross-spectral analysis is required for the observed fluctuations in temperatures and airglow brightness. Because such an analysis still needs to be developed in a future work, this section primarily focuses on the sign of the Krassovsky's ratio based on manually selected case examples. In addition, these examples give a first impression of the contained wave characteristics in our data set.

We limit our discussion to the results based on hourly averaged spectra. At these temporal scales, harmonic perturbations can be caused by vertically propagating tidal as well as gravity waves. Because of the same intrinsic nature of their perturbations, as stated in Nikoukar et al. [2007], both wave types may serve as an explanation for the observed hourly perturbations. However, some particular features exist that help us to discriminate between tidal and gravity wave induced perturbations.

Tidally induced perturbations typically occur at a range of sub-harmonic frequencies

[5] "Vertical wavelengths from airglow intensity and temperature observations of a single emission. A mini-review (Latest update: October 6, 2010)", by Jürgen Scheer, accessed on July, 2014 at: http://www.iafe.uba.ar/docs/aeronomia/HT.HTM

of the 24 h solar day, i.e. 12,8,6,4 h and so on. At first glance, their occurrence during the polar nighttime conditions may appear surprising due to the absence of local solar heating at the lower atmosphere. However, while theoretical tidal models suggest that high order tidal modes are weakly excited by the global solar forcing, the zonally symmetric non-migrating tide is a commonly reported pronounced tidal feature of the polar regions (e.g. see Walterscheid and Schubert [1995], Oznovich et al. [1995, 1997], Won et al. [2003]). In addition to their distinct sub-harmonic periodicities, tidal oscillations may last for several cycles, while gravity wave induced perturbations usually persist for two cycles or even less according to Oznovich et al. [1995].

At higher frequencies, gravity wave perturbations become the dominant forcing mechanism. For instance, Reisin and Scheer [2001] set an upper limit of a 3 h periodicity to discriminate between the gravity and tidal wave ranges. We should therefore expect that the hourly averaged results from the OH* emission measurements at Ny-Ålesund mainly reflect harmonic perturbations in the tidal range, but as discussed above, large scale gravity waves may still serve as an explanation. In addition, wave-to-wave interactions can further generate specific harmonic perturbations (e.g. see Ghodpage et al. [2012]).

Based on a visual inspection of the time series of this work, about 30 events were identified that show similar periodicities in the brightness of the OH* emission and derived rotational temperatures. In contrast to the brightness modulation through interfering clouds, which may not have been fully rejected by the data filtering procedure, similar periodicities in both parameters are most likely related to the intrinsic fluctuation of the OH* airglow layer.

The visually identified events contain various sub-harmonics ranging down to 4 h but also intermediate periods of 10 h and 5 h are present. In some events, different harmonics are superimposed upon each other.

4.4.1. Case examples of hourly perturbations

A selection of six case examples that contain distinct oscillations in the derived rotational temperatures and OH* emission brightness is shown in Fig. 4.17 to 4.19 (see **pp. 94-96**).

The left panels show the time series of OH(3-1) and OH(4-2) temperatures and relative intensity changes of the associated $Q_1(1)$ rotational lines. Ideally, one should relate changes in the OH* brightness to the intensity changes of the selected entire emission band, which needs to be reconstructed from the observed emission lines. However, Reisin and Scheer [2001] found that the direct use of measured band intensities also gives consistent results in terms of brightness fluctuations. Even though, the consideration of intensity changes of a single rotational line is a further simplification, the additional consideration of the three most intense P_1 rotational lines of the OH(3-1) and OH(4-2)

bands did not appear to change the characteristics of the brightness fluctuations in the measurements of this work.

The right panels of Fig. 4.17 to 4.19 show normalised periodograms that were computed by means of a Lomb-Scargle analysis of the time series shown in the left panels. Similarly to the Fourier analysis, the Lomb-Scargle analysis allows us to decompose the spectral harmonic components of a time dependent signal. One important difference between both methods is that the Lomb-Scargle analysis does not require an equal distribution of time steps (e.g. see Press and Rybicki [1989]). Therefore, it can be directly applied to a time series that contains several data gaps. The Lomb-Scargle analysis also allows us to estimate the significance of different spectral components. Because gravity and tidal wave perturbations can only be observed for a few cycles, the significance level can be largely affected by the choice of the time window (e.g. see Oznovich et al. [1997]). Further techniques, such as the removal of additional harmonic components in the time series, can be applied to improve the significance levels, but for the initial investigation of harmonic components in this section the Lomb-Scargle analysis is directly applied to the time series on the left panels.

It is worth noting that the qualitative characteristics of each example are kept, if we switch off the correction for the atmospheric transmission, which according to Sect. 3.8 has a particularly strong impact on the OH(4-2) temperatures. Accordingly, as long as we may suppose that the atmospheric transmission is constant with time, the observed harmonic perturbations are essentially representing the intrinsic response of the OH* airglow layer to atmospheric waves.

Discussion of results

Figure 4.17 shows the first two examples of harmonic hourly temperature/line-intensity fluctuations in the OH(3-1) and OH(4-2) bands. Signatures of an approximate 6 h oscillation, matching with the tidal sub-harmonics, are present in the first example (Fig. 4.17a). The second example (Fig. 4.17b) is dominated by an approximate 8.5 h to 9 h oscillation, which is close to a ter-diurnal periodicity.

If we consider the periodograms on the right panels of Fig. 4.17, the dominant frequency component of each example is reflected in the associated power spectrum of each parameter (i.e. temperatures and line-intensities). With respect to the indicated α-significance level[6], we find that almost all parameters reach at least the $\alpha = 0.5$ level. The only exception exists for the 6 h oscillation of the OH(3-1) temperatures (Fig. 4.17a: right panel). However, we also notice that all spectral power peaks are clearly above the background level of the periodograms, while further techniques may increase the significance levels, as noted above. Therefore, we will mainly focus on the frequency

[6]The α level is the probability of rejecting the null hypothesis, i.e. in this case the assumption of a pure noise signal. It is related to the level of confidence C as follows: $1 - C = \alpha$

power relative to the background level in the following.

An interesting feature of both examples in Fig. 4.17 is the phase shift between temperature and line-intensity perturbations. In this case, temperature perturbations are preceding the intensity perturbations, which according to the SG theory suggests an upward energy propagation as discussed above. The visual inspection of the time series confirms that leading temperature perturbations are the most common feature, which is also in agreement with the principal excitation mechanisms of tidal and gravity waves in the lower atmospheric layers. Examples of the opposite case (i.e. positive sign of η) are also shown by other studies (e.g. Ghodpage et al. [2012]), but these typically appear on rare occasions. This is also the case for the time series of this work, where only two events with preceding line-intensity perturbations were visually identified.

Figure 4.18a shows one example of a preceding intensity perturbation event. According to the periodogram, the oscillation is dominated by a ter-diurnal component. Again, all parameters show a low significance (i.e. higher α values) but with the ter-diurnal line-intensity component peaking above the background level in the periodogram. Only the ter-diurnal oscillation of the OH(4-2) temperatures is not evident in the periodogram, but if we compare their maximum and minimum values with the OH(3-1) temperatures in the time series, we still find characteristics of a ter-diurnal oscillation.

While the SG theory gives an explanation for the time delay between temperature and brightness perturbations, the vertical shifts in the OH* Meinel bands imply a further delay in the airglow response between different OH* Meinel bands. In comparison to the vertical shift of about 3 km between the maximum responses in brightness and temperature altitudes of the same emission band, the vertical shift between two adjacent OH* Meinel bands is typically in the order of a few hundred metres as stated earlier. This implies that the time delay between the OH(3-1) and (4-2) bands should be smaller compared to the delay between the temperature/line-intensity responses of the same band. With respect to the first two examples (Fig. 4.17), the temperature/line-intensity delays are roughly in the order of 1 h to 3 h, which makes the detection of an even smaller phase shift difficult due to the hourly resolution and short duration of the signals. This also gives an explanation why the temperature and line-intensity changes appear to be in phase between both OH* Meinel bands. The situation looks slightly different in the third example (Fig. 4.18a), if we look at the shifted maxima between OH(3-1) and OH(4-2) temperatures around 04:00 to 05:00 (UTC). In contrast, no significant phase shift is evident between the associated line-intensity fluctuations.

Another example of a phase shift between OH(3-1) and OH(4-2) temperatures is shown in Fig. 4.18b. Interestingly, the leading OH(3-1) temperatures are quite evident in this example, but we also notice that a similar phase shift is again missing between the fluctuations of both line-intensities. In terms of the SG theory, this implies that the bottom side profile altitudes of the OH(3-1) and OH(4-2) emissions, which are most

sensitive in their brightness fluctuations, are less distinct compared to their profile peak altitudes, which are more sensitive in their temperature responses.

Figure 4.19a gives another example of pronounced oscillations in temperatures and line-intensities that could be observed during a 24 h observational period. The interesting feature of this example is a transition from an approximate semi-diurnal frequency to a higher 6-8 h frequency during the day, while both frequencies lie in the tidal frequency range.

Figure 4.19b shows an even larger time range of several days where exceptional weather conditions allowed for almost continuous observations. Pronounced temperature / line-intensity oscillations exist that are superimposed by a coherent change in both parameters at daily time scales. The coherent large scale response in both parameters indicates an interesting feature, which we will get back to at the end of the next chapter in Sect. 5.11.3. With regard to the Lomb-Scargle analysis, the corresponding low frequency component reaches spectral power values as high as $P(f_{\mathrm{low}}) = 45$ in the periodogram, which is clearly above the values of the higher frequencies. Despite the large time window compared to the previous examples, we also notice a 9.1 h frequency component in OH(3-1) and OH(4-2) line-intensities in the periodogram close to the $\alpha = 0.5$ level. Similarly to the second example in Fig. 4.17b, this frequency is close to a ter-diurnal oscillation. In this context, Oznovich et al. [1997] suggest that "*terdiurnal oscillations are a common feature of the winter polar mesopause, possibly the most recurring disturbance of the region*". Despite the slightly lower frequency in our example, this may also indicate a dominant ter-diurnal feature during the considered period, which is evident for the line-intensities at least. The missing signature of a ter-diurnal temperature oscillation in the periodogram is probably related to the smaller amplitudes of temperature versus line-intensity perturbations.

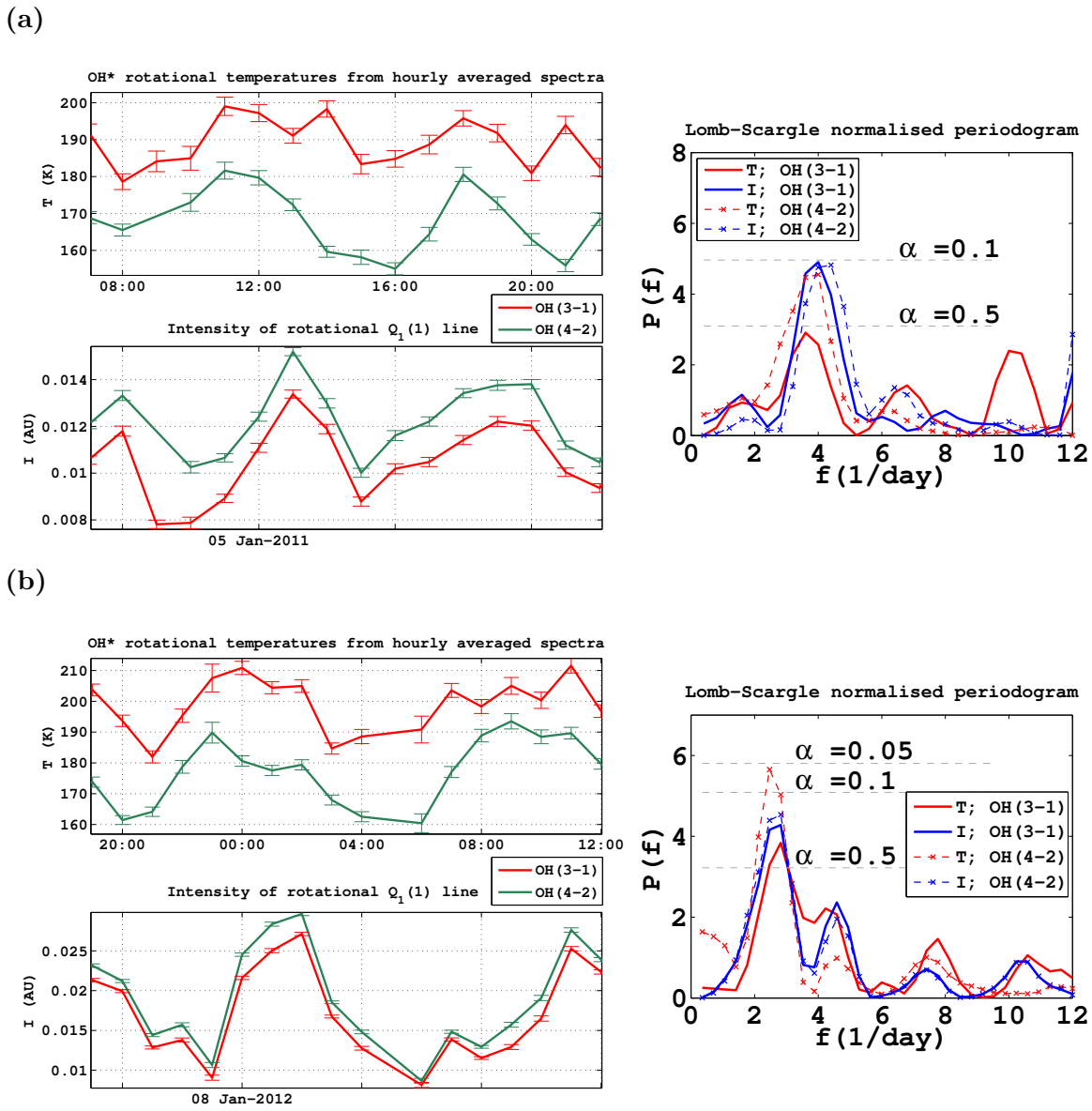

Figure 4.17.: Two examples of temperature perturbations that lead line-intensity perturbations. Left panels: OH$(3-1)$, OH$(4-2)$ temperatures and $Q_1(1)$ line-intensities (arbitrary units). The temperature error bars indicate the fitting error of the hourly averaged spectrum. The uncertainty in the measured intensity is expressed in terms of the standard deviation of noise in the spectral domain. Right panels: Normalised Lomb-Scargle periodograms of temperatures and intensities (see legend) referring to the same time window of the displayed time series.

(a)

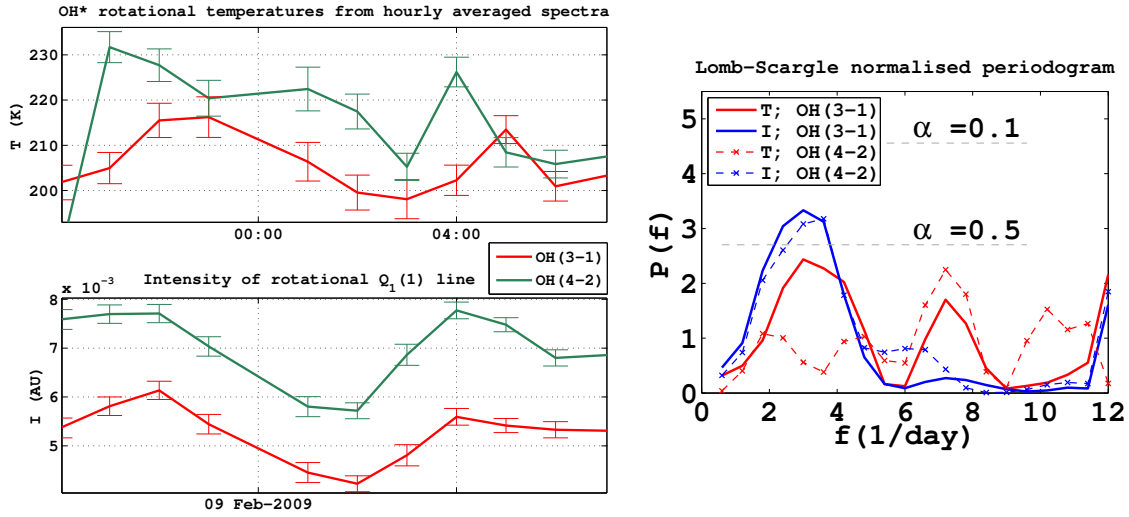

(b)

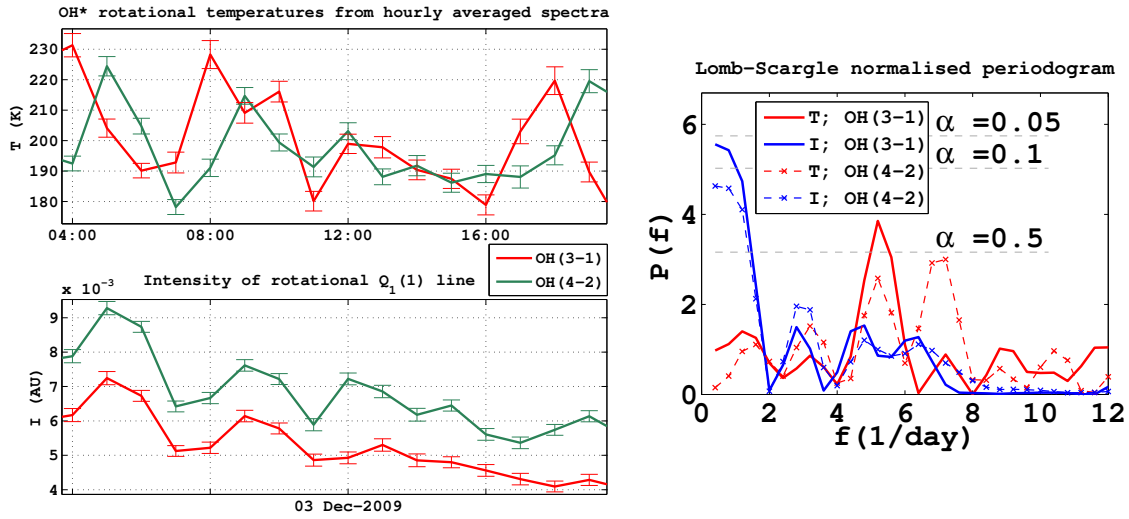

Figure 4.18.: (a): Line-intensity perturbations lead temperature perturbations. (b): OH(3-1) temperature perturbations lead OH(4-2) temperature perturbations. Same designations as used in Fig. 4.17.

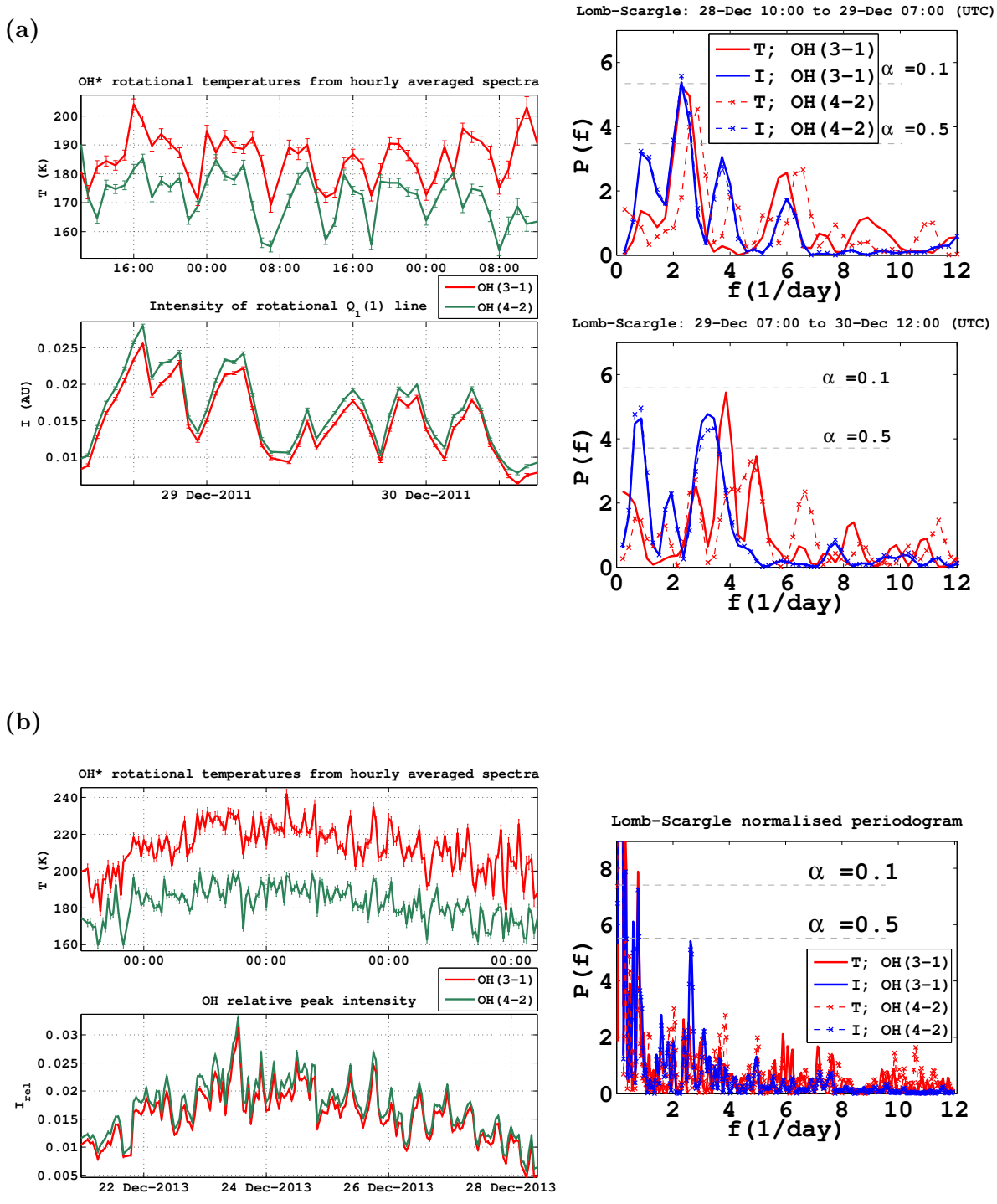

Figure 4.19.: (a): Example of frequency change in hourly perturbations. (b): Low frequency modulation (daily scale) superimposed by hourly perturbations. Same designations as used in Fig. 4.17.

4.5. Summary and conclusions

A time series of rotational temperatures from the OH* emission above Ny-Ålesund was created for six polar winter seasons between 2007 and 2014 in the frame of this work. Potential impacts from artificial village lights as well as auroral emission lines could be ruled out for the OH* emission measurements in Ny-Ålesund. In addition, no evidence was found for a critical impact of the thermal stability of the uncooled detector to the measurements. Further refinements in the automated operation of the FTIR measurements and the change from a zenith to a low elevation LOS led to an improvement of the number of non-discarded spectra against operational time by more than a factor of three compared to the precedent 2008-10 winter seasons.

This work considered rotational temperature estimates from the OH(3-1), OH(4-2), and OH(8-5) Meinel bands, the three most intense emission features in the recorded spectra. Systematic differences between these rotational temperatures were identified. Observed common features are:

- $T_{\mathrm{OH}(3-1)} > T_{\mathrm{OH}(4-2)} > T_{\mathrm{OH}(8-5)}$ (and $T_{\mathrm{OH}(4-2)} > T_{\mathrm{OH}(3-1)}$ in 2009),
- OH(8-5) temperatures are exceptionally low in most cases, i.e. up to 76 K lower compared to OH(3-1) temperatures,
- a small fraction of OH(8-5) temperatures remains after data filtering.

Furthermore, a significant increase in the offset between OH(3-1) and OH(4-2) temperature estimates coincides with the change of the LOS in 2010. Simultaneously, the correction for the atmospheric transmission shows the largest potential impact on the iterative retrieval of OH(4-2) temperatures, hence, it is found to be the most critical factor with respect to the temperature offset between the OH(3-1) and OH(4-2) bands. In this connection, the persistent offsets in the order of 20 K during 2011 and 2013 must be considered with caution, as they appear exceptionally high with regard to the thermal gradient of the OH* airglow layer only. Similarly, the larger negative offset of OH(8-5) to OH(3-1) temperatures is a surprising result, even when considering the impact of the atmospheric transmission on the retrieval.

In addition to the intercomparison of OH(3 - 1), OH(4 - 2), and OH(8 - 5) temperatures, the comparison with MLS temperatures shows that:

- ground-based temperature estimates have a larger dynamic range,
- relative temperature changes are highly correlated between MLS and ground-based measurements,
- the smallest offset to MLS is found for OH(3-1) temperatures (but still negative).

The comparison with published results from spaceborne observations by SABER and ground-based OH(6-2) observations at Longyearbyen, Spitsbergen, showed a similar temperature offset between the independent ground-based and spaceborne data sets during 2009, while the temperature offset after 2010 mainly persists for the ground-based measurements in Ny-Ålesund, including the OH(3-1) temperatures. As with the differences between rotational temperatures from different OH* Meinel bands, the offset between OH* rotational temperatures relative to MLS temperatures remains subject to ongoing investigations.

In addition to the comparison of absolute temperatures, the dynamic response of mesopause temperatures to changes in the stratospheric dynamic conditions was identified in ground-based as well as spaceborne temperature measurements. The impact of the 2009 major SSW to the mesospheric dynamics was by far the most dramatic event. Unfortunately, ground-based temperature estimates only exist after the associated strong mesospheric cooling due to the applied data filtering. However, further evidence of a mesospheric temperature anomaly was found in the rotational temperatures during two minor SSW events in 2011 and 2012. Interestingly, in contrast to the SSW events in 2009 and 2012, the changes in mesopause temperatures seem to precede the dynamic changes in the stratospheric zonal winds in 2011. This could imply a special situation of the coupling between the stratosphere and MLT region, but it may also be related to the comparison of our local measurements with the stratospheric zonal mean conditions.

Finally, the investigation of the OH* emission at hourly scales revealed harmonic signatures in the rotational temperatures as well as emission line-intensities. The coherency between temperature and brightness changes at these time scales suggests the response of the OH* emission to the passage of vertically propagating tidal as well as large scale gravity waves. Following the HTS and SG theories, phase lags with primarily leading temperature perturbations were found, which is consistent with the predominant wave forcing from the lower atmospheric layers. Similarly, phase lags between OH(3-1) and OH(4-2) rotational temperature estimates were found, suggesting a delayed response due to the vertical shifts in the OH* emission. However, a similar phase lag in the relative line-intensity changes is not evident in the considered examples. In terms of the SG theory, this implies that the vertical separation of both vibrational populations must be more pronounced at their profile peak altitudes rather than at the profile bottom sides.

A future analysis that filters out additional frequency components in the time series and considers temperature/brightness estimates from single spectra at a minute scale will further improve the harmonic signatures in the time series. With regard to the HTS and SG theory, the quantification of Krassovsky's ratio η is expected to be a promising future application for the OH* measurements of this work.

5. OH* model study

This chapter addresses the second main part of this work, which develops a model to simulate vertical OH* number density profiles as a function of vibrational excitation state ν. Based on this model, the aim is to improve our understanding of the systematic vertical shifts between different OH* Meinel bands and their temporal variability. According to our discussion in the previous chapter, these vertical shifts can introduce systematic differences between rotational temperatures estimated from different OH* Meinel bands. Even though, the time series of rotational temperatures above Ny-Ålesund shows differences between the observed OH* Meinel bands that are difficult to explain by the vertical shifts of their emission only, the impact of the vertical shifts can still be relevant. Improving our fundamental understanding of the processes that drive the vertical shifts within the OH* emission is therefore of great value, in particular with regard to long-term studies that consider different OH* Meinel bands.

The main emphasis of this chapter will be on the collisional quenching process of the vibrationally excited OH* radical with other species. As mentioned in the beginning of Sect. 2.3, the collisional quenching is affecting the lifetimes of vibrational states and therefore plays an important role for the vertical distribution of the OH* emission bands. In this connection, we can distinguish between different OH(ν) layers with respect to their associated vibrational excitation state. Previous studies have shown that the quenching process leads to pronounced vertical shifts between these OH(ν) layers (e.g. Adler-Golden [1997], Dodd et al. [1994], Makhlouf et al. [1995]).

In particular atomic oxygen is an effective quencher and its impact on the vertical shifts between different OH(ν) layers has recently been investigated by von Savigny et al. [2012b]. Based on a sensitivity study, which relies on an updated version of the McDade quenching model [McDade, 1991], they suggest that quenching with atomic oxygen causes an upward shift of the individual OH(ν) layers with increasing vibrational state. In a follow-up study von Savigny and Lednyts'kyy [2013] provided experimental evidence that the vertical shifts between different OH* Meinel bands are indeed correlated with the concentrations of atomic oxygen at OH* layer altitudes. However, in addition to atomic oxygen other quenching species exist that may also significantly affect the vertical structure of the OH(ν) layers. Furthermore, temporal changes in the $H + O_3$ source gases of OH* can also affect the vertical shifts between different OH(ν) layers. Hence, it remains an open question whether the temporal evolution of these vertical shifts is mainly driven by the process of collisional quenching with atomic oxygen or additional processes must be taken into account for a proper understanding.

To address this question, this work uses chemical as well as temperature/pressure fields from simulations made with the SD–WACCM4 model to study the impact of the collisional quenching on the temporal evolution of the OH* Meinel bands. With regard to the previous studies of von Savigny et al. [2012b] and von Savigny and Lednyts'kyy [2013], the novelties of this approach are threefold: Firstly, the sensitivity study of von Savigny et al. [2012b] is limited to static quencher profiles that were taken from the MSIS climatology, while the effect of O quenching is investigated by scaling the O concentrations at all altitudes with a constant factor. In contrast, the temporal variability of the quencher profiles is explicitly taken into account by the SD–WACCM4 model runs in this work. Secondly, the sensitivity study of von Savigny et al. [2012b] uses further simplifying assumptions on the OH* profile shape, i.e. it assumes a Gaussian profile as a weighting function for their simulated fractional populations of OH* vibrational levels $\nu = 1, ..., 9$, while this work directly determines the OH* profile shape from the $H + O_3$ source gases taken from SD–WACCM4. Finally, the main focus of von Savigny et al. [2012b] and von Savigny and Lednyts'kyy [2013] is on the effect of O quenching and the related hypothesis that vertical shifts between different OH* Meinel bands are the consequence of this process. This work expands the focus to the effects of O_2 and N_2 quenching, which together with O are the three most important quenching species of OH*. Based on a sensitivity study this work investigates their impact on the seasonal as well as the diurnal variability between two selected OH(ν) layers.

Because of the emphasis of this work on the process of collisional quenching, we now shift our focus from polar to equatorial latitudes where the large amplitude of the diurnal migrating tide results in a prominent seasonal as well as diurnal oscillation in O concentrations (see Shepherd et al. [2006], Marsh et al. [2006], von Savigny and Lednyts'kyy [2013] among others). It is for this reason that the equatorial regions offer the best testing ground for the provided SD–WACCM4 data to this work. In addition to the simulated OH* concentrations, which are computed from the quenching model that is introduced in the next section, this work also considers measurements of the OH* radiance from the spaceborne SABER/TIMED instrument. This instrument is equipped with two channels to sense the OH* radiance from different emission bands in limb direction. From the vertical profiles of each channel, we can study their relative vertical displacements to each other and relate these to our model results.

In the following section, we introduce the OH* quenching model that is applied to the SD–WACCM4 data and give a brief review of the SD–WACCM4 and SABER data. The methodology of this study is explained in Sect. 5.5, followed by a discussion on potential error sources in Sect. 5.6. The results of this study are presented in the subsequent sections.

The results discussed and presented in this chapter have been published in the frame of this work in Kowalewski et al. [2014]. The corresponding discussion and plots are

adopted in large parts in this chapter (Sect. 5.1 to 5.9.2 and Sect. 5.11.2) and specific contributions of co-authors are stated therein.

5.1. Hydroxyl quenching model

The quenching model introduced herein is based upon the model described by McDade and Llewellyn [1988] and McDade [1991]. A corresponding model algorithm, which includes necessary assumptions on the nascent OH* production rate, the quenching rate constants, and the radiative OH* lifetimes was provided to this work by courtesy of Ian McDade, York University, Toronto, Canada. The same algorithm was also applied in the study of von Savigny et al. [2012b], who included updated quenching rate constants for their simulations. The core of this model assumes the following processes to populate lower vibrational states from the initial higher vibrational population of the produced OH* radicals:

- **radiative cascade**

  $$\mathrm{OH}(\nu') \rightarrow \mathrm{OH}(\nu'') + h\nu \qquad A(\nu', \nu'') \quad \text{(R3)}$$

- **collisional relaxation**

  $$\mathrm{OH}(\nu') + \mathrm{Q} \rightarrow \mathrm{OH}(\nu'') + \mathrm{Q} \qquad k_3^{\mathrm{Q}}(\nu', \nu'') \quad \text{(R4)}$$

  with $\mathrm{Q} = \mathrm{O_2}$, $\mathrm{N_2}$.

- **complete OH removal**

  $$\mathrm{OH}(\nu') + \mathrm{Q} \rightarrow \text{other products} \qquad k_4^{\mathrm{Q}}(\nu', \nu'') \quad \text{(R5)}$$

  with $\mathrm{Q} = \mathrm{O}$, $\mathrm{O_2}$, $\mathrm{N_2}$.

As outlined in McDade [1991], the processes (R4) and (R5) introduce an altitude variation to the vibrational population because of the dependency on the vertical quenching profiles. To construct a quenching model from the above stated processes, we have to specify to what extent these processes participate in the vibrational relaxation and removal of OH*.

We can think of the following two extreme cases:

- **sudden–death–model**: dominating removal of $\mathrm{OH}(\nu')$ via (R5)
- **collisional–cascade–model**: dominating stepwise deactivation of $\mathrm{OH}(\nu')$ via (R4).

constant	reference	remark
P_{nasc}	Adler-Golden [1997]	based on values from Steinfeld et al. [1987]
k_1	Sander et al. [2011]	temperature dependent rate constant of Bates–Nicolet mechanism (R1)
A	Xu et al. [2012]	values based on Hitran database, [Rothman et al., 2009]
$k_3^{O_2}$; α	Adler-Golden [1997]	based on Tab. 2 in Adler-Golden [1997]; α–correction factor from Xu et al. [2012]
$k_L^{\mathrm{N_2}}$	Adler-Golden [1997]	taken from Tab. 1 in Adler-Golden [1997]
k_L^{O} ; β	Smith et al. [2010]	β–correction factor from Xu et al. [2012]

Table 5.1.: Employed constants to Eq. (5.3). The corresponding values are listed in the appendix A.3.

While the model of McDade [1991] only allows for single-quantum collisional deactivation, von Savigny et al. [2012b] extended the model to multi-quantum collisional deactivation by O_2.

According to McDade [1991], we may formulate the number density of each vibrational level of OH* under steady state conditions as follows:

$$[\mathrm{OH}(\nu)] = \frac{p_{\mathrm{nasc}}(\nu) + \sum\limits_{\nu^*=\nu+1}^{9} [\mathrm{OH}(\nu^*)] \left\{ A(\nu^*, \nu) + \sum\limits_{\mathrm{Q}} k_3^{\mathrm{Q}}(\nu^*, \nu) \, [\mathrm{Q}] \right\}}{\left\{ A(\nu) + \sum\limits_{\mathrm{Q}} k_L^{\mathrm{Q}}(\nu) \, [\mathrm{Q}] \right\}} \, , \tag{5.1}$$

where $p_{\mathrm{nasc}}(\nu)$ is the nascent volume production rate, $A(\nu)$ is the inverse radiative lifetime of $\mathrm{OH}(\nu)$, and k_L^{Q} is the total rate constant for removal of OH* in vibrational level ν through reactions (R4) and (R5). Accordingly, we can construct different model cases by selecting corresponding rate constants for Eq. (5.1).

Different model cases are already included in the provided OH* quenching algorithm. However, instead of directly calculating number densities of $\mathrm{OH}(\nu = 1, 2, ..., 9)$ from the steady state conditions in Eq. (5.1), the algorithm applies a further transformation of Eq. (5.1) from number densities to the normalised relative $\mathrm{OH}(\nu)$ populations with respect to the $\mathrm{OH}(\nu = 9)$ population. As discussed by McDade [1991], this normalisation was included to avoid making any assumptions about absolute Meinel band transition probabilities, which were highly controversial during the initial proposal of this model by McDade and Llewellyn [1987].

Instead of calculating normalised concentrations of the vibrational OH* populations, this work uses Eq. (5.1) as a basis to calculate absolute number densities. This gives us the advantage that we can directly compare the simulated vertical $\mathrm{OH}(\nu)$ profiles with the SABER VER measurements in the later analysis of this chapter.

The calculation of absolute number densities requires further adjustments to the provided algorithm. First of all, we substitute the nascent volume production rate p_{nasc} in (5.1) by:

$$p_{\mathrm{nasc}} = P_{\mathrm{nasc}}(\nu)\{k_1[\mathrm{H}][\mathrm{O_3}]\} \ , \tag{5.2}$$

with the reaction rate coefficient k_1 ($\mathrm{cm^3 sec^{-1} molec^{-1}}$) and the nascent vibrational level distribution P_{nasc}. Thus, we assume that the entire production of vibrationally excited OH* is entirely based upon the Bates–Nicolet mechanism (Sect. 2.3).

In accordance with von Savigny et al. [2012b], we assume that multi-quantum relaxation only applies for quenching with O_2, while the less efficient N_2 quenching is limited to single-quantum relaxation only. In contrast to von Savigny et al. [2012b], who were using the McDade quenching model to calculate normalised OH(ν) with respect to the OH($\nu = 9$) population, this work assumes absolute constants, which are selected from the literature as summarised in Tab. 5.1.

Given these assumptions, we can finally construct the quenching model as follows:

$$\begin{aligned}[\mathrm{OH}(\nu)] = &\left(A(\nu) + k_L^{\mathrm{O_2}}(\nu)[\mathrm{O_2}] + k_L^{\mathrm{N_2}}(\nu)[\mathrm{N_2}] + k_L^{\mathrm{O}}(\nu)[\mathrm{O}]\right)^{-1} \times \\ &\left(P_{\mathrm{nasc}}(\nu)\{k_1[\mathrm{H}][\mathrm{O_3}]\} + \sum_{\nu^*=\nu+1}^{9} [\mathrm{OH}(\nu^*)]\{A(\nu^*,\nu) + k_3^{\mathrm{O_2}}(\nu^*,\nu)[\mathrm{O_2}] + k_3^{\mathrm{N_2}}(\nu^*,\nu)[\mathrm{N_2}]\}\right),\end{aligned} \tag{5.3}$$

with $k_3^{\mathrm{N_2}}(\nu^*,\nu) = 0$ for all $\{\nu^* > \nu + 1\}$

and $k_3^{\mathrm{N_2}}(\nu^*,\nu) = k_L^{\mathrm{N_2}}(\nu^*)$ for $\{\nu^* = \nu + 1\}$.

5.2. SD–WACCM4

The SD–WACCM4 simulations are based on the Whole Atmosphere Community Model, version 4 (WACCM4), which is a comprehensive free-running chemistry-climate model. This model version is based on an earlier version described by Garcia et al. [2007] and has been recently extended, such that it is nudged to meteorological fields that are taken from the Global Earth Observing System Model, Version 5 (GEOS-5) of NASA's Global Modeling and Assimilation Office (GMAO).

SD–WACCM4 data were provided to this work by courtesy of R. R. Garcia and D. E. Kinnison, NCAR Boulder. The same SD–WACCM4 simulations, which are considered herein, were already applied to another study by Hoffmann et al. [2012], who investigated the dynamics of the model using mesospheric CO volume-mixing-ratio (VMR) measurements. Following the discussion of Hoffmann et al. [2012], we now summarise

the most relevant aspects of the SD–WACCM4 model to this study.

The nudging of SD–WACCM4 with GEOS-5 meteorological fields M_{GEOS} is performed up to 50 km altitude for each time step t by replacing the model-predicted fields M_{pred} according to:

$$M_{pred}(t) = 0.99 \cdot M_{pred}(t) + 0.01 \cdot M_{GEOS}(t).$$

Between 50 km and 60 km altitude a linearly decreasing relaxation scheme follows until it completely switches to a free-running mode above 60 km.

Despite the weak constraint of SD–WACCM4 by its relaxation to external meteorological fields from GEOS-5, Hoffmann et al. [2012] show that the upper (free-running) part is still strongly driven by the described nudging and closely reflecting the dynamic response, which they deduce from CO based measurements.

The horizontal resolution of the SD–WACCM4 data is $1.9° \times 2.5°$ in latitude and longitude. Its vertical extent reaches from the ground up to the lower thermosphere at about 137 km geometric height and it is divided into 66 height levels. In the region from 80 km up to 95 km, which encloses the hydroxyl emission, the vertical distance between the model grid points ranges between about 1.2 km and 3.6 km. The SD–WACCM4 simulations are initially performed at 0.5 h time increments, however, to save computational resources, global model results are stored as daily increments at 00:00 UTC. This limitation of the provided dataset prevents us from studying the diurnal evolution of the OH* vertical profiles at a fixed geolocation. To overcome this constraint we make the assumption that the diurnal evolution of the vertical profiles is already contained within the zonal variation of each daily model result, i.e. we convert the longitudinal information to the local solar time (LST). However, as we will discuss in Sect. 5.9.2, other processes exist, which can still complicate a comparison of the diurnal variability between SD–WACCM4 and SABER.

To simulate OH(ν) profiles by means of Eq. (5.3), this work uses the O_3, H and O VMR profiles from the SD–WACCM4 simulations. For the remaining quenchers, i.e. O_2 and N_2, it is assumed that their vertical profiles have constant VMRs (mol/mol) of 0.78 for N_2 and 0.205 for O_2. Because we are still considering altitudes within the homospheric region (Chap. 2), this assumption should be justified.

Before applying these profiles to Eq. (5.3), we have to convert them from VMR to number density units to get absolute concentrations of OH(ν). For this task we assume that the ideal gas law at mesopause altitudes is satisfied, so that we can calculate the number density from the given SD–WACCM4 temperature/pressure fields. The ideal gas law is given by:

$$PV = NRT \ , \tag{5.4}$$

with pressure P (hPa), volume V (m^3), gas constant $R = 8.31$ $Jmol^{-1}K^{-1}$, number of moles N, and ambient temperature T (K). From this equation, we can estimate the number density n_{air} of air from the following relation (e.g. see Jacob [1999]):

$$n_{air} = \frac{A_v N}{V} \tag{5.5}$$

with the Avogadro constant $A_v \approx 6.022 \times 10^{23}$ mol^{-1}. From the estimated number density of air according to Eq. (5.4,5.5) and the volume-mixing-ratio C_Q of a species Q, we can calculate the corresponding number density as follows:

$$n_Q = C_Q \frac{A_v P}{RT} \tag{5.6}$$

Based on this equation, we can finally convert the SD–WACCM4 profiles as well as the constant O_2 and N_2 VMR profiles to absolute number density units.

In addition to the conversion from VMR to number density profiles, SD–WACCM4 temperatures are also considered for the temperature dependent rate constant k_1 of the Bates-Nicolet mechanism (see Tab. 5.1).

The provided SD–WACCM4 data cover the period between April 2010 and June 2011.

5.3. SABER

SABER (Sounding of the Atmosphere using Broadband Emission Radiometry) is a multichannel infrared radiometer onboard of the TIMED (Thermosphere Ionosphere Mesosphere Energetics Dynamics) satellite. Limb profiles are taken from a circular orbit at 625 km inclined at 74° to the equator and cover a latitudinal range from 54°S to 82°N or 82°S to 54°N, depending on the phase of the yaw cycle [Russell III et al., 1999]. One yaw cycle corresponds to the period required to cover the full range of 24 hours LST by the spaceborne observations. It results from the slowly precessing orbit of TIMED and has a period of 60 days.

SABER is equipped with two channels sensitive to the OH* emission, i.e. the 1.6 μm channel covers the emission from the OH(5-3), OH(4-2) Meinel bands and the 2.0 μm channel covers the emission from the OH(9-7), OH(8-6) Meinel bands.

VER profiles from both channels are contained in the SABER Level 2a data products and are used in this work. According to Mertens et al. [2009] the vertical resolution of the SABER VER profiles is approximately 2 km.

Because the effect of self-absorption should be negligible for wavelengths between 0.35 μm and 2.0 μm (see Sect. 3.8), we may directly compare temporal changes in the

simulated absolute concentrations of OH* with temporal changes in the vertical VER profiles.

In addition to measurements of the OH* radiance, the latest SABER V2.0 data contain atomic oxygen profiles, which this work uses to study the impact of O quenching on the observed vertical shifts between the 1.6 μm and 2.0 μm VER profiles. As explained in Mlynczak et al. [2013], the SABER O concentrations are indirectly determined from the measured 2.0 μm VER profiles based on the steady state assumption:

$$\underbrace{k_1[\mathrm{H}][\mathrm{O_3}]}_{\propto \mathrm{VER}(2.0\mu\mathrm{m})} = k_2[\mathrm{O}][\mathrm{O_2}] \tag{5.7}$$

with k_2 denoting the reaction rate constant between O and O_2 and $k_1[H][O_3]$ being directly proportional to the observed VER. At first glance, this seems to introduce a circular reasoning in the attempt of this work to correlate O concentrations with the vertical shifts between the 1.6 μm and 2.0 μm VER profiles. This could potentially introduce a spurious (i.e. non-physical) correlation between both quantities, if the SABER model did not properly consider the real photochemistry and gaseous kinetics based on the steady state assumption Eq. (5.7). However, Mlynczak et al. [2013] find a close agreement between their derived day- and nighttime O concentrations, which both rely on completely different retrieval methods. This indicates that the SABER model is reproducing physically meaningful O profiles. In turn, this should justify a direct comparison between SABER O concentrations and vertical shifts between both VER profiles, because we may suppose that any correlation between both quantities represents a real dependency between them.

The SABER data are made available by the TIMED Mission Data Center/NASA at their project site (http://www.timed.jhuapl.edu). From this data vertical VER- and atomic oxygen profiles were extracted for each SABER yaw cycle by C. von Savigny, Institute of Physics, Ernst-Moritz-Arndt-University of Greifswald, Germany. These profiles are binned according to 10° latitudinal and hourly LST bins. Following the same methodology of this work to quantify temporal changes of the vertical Meinel shifts and the collisional quenching process, corresponding results were contributed by C. von Savigny to this study and used to generate the SABER plots shown in Sect. 5.9.2 and 5.8.2.

5.4. Case example of simulated OH* source and quenching gas profiles

For the beginning of this study let us consider some general features of the vertical profiles of OH* source gases and the most important quenching species, namely O, O_2, and N_2 to provide a basis for our later discussion on the collisional quenching effect. A case example of simulated vertical SD–WACCM4 profiles is shown in Fig. 5.1. Each profile is a monthly average of the daily 00:00 UTC model output during September 2010. Solid lines denote exemplary nighttime profiles at the 0° longitude/latitude geolocation and dashed lines refer to corresponding sunlit conditions at 120°W. All units have already been transformed from VMRs to absolute concentrations according to Eq. (5.6), while a semi-logarithmic scale is chosen in Fig. 5.1 to account for the large changes in concentrations within the considered altitude range.

The upper panels display the source gases of OH* according to the Bates–Nicolet mechanism (R1). We notice the local ozone maximum at mesopause altitudes, which is a typical feature of this region as discussed in Smith and Marsh [2005]. In summary, it is formed via the three body reaction:

$$O + O_2 + M \rightarrow O_3 + M \ , \tag{R6}$$

which benefits from the increasing amount of atomic oxygen due to photolysis of O_2 in the Schumann-Runge bands (between 175 and 200 nm, Andrews [1987]) at mesopause altitudes. Vice versa, due to the participation of O_3 in the production of OH* via the Bates–Nicolet mechanism, a catalytic ozone destruction cycle is establishing by the following reaction:

$$OH + O \rightarrow H + O_2 \ . \tag{R7}$$

Nonetheless, the production of O_3 according to reaction (R6) is efficient enough to form a maximum around mesopause altitudes. Due to the fast photolysis of O_3, the daytime abundances are reduced and in photochemical equilibrium with atomic oxygen [Brasseur and Solomon, 2005].

For the atomic hydrogen profiles we find a strong peak at mesopause altitudes, which is rapidly decreasing with lower altitudes. Following Brasseur and Solomon [2005], the lifetime of H below mesopause altitudes is significantly reduced by its conversion to the hydroperoxy radical (HO_2) according to the following reaction:

$$H + O_2 + M \rightarrow HO_2 + M \ . \tag{R8}$$

Again, H is further efficiently removed by its reaction with HO_2 at mesospheric altitudes in different ways (see Eq. 5.93a,b,c in Brasseur and Solomon [2005]). Interestingly, the decrease in H concentrations below its mesopause peak altitude is less pronounced

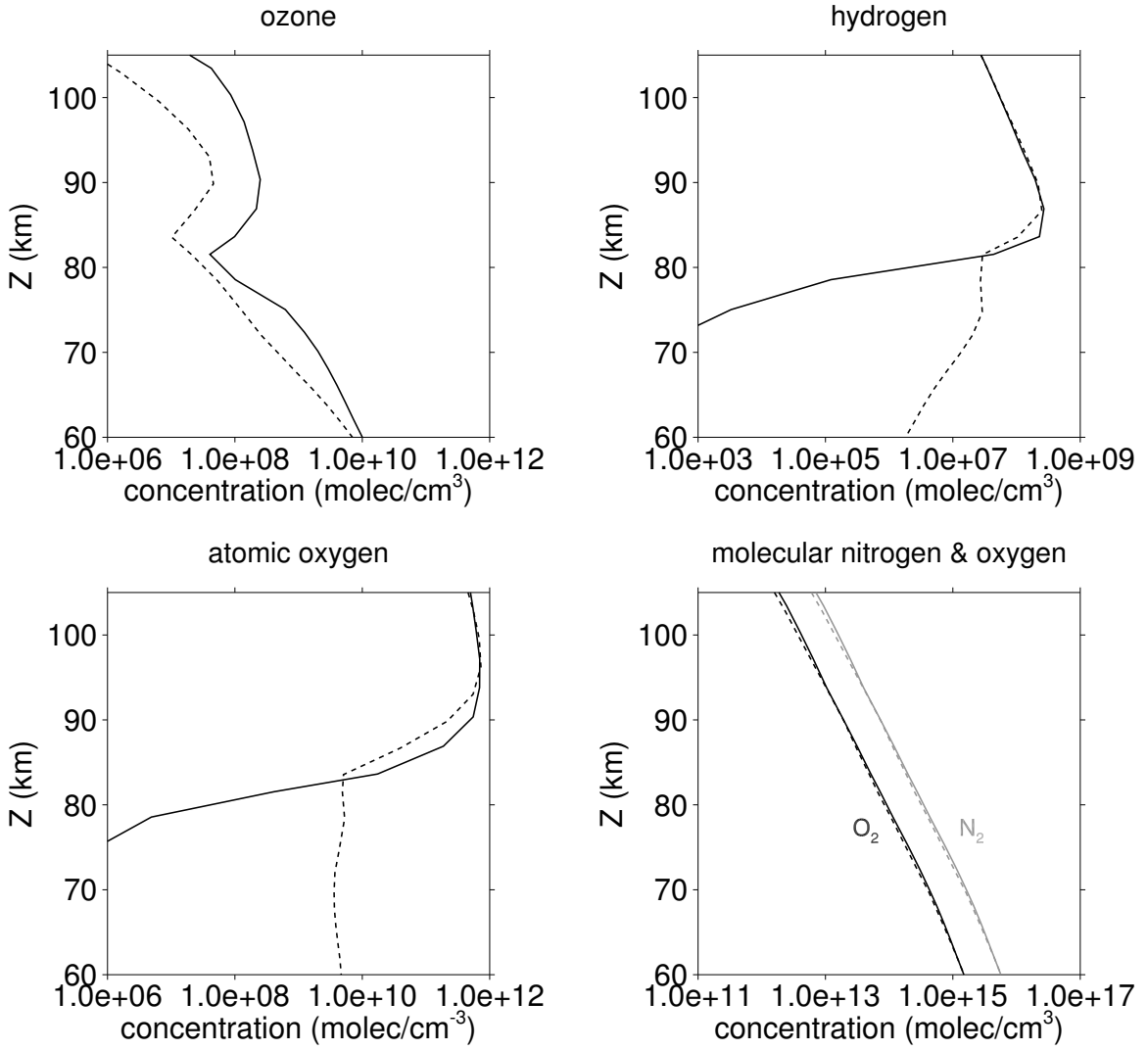

Figure 5.1.: Monthly averages of daily (00:00 UTC) SD–WACCM4 profiles of H , O_3 source gases of OH* (upper panels) and its most important quenching species (lower panes) during September 2010 at the equator. Sunlit examples (dashed lines) taken at 120°W and nighttime examples (solid lines) taken at 0° longitude.

during daytime, when photochemistry becomes an important factor. We will revisit this feature in Sect. 5.11.2.

A similar difference between day- and nighttime profiles at lower altitudes also exists for the atomic oxygen species. At mesopause altitudes the diurnal change of O concentrations is relatively small, which is due to the increasing lifetime of O with altitude (i.e. already exceeding one day according to Brasseur and Solomon [2005]). Accordingly, changes in O concentrations at these altitudes and above are largely controlled by the

dynamic conditions.

Another important aspect is the steep vertical gradient in O concentrations at the OH* airglow layer altitudes. As mentioned in the beginning of this chapter, atomic oxygen is a very effective quencher and due to its strong vertical gradient, the effective O quenching with OH* is expected to be noticeably increasing with altitude. Because of the increasing radiative lifetime of OH(ν) with decreasing vibrational excitation level (see Sect. 2.3), the probability of deactivation of lower vibrational excitation levels through collisional quenching with atomic oxygen is much higher at the upper fraction of the OH* airglow layer. Accordingly, this suggests a vertical layering of OH(ν) according to the vibrational excitation levels as discussed earlier.

In contrast to atomic oxygen, the abundances of the molecular quenchers N_2 and O_2 are generally decreasing with altitude. Because of our assumption of constant VMR profiles for both species, they both have the same altitude dependency. Despite N_2 being the most abundant quenching species of OH*, its contribution to the collisional relaxation process is expected to be significantly smaller compared to O and O_2 due to its less efficient quenching (i.e. one order of magnitude difference in the stepwise deactivation rate compared to the O_2 quenching species according to Tab. 5.1). Even though, the quenching rates of O_2 are still lower than those of O, i.e. one order of magnitude for the complete deactivation case of vibrational levels between $\nu = 4$ and $\nu = 6$, the smaller quenching efficiency is partly compensated by the higher absolute concentration.

5.5. Methodology

We now consider exemplary OH(ν) profiles that were calculated from the source and quenching gases based on Eq. (5.3). From these profiles we develop the methodology to quantify relative vertical displacements between different OH(ν) profiles.

By analogy with the previous section, Fig. 5.2 shows the monthly average of vertical OH($\nu = 1, 2, ..., 9$) profiles from the daily 00:00 UTC model results during September 2010 at the 0° longitude/latitude geolocation. In the following, we limit our discussion to the nighttime conditions, because the relatively low abundances of daytime OH* and the large Rayleigh scattering background make a comparison with OH* daytime observations more difficult. Furthermore, the earlier work of McDade and Llewellyn [1988] and McDade [1991], which provides the basis for the quenching model according to Eq. (5.3), explicitly assumes nighttime conditions. Thus, further corrections may be necessary to Eq. 5.3 to adequately account for sunlit conditions.

In accordance with our previous discussions, the vertical distributions of nighttime OH(ν) follow single peak profiles that are shifted upwards with respect to their vibrational state according to Fig. 5.2. If we normalise each OH(ν) profile, the relative vertical

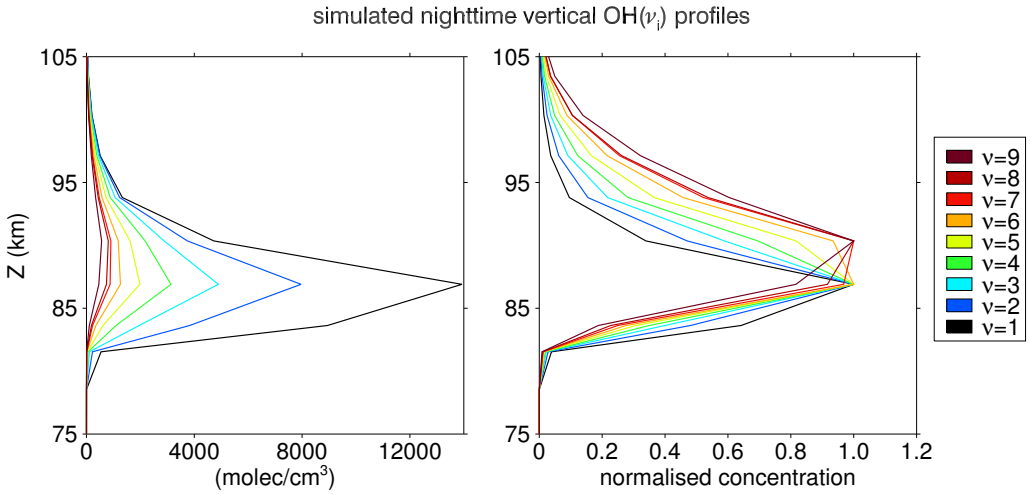

Figure 5.2.: Monthly average of simulated vertical OH(ν) profiles calculated from daily SD-WACCM4 model outputs during September 2010 (00:00 UTC) at the same geolocation as considered in the nighttime example in Fig. 5.1. Left panel: absolute number densities. Right panel: normalised OH(ν) profiles. Adopted from Kowalewski et al. [2014].

shifts become clearly visible. In addition, we notice a more pronounced vertical separation above the OH(ν) peak altitudes, which according to von Savigny et al. [2012b] is related to the steep vertical gradient in O concentrations and the associated more pronounced collisional deactivation of OH* at the upper fraction of the OH* airglow layer. By comparison, the vertical shifts between the OH(ν) profiles are significantly less pronounced below the profile peak altitudes.

The systematic increase of the vertical OH(ν) shifts above the profile peak altitudes seems to favour this altitude region for the investigation of the impact of collisional quenching with O on the vertical OH(ν) shifts. However, it is important to keep in mind that any changes in the vertical OH(ν) shifts are the convolved response to changes in the quenching and source gas concentrations according to Eq. (5.3). Therefore, finding the optimum reference points to compare the vertical shifts between two layers turns out to be less obvious than it might appear at first glance.

Another difficulty arises for the determination of relative vertical OH(ν) shifts from the rather coarse vertical resolution of the simulated OH* profiles and observed SABER VER profiles. Despite this constraint on the vertical resolution, we can benefit from the significantly higher dynamic range of the calculated number densities and observed VERs.

To quantify the vertical OH(ν) shifts at the peak altitudes and above, we therefore define two different reference points, which we determine for each vertical OH(ν) profile:

D.1 weighted peak altitude: $Zpk_{\mathbf{weighted}}$

By analogy with von Savigny and Lednyts'kyy [2013], we weight the altitudes with the number density profile $N_{\mathrm{OH}}(\nu, z)$ for each OH(ν) layer:

$$Zpk_{\mathrm{weighted}}(\nu) = \frac{\int_0^\infty N_{\mathrm{OH}}(\nu, z')z'\mathrm{d}z'}{\int_0^\infty N_{\mathrm{OH}}(\nu, z')\mathrm{d}z'}$$

D.2 shifted peak altitude: $Zpk_{+\mathbf{HWHM}}$

To sense changes between the vertical OH(ν) shifts at the upper fraction of the OH* airglow layer, we interpolate the altitude above the profile peak of each individual OH(ν) layer where $N_{\mathrm{OH}}(\nu, z)$ has dropped by a factor of 0.5, i.e. the position that is shifted by the Half Width at Half Maximum (HWHM) above the profile peak.

For the SABER VER profiles, we can simply replace the number densities by the VERs in the above definitions.

5.6. Sources of error

While the inclusion of number densities according to D.1 and D.2 helps us to improve the vertical sensitivity of this model study, systematic departures between simulated and real number densities are a source of error for the investigation of the collisional quenching effects. The recently published study by Smith et al. [2013] indicates that WACCM tends to underestimate mesospheric ozone concentrations, which in turn will impact the Bates–Nicolet mechanism (R1). In addition, WACCM4 tends to overestimate mesospheric temperatures according to Smith [2012a], which will affect the calculation of the rate constant k_1 and absolute number densities from the SD–WACCM4 temperature/pressure fields.

Inspection of Eq. (5.3) shows that at least a linear departure in the H + O_3 source profiles from reality is not critical for this study, because it will cancel out in the calculation of the OH(ν) layer altitudes according to the above stated definitions. The situation is different for the quencher profiles, because any linear scaling of their concentrations cannot be completely factored out in Eq. (5.3). An overestimation of temperatures should in principle lead to an underestimation of the absolute quenching gas concentrations based on the ideal gas law according to Eq. (5.6). In addition, too high temperatures will lead to an overestimation of the temperature dependent rate constant k_1. To get an estimate of the associated impact on the vertical shifts between different OH(ν) layers, a constant offset of -20 K was applied to the SD–WACCM4 temperatures. Based on this approach, the impact appears to be minor, i.e. in the order of a few tens of metres with regard to the later analysis of profile shifts based on D.1. With respect

to the O quenching species the simulated concentrations tend to be lower compared to concentrations derived from SABER as shown in Smith et al. [2011]. According to the initial hypothesis on the impact of the collisional quenching with O on the vertical shifts between different OH(ν) layers, an underestimated rate of collisional quenching should result in less pronounced vertical shifts. Apart from the discrepancies in simulated O concentrations, the uncertainty of its collisional rate constant k_L^O will also affect the results of this study. By comparison with the other quenchers, k_L^O has the greatest uncertainty. If we apply the upper and lower boundary of the uncertainty estimates of k_L^O from Xu et al. [2012], the changes to the vertical OH(ν) shifts based on D.1 range between about 100 m and 160 m with regard to the later analysis.

In addition to the uncertainties contained in the SD–WACCM4 data and the applied rate constants in Eq. (5.3), OH(ν) number densities are calculated offline in this study, i.e. any feedbacks to the chemical, dynamic, and thermodynamic state of the ambient air that arise from the formation of OH* are neglected by this approach. This gives rise to the question as to whether these feedbacks can become critical for the following analysis on vertical OH(ν) shifts. The assessment of this question would require an interactive calculation of the OH(ν) species within the SD-WACCM4 model runs, which is already exceeding the scope of this study. However, first test runs have already been performed by A. K. Smith, National Center for Atmospheric Research (NCAR), Boulder, that implement the interactive calculation of the OH(ν) species in WACCM. We will shortly address a comparison between the offline modelling approach of this work and a provided example of interactively calculated OH(ν) profiles by A. K. Smith in Sect. 5.11.1.

5.7. Simulated tidal signatures in OH* and quenching species

Before we will address the temporal variability of vertical OH(ν) shifts, we have to reexamine systematic temporal changes of the entire OH* airglow layer and the O, O_2, N_2 quenching species for two reasons: Firstly, we have to make sure that the temporal variability in the SD–WACCM4 data leads to a consistent evolution of the OH, O, O_2, and N_2 species compared to previous studies. Secondly, this reexamination helps us to establish an expectation about the impact of temporal changes in the collisional quenching on the vertical OH(ν) shifts.

As with the previous case examples, we now consider the monthly average of daily 00:00 UTC model results during September 2010. Because the amplitude of the diurnal migrating tide maximises around equinox, we should expect the strongest tidal signatures in the model results during this period. The model results are shown in Fig. 5.3. The global distribution of the integrated total column of all OH($\nu = 1, 2, .., 9$) layers is displayed in panel (a). A general eastward decrease in the integrated OH* concentrations is clearly visible. In terms of LSTs, this corresponds to a decrease of integrated

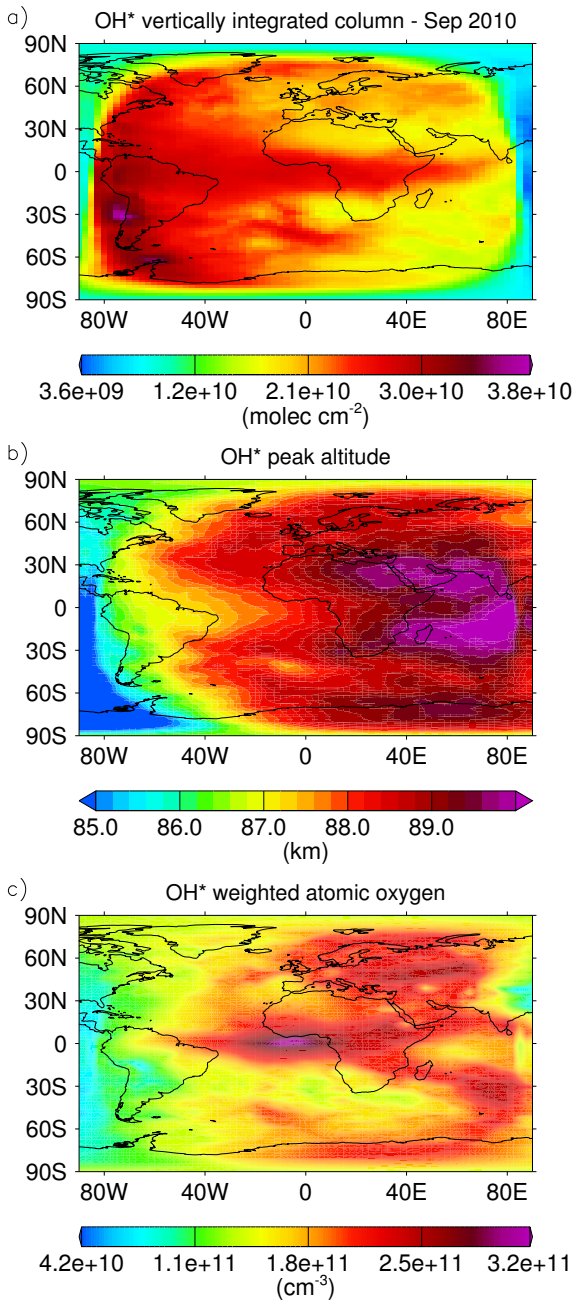

Figure 5.3.: Monthly averaged model results around September 2010 equinox. (a): Vertically integrated number density of simulated $\sum_{i=1}^{9} \mathrm{OH}(\nu_i)$. (b): Weighted peak altitudes of simulated OH* airglow layer according to definition D.1. (c): O concentrations weighted with the vertical $\sum_{i=1}^{9} \mathrm{OH}(\nu_i)$ profiles. Adapted from Kowalewski et al. [2014].

OH* concentrations over the course of the night. In addition, the OH* concentrations are generally high at equatorial latitudes and minimise around ±30° latitude, which is consistent with the study of Marsh et al. [2006] and other observational studies stated therein. The steep decrease of integrated OH* concentrations at the outer latitudinal and longitudinal margins marks the terminator between day- and nighttime conditions.

Weighted OH* peak altitudes Zpk_{weighted} according to the previous definition D.1 are displayed in panel (b). A systematic nighttime increase in the weighted OH* peak altitudes by up to 4 km is again clearly visible. Accordingly, we find a significant anti-correlation between OH* peak altitudes and vertically integrated concentrations by comparison with panel (a). Indeed, previous studies based on observations made with the high-resolution Doppler imager (HRDI) instrument and the Wind Imaging Interferometer (WINDII) instrument onboard the upper atmosphere research satellite (UARS) revealed the same coherent anti-correlation between OH* peak altitudes and integrated concentrations. Following Liu and Shepherd [2006] and stated referenced therein, this anti-correlation may be driven by the vertical motions associated with tides or other processes (see also Sect. 5.11.3).

As with the determination of OH(ν) profile peak altitudes, several possibilities exist to quantify temporal changes in the quenching species concentrations. The simplest method is to look at the diurnal evolution of a quenching species at a constant height level. However, this method neglects any changes of the quenching species concentrations that arise from the vertical motion of the entire OH* airglow layer. To account for this, we may determine the quenching species concentration at a fixed reference point of the OH* airglow layer. Again, this method is still rather simple, because the collisional quenching is not constrained to a fixed point at the OH* airglow layer. Thus, a more sophisticated approach is to quantify the collisional quenching by weighting the vertical quencher profiles with the corresponding OH(ν) profiles (i.e. replace z' in D.1 with the number density $N_{\mathrm{Q}}(z')$ of the quenching species).

The latter approach is also applied in Fig. 5.3c, which shows weighted O concentrations for the monthly case example of this section. As we can see, the equatorial weighted O concentrations show a pronounced maximum before midnight, which has also been confirmed by other observational studies (e.g. see Smith et al. [2010]) and should therefore lead to a pronounced collisional quenching of OH* with O during this time. Furthermore, Smith et al. [2010] report another wavenumber 1 type feature at ±30° with opposite phase, which at least seems to be reflected at 30°S in the model results. Of course, we have to bear in mind that we are considering a single monthly average only and that the temporal variability of the OH* airglow layer is also affecting the weighted O concentrations. Moreover, following the study of Lu et al. [2012] the magnitude of the tidal amplitude seems to be slightly underestimated by WACCM4. Despite this slight underestimation, the tidal signatures in the OH* profile weighted O concentrations as well as the vertically integrated OH* concentrations of the monthly case

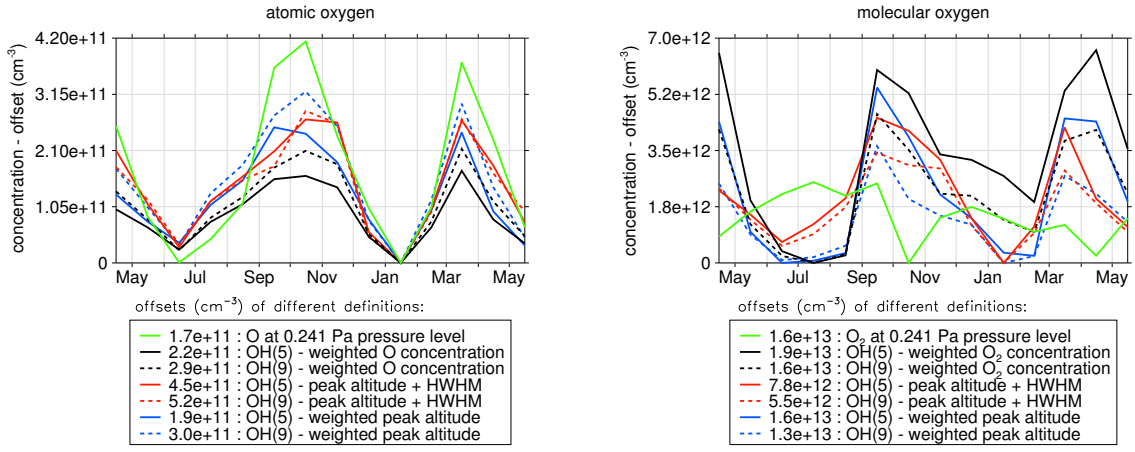

Figure 5.4.: Seasonal variability of simulated O and O_2 concentrations from April 2010 to June 2011 according to the following definitions: O,O_2 concentration at fixed pressure level (green line), O,O_2 concentration interpolated at +HWHM shifted and weighted peak altitudes (red and blue lines), O,O_2 concentration weighted with OH concentrations (black lines). From each curve the offset listed in the legend is subtracted to allow for a better intercomparison of the temporal changes. Adopted from Kowalewski et al. [2014].

example show consistent characteristics with previous observations and should therefore serve as a plausible testing ground for the initial hypothesis on the effect of collisional quenching with O on the vertical structure of the OH(ν) profiles.

By expanding the monthly case example of this section to a full seasonal cycle, we expect a semi-annual oscillation in the O concentrations that is in phase with the seasonal modulation of the diurnal migrating tide. Indeed, this oscillation is clearly visible in the simulated O concentrations, as shown in the left panel of Fig. 5.4. For this figure the LST bin was chosen between -1 and 0 h around equatorial latitudes. Each curve represents one of the above discussed methods to quantify the O concentrations, i.e. O determined at the 0.241 Pa pressure level (green line), O interpolated at OH($\nu = 5$) and OH($\nu = 9$) weighted profile peak altitudes according to the definition D.1 (blue lines), O interpolated at the HWHM shifted position above the profile peak (see definition D.2 and red lines), and O weighted with either the OH($\nu = 5$) or OH($\nu = 9$) profile (black lines). To allow for a better intercomparison of the temporal changes in the quenching species, each curve is subtracted by its minimum value (see legend).

In addition to atomic oxygen, the seasonal variability of molecular oxygen is included in the right panel of Fig. 5.4. Interestingly, we can find another semi-annual oscillation in phase with the atomic oxygen species, if we consider the curves that do not refer to the fixed 0.241 Pa level. Despite the lower quenching efficiency of O_2 compared to O,

the higher absolute O_2 abundances will at least partially compensate this. Because of the increasing O_2 number density with decreasing altitude (see Fig. 5.1), the collisional deactivation of excited OH* through O_2 quenching will be most pronounced at the lower fraction of the OH* airglow layer. Vice versa, the O quenching is rapidly decreasing at the lower fraction of the OH* airglow layer due to the steep vertical gradient in O number densities, thus, O_2 quenching is expected to be the dominant process of vibrational deactivation of OH* at the bottom side of the OH* airglow layer. This already indicates an important role of the seasonality in the O_2 quenching with regard to the temporal evolution of vertical OH(ν) shifts.

5.8. Seasonal evolution of OH(ν) layer shifts

5.8.1. Sensitivity study

In the following, we compare the relative changes in the vertical shifts between the OH($\nu = 9$) and OH($\nu = 5$) profiles. We select these two vibrational levels because each of them contributes to emissions that are observed by either the 1.6 μm or 2.0 μm SABER channel. Ideally, one must consider that each SABER channel captures a mixture of emissions that belong to two different OH* Meinel bands. However, because the difference in vibrational levels between each transition is limited to $\Delta\nu = 1$, we assume that we can neglect the effect of profile mixing for each channel, if we are interested in the relative vertical shift between both (mixed) OH* profiles. The vertical shift between a simulated OH($\nu = 9$) and OH($\nu = 5$) profile is calculated from the difference between either their weighted peak altitudes:

$$\Delta Zpk_{\text{weighted}} = Zpk_{\text{weighted}}[\text{OH}(\nu = 9)] - Zpk_{\text{weighted}}[\text{OH}(\nu = 5)], \tag{5.8}$$

or from the difference between the HWHM shifted altitudes above the profile peaks:

$$\Delta Zpk_{+\text{HWHM}} = Zpk_{+\text{HWHM}}[\text{OH}(\nu = 9)] - Zpk_{+\text{HWHM}}[\text{OH}(\nu = 5)]. \tag{5.9}$$

The vertical shifts between the SABER 1.6 μm and 2.0 μm VER profiles are determined in the same way.

We now investigate the seasonal variability of the relative vertical shifts between the simulated OH($\nu = 9$) and OH($\nu = 5$) profiles, which we denote as OH(9;5) profile shifts in the following. For this task, four different model runs are performed:

- all quenching species are activated
- O quenching species is deactivated
- O_2 quenching species is deactivated
- N_2 quenching species is deactivated

This allows us to study the impact of collisional quenching on the OH(9;5) profile shifts for each quenching species.

The results from the four model runs are shown in Fig. 5.5. Panel (a) displays the seasonal evolution of OH(9;5) profile shifts for the first model run (i.e. complete quenching considered). The left axis/solid line refers to the relative vertical shifts between weighted peak altitudes according to Eq. (5.8). The right axis/dashed line refers to the relative vertical shifts at the upper fraction of the OH(9;5) layers according to Eq. (5.9). If we concentrate on the solid line first, we find indeed a semi-annual oscillation in the OH(9;5) profile shifts that is in phase with the observed changes in the O and O_2 concentrations according to Fig. 5.4. On the other hand, if we look at the upper fraction of the OH(9;5) layers (dashed line), the fluctuations in the seasonal variability are much more pronounced and the response to the seasonal changes in the quenching species is less clear. So far, we find the best agreement with the initial hypothesis on the effect of the collisional quenching process on the vertical OH($\nu_i;\nu_j$) profile shifts for the weighted peak altitude definition D.1.

Similarly to panel (a), panel (b) shows the model run with the deactivated O quenching process. For both lines, we find a significant decrease in the OH(9;5) profile shifts, which again is consistent with the initial hypothesis. On the other hand, we still find a persisting semi-annual oscillation for the solid line (i.e. OH(9;5) profile shifts with respect to weighted peak altitudes) that is superimposed by another temporal maximum around mid January 2010. The seasonal response at the upper fraction of the OH(9;5) layers (dashed line) remains less clear. If we now subtract the results from the model runs with and without O quenching, we find a clear semi-annual response in the OH(9;5) profile shifts according to the solid line in panel (c). Interestingly, if we compare the increase in the OH(9;5) profile shifts from July to October between panels (b) and (c), the contribution of the O quenching process to the temporal changes in the OH(9;5) profile shifts is just slightly above the remaining temporal changes for the model run with deactivated O quenching. With regard to the initial hypothesis, this suggests that we cannot address the observed seasonality in OH(9;5) profile shifts to the modulation in the collisional O quenching only.

We therefore repeat the same investigation of the collisional quenching process for the O_2 quencher. By analogy with panel (c), panel (d) shows the difference in OH(9;5) profile shifts when subtracting the results from the model runs with activated and deactivated O_2 quenching. Again, the upper fraction of the OH(9;5) layers shows strong fluctuations (dashed lines), thus we limit our discussion to the relative shifts between weighted peak altitudes (solid line). First of all, we find that the deactivation of the O_2 quenching in our model run also leads to a noticeable decrease in the vertical OH(9;5) profile shifts. If we neglect the maximum around January 2011, we can find a further semi-annual response in the vertical OH(9;5) profile shifts due to the switching between the deactivated and activated O_2 quenching. In comparison with the seasonal change

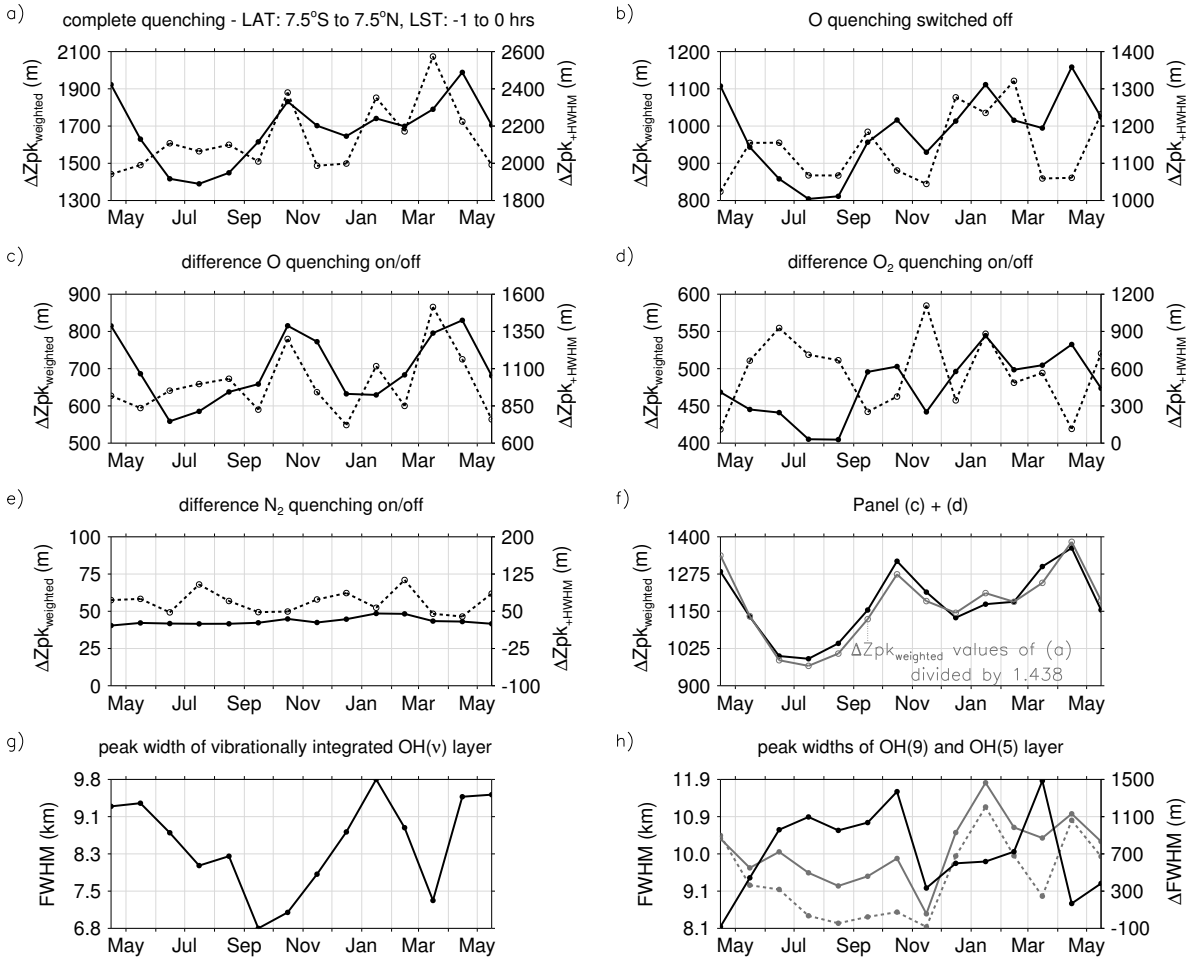

Figure 5.5.: (a-e): Seasonal variability of vertical OH(9;5) profile shifts from April 2010 to June 2011 for different model runs within the equatorial range between $\pm 7.5°$ and the LST range from -1 to 0 h. Solid line/left axis: OH(9;5) vertical shifts between weighted peak altitudes (see definition D.1). Dashed line/right axis: OH(9;5) vertical shifts between the +HWHM shifted peak positions (see definition D.2). (a): Full quenching model run. (b): Deactivated O quenching model run. (c,d,e): Difference in vertical OH(9;5) shifts when switching O,O_2, and N_2 quenching on/off. (f): sum of (c) and (d) (black line). In addition, $\Delta Zpk_{\mathrm{weighted}}$ from (a) divided by 1.438 shown by grey line. (g): Full peak width of the vibrationally integrated OH(ν) layer. (h)/left axis: Full peak widths of OH(9) and OH(5) layers (dashed and solid grey lines). (h)/right axis: Relative difference between the full peak widths of the OH(9) and OH(5) layers (black solid line). Adapted from Kowalewski et al. [2014].

in the OH(9;5) profile shifts between July and October due to the deactivation of the O quenching (see panel c), the impact of the deactivation of O_2 quenching is less than one half.

The effect of N_2 quenching is illustrated in panel (e). Again, the model run with deactivated N_2 quenching is subtracted from the full quenching model run displayed in panel (a). For both profile shift definitions the effect of N_2 quenching is rather small, i.e. about one order of magnitude less compared to the effect of O_2 quenching according to panel (d). Moreover, panel (e) barely contains any seasonal fluctuation, which indicates that the modulation of the N_2 quenching plays a negligible role for the seasonality of vertical OH(9;5) profile shifts. It is for this reason that we will further limit our discussion on the effects of O and O_2 quenching.

With respect to the model run that considers all quenching species (panel a), we notice that simply adding the effect of O and O_2 quenching according to panels (c) and (d) still leads to considerably smaller vertical OH(9;5) profile shifts, as shown in panel (f). On the other hand, the agreement in the seasonal variability between panels (a) and (f) is quite good. This becomes evident when we determine the best scaling factor between both functions in a least-squares sense. Accordingly, the grey line in panel (f) denotes the $\Delta Zpk_{\text{weighted}}$ profile shift values from panel (a) divided by 1.438. Apparently, taking the sum of panels (c) and (d) leads to an improved agreement in the seasonal variability with respect to panel (a) rather than considering the effect of deactivating either O or O_2 quenching only. This again suggests the importance of the O_2 quenching to the seasonal variability. Still, the question remains why the sum of panels (c) and (d) is smaller by a factor of 1.438 compared to the full quenching model run in panel (a). According to panel (e), the contribution of N_2 quenching is insufficient to serve as an explanation for the above mentioned scaling factor. This indicates that the combined effect of O and O_2 quenching is larger than the sum of their individual contributions.

As discussed in the beginning, seasonal changes in the vertical H + O_3 profiles will affect the OH* airglow layer width, which in turn will also affect the OH(9;5) profile shifts. In addition to the combined effect of O and O_2 quenching, this could provide another mechanism, which is driving the temporal variability. The seasonal evolution of the OH* airglow layer width is shown in panel (g) of Fig. 5.5. In this case, the width of the vertical profile is determined by the FWHM to account for changes above and below the profile peak altitude. Accordingly, we find a pronounced increase around the mid of January 2011 in the FWHM values, which is coherent with the observed additional increase in the OH(9;5) profile shifts for the deactivated O quenching case (panel b). This gives an explanation why the drop in the vertical OH(9;5) profile shifts is less pronounced after the winter solstice according to panel (a). Furthermore, the larger extent of the OH* profile width may also favour the rate of collisional O_2 quenching, which could explain the coherent response according to panel (d) of Fig. 5.5. On the other hand, a coherent semi-annual variability with respect to the $\Delta Zpk_{\text{weighted}}$ profile shift

values in panel (a) is not evident, which strengthens the argument of the combined effect of O and O_2 quenching as the dominant driving mechanism of the seasonal variability in the OH(9;5) profile shifts.

Finally, we also consider the relative changes of the OH(9) and OH(5) peak widths, which should particularly influence the OH(9;5) profile shifts above the profile peak altitudes. The seasonal evolution of each peak width is denoted by the grey lines in panel (h) of Fig. 5.5 (see caption). The difference we get by subtracting both temporal evolutions with each other is shown by the black solid line. We find that the large relative changes in the profile widths around October 2010 and May 2011 are coherent with the observed jumps in the OH(9;5) profile shifts at the upper fraction of the OH(9;5) layers (see dashed line in Fig. 5.5a), i.e. the vertical shifts $\Delta Zpk_{+\mathrm{HWHM}}$ appear to respond more sensitively to relative changes in the OH(9;5) profile widths.

5.8.2. Comparison with SABER

We now focus on the seasonal variability of the vertical shifts between the SABER 1.6 μm and 2.0 μm VER profiles for the period from January 2009 to December 2011. By analogy with the sensitivity study of the previous section, we choose the same -1 h to 0 h LST bin for the results presented in Fig. 5.6. Here, each point represents the mean value based on three matching yaw cycles between 2009 to 2011. Each error bar denotes the corresponding standard deviation. Panels (a-b) show the seasonal variability in the VER profile shifts for two equatorial latitude bins. Again, the solid line refers to the vertical shifts between weighted peak altitudes according to Eq. 5.8 (left axis) and the dashed line refers to the vertical shifts at the upper fraction of the VER profiles according to Eq. 5.9 (right axis). The seasonal variability of derived O concentrations is displayed in panels (c) and (d). The black line shows the O concentrations at 90 km altitude (left axis). The grey dotted and dashed lines show the VER profile weighted O concentrations with respect to the 1.6 μm and 2.0 μm channel (right axis). Panels (e) and (f) show the seasonal variability of the 1.6 μm and 2.0 μm VER profile widths (dashed and dotted, left axis) as well as their relative difference (black solid line, right axis).

First of all, we notice that a semi-annual oscillation - with maxima around May and October - is also present in the SABER VER profile shifts. Indeed, we find another coherent semi-annual oscillation in the O concentrations for the 0° to 10° S bin. With regard to the 0° to 10° N bin a faint semi-annual structure is present, but the overall change is dominated by an annual oscillation. Interestingly, in comparison with the changes in the SABER VER profile shifts, the semi-annual response is more dominating in the 10° N rather than the 10° S latitude bin. Again, this indicates that the consideration of O quenching alone cannot sufficiently explain the seasonal variability of SABER VER profile shifts. In contrast to the model results of this study, we cannot directly rule out that changes in the OH* sources gases may significantly affect the seasonality

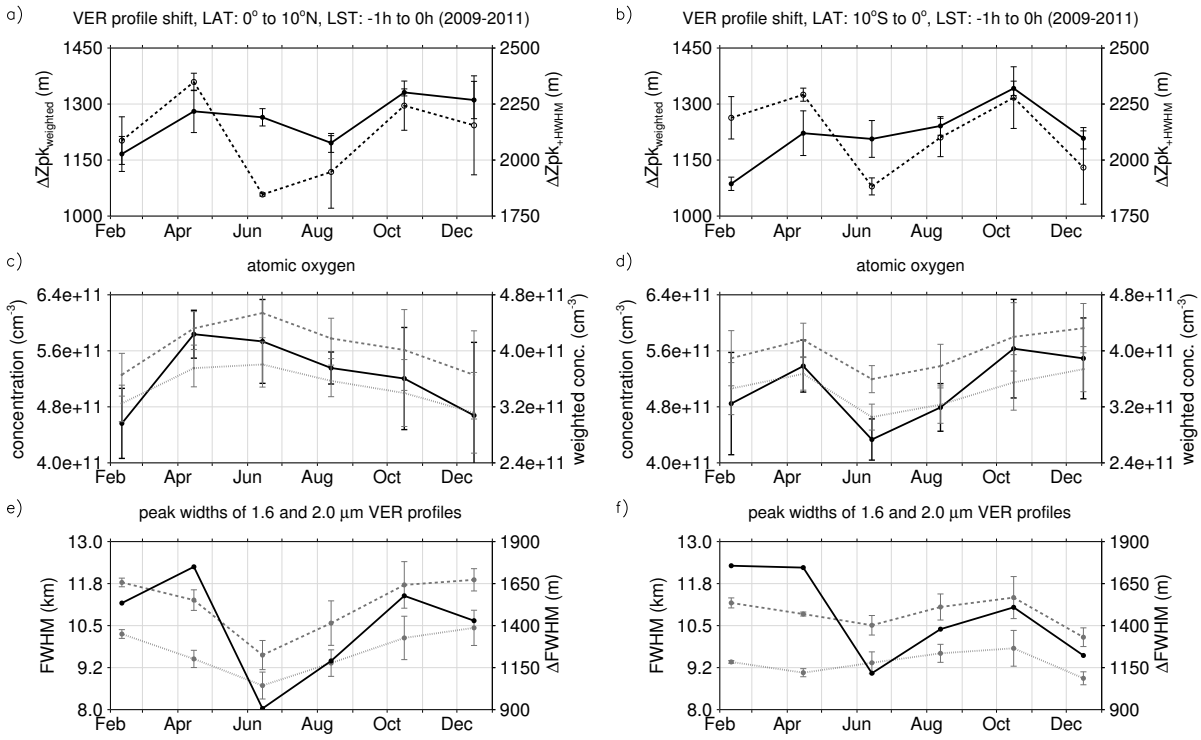

Figure 5.6.: SABER results based on three years of observation. Each point represents the mean value of three yaw cycles according to each year. The standard deviation is denoted by the error bars. (a-b): Seasonal variability in the vertical shifts between the 1.6 and 2.0 μm VER profiles. Solid line/left axis: Vertical VER profile shifts between weighted peak altitudes according to Eq. (5.8). Dashed line/right axis: Vertical VER profile shifts between the +HWHM shifted peak positions according to Eq. (5.9). (c-d): O concentrations at 90 km (left axis, black solid line) and 1.6 as well as 2.0 μm VER profile weighted atomic oxygen concentrations (right axis, dotted and dashed grey lines). (e-f)/left axis: Full peak widths of 1.6 and 2.0 μm VER profiles (dotted and dashed grey lines). (e-f)/right axis: Relative difference between the full peak widths of the 1.6 and 2.0 μm VER profiles (black solid line). Adopted from Kowalewski et al. [2014].

of the observed VER profile shifts. This would require the full spectral coverage of the OH* emission, which exceeds the spectral bandwidth of the existing SABER channels.

If we consider the relative changes of the VER profile widths according to the black solid line in panels (e) and (f) of Fig. 5.6, we can find a similar coherent response in the vertical shifts at the upper fraction of both VER profiles [see dashed line in panels (a) and (b)], which again shows the stronger sensitivity of this profile shift definition to changes in the relative profile shapes.

5.9. Diurnal evolution of OH(ν) layer shifts

5.9.1. Sensitivity study

By analogy with the analysis of the seasonal variability of the vertical OH(9;5) profile shifts according to the previous section, different model runs are performed where we consider the full quenching case, the deactivation of O quenching, and the deactivation of O_2 quenching. Because of the negligible impact of N_2 quenching on the vertical OH(9;5) profile shifts according to the previous section, we limit our following discussion to the O and O_2 quenching. To improve the later comparison with the observed diurnal variability by SABER, we adjust the temporal averaging period in the model runs to the same period that is required for a full SABER yaw cycle.

Accordingly, Fig. 5.7 shows the diurnal variability of both simulated quenching species around the September 2010 equinox at equatorial latitudes where the amplitude of the diurnal migrating tide maximises. Again, the same definitions are used to quantify changes in the O and O_2 concentrations as in Fig. 5.4.

While the different definitions of O concentrations only lead to a slight phase shift in the temporal evolution of the O concentrations of up to one hour, the different definitions of O_2 concentrations can result in quite different diurnal evolutions. With regard to the

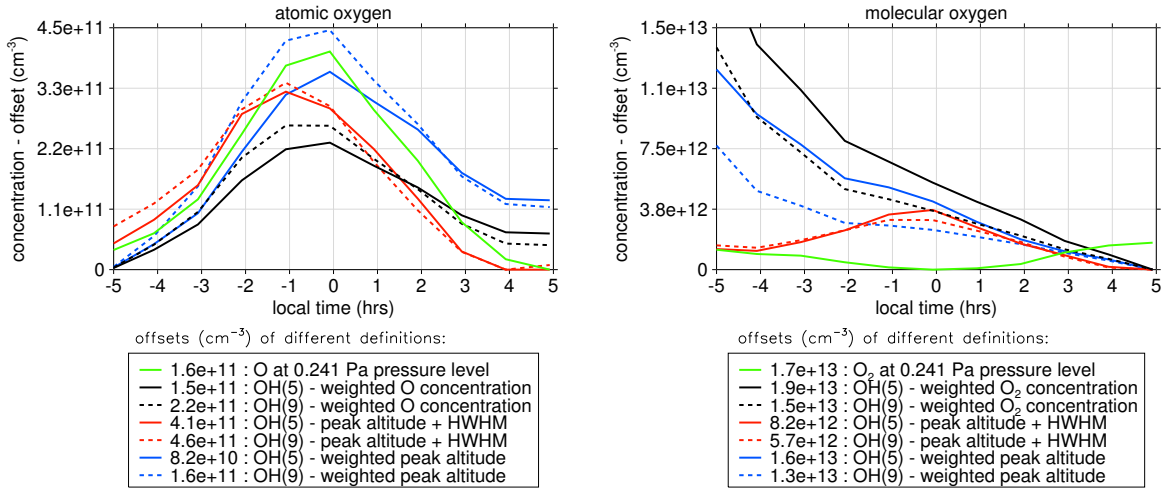

Figure 5.7.: Diurnal variability of simulated atomic and molecular oxygen concentrations. The same designations apply that are used for the seasonal variability of both species in Fig. 5.4. The temporal averaging interval ranges from 15-Sep 2010 to 15-Nov 2010 to match the same period in the simulations that is needed for a full SABER yaw cycle. Adopted from Kowalewski et al. [2014].

systematic increase in the nighttime OH* peak altitudes (Fig. 5.3b), the decrease in the OH(ν) profile weighted O_2 concentrations (black lines) and interpolated O_2 concentrations at the weighted OH(ν) peak altitude (blue lines) appears to be the most consistent.

The results from the three model runs are shown in Fig. 5.8 with the solid lines (left axis) referring to the OH(9;5) profile shift according to Eq. (5.8) and the dashed lines (right axis) referring to Eq. (5.9) correspondingly. Panel (a) displays the OH(9;5) profile shifts for the first model run, which considers all quenching species. Panel (b) shows the OH(9;5) profile shifts for the model run with deactivated O quenching. Panels (c) and (d) show the difference in OH(9;5) profile shifts, if we subtract either the model run with deactivated O or O_2 quenching from the full quenching model run shown in panel (a). Similarly to the previous section, the sum of panels (c) and (d) is displayed in panel (e).

Keeping in mind the initial hypothesis on the collisional O quenching as the main driver of the OH($\nu_i;\nu_j$) profile shifts, we would expect that the vertical OH(9;5) profile shifts should maximise shortly before midnight according to the maximising O concentrations. However, neither of both OH(9;5) profile shift definitions match with this expectation according to panel (a). Furthermore, we notice that the diurnal variability in the OH(9;5) profile shifts is rather opposite for both definitions. If we switch off the O quenching according to the second model run (panel b), the vertical OH(9;5) profile shifts are significantly reduced as it was also the case for the investigation of the seasonal variability in Fig. 5.5b. Moreover, if we consider the impact of the collisional O quenching according to panel (c), a coherent response to the diurnal evolution of O is clearly visible for the $\Delta Zpk_{\mathrm{weighted}}$ values (solid line). For the HWHM shifted positions above the profile peaks (dashed line), we can still find a significant internal variability, such that the impact of collisional O quenching remains again less clear.

As with the analysis of the seasonal variability, the collisional O_2 quenching is also significantly affecting the vertical OH(9;5) profile shifts according to panel (d) of Fig. 5.8. By comparison with the effect of the collisional O quenching on the weighted peak altitudes, the corresponding effect of the O_2 quenching is still smaller. Furthermore, the temporal changes due to the deactivation of O_2 quenching remain rather constant after -2 h. In contrast, if we consider the results based on the HWHM shifted profile reference points, the effect of the deactivation of O_2 quenching strongly exceeds the corresponding effect for O. Moreover, the early Zpk_{weighted}[OH(5)] profile reference points are even higher than those of the Zpk_{weighted}[OH(9)] profile reference points, which leads to the negative $\Delta Zpk_{+\mathrm{HWHM}}$ values before -3 h.

If we consider the sum of panels (c) and (d), as shown in panel (e), the resulting OH(9;5) profile shifts are again significantly smaller compared to the model run in panel (a), which considers all quenching species simultaneously. Interestingly, if we search for the best scaling factor between both panels, we obtain a factor of 1.430, which is very close to the estimated scaling factor for the seasonal variability. On the other

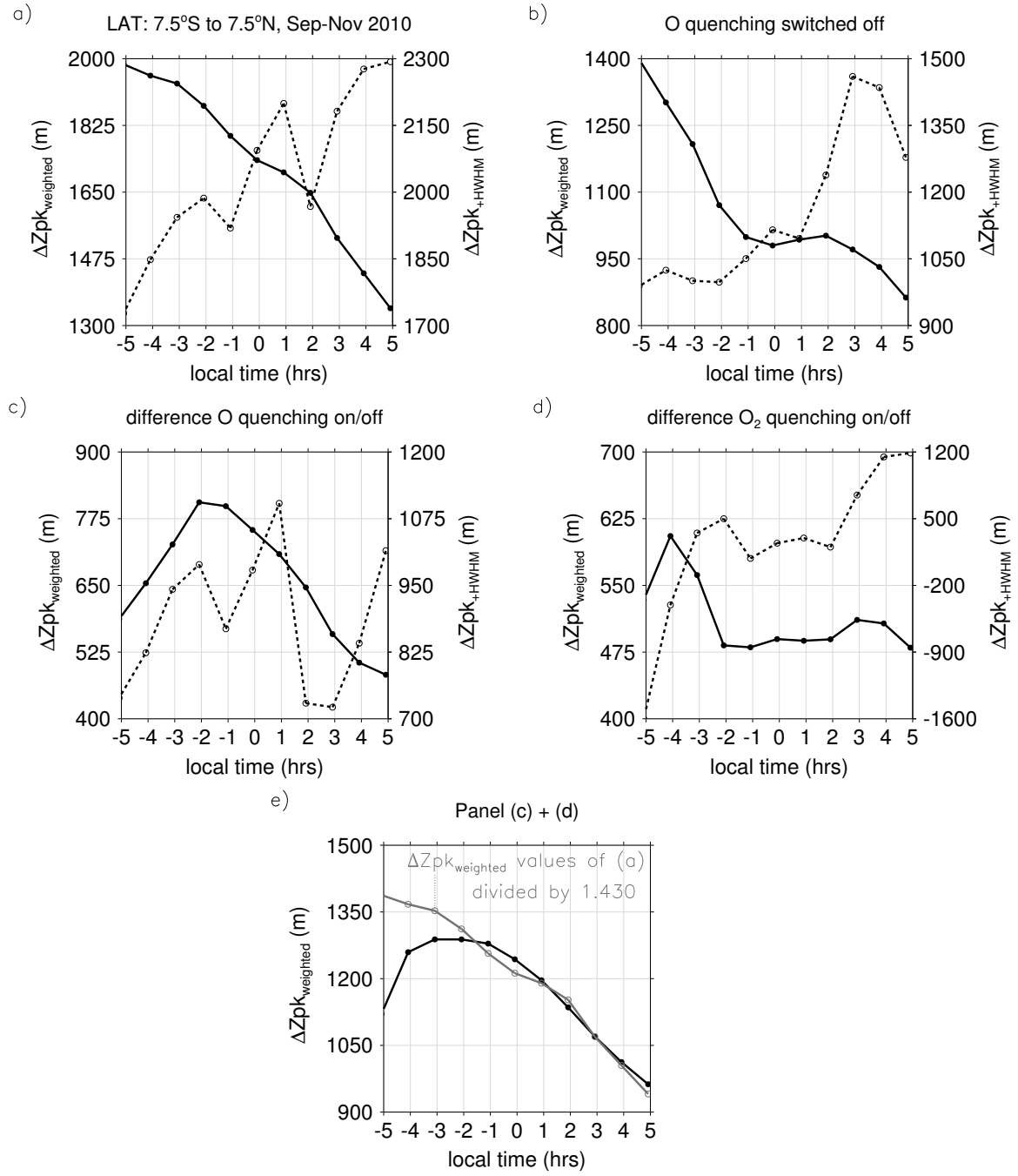

Figure 5.8.: Simulated diurnal evolution of vertical OH(9;5) profile shifts at equatorial latitudes for the same averaging period as in Fig. 5.7. (a): Profile shifts based on the full quenching model run. The solid line refers to profile shifts with respect to weighted peak altitudes (Eq. 5.8), the dashed line refers to profile shifts with respect to peak altitudes + HWHM (Eq. 5.9). (b): Profile shifts based on the model run with deactivated O quenching. (c): Difference between (a) and (b). (d): Difference between the full quenching model run and the model run with deactivated O_2 quenching. (e): sum of (c) and (d) (black line). Adopted from Kowalewski et al. [2014].

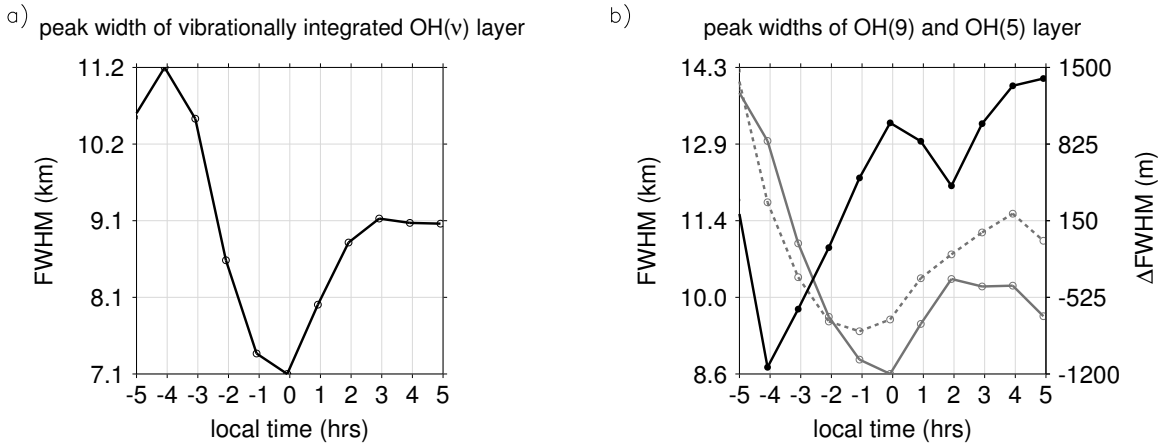

Figure 5.9.: (a) Diurnal variability of OH* peak widths for the same spatial and temporal bin considered in Fig. 5.8. (b)/left axis: Full peak widths of OH(9) and OH(5) layers (dashed and solid grey lines). (b)/right axis: Relative difference between the full peak widths of the OH(9) and OH(5) layers (black solid line). Adopted from Kowalewski et al. [2014].

hand, the agreement between the diurnal evolution according to the sum of panels (c) and (d) and the scaled panel (a), which is denoted by the grey line in panel (e), is less clear for the early evening hours. During the same hours we notice a strong shrinking of the entire OH* airglow layer by up to 4 km due to the nighttime evolution of the $H + O_3$ source gases according to Fig. 5.9a. This may also provide an explanation for the departure between the sum of panels (c) and (d) and scaled panel (a), presuming that the combined effect of O and O_2 quenching can be described by its linearly scaled sum according to Fig. 5.8. With regard to the OH(9;5) profile shifts based on $\Delta Zpk_{+\mathrm{HWHM}}$ values (dashed lines), we find that these are again strongly correlated with the relative changes in the OH(9,5) profile widths according to Fig. 5.9b.

We now expand the analysis to the full year of simulated OH(ν) populations and summarise the found correlations between vertical OH(9;5) profile shifts and quenching species concentrations in Fig. 5.10 and Fig. 5.11. Following the displayed correlation plots in Fig. 5.10, we find no significant correlation between the vertical OH(9;5) profile shifts and OH(9) weighted O concentrations for almost all seasons and both profile shift definitions. A weak positive correlation is visible, if we include all data points in panel (a). As with the equinoctial case example according to Fig. 5.8c, the correlation between vertical OH(9;5) profile shifts and weighted O concentrations significantly improves, if we compare the relative changes between the model runs with activated and deactivated O quenching for weighted peak altitudes (Fig. 5.10c). In contrast, the correlation remains poor, if we consider OH(9;5) profile shifts at the upper fraction of both layers (Fig. 5.10d).

Figure 5.11 shows the corresponding correlations for the O_2 quencher. In contrast to

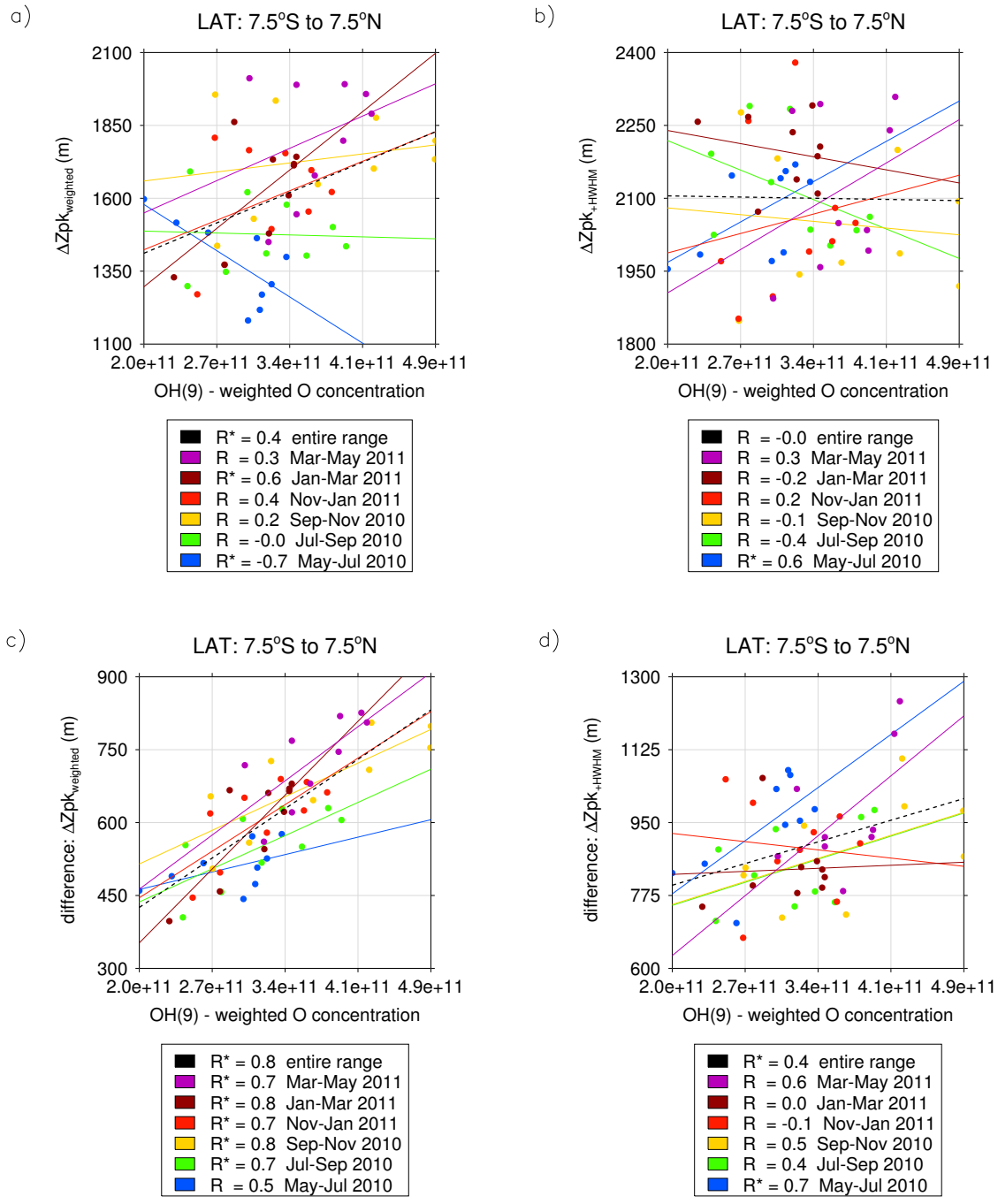

Figure 5.10.: Correlation plots of vertical OH(9;5) profile shifts (left panels Eq. 5.8, right panels Eq. 5.9) against OH(9) profile weighted O concentrations. Panels (a) and (b) show the correlation between OH(9;5) profile shifts and O concentrations for the full quenching model run (similar to Fig. 5.8a). Similarly to Fig. 5.8c, panels (c) and (d) consider the difference in vertical OH(9;5) profile shifts between the full quenching and the deactivated O quenching model runs. Correlation coefficients are shown in the legend and denoted with the asterisk symbol, if they are found to be significant according to a 90% confidence level. Adopted from Kowalewski et al. [2014].

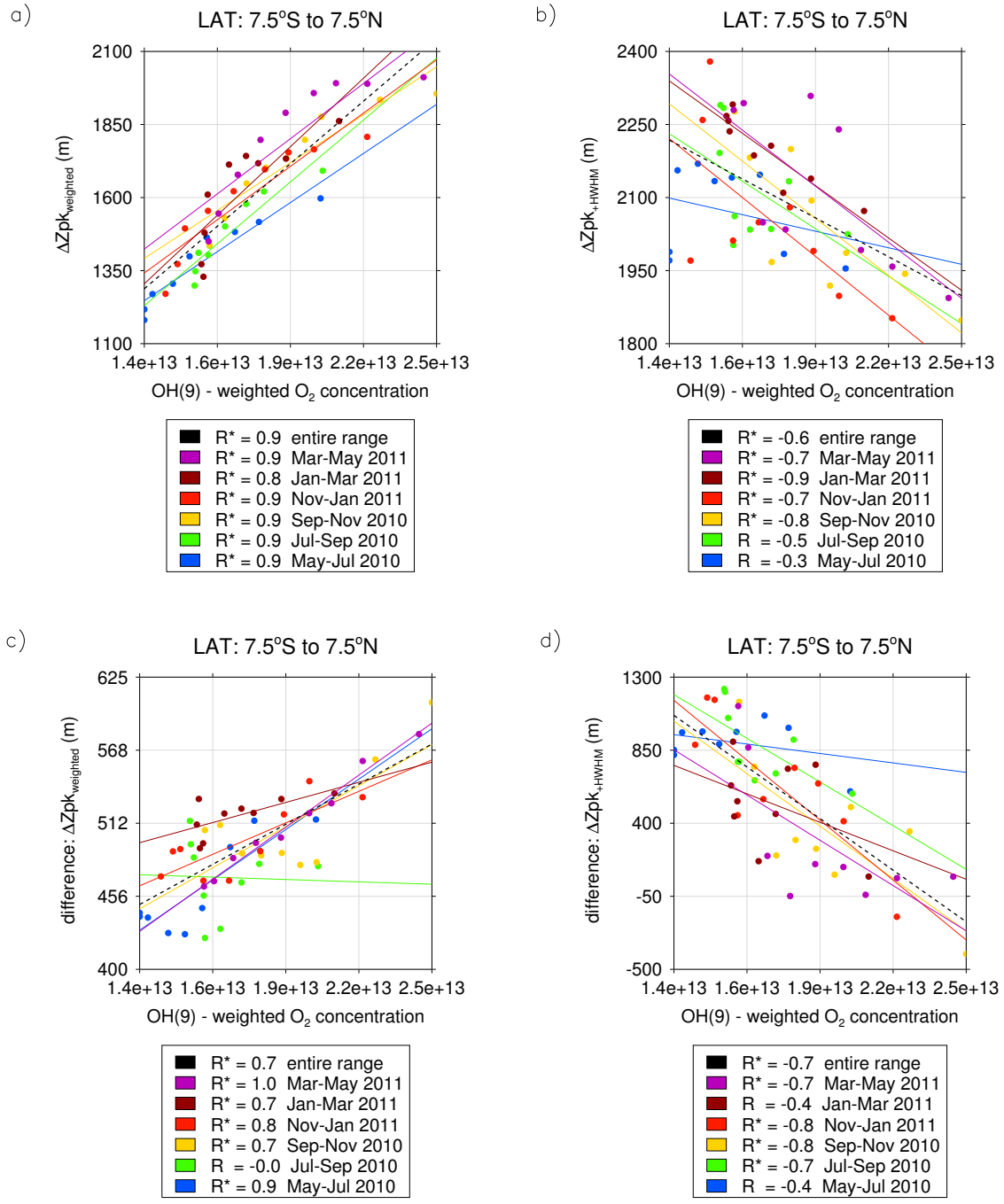

Figure 5.11.: Similarly to Fig. 5.10 but referring to the O_2 quenching species. Adopted from Kowalewski et al. [2014].

the O quencher, the correlations with the vertical OH(9;5) profile shifts are exceptionally high. Of course we have to bear in mind that the systematic increase in the OH* nighttime altitudes (see Fig. 5.3b) will also be reflected in the systematic decrease in OH(9) weighted O_2 concentrations. However, for the relative changes between the model runs with activated and deactivated O_2 quenching we still find a significant correlation in Fig. 5.11c, respectively anti-correlation in Fig. 5.11d.

In summary, the nighttime evolution in the OH(9;5) profile shifts can hardly be explained by the process of collisional quenching with atomic oxygen only. Again, the inclusion of molecular oxygen quenching further improves the correlation with the OH(9;5) profile shifts. In addition, the simultaneous strong decrease of the entire OH* airglow layer width, driven by the H + O_3 source profiles is further impacting the nighttime evolution of OH(9;5) profile shifts. Interestingly, the systematic changes in OH* peak altitudes and associated changes in O_2 concentrations show a very strong correlation with the temporal changes in the vertical OH(9;5) profile shifts.

5.9.2. Observed diurnal variability by SABER

For the SABER observations we first consider the same yaw cycle that was also used for the model simulations presented in Fig. 5.8 and compare the relative shifts between the 1.6 μm and 2.0 μm VER profiles with the OH-VER weighted atomic oxygen profiles similarly to the analysis of the seasonal variability. For the observed diurnal variability, it is important to note that the temporal evolution of the observed relative OH* profile shifts may significantly differ from the model results because of the existence of additional non-migrating tides, as reported by Xu et al. [2010] from SABER observations at lower latitudes. These tides would complicate a direct comparison with the model results, since we have to extract the temporal evolution from the longitudinal variability of the 00:00 UTC model output. However, despite the possible existence of non-migrating tides, this does not prevent us from testing the hypothesis on the impact of collisional quenching with regard to the temporal variability of the O quenching species.

By analogy with Fig. 5.8 the SABER results are shown in Fig. 5.12 for the same yaw cycle and for two latitudinal bins nearby the equator. Indeed, the nighttime evolution of relative OH(9;5) profile shifts looks quite different compared to the modelled vertical OH(9,5) profile shifts. Furthermore, the amplification of atomic oxygen before midnight is not as evident as in the model results. Despite these discrepancies, we would expect from the systematic nighttime decrease in atomic oxygen a corresponding feedback in the vertical VER profile shifts, which clearly is not the case. Again, we also notice strong changes in the relative peak widths according to panels (e) and (f) of Fig. 5.8 that are partially reflected in the nighttime changes of the vertical VER profile shifts.

If we expand the analysis to a full seasonal cycle, the missing correlation between VER profile shifts and O concentrations remains (see Fig. 5.13). Accordingly, the process of

collisional O quenching appears to be insufficient to explain the nighttime evolution of the OH VER profile shifts, which also agrees with our model expectations in at least a qualitative sense.

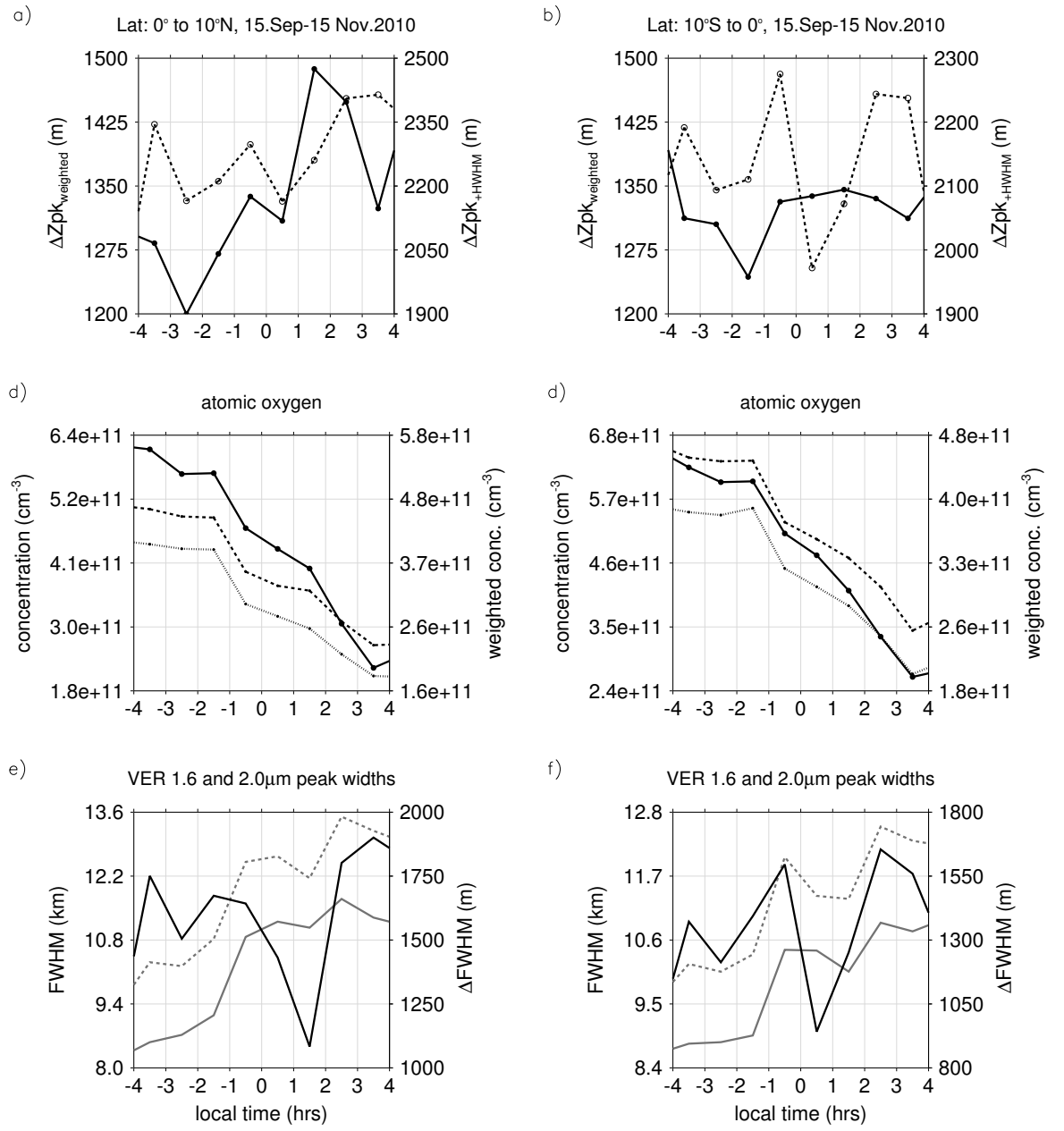

Figure 5.12.: Diurnal variability according to SABER OH VER observations. (a-b): Relative vertical shifts between VER(1.6μm) and VER(2.0μm) profiles by analogy with Fig. 5.8. (c-d): O concentrations at 90 km level (left axis, solid line) and weighted with VER(1.6μm) and VER(2.0μm) profiles (right axis, dotted and dashed line). (e-f): FWHM of VER(1.6μm) profile (grey dashed line), FWHM of VER(2.0μm) profile (grey solid line) and the difference ΔFWHM between both FWHM values (black solid line). Adopted from Kowalewski et al. [2014].

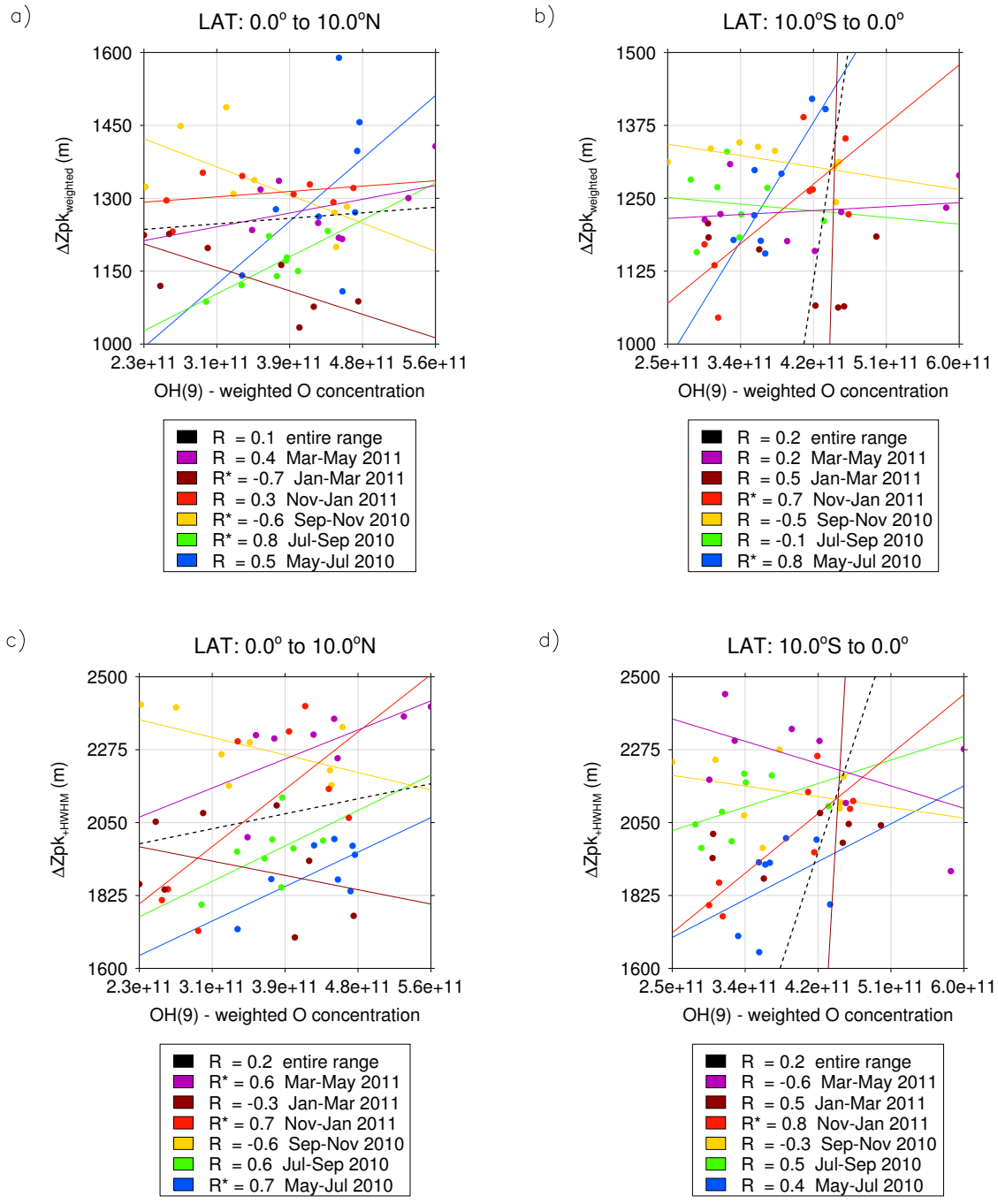

Figure 5.13.: Correlation between relative nighttime VER shifts and O concentrations from SABER observations by analogy with Fig. 5.10. Adopted from Kowalewski et al. [2014].

5.10. Summary and conclusions

The model study of this work investigated the temporal evolution of relative vertical shifts that exist between different Meinel bands of the OH* emission. For this task gas-kinetic simulations were performed based on a quenching model that is driven by model runs from the state-of-the-art 3D chemistry climate model SD-WACCM4. Following the hypothesis of previous studies that the process of collisional quenching with atomic oxygen is largely influencing the vertical shifts between different OH* Meinel bands, the impact on the simulated seasonal and diurnal evolution of the ambient O concentrations was studied by means of a sensitivity study. In addition, this study was extended to further sensitivity tests that include the impact of quenching with molecular oxygen and nitrogen, the second and third most important quenching species of OH*.

The results of this sensitivity study confirm that the semi-annual oscillation in the ambient O concentrations, which is driven by the seasonal modulation of the amplitude of the diurnal-migrating tide at equatorial latitudes, is reflected in the relative vertical changes of simulated OH(9) and OH(5) profiles. Further experimental evidence of the same seasonality was found for SABER VER measurements taken by its 1.6 μm and 2.0 μm channels. However, the sensitivity study on the effect of O_2 quenching also showed a significant contribution of this process on the vertical shifts between simulated OH(9) and OH(5) profiles, while the impact of N_2 quenching turns out to be negligible. The comparison of the effects of O and O_2 quenching revealed that the combined effect of both quenching species leads to a 1.4 times stronger vertical separation of simulated OH(9) and OH(5) profiles compared to the sum of their individual contributions. Furthermore, the temporal changes in the collisional O_2 quenching show a similar semi-annual variation as observed for the O quenching. With regard to the previous studies that were mainly focusing on the effects of O quenching on the vertical structure of the OH* emission, the importance of the combined effect of O and O_2 quenching reveals a new fundamental aspect of the driving processes of the vertical structure of the OH* emission according to this work.

With regard to the nighttime evolution of vertical shifts between different OH* Meinel bands, the model study of this work demonstrates that the effect of collisional O quenching alone is insufficient to explain their nighttime variability. In a qualitative sense, this finding is further confirmed by the considered SABER observations. Again, the sensitivity study of this work shows that the combined effect of O and O_2 quenching leads to a larger vertical separation between different OH* Meinel bands. In addition to that, pronounced changes in the nighttime evolution of the simulated H + O_3 source gases reveal another process that is affecting the vertical shifts between different OH* Meinel bands. With regard to the seasonal evolution, further evidence of the impact of temporal changes in the H + O_3 source gases on the vertical OH(ν) shifts was found for the model results around January 2011 where the peak width of the entire OH* layer is maximising in response to the temporal evolution of the H + O_3 source gases.

In summary, this study has shown that the proper understanding of the temporal evolution of vertical shifts between different OH* Meinel bands requires the combined effect of O and O_2 quenching. Moreover, changes in the H + O_3 source gases can further affect the temporal evolution of these vertical shifts. While the model results are confirmed in a qualitative sense by the SABER observations, noticeable departures between their quantitative results do exist. These departures may be resolved by a further investigation of some critical assumptions made in this study, including the:

- absolute number densities derived from SD–WACCM4 temperatures (too high),
- simulated diurnal variability described by zonal variation of daily model output (among others, conflicting with non-migrating tides),
- SABER O concentrations indirectly determined from OH* emission.

Furthermore, the large uncertainty in the collisional quenching rate constant k_L^O has the most significant impact on the model results, showing the need for improving our quantitative understanding of the collisional quenching process.

5.11. Outlook

In addition to the investigation of the effect of collisional quenching on the vertical shifts in the OH* emission according to the previous sections, we now briefly address some further side aspects of the performed model runs that are of potential interest for future studies.

5.11.1. Interactive implementation of OH* model runs

As mentioned in Sect. 5.6, the vertical OH(ν) profiles were calculated offline from the SD–WACCM4 data fields, i.e. any feedbacks to the ambient air were neglected in the OH* model study of this work. Vice versa, the OH* emission yields to an energy sink in the mesopause region and is therefore affecting its energy balance. The interactive implementation of an OH* quenching model in a chemistry climate model, such as WACCM, would provide us a tool to study critical feedbacks to the ambient atmosphere due to the formation of OH*.

A recent interactive model to calculate OH(ν) within the WACCM simulations was established by A. K. Smith. From this model, a preliminary result based on the same constants listed in Tab. 5.1 was provided to this work. In addition to the provided OH(ν) fields, pressure/temperature fields as well as the OH* source and quenching gases were provided so that we can calculate offline OH(ν) concentrations based on Eq. (5.3) and compare the results between the interactively and offline simulated OH(ν) fields.

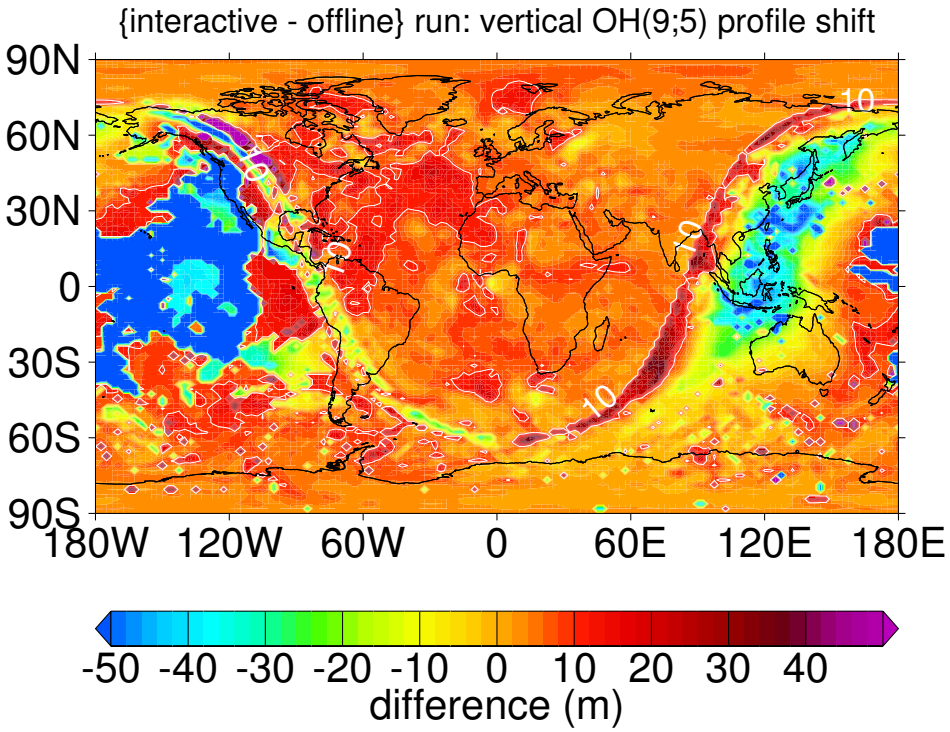

Figure 5.14.: Difference between OH(9), OH(5) vertical shifts from two different modelling approaches. Vertical shifts are determined based on weighted peak altitudes of the OH(9) and OH(5) populations. Simulated fields refer to 07 Dec 2012 - 01:17 (UTC).

With regard to the OH* model study of this work, this gives us the opportunity to get an estimate of the impact of interactive model runs on the vertical OH(9;5) profile shifts. From both modelling approaches, we first determine the weighted peak altitudes according to (D.1) and subtract the peak altitudes of the OH(9) and OH(5) layers to get the corresponding vertical OH(9;5) profile shifts. The difference in the determined vertical OH(9;5) profile shifts between both model approaches is shown in Fig. 5.14. The difference in the model results is mainly below 10 m during nighttime conditions. This indicates that the interactive calculation of OH(9;5) has a minor impact on the model results of this work. The difference slightly increases during sunlit conditions, which we shortly address in the next section.

5.11.2. Simulation of OH* daytime concentrations

According to the exemplary chemical profiles shown in Sect. 5.4, the higher daytime abundances of mesospheric atomic hydrogen should in principle affect the formation of OH* via the Bates–Nicolet mechanism (R1). Figure 5.15 shows vertical OH(ν) profiles that were calculate based on the same averaging period and geolocation as considered in the daytime examples of Sect. 5.4. In this case, we assume that we may also apply the quenching model in Eq. (5.3) to daytime conditions. While the absolute concentrations of calculated OH(ν) are reduced, we find a secondary peak below the main peak. Indeed, Funke et al. [2012] found further evidence of a daytime OH(ν) double peak structure in their simulated vertical profiles, which they also explain by the higher abundances of daytime H. In addition to the simulations of vertical OH(ν) profiles, Kumar et al. [2008] show a pronounced double peak structure in their derived vertical SABER 2.0 μm daytime VER profiles. Multiple peak structures of vertical nighttime OH* radiance profiles derived from WINDII measurements were also reported by Melo et al. [2000]. However, these complex structures may reflect lateral rather than vertical inhomogeneities in the nighttime OH* radiance. This also seems to be supported by the model results of this study, as illustrated in Fig. 5.16. As a simple counting rule, local maxima in the vertical OH* density profiles, which are above 50 km altitude and have an amplitude of at least 10 % with respect to the main peak, are counted for each daily (00:00 UTC) profile. Figure 5.16 shows the corresponding monthly average of peak counts during September 2010. As we can see, the simulated OH* nighttime profiles are dominated by a single peak structure, while the simulated daytime profiles largely show double peak or even more complex structures. Presuming that the formation of daytime OH* is dominated

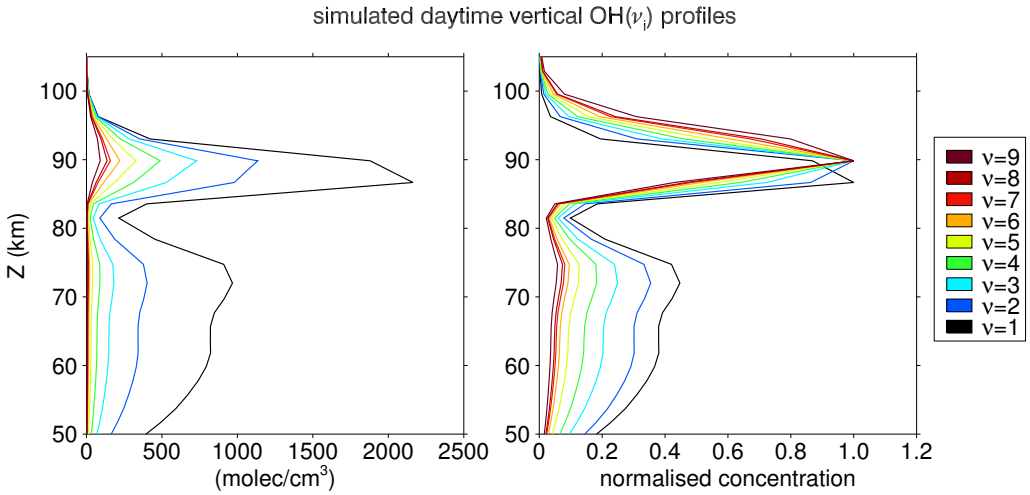

Figure 5.15.: Monthly average of simulated vertical OH(ν) profiles calculated from daily SD-WACCM4 model output during September 2010 (00:00 UTC) at 0°/120°W latitude/longitude. Left panel: absolute number densities. Right panel: normalised OH(ν) profiles.

by the Bates–Nicolet mechanism (R1) and that the relative changes between night and daytime abundances are most pronounced for atomic hydrogen (see Fig. 5.1), this could indicate that atomic hydrogen is the main driver of the complex structures of OH* daytime profiles. Vice versa, spaceborne observations of the OH* emission provides a useful tool in studying the global distribution of atomic hydrogen abundances.

In addition to the multiple peak structures of simulated (and observed) vertical OH(ν) profiles, another interesting daytime feature can be observed in the model simulations of this work. An example of these daytime features is illustrated in Fig. 5.17 where two large synoptic scale features of high OH* abundances are visible at about 50°S. These features predominantly occur at these latitudes around solstice and propagate in eastward direction. This gives raise to the question whether these features are real or representing a model artefact. A validation with spaceborne observations could potentially shed light on this question.

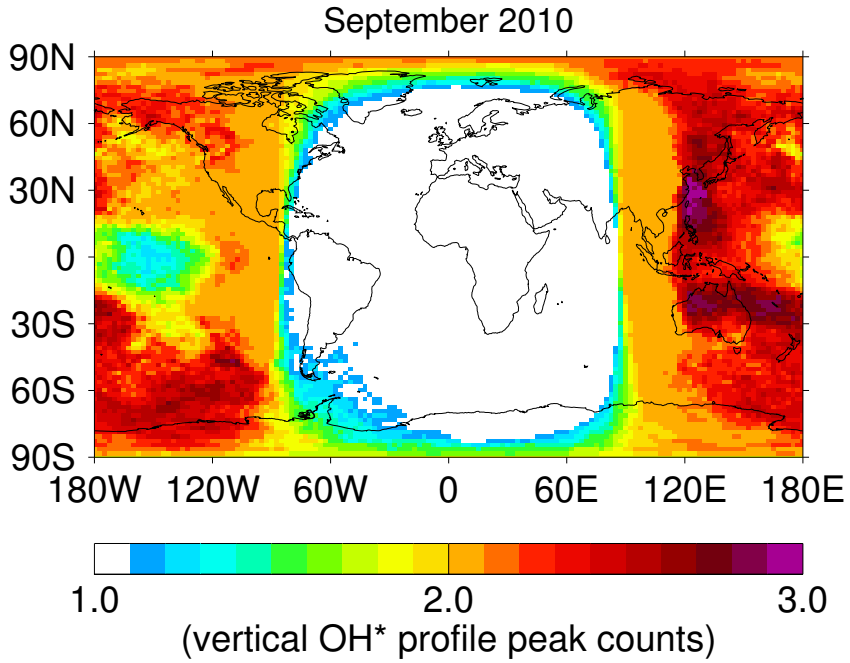

Figure 5.16.: Monthly averaged counts of detected multiple peak numbers of vertical OH* profiles (see text for counting rules).

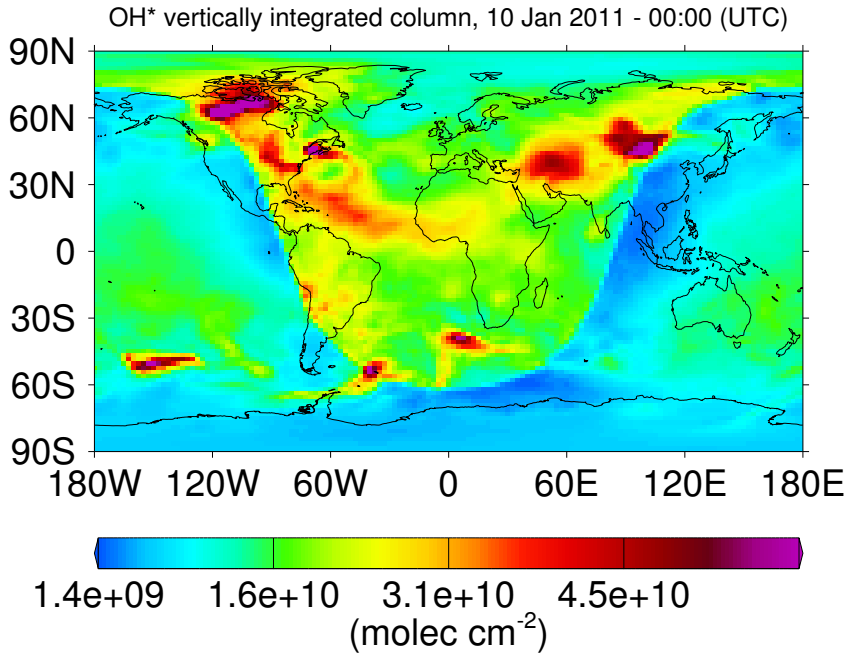

Figure 5.17.: Vertically integrated number density of simulated $\sum_{i=1}^{9} \mathrm{OH}(\nu_i)$ based on a daily SD–WACCM4 model run showing two distinct daytime synoptic scale features of high OH* concentrations at about 50°S. Adopted from the discussion version of Kowalewski et al. [2014].

5.11.3. Ground-based derivation of OH* emission height changes

Ground-based measurements of the OH* emission, as performed in the frame of this work, lack the information of the actual emission peak altitude. Apparently, this complicates the interpretation of observed temperature changes, which can be largely affected by the dynamic response of the MLT region. Additional measurements are necessary to quantify departures from the nominal emission peak altitude, but may typically contain several limitations (i.e. limited latitudinal coverage from spaceborne sensors, different footprint sizes and temporal averaging times, and further simplifying assumptions that apply to the peak height derivation).

Ideally, the altitude information should be simultaneously contained in the ground-based observations. The striking anti-correlation between simulated vertically integrated OH* number densities and peak altitudes according to Fig. 5.3, Sect. 5.7 is a highly interesting feature in this respect. To illustrate this anti-correlation more clearly, Fig. 5.18 shows a scatter plot of monthly averaged results that lie in the ±20° latitudinal and ±4 hourly LST range (i.e. nighttime conditions). Monthly results are colour coded and a regression line is added to each monthly sample of scattering points. In most cases, the correlation coefficients are very close to -1. Furthermore, we notice that the regression lines have an offset that is varying with the season, while the slopes of the regression lines appear to be roughly similar for all months. This implies for zenith looking ground-

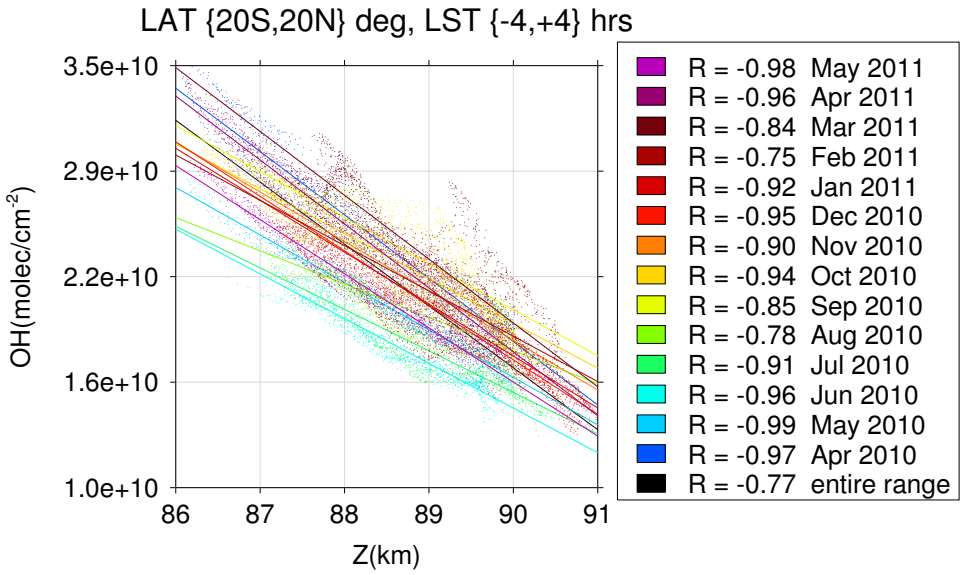

Figure 5.18.: Vertically integrated OH* number densities plotted against weighted OH* profile peak altitudes. Each point represents a monthly averaged model result calculated from SD–WACCM4 data fields within the ±20° latitudinal and ±4 hourly LST bins.

based observations that we may directly infer the OH* emission peak altitude from the emission brightness under consideration of a seasonal varying offset factor.

Based on this idea, the previous studies of Liu and Shepherd [2006] and Mulligan et al. [2009] derived empirical formulae from spaceborne observations to infer the OH* emission peak altitude from ground-based brightness measurements in the tropical/extra-tropical, respectively high latitudinal regions. In fact, both studies were quite successful in determining consistent peak altitudes from the ground-based observations. Finding a similar empirical formula for the (oblique) ground-based observations in Ny-Ålesund is a valuable future task, because it will enable us to study dynamic perturbations in a more quantitative sense.

According to our current understanding, the anti-correlation between OH* brightness and peak altitudes seems to be mainly driven by changes in O concentrations associated with the vertical motion of air as described in Yee et al. [1997]. If we recall the steady state assumption Eq. (5.7) in Sect. 5.3, it is evident that changes in O concentrations will directly impact the production of OH*, i.e. the higher the O concentrations, the brighter the OH* emission. On the other hand, the recombination rate k_2 in the steady state assumption Eq. (5.7) is proportional to $T^{-2.4}$ according to Sander et al. [2011], i.e. the impact of temperature changes to the OH* brightness is opposite. However, if we recall the strong correlation between rotational temperatures and $Q_1(1)$ line-intensities of the OH(3-1), OH(4-2) bands in Fig. 4.19b, Sect. 4.4, this suggests that large scale changes in O concentrations are the dominating controlling mechanism of the emission brightness in this case. The same situation is also reported by other studies (see Cho and Shepherd [2006], Espy et al. [2007], Smith [2012b]), which appears to be consistent with the observed anti-correlation between OH* brightness and peak altitudes. On the other hand, Smith [2012b] could find experimental evidence of the above mentioned non-linear T-dependent chemistry in their OH* brightness measurements when considering larger temporal averaging periods such that the dynamic variability is smeared out. A future sensitivity study based on the model approach of this work may further quantify the importance of the T-dependent chemistry to the temperature, brightness, and altitude relations of the OH* emission as a function of latitude and season.

6. Summary and outlook

This work has focussed on the dynamic variability of the upper mesospheric region, which is largely driven by the interaction of vertically propagating atmospheric waves at various temporal and spatial scales. Understanding the dynamic response of the mesospheric region is crucial for our general understanding of its response to climate change. While previous studies proposed this region to be a potential candidate of an early indicator of climate change (e.g. see Beig et al. [2003] and the following paper series of the same author/s), the complex interaction with the surrounding atmospheric layers but also its remote location make its assessment as a climate change indicator a challenging task.

The hydroxyl airglow layer was studied in the frame of this work as a diagnostic tool for dynamical perturbations at the mesopause region. In summary, the key achievements of this work include the

1. further refinements of FTIR based observations of the OH* emission at the high latitudinal AWIPEV/Koldewey station in Ny-Ålesund, Spitsbergen,

2. continuous operation of these measurements during the polar winter season,

3. establishing and evaluation of a multiyear time series of rotational temperatures above Ny-Ålesund,

4. establishing of gas-kinetic simulations that are driven by a state-of-the-art 3D chemistry climate model.

The important aspects of these achievements are briefly summarised as follows:

(1.-2.): The instrumental sensitivity function was characterised by an external blackbody calibration source. In addition, the transmittance of the hatch windows was determined. Following these calibration measurements a correction for the spectral sensitivity was estimated for each OH(3-1), OH(4-2), and OH(8-5) Meinel band. In each case, the relative change in the instrumental sensitivity was typically below about 2 % and even less with respect to the window transmittance. Hence, the overall impact of the correction for the instrumental sensitivity and window transmittance on the results was found to be minor, i.e. less than $|\Delta T| = 1.6\,\mathrm{K}$ for all bands.

A further comparison between the uncooled narrow band InGaAs detector and a new detector equipped with a thermoelectrically cooled extended InGaAs diode revealed that

despite the enhanced thermal noise, the performance of the uncooled InGaAs detector in measuring the OH* emission is superior due to its narrow band capability. Existing concerns with regard to its thermal stability were addressed by investigating time invariant intensity ratios of the OH* emission, which did not imply major drifts in the instrumental sensitivity with the instrumental temperature changes.

The installation of a new hatch window allowed for continuous low elevation measurements throughout the polar night. Owing to the increased apparent OH* layer thickness along the oblique LOS, the SNR of the emission spectra was significantly improved, such that the number of non-discarded spectra relative to the total number of measurements increased by more than factor of three compared to the previous seasons where the zenith hatch window was used. In turn, simulations of the atmospheric transmission at low viewing angles indicate that the iterative retrieval of OH(4-2) and OH(8-5) temperatures critically depends on the simulated atmospheric transmission spectrum.

(3.): Simultaneous measurements of rotational emission lines from the OH(3-1) and OH(4-2) Meinel bands allowed for the derivation of rotational temperatures. In principle, further emission lines of the OH(8-5) Meinel band could be detected but only with weak SNRs.

Following the criteria of Bittner et al. [2002] for the spectral averaging and including several criteria for the automated data filtering allowed for the derivation of a rotational temperature time series for six polar winter seasons between 2007 and 2014. In comparison with MLS temperature estimates, the best absolute agreement was found for the OH(3-1) temperatures for the entire time series, while OH(4-2) temperatures are significantly lower after 2010. The largest offset to MLS is found for the OH$(8-5)$ temperatures of the entire time series. In particular the increased offset between OH(3-1) and OH$(4-2)$ temperatures after 2010 is a striking feature of the time series. With respect to the critical dependency of the OH(4-2) temperature retrieval from the simulated atmospheric transmission, it is likely that the observed offsets to the OH(3-1) temperatures, having average magnitudes between 10 K to 20 K, are partially affected by deviations from the true atmospheric transmission spectrum, otherwise, the observed thermal gradient between both Meinel bands would be exceptionally large. In addition, the exceptionally low OH(8-5) temperature estimates are a quite surprising result compared to previous studies and suggest a further investigation of the origin of the low temperature estimates.

The determination of absolute temperatures in the MLT region remains a challenging task as illustrated in this work. Nonetheless, the relative changes in OH(3-1), OH(4-2), and MLS temperatures are highly correlated, implying a consistent dynamic response in each temperature time series. Furthermore, a comparison with the stratospheric dynamic conditions revealed a coupling with the upper mesospheric fraction that is reflected in its adiabatic temperature response and gives further support to the theory of the gravity

wave interaction with the zonal mean flow. Interestingly, the minor SSW event in 2011 seems to reflect a peculiar case where an anomaly in upper mesospheric temperatures appears to precede the dynamic changes in the stratosphere. This contradicts the typical explanation of an upward propagating disturbance. Vice versa, inspection of the solar conditions before and during the SSW did not reveal any major events that could have perturbed the MLT region, hence, the question of the driving perturbing mechanism remains subject to further investigations.

In addition to the large scale coupling with the lower atmospheric layers, the temperature time series above Ny-Ålesund revealed harmonic perturbations at hourly scales. Furthermore, a coherent response in a selected rotational line intensity could be found in many cases. In comparison, temperature perturbations are preceding the intensity perturbations in most cases, corroborating current theoretical models on gravity/tidal wave perturbations of airglow and the predominant origin of these waves at the lower atmospheric layers. Another interesting aspect was revealed during two events where a phase shift between the OH(3-1) and OH(4-2) temperature oscillations exists, which can be explained by the vertically displaced VER profiles of both emission bands. However, a similar phase shift could not be observed for the intensity oscillations. Following the HTS theory, this must be explained by the different altitudes of the maximum temperature and intensity responses to wave perturbations, i.e. the altitude difference of the bottom side profiles (maximising intensity response) is less distinct compared to the profile peak altitudes (maximising temperature response).

(4.): While the systematic vertical shifts in the OH* emission affect the rotational temperature estimates depending on the observed emission band, the gas-kinetic simulations of this work provide a deeper insight into the role of the collisional quenching process on the temporal modulation of these shifts. A semi-annual modulation of simulated vertical OH(ν) profile shifts at equatorial latitudes, where the amplitude of the diurnal migrating tide maximises, was successfully revealed in this work. This result provides further support to previous observational studies on the OH* airglow response to the diurnal migrating tide. However, while previous studies were mainly addressing the impact of collisional quenching with atomic oxygen on the vertical shifts in the OH* emission, this work has demonstrated that the combined effect of atomic and molecular oxygen has a strong impact on the vertical shifts. In addition, the model study of this work shows that the seasonal variation in O and O_2 quenching is in phase with the semi-annual oscillation of vertical OH(ν) profile shifts at the equator. On the contrary, the diurnal evolution of O and O_2 quenching is less coherent and, in addition, the source gas profiles strongly vary. Both aspects provide an explanation for the poor nighttime correlation between observed and simulated vertical OH(ν) profile shifts and atomic oxygen only.

Outlook: A further improvement of the OH* measurements at the AWIPEV/Koldewey station is expected for the ongoing winter season 2014–15 with the recently upgraded hatch, which is equipped with an automated shutter instead of a hatch window. Accordingly, the SNR will further increase due to the avoided transmission loss at the hatch windows. Furthermore, with the disassembling of the old hatch, the measurements of the window transmittance can be repeated inside the laboratory. In comparison with the earlier blackbody setup on the roof of the building, this will significantly simplify the instrumental alignment and further improve the characterisation of the window transmittance.

The revealed temperature differences between different OH* Meinel bands and spaceborne measurements remain an important subject of ongoing investigations. With regard to the temporal variability of the OH* airglow layer, the inclusion of its brightness fluctuations to the analysis of rotational temperature appears to be most promising as demonstrated in the frame of this work. In this context, a future cross-correlation analysis would enable us to derive vertical wave properties from the measurements in Ny-Ålesund.

Moreover, the strong anti-correlation between the OH* emission brightness and peak altitude, which could also be found in the model study of this work, implies a further crucial information that is contained in the OH* emission. Finding a corresponding empirical relationship between OH* brightness and peak altitudes would be of great value for the assessment of the dynamic conditions above Ny-Ålesund.

Finally, the updated quenching model that was established in this work provides the opportunity to study the correlations between rotational temperatures, OH* peak altitudes and emission brightness at various temporal and spatial scales. With regard to the OH* measurements in Ny-Ålesund, it is a desirable future task to combine these measurements with corresponding model runs. Ideally, these model runs will resolve the diurnal variability at the fixed geolocation of Spitsbergen in order to study the underlying processes of the dynamic variability of the OH* layer at various scales in more depth.

A. Appendix

A.1. Blackbody calibration

Table A.1 presents a list of several blackbody measurements and includes some general information on the applied settings as well as the determined signal strength from the spectroscopic software. As discussed in Sect. 3.4, the instrumental sensitivity is determined from each measurement by dividing the measured spectrum with its corresponding theoretical Planck curve. From the linearly fitted instrumental sensitivity its relative change ΔS_{inst} is estimated for the spectral interval from 6480 to 6584 cm^{-1}, which corresponds to the transitions of the outer $P_1(4)$ and $P_2(2)$ lines of the $OH(3-1)$ band used for the temperature retrieval. The resulting values for each measurement are presented in Tab. A.2. Here, the first value refers to the forward-scan and the second value refers to the backward-scan mode of the scanner arm. The uncertainty of the relative change in the instrumental sensitivity is estimated from the calculated standard error of the slope parameter. By means of propagation of uncertainties, we may simply express the uncertainty in the change of instrumental sensitivity by

$$u_{(\Delta S_{\text{inst}})} \approx \left|(\sigma_2 - \sigma_1) \cdot u_{\text{slope}}\right| \ , \tag{A.1}$$

where $\sigma_1 = 6480$ cm^{-1} and $\sigma_2 = 6584$ cm^{-1} denote the wavenumbers of the selected interval and u_{slope} is the uncertainty of the slope parameter, which is estimated by the corresponding standard error from the linear regression. Finally, the relative proportion of the estimated uncertainty $u_{(\Delta S_{\text{inst}})}$ to the instrumental sensitivity $S_{\text{inst}}(\sigma_1)$ is determined and included in Tab. A.2.

In addition to the spectral region of the OH(3-1) band, the relative change in the instrumental sensitivity is estimated for the $P_1(4)$ and $P_2(2)$ transitions of the $OH(4-2)$ band. Because of the rather non-linear instrumental response in this wavelength region (see also Fig. 3.10), the fitting is performed with a cubic polynomial function. Because of the correlation between the regression parameters of the cubic fit, a similar estimate of uncertainty as done for the linear case would require the consideration of the covariance of regression coefficients in addition. Because of the rather similar residuum between the fitted and measured instrumental sensitivity in the OH(4-2) spectral region compared to the OH(3-1) spectral region, we may assume that the uncertainty will be somewhat similar, hence, we skip the explicit calculation in this case. The corresponding ΔS_{inst} values for the OH(4-2) band are shown on the right side of Tab. A.2.

No.	date	time (UTC)	T (°C)	ADC	APT (mm)	PreGain
01	03.11.2010	00:40	650	16524/17017	0.5	4
02	03.11.2010	10:50	450	22000/23341	12.5	2
03	03.11.2010	17:02	580	15838/16446	12.5	1
04	03.11.2010	21:12	580	15836/16440	12.5	1
05	04.11.2010	21:27	1000	8911/8843	0.8	1
06	05.11.2010	22:50	600	7218/7104	0.5	3
07	05.11.2010	23:33	590	18035/15515	0.5	4
08	08.11.2010	00:56	1000	16423/16480	0.8	1
09	08.11.2010	01:02	1000	28184/28186	0.5	1
10	03.11.2010	21:12	580	16138	12.5	1
11	18.02.2011	09:46	230	17056/16011	12.5	4
12	27.03.2012	08:54	230	11095/12525	12.5	4
13	08.10.2011	14:31	230	16541/15726	12.5	4

Table A.1.: Blackbody settings including blackbody temperature T, amplitude digital counts (ADC) for forward and backward-scan (measurement No. 10 combines both scans), aperture size (APT) and Pre-amplifier stage (No. 1-4).

OH(3-1) rel. change of instr. sensitivity: ΔS_{inst} (%)			OH(4-2) ΔS_{inst} (%)	
No.	fw-scan	bw-scan	fw-scan	bw-scan
01	1.12 ± 0.03	1.15 ± 0.03	0.76	0.75
02	1.262 ± 0.009	1.406 ± 0.008	1.3	1.4
03	1.179 ± 0.004	1.309 ± 0.004	1.3	1.4
04	1.166 ± 0.004	1.316 ± 0.004	1.2	1.4
05	1.828 ± 0.006	1.801 ± 0.006	1.40	1.42
06	1.21 ± 0.03	0.29 ± 0.03	1.45	1.46
07	0.29 ± 0.03	0.29 ± 0.03	0.7	0.5
08	1.676 ± 0.004	$1,674 \pm 0.004$	1.88	1.87
09	1.711 ± 0.008	1.731 ± 0.008	1.91	1.88
10	1.218 ± 0.003		1.2	
11	2.25 ± 0.05	2.28 ± 0.03	2.2	2.1
12	1.14 ± 0.09	1.2 ± 0.1	0.8	1.3
13	2.15 ± 0.05	1.96 ± 0.05	2.02	2.02

Table A.2.: Left table: Relative change of (linearly) fitted instrumental sensitivity ΔS_{inst} (forward-/backward-scan) between spectral line positions of OH(3-1)/$P_1(4)$ and $P_2(2)$ transitions. Right table: Corresponding ΔS_{inst} values for the OH(4-2)/$P_1(4)$ and $P_2(2)$ transitions based on a cubic polynomial fit. See Tab. A.1 for the instrumental settings of each result.

A.2. Apparent layer thickness

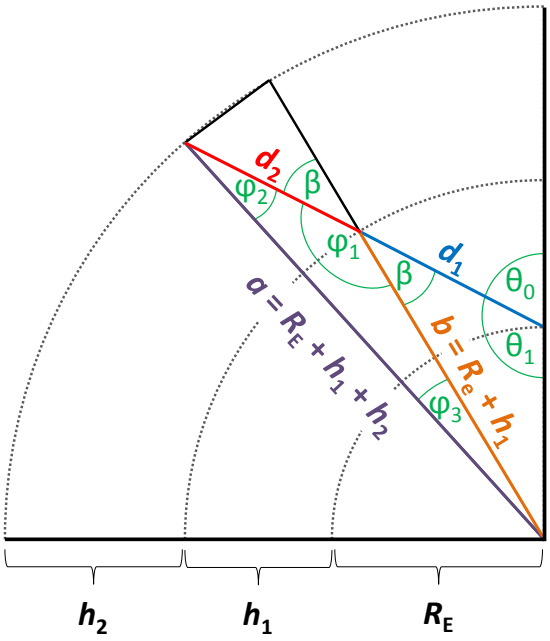

Figure A.1.: Geometry of apparent OH layer thickness d_2 as a function of zenith angle Θ_0. The scale of the centric layer is exaggerated for better illustration.

The geometry used for the derivation of the apparent layer thickness as a function of zenith angle Θ_0 (Eq. A.14) is presented in Fig. A.1. Accordingly, we assume a spherical Earth with radius R_E, which is surrounded by a spherical layer with known altitude h_1, known thickness h_2, and having the same centre. For the sake of simplicity, we further define the parameters a and b as shown in this figure. From the law of sines we find the following relation to d_2:

$$d_2 = a\,\frac{\sin(\varphi_3)}{\sin(\varphi_1)}. \tag{A.2}$$

Accordingly, we need to relate the known values of the parameter a as well as the zenith angle to the arguments of the sine functions on the right hand side of this equation. For this task, let us first set up the following relations:

$$\varphi_1 = \pi - \beta \tag{A.3}$$
$$\Theta_1 = \pi - \Theta_0. \tag{A.4}$$

Again, making use of the law of sines and applying Eq. (A.3) leads to:

$$\frac{R_\mathrm{E}}{\sin(\beta)} = \frac{b}{\sin(\Theta_1)} \overset{(A.3)}{\Rightarrow} \frac{R_\mathrm{E}}{\sin(\pi-\varphi_1)} = \frac{b}{\sin(\Theta_1)}\ . \tag{A.5}$$

Two further expressions are needed to resolve the φ-terms of Eq. (A.2). From the law of sines we get:

$$\frac{a}{\sin(\varphi_1)} = \frac{b}{\sin(\varphi 2)} \ . \tag{A.6}$$

By resolving Eq. (A.5), (A.6), and by considering the sum of angles in a triangle, we get the following expressions for φ:

$$\varphi_1 = \pi - \arcsin\left(\frac{R_\mathrm{E}}{b}\sin(\Theta_1)\right) \tag{A.7}$$

$$\varphi_2 = \arcsin\left(\frac{b}{a}\sin(\varphi_1)\right) \tag{A.8}$$

$$\varphi_3 = \pi - (\varphi_1 + \varphi_2). \tag{A.9}$$

We can now substitute the above expressions in Eq. (A.2) and receive:

$$d_2 = a\ \frac{\sin\left[\arcsin\left(\frac{R_\mathrm{E}}{b}\sin(\Theta_1)\right) - \arcsin\left(\frac{b}{a}\sin(\varphi_1)\right)\right]}{\sin\left[\pi - \arcsin\left(\frac{R_\mathrm{E}}{b}\sin(\Theta_1)\right)\right]}. \tag{A.10}$$

In the next step, we make use of the following property of the sine function:

$$\sin(\pi - x) = \sin(x). \tag{A.11}$$

Consideration of Eq. (A.4,A.5,A.11) resolves Eq. (A.10) accordingly:

$$d_2 = a\ \frac{\sin\left[\arcsin\left(\frac{R_\mathrm{E}}{b}\sin(\Theta_0)\right) - \arcsin\left(\frac{R_\mathrm{E}}{a}\sin(\Theta_0)\right)\right]}{\frac{R_\mathrm{E}}{b}\sin(\Theta_0)}. \tag{A.12}$$

This expression can be further simplified. According to Semendjaev and Bronstein [2005] the following addition theorem exists:

$$\arcsin(x) - \arcsin(y) = \arcsin\left(x\sqrt{1-y^2} - y\sqrt{1-x^2}\right), \text{ if } xy \geq 0. \tag{A.13}$$

Because $(0 < R_\mathrm{E} < b < a)$ and $(0 \leq \Theta_0 \leq \pi/2)$, Eq. (A.12) satisfies the condition of Eq. (A.13), this finally leads to the following simplified expression of the apparent layer thickness:

$$d_2 = \sqrt{a^2 - \left(R_\mathrm{E}\sin(\Theta_0)\right)^2} - \sqrt{b^2 - \left(R_\mathrm{E}\sin(\Theta_0)\right)^2} \ . \tag{A.14}$$

A.3. OH* rate constants and radiative lifetimes

The following tables summarise the applied rate constants and radiative lifetimes to the OH* quenching model Eq. (5.3). References to the values listed herein are provided in Tab. 5.1.

In addition, the $\alpha = 0.723$ correction factor for the quenching rate constants of molecular oxygen and the $\beta = 1.293$ correction factor for the quenching rate constant of atomic oxygen are adapted from Xu et al. [2012] in this work. All tables in this section show the rate constants without any applied correction.

ν'	1	2	3	4	5	6	7	8	9
P_{nasc}	0.00	0.00	0.00	0.00	0.01	0.03	0.15	0.34	0.47

Table A.3.: Nascent vibrational population

	ν''									
	0	1	2	3	4	5	6	7	8	$\sum A(\text{sec}^{-1})$
$\nu' = 1$	17.6222									17.6222
$\nu' = 2$	10.4814	23.9335								34.4149
$\nu' = 3$	1.1397	27.9637	22.4993							51.6027
$\nu' = 4$	0.1365	4.1771	49.2969	16.6444						70.2549
$\nu' = 5$	0.0198	0.6339	9.5405	71.5895	9.4585					91.2422
$\nu' = 6$	0.0034	0.1115	1.7670	17.3699	92.1496	3.8102				115.2116
$\nu' = 7$		0.0231	0.3687	3.8297	27.5363	108.2748	2.3080			142.3406
$\nu' = 8$			0.0887	0.9336	7.0718	39.8385	116.6081	6.9831		171.5238
$\nu' = 9$				0.2551	2.0248	11.4909	54.7226	112.4054	18.3507	199.2495

$A(\nu', \nu'')$ in (sec^{-1}) at the rotational temperature of 200 K

Table A.4.: Einstein coefficients

	ν''									
	0	1	2	3	4	5	6	7	8	$\sum k_3^{O_2}$
$\nu' = 1$	1.9									1.9
$\nu' = 2$	0.3	3.7								4.0
$\nu' = 3$	0.1	1.0	6.6							7.7
$\nu' = 4$	0.1	0.5	2.3	10.1						13.0
$\nu' = 5$	0.3	0.7	2.1	5.7	15.8					24.6
$\nu' = 6$	0.7	1.4	2.8	5.5	11.0	22.0				43.4
$\nu' = 7$	4.4	6.1	8.5	11.8	16.4	22.8	31.7			101.7
$\nu' = 8$	4.4	5.9	7.8	10.4	13.9	18.6	24.8	33.0		118.8
$\nu' = 9$	27.7	29.2	30.7	32.3	34.1	35.8	37.7	39.7	41.8	309.0

$k_3^{O_2}(\nu', \nu'')$ in units of $10^{-13}\text{cm}^3(\text{molec} \cdot \text{sec})^{-1}$

Table A.5.: Multi-quantum relaxation through quenching with molecular oxygen

ν'	1	2	3	4	5	6	7	8	9
$k_L^O(\nu')$	500	500	500	500	500	500	500	500	500

in units of $10^{-13}\text{cm}^3(\text{molec} \cdot \text{sec})^{-1}$

Table A.6.: Complete removal of vibrational state ν' by atomic oxygen through either collisional quenching (R4) or chemical destruction (R5).

ν'	1	2	3	4	5	6	7	8	9
$k_L^{N_2}(\nu')$	0.06	0.1	0.17	0.3	0.52	0.91	1.6	7	4.8

in units of $10^{-13}\text{cm}^3(\text{molec} \cdot \text{sec})^{-1}$

Table A.7.: Single–quantum relaxation through quenching with molecular nitrogen

List of Figures

List of Acronyms

AU Arbitrary Units

BH4 Blackman-Harris 4-term apodization

EEP Energetic Electron Precipitation

ENVISAT Environmental Satellite

EPP Energetic Particle Precipitation

ESRL Earth System Research Laboratory

FFT Fast Fourier Transform

FTIR Fourier Transform Infrared Spectroscopy

FWHM Full Width at Half Maximum

HRDI High-Resolution Doppler Imager

HTS Hines, Tarasick and Shepherd theory

HWHM Half Width at Half Maximum

ILS Instrumental Line Shape

IR infrared

LOS Line-Of-Sight

LST Local Solar Time

LTE Local Thermal Equilibrium

MAMSL Metres above sea level

MLS Microwave Limb Sounder

MLT Mesopause and Lower Thermosphere region

NCAR National Center for Atmospheric Research

NCEP National Centers for Environmental Prediction

NDMC The Network for the Detection of Mesospheric Change

NOAA National Oceanic and Atmospheric Administration

OAR Office of Oceanic and Atmospheric Research

OPD Optical Path Difference

PSD Physical Sciences Division

PV Potential Vorticity

SABER Sounding of the Atmosphere using Broadband Emission Radiometry

SD–WACCM4 Specified Dynamics version of the Whole Atmosphere Community Climate Model, Version 4

SCIAMACHY SCanning Imaging Absorption spectroMeter for Atmospheric CHartographY

SG Swenson and Gardner theory

SPE Solar Proton Event

SSW Sudden Stratospheric Warming

UARS upper atmosphere research satellite

VMR volume-mixing-ratio

WINDII Wind Imaging Interferometer

List of Publications

Peer-reviewed article

S. Kowalewski, C. von Savigny, M. Palm, I.C. McDade, and J. Notholt. On the impact of the temporal variability of the collisional quenching process on the mesospheric OH emission layer: a study based on SD–WACCM4 and SABER. *Atmos. Chem. Phys.*, 14(18):10193–10210, Sept. 2014. doi: 10.5194/acp-14-10193-2013.

Conference contributions

S. Kowalewski, M. Palm, C. Weinzierl, and J. Notholt. The Mesospheric OH layer above Spitsbergen: Observation of the OH rotational emission with high resolution Fourier Transform Spectroscopy. EGU General Assembly 2011, Vienna, Austria. (Poster presentation)

S. Kowalewski, M. Palm, and J. Notholt. Observation of the OH rotational emission with high resolution Fourier Transform Spectroscopy: First results from measurements above Ny-Ålesund, Spitsbergen. 4^{th} NDMC Meeting 2011 at DLR Oberpfaffenhofen, Germany. (Oral presentation)

S. Kowalewski, M. Palm, C. Weinzierl, and J. Notholt. Investigation of polar mesospheric dynamics and temperature trends by means of ground-based OH* airglow measurements and model studies above Spitsbergen. EGU General Assembly 2012, Vienna, Austria. (Poster presentation)

S. Kowalewski, M. Palm, C. Weinzierl, and J. Notholt. OH*-airglow measurements at Ny-Ålesund, Spitsbergen via Fourier Transform Spectroscopy: An update on the establishment of OH*-airglow observations and current model studies. 5^{th} NDMC Meeting 2012 at DLR Oberpfaffenhofen, Germany. (Oral presentation)

S. Kowalewski, C. von Savigny, M. Palm, C. Weinzierl, and J. Notholt. Investigation of polar mesospheric dynamics and temperature changes by means of ground-based OH* airglow spectroscopy and model studies above Spitsbergen. NSERC CREATE Summer School in Arctic Atmospheric Science 2013, Alliston, Ontario, Canada. (Poster presentation)

S. Kowalewski, C. von Savigny, M. Palm, I.C. McDade, and J. Notholt. A sensitivity study on the quenching process of OH* by O and O_2 based on SD-WACCM4. 6^{th} NDMC Meeting 2014, Grainau, Germany. (Oral presentation)

Bibliography

S. Adler-Golden. Kinetic parameters for OH nightglow modeling consistent with recent laboratory measurements. *J. Geophys. Res.*, 102(A9):19969–19976, 1997. doi: 10.1029/97JA01622.

D. G. Andrews. *Middle atmosphere dynamics / David G. Andrews, James R. Holton, Conway B. Leovy.* Academic Press, Orlando, 1987.

V. V. Bakanas, V. I. Perminov, and A. I. Semenov. Some features in the seasonal behavior of the hydroxyl emission characteristics in the upper atmosphere. *Geomagn. Aeron.*, 43(3):363—-369, 2003. ISSN 0273-1177.

D. J. Baker and A. T. Stair Jr. Rocket measurements of the altitude distributions of the hydroxyl airglow. *Phys. Scr.*, 37(4):611–622, 1988. doi: 10.1088/0031-8949/37/4/021.

D. Bates. Excitation of 557.7 nm OI line in nightglow. *Planet. Space Sci.*, 36(9): 883–889, Sept. 1988. doi: 10.1016/0032-0633(88)90094-3.

D. R. Bates and M. Nicolet. The photochemistry of atmospheric water vapor. *J. Geophys. Res.*, 55(3):301–327, Sept. 1950. doi: 10.1029/JZ055i003p00301.

E. Becker. Dynamical control of the middle atmosphere. *Space Sci. Rev.*, 168(1-4): 283–314, 2012. doi: 10.1007/s11214-011-9841-5.

E. Becker and C. von Savigny. Dynamical heating of the polar summer mesopause induced by solar proton events. *J. Geophys. Res.*, 115(D1):D00I18, Jan. 2010. doi: 10.1029/2009JD012561.

G. Beig. Trends in the mesopause region temperature and our present understanding–an update. *Phys. Chem. Earth*, 31(1-3):3–9, 2006. ISSN 1474-7065. doi: 10.1016/j.pce.2005.03.007.

G. Beig. Long–term trends in the temperature of the mesosphere/lower thermosphere region: 2. Solar response. *J. Geophys. Res.*, 116(A2):A00H12, Feb. 2011. doi: 10.1029/2011JA016766.

G. Beig, P. Keckhut, R. P. Lowe, R. G. Roble, M. G. Mlynczak, J. Scheer, V. I. Fomichev, D. Offermann, W. J. R. French, M. G. Shepherd, A. I. Semenov, E. E. Remsberg, C. Y. She, F. J. Lübken, J. Bremer, B. R. Clemesha, J. Stegman, F. Sigernes, and S. Fadnavis. Review of mesospheric temperature trends. *Rev. Geophys.*, 41(4):1015, Oct. 2003. doi: 10.1029/2002RG000121.

G. Beig, J. Scheer, M. G. Mlynczak, and P. Keckhut. Overview of the temperature response in the mesosphere and lower thermosphere to solar activity. *Rev. Geophys.*, 46(3):RG3002, July 2008. doi: 10.1029/2007RG000236.

P. F. Bernath and R. Colin. Revised molecular constants and term values for the $X^2\Pi$ and $B^2\Sigma^+$ states of OH. *J. Mol. Spectrosc.*, 257(1):20–23, Sept. 2009. doi: 10.1016/j.jms.2009.06.003.

M. Birk and J. W. Brault. Detector quantum efficiency: An important parameter for FT-IR spectroscopy. *Mikrochim. Acta*, 95(1-6):243–247, 1988. doi: 10.1007/BF01349762.

M. Bittner, D. Offermann, and H. H. Graef. Mesopause temperature variability above a midlatitude station in Europe. *J. Geophys. Res.*, 105(D2):2045–2058, Jan. 2000. doi: 10.1029/1999JD900307.

M. Bittner, D. Offermann, H. H. Graef, M. Donner, and K. Hamilton. An 18–year time series of OH rotational temperatures and middle atmosphere decadal variations. *J. Atmos. Sol. Terr. Phys.*, 64(8-11):1147–1166, May 2002. doi: 10.1016/S1364-6826(02)00065-2.

G. P. Brasseur and S. Solomon. *Aeronomy of the middle atmosphere*. Springer, 3rd rev. and enlarged ed. edition edition, Dec. 2005.

Bruker. *Guide for Infrared Spectroscopy*. Bruker Optik, Ettlingen, Germany, bopt-4000059-01 edition, 2011. URL `http://bruker.com`.

H. C. Carlson and A. Egeland. *The aurora and the auroral ionosphere*. Cambridge atmospheric and space science series. in Introduction to Space Physics (eds Kivelson and Russel), Cambridge Univ. Press, 1995. ISBN 9780521457149.

Y.-M. Cho and G. G. Shepherd. Correlation of airglow temperature and emission rate at Resolute Bay (74.68°N), over four winters (2001–2005). *Geophys. Res. Lett.*, 33(6):L06815, Mar. 2006. doi: 10.1029/2005GL025298.

P. C. Cosby and T. G. Slanger. OH spectroscopy and chemistry investigated with astronomical sky spectra. *Can. J. Phys.*, 85(2):77–99, Feb. 2007. doi: 10.1139/P06-088.

S. P. Davis, M. C. Abrams, and J. W. Brault. *Fourier Transform Spectrometry*. Academic Press, San Diego, 2001. doi: 10.1016/B978-012042510-5/50002-0.

J. A. Dodd, S. J. Lipson, J. R. Lowell, P. S. Armstrong, W. A. M. Blumberg, R. M. Nadile, S. M. Adler-Golden, W. J. Marinelli, K. W. Holtzclaw, and B. D. Green. Analysis of hydroxyl earthlimb airglow emissions: Kinetic model for state-to-state dynamics of OH (ν,N). *J. Geophys. Res.*, 99(D2):3559–3585, Feb. 1994. doi: 10.1029/93JD03338.

M. E. Dyrland and F. Sigernes. An update on the hydroxyl airglow temperature record from the auroral station in adventdalen, svalbard (1980-2005). *CANADIAN JOURNAL OF PHYSICS*, 85(2):143–151, Feb. 2007. doi: 10.1139/P07-040. 32nd Annual European Meeting on Atmospheric Studies by Optical Methods, Univ Western Ontario, Phys & Astron Dept, London, CANADA, AUG 29-SEP 01, 2005.

M. E. Dyrland, F. J. Mulligan, C. M. Hall, F. Sigernes, M. Tsutsumi, and C. S. Deehr. Response of oh airglow temperatures to neutral air dynamics at 78°N, 16°E during the anomalous 2003–2004 winter. *J. Geophys. Res.*, 115(D7): D07103, Apr. 2010. doi: 10.1029/2009JD012726.

P. J. Espy, J. Stegman, P. Forkman, and D. Murtagh. Seasonal variation in the correlation of airglow temperature and emission rate. *Geophys. Res. Lett.*, 34 (17):L17802, Sept. 2007. doi: 10.1029/2007GL031034.

W. French, G. Burns, K. Finlayson, P. Greet, R. Lowe, and P. Williams. Hydroxyl (6/2) airglow emission intensity ratios for rotational temperature determination. *Ann. Geophys.*, 18(10):1293–1303, 2000. doi: 10.1007/s00585-000-1293-2.

D. C. Fritts. Gravity wave saturation in the middle atmosphere: A review of theory and observations. *Rev. Geophys.*, 22(3):275–308, Aug. 1984. doi: 10.1029/RG022i003p00275.

D. C. Fritts and M. J. Alexander. Gravity wave dynamics and effects in the middle atmosphere. *Rev. Geophys.*, 41(1):1003, Mar. 2003. doi: 10.1029/2001RG000106.

B. Funke, M. Lopez-Puertas, M. Garcia-Comas, M. Kaufmann, M. Höpfner, and G. Stiller. GRANADA: A Generic RAdiative traNsfer AnD non-LTE population algorithm. *JQSRT*, 113(14):1771–1817, Sept. 2012. doi: 10.1016/j.jqsrt.2012.05.001.

H. Gao, J. Xu, W. Ward, and A. K. Smith. Temporal evolution of nightglow emission responses to SSW events observed by TIMED/SABER. *J. Geophys. Res.*, 116(D19):D19110, Oct. 2011. doi: 10.1029/2011JD015936.

R. R. Garcia, D. R. Marsh, D. E. Kinnison, B. A. Boville, and F. Sassi. Simulation of secular trends in the middle atmosphere, 1950;2003. *J. Geophys. Res.*, 112 (D9):D09301, May 2007. doi: 10.1029/2006JD007485.

R. R. Garcia, D. E. Kinnison, and D. R. Marsh. "World avoided" simulations with the Whole Atmosphere Community Climate Model. *J. Geophys. Res.*, 117 (D23):D23303, Dec. 2012. doi: 10.1029/2012JD018430.

R. L. Gattinger and A. Vallance Jones. Quantitative spectroscopy of the aurora. v - the spectrum of strong aurora between 10 000 and 16 000 Å. *Can. J. Phys.*, 59:480–487, Mar. 1981. doi: 10.1139/p81-059.

R. Ghodpage, D. Siingh, R. Singh, G. Mukherjee, P. Vohat, and A. Singh. Tidal and gravity waves study from the airglow measurements at Kolhapur (India). *J. Earth Syst. Sci.*, 121(6):1511–1525, 2012. doi: 10.1007/s12040-012-0240-4.

F. J. Harris. On the use of windows for harmonic analysis with the discrete Fourier transform. *Proc. IEEE*, 66(1):51–83, June 1978. doi: 10.1109/PROC.1978.10837.

F. Hase. Improved instrumental line shape monitoring for the ground-based, high-resolution FTIR spectrometers of the Network for the Detection of Atmospheric Composition Change. *Atmos. Meas. Tech.*, 5(3):603–610, Mar. 2012. doi: 10.5194/amt-5-603-2012.

F. Hase, J. Hannigan, M. Coffey, A. Goldman, M. Höpfner, N. Jones, C. Rinsland, and S. Wood. Intercomparison of retrieval codes used for the analysis of high-resolution, ground-based ftir measurements. *J. Quant. Spectrosc. Radiat. Transfer*, 87(1):25–52, Aug. 2004. doi: 10.1016/j.jqsrt.2003.12.008.

W. Herres and J. Gronholz. Understanding FT-IR data processing part 1: Data acquisition and Fourier transformation. *Computer Applications in the Laboratory*, 4:216–220, 1984.

G. Herzberg. *Spectra of diatomic molecules*, volume 1. Van Nostrand Reinhold: New York, 1950.

C. O. Hines and D. W. Tarasick. On the detection and utilization of gravity waves in airglow studies. *Planet. Space Sci.*, 35(7):851–866, July 1987. ISSN 0032-0633. doi: 10.1016/0032-0633(87)90063-8.

C. G. Hoffmann, U. Raffalski, M. Palm, B. Funke, S. H. W. Golchert, G. Hochschild, and J. Notholt. Observation of strato-mesospheric CO above Kiruna with ground-based microwave radiometry – retrieval and satellite comparison. *Atmos. Meas. Tech.*, 4(11):2389–2408, 2011. doi: 10.5194/amt-4-2389-2011.

C. G. Hoffmann, D. E. Kinnison, R. R. Garcia, M. Palm, J. Notholt, U. Raffalski, and G. Hochschild. CO at 40-80 km above Kiruna observed by the ground-based microwave radiometer KIMRA and simulated by the Whole Atmosphere Community Climate Model. *Atmos. Chem. Phys.*, 12(7):3261–3271, Apr. 2012. doi: 10.5194/acp-12-3261-2012.

P. Hoffmann, W. Singer, D. Keuer, W. Hocking, M. Kunze, and Y. Murayama. Latitudinal and longitudinal variability of mesospheric winds and temperatures during stratospheric warming events. *J. Atmos. Sol. Terr. Phys.*, 69(17-18):2355–2366, Dec. 2007. doi: 10.1016/j.jastp.2007.06.010.

S. Holmen, M. Dyrland, and F. Sigernes. Mesospheric temperatures derived from three decades of hydroxyl airglow measurements from Longyearbyen, Svalbard (78°N). *Acta Geophys.*, pages 1–14, 2013. doi: 10.2478/s11600-013-0159-4.

S. E. Holmen, M. E. Dyrland, and F. Sigernes. Long-term trends and the effect of solar cycle variations on mesospheric winter temperatures over Longyearbyen, Svalbard (78°N). *J. Geophys. Res. Atmos.*, page 2013JD021195, May 2014. doi: 10.1002/2013JD021195.

J. R. Holton. *An introduction to dynamic meteorology*, volume Volume 88. Academic Press, 2004. doi: 10.1016/S0074-6142(04)80034-2.

T.-Y. Huang and M. Hickey. Secular variations of OH nightglow emission and of the OH intensity-weighted temperature induced by gravity–wave forcing in the MLT region. *Adv. Space Res.*, 41(9):1478–1487, 2008. doi: 10.1016/j.asr.2007.10.020.

C. J. Humphreys. The first spectrum of mercury in the region between 1.3 and 2.0 μ*. *J. Opt. Soc. Am.*, 43(11):1027–1029, 1953. doi: 10.1364/JOSA.43.001027.

C. H. Jackman, R. G. Roble, and E. L. Fleming. Mesospheric dynamical changes induced by the solar proton events in October–November 2003. *Geophys. Res. Lett.*, 34(4):L04812, Feb. 2007. doi: 10.1029/2006GL028328.

C. H. Jackman, C. E. Randall, V. L. Harvey, S. Wang, E. L. Fleming, M. López-Puertas, B. Funke, and P. F. Bernath. Middle atmospheric changes caused by the January and March 2012 solar proton events. *Atmos. Chem. Phys.*, 14(2): 1025–1038, Jan. 2014. doi: 10.5194/acp-14-1025-2014.

D. Jacob. *Introduction to atmospheric chemistry.* Princeton University Press, 1999.

E. Kalnay, M. Kanamitsu, R. Kistler, W. Collins, D. Deaven, L. Gandin, M. Iredell, S. Saha, G. White, J. Woollen, Y. Zhu, A. Leetmaa, R. Reynolds, M. Chelliah, W. Ebisuzaki, W. Higgins, J. Janowiak, K. C. Mo, C. Ropelewski, J. Wang, R. Jenne, and D. Joseph. The NCEP/NCAR 40-Year Reanalysis Project. *Bull. Amer. Meteor. Soc.*, 77(3):437–471, Mar. 1996. doi: 10.1175/1520-0477(1996)077⟨0437:TNYRP⟩2.0.CO;2.

J. Kauppinen and J. Partanen. *Fourier Transforms in Spectroscopy.* Wiley-VCH, 1 edition, 2001. doi: 10.1002/3527600299.

V. Khomich, A. Semenov, and N. Shefov. *Airglow as an indicator of upper atmospheric structure and dynamics.* Springer Berlin Heidelberg, 2008. doi: 10.1007/978-3-540-75833-4.

I. Kovács. *Rotational Structure in the Spectra of Diatomic Molecules*, volume 11. Adam Hilger Ldt, London, 1969. doi: 10.1016/0022-2860(72)85019-1.

S. Kowalewski, C. von Savigny, M. Palm, I. C. McDade, and J. Notholt. On the impact of the temporal variability of the collisional quenching process on the mesospheric OH emission layer: a study based on SD-WACCM4 and SABER. *Atmos. Chem. Phys.*, 14(18):10193–10210, Sept. 2014. doi: 10.5194/acp-14-10193-2014.

V. Krassovsky. Infrasonic variations of OH emission in the upper atmosphere. *Ann. Geophys.*, 28:739–746, 1972.

V. I. Krassovsky. Chemistry of the upper atmosphere. *Space Res.*, 3:96–116, 1963.

K. K. Kumar, C. Vineeth, T. M. Antonita, T. K. Pant, and R. Sridharan. Determination of day-time OH emission heights using simultaneous meteor radar, dayglow photometer and TIMED/SABER observations over Thumba (8.5°N, 77°E). *Geophys. Res. Lett.*, 35(18):L18809, Sept. 2008. doi: 10.1029/2008GL035376.

J. Kurihara, Y. Ogawa, S. Oyama, S. Nozawa, M. Tsutsumi, C. M. Hall, Y. Tomikawa, and R. Fujii. Links between a stratospheric sudden warming and thermal structures and dynamics in the high–latitude mesosphere, lower thermosphere, and ionosphere. *Geophys. Res. Lett.*, 37(13):L13806, July 2010. doi: 10.1029/2010GL043643.

J. Kuttippurath and G. Nikulin. A comparative study of the major sudden stratospheric warmings in the Arctic winters 2003/2004–2009/2010. *Atmos. Chem. Phys.*, 12(17):8115–8129, Sept. 2012. doi: 10.5194/acp-12-8115-2012.

K. Labitzke. Stratospheric–mesospheric midwinter disturbances: A summary of observed characteristics. *J. Geophys. Res*, 86(C10):9665–9678, Oct. 1981. doi: 10.1029/JC086iC10p09665.

K. Labitzke and M. Kunze. On the remarkable Arctic winter in 2008/2009. *J. Geophys. Res.*, 114(D1):D00I02, Jan. 2009. doi: 10.1029/2009JD012273.

B. S. Lanchester, M. Ashrafi, and N. Ivchenko. Simultaneous imaging of aurora on small scale in OI (777.4 nm) and $N_2$1P to estimate energy and flux of precipitation. *Ann. Geophys.*, 27(7):2881–2891, July 2009. doi: 10.5194/angeo-27-2881-2009.

S. R. Langhoff, H.-J. Werner, and P. Rosmus. Theoretical transition probabilities for the OH meinel system. *J. Mol. Spectrosc.*, 118(2):507–529, Aug. 1986. doi: 10.1016/0022-2852(86)90186-4.

H. Le Texier, S. Solomon, and R. Garcia. Seasonal variability of the OH Meinel bands. *Planet. Space Sci.*, 35(8):977–989, Aug. 1987. doi: 10.1016/0032-0633(87)90002-X.

W. B. Leigh. *Devices for Optoelectronics*. Optical Science and Engineering. Marcel Dekker Inc, 1996. ISBN 9780824794323.

R. S. Lindzen. Turbulence and stress owing to gravity wave and tidal breakdown. *J. Geophys. Res*, 86(C10):9707–9714, Oct. 1981. doi: 10.1029/JC086iC10p09707.

A. Z. Liu and G. R. Swenson. A modeling study of O_2 and OH airglow perturbations induced by atmospheric gravity waves. *J. Geophys. Res.*, 108(D4):4151, Feb. 2003. doi: 10.1029/2002JD002474.

G. Liu and G. G. Shepherd. An empirical model for the altitude of the OH nightglow emission. *Geophys. Res. Lett.*, 33(9):L09805, May 2006. doi: 10.1029/2005GL025297.

H.-L. Liu and R. G. Roble. A study of a self-generated stratospheric sudden warming and its mesospheric-lower thermospheric impacts using the coupled TIME–GCM/CCM3. *J. Geophys. Res.*, 107(D23):4695, Dec. 2002. doi: 10.1029/2001JD001533.

A. Lofthus and P. H. Krupenie. The spectrum of molecular nitrogen. *J. Phys. Chem. Ref. Data*, 6(1):113–307, 1977. doi: 10.1063/1.555546.

X. Lu, H.-L. L. Liu, A. Z. Liu, J. M. Yue, J.M. McInerney, and L. Z. Momentum budget of the migrating diurnal tide in the Whole Atmosphere Community Climate Model at vernal equinox. *J. Geophys. Res.*, 117:D07112, 2012. URL doi:10.1029/2011JD017089.

U. B. Makhlouf, R. H. Picard, and J. R. Winick. Photochemical-dynamical modeling of the measured response of airglow to gravity waves 1. Basic model for OH airglow. *J. Geophys. Res.*, 100(D6):11289–11311, 1995. doi: 10.1029/94JD03327.

G. L. Manney, M. J. Schwartz, K. Krüger, M. L. Santee, S. Pawson, J. N. Lee, W. H. Daffer, R. A. Fuller, and N. J. Livesey. Aura Microwave Limb Sounder observations of dynamics and transport during the record-breaking 2009 Arctic stratospheric major warming. *Geophys. Res. Lett.*, 36(12):L12815, June 2009. doi: 10.1029/2009GL038586.

D. R. Marsh, A. K. Smith, M. G. Mlynczak, and J. M. Russell. SABER observations of the OH Meinel airglow variability near the mesopause. *J. Geophys. Res.*, 111(A10):A10S05, Oct. 2006. doi: 10.1029/2005JA011451.

T. Matsuno. A dynamical model of the stratospheric sudden warming. *J. Atmos. Sci.*, 28(8):1479–1494, Nov. 1971. doi: 10.1175/1520-0469(1971)028⟨1479:ADMOTS⟩2.0.CO;2.

L. McArthur. *Baseline Surface Radiation Network*. World Meteorological Organization, 2.1 edition, Apr. 2005.

I. C. McDade. The altitude dependence of the OH($X^2\Sigma$) vibrational distribution in the nightglow: Some model expectations. *Planet. Space Sci.*, 39(7):1049–1057, July 1991. doi: 10.1016/0032-0633(91)90112-N.

I. C. McDade and E. J. Llewellyn. Kinetic parameters related to sources and sinks of vibrationally excited OH in the nightglow. *J. Geophys. Res.*, 92(A7): 7643–7650, 1987. doi: 10.1029/JA092iA07p07643.

I. C. McDade and E. J. Llewellyn. Mesospheric oxygen atom densities inferred from night-time OH Meinel band emission rates. *Planet. Space Sci.*, 36(9):897–905, Sept. 1988. doi: 10.1016/0032-0633(88)90097-9.

A. B. Meinel. OH emission bands in the spectrum of the night sky .1. *ApJ*, 111: 555–564, 1950a. doi: 10.1086/145296.

A. B. Meinel. OH emission bands in the spectrum of the night sky .2. *ApJ*, 112: 120–130, 1950b. doi: 10.1086/145321.

S. M. L. Melo, R. P. Lowe, and J. P. Russell. Double–peaked hydroxyl airglow profiles observed from WINDII/UARS. *J. Geophys. Res.*, 105(D10):12397–12403, 2000. doi: 10.1029/1999JD901169.

J. W. Meriwether and A. J. Gerrard. Mesosphere inversion layers and stratosphere temperature enhancements. *Rev. Geophys.*, 42(3):RG3003, Sept. 2004. doi: 10.1029/2003RG000133.

C. J. Mertens, J. M. Russell III, M. G. Mlynczak, C.-Y. She, F. J. Schmidlin, R. A. Goldberg, M. Lopez-Puertas, P. P. Wintersteiner, R. H. Picard, J. R. Winick, and X. Xu. Kinetic temperature and carbon dioxide from broadband infrared limb emission measurements taken from the TIMED/SABER instrument. *Adv. Space Res.*, 43(1):15–27, Jan. 2009. doi: 10.1016/j.asr.2008.04.017.

F. H. Mies. Calculated vibrational transition probabilities of oh($X^2\pi$). *J. Mol. Spectrosc.*, 53(2):150–188, 1974. doi: 10.1016/0022-2852(74)90125-8.

M. G. Mlynczak, L. A. Hunt, J. C. Mast, B. Thomas Marshall, J. M. Russell, A. K. Smith, D. E. Siskind, J.-H. Yee, C. J. Mertens, F. Javier Martin-Torres, R. Earl Thompson, D. P. Drob, and L. L. Gordley. Atomic oxygen in the mesosphere and lower thermosphere derived from SABER: Algorithm theoretical basis and measurement uncertainty. *J. Geophys. Res. Atmos.*, pages 5724—5735, June 2013. doi: 10.1002/jgrd.50401.

F. J. Mulligan, M. E. Dyrland, F. Sigernes, and C. S. Deehr. Inferring hydroxyl layer peak heights from ground-based measurements of OH(6-2) band integrated emission rate at Longyearbyen (78°N, 16°E). *Ann. Geophys.*, 27(11):4197–4205, 2009. doi: 10.5194/angeo-27-4197-2009.

C. Nappo. *An introduction to atmospheric gravity waves*. Elsevier Science, 2002.

R. Nikoukar, G. R. Swenson, A. Z. Liu, and F. Kamalabadi. On the variability of mesospheric OH emission profiles. *J. Geophys. Res.*, 112(D19):D19109, Oct. 2007. doi: 10.1029/2007JD008601.

J. Notholt, G. Toon, F. Stordal, S. Solberg, N. Schmidbauer, E. Becker, A. Meier, and B. Sen. Seasonal variations of atmospheric trace gases in the high Arctic at 79°N. *J. Geophys. Res.*, 102(D11):12855–12861, June 1997. doi: 10.1029/97JD00337.

D. Offermann and R. Gerndt. Upper mesosphere temperatures from OH*-emissions. *Adv. Space Res.*, 10:217–221, 1990. doi: 10.1016/0273-1177(90)90399-K.

I. Oznovich, D. McEwen, and G. Sivjee. Temperature and airglow brightness oscillations in the polar mesosphere and lower thermosphere. *Planet. Space Sci.*, 43(9):1121–1130, Sept. 1995. doi: 10.1016/0032-0633(95)00029-5.

I. Oznovich, R. Walterscheid, G. Sivjee, and D. McEwen. On Krassovsky's ratio for ter-diurnal hydroxyl oscillations in the winter polar mesopause. *Planet. Space Sci.*, 45(3):385–394, Mar. 1997. doi: 10.1016/S0032-0633(96)00130-4.

J. Pendleton, W. R., P. J. Espy, and M. R. Hammond. Evidence for Non-Local-Thermodynamic-Equilibrium rotation in the OH nightglow. *J. Geophys. Res.*, 98(A7):11567–11579, 1993. doi: 10.1029/93JA00740.

V. Perminov. Seasonal temperature variations near the mesopause according to the hydroxyl emission measurements in Zvenigorod. *Geomagn. Aeron.*, 49:797–804, 2009. doi: 10.1134/S0016793209060139.

V. Perminov, A. Semenov, and N. Shefov. On rotational temperature of the hydroxyl emission. *Geomagn. Aeron.*, 47:756–763, 2007. doi: 10.1134/S0016793207060084.

W. H. Press and G. B. Rybicki. Fast algorithm for spectral analysis of unevenly sampled data. *ApJ*, 338:277–280, Mar. 1989. doi: 10.1086/167197.

I. Reda and A. Andreas. Solar position algorithm for solar radiation applications. *Sol. Energy*, 76(5):577–589, 2004. doi: 10.1016/j.solener.2003.12.003.

E. Reisin and J. Scheer. Vertical propagation of gravity waves determined from zenith observations of airglow. *Adv. Space Res.*, 27(10):1743–1748, 2001. doi: 10.1016/S0273-1177(01)00313-1.

E. R. Reisin and J. Scheer. Characteristics of atmospheric waves in the tidal period range derived from zenith observations of O2(0-1) Atmospheric and OH(6-2) airglow at lower midlatitudes. *J. Geophys. Res.*, 101(D16):21223–21232, Sept. 1996. doi: 10.1029/96JD01723.

R. G. Roble, B. A. Emery, T. L. Killeen, G. C. Reid, S. Solomon, R. R. Garcia, D. S. Evans, P. B. Hays, G. R. Carignan, R. A. Heelis, W. B. Hanson, D. J. Winningham, N. W. Spencer, and L. H. Brace. Joule heating in the mesosphere and thermosphere during the July 13, 1982, solar proton event. *J. Geophys. Res.*, 92(A6):6083–6090, June 1987. doi: 10.1029/JA092iA06p06083.

L. Rothman, I. Gordon, A. Barbe, D. Benner, P. Bernath, M. Birk, V. Boudon, L. Brown, A. Campargue, J.-P. Champion, K. Chance, L. Coudert, V. Dana, V. Devi, S. Fally, J.-M. Flaud, R. Gamache, A. Goldman, D. Jacquemart, I. Kleiner, N. Lacome, W. Lafferty, J.-Y. Mandin, S. Massie, S. Mikhailenko, C. Miller, N. Moazzen-Ahmadi, O. Naumenko, A. Nikitin, J. Orphal, V. Perevalov, A. Perrin, A. Predoi-Cross, C. Rinsland, M. Rotger, M. Šimečková, M. Smith, K. Sung, S. Tashkun, J. Tennyson, R. Toth, A. Vandaele, and J. Vander Auwera. The HITRAN 2008 molecular spectroscopic database. *JQSRT*, 110 (9-10):533–572, June 2009. doi: 10.1016/j.jqsrt.2009.02.013.

J. M. Russell III, M. G. Mlynczak, L. L. Gordley, J. J. Tansock, Jr., and R. W. Esplin. Overview of the SABER experiment and preliminary calibration results. volume 3756, pages 277–288, 1999. doi: 10.1117/12.366382.

S. P. Sander, J. Abbatt, J. R. Barker, J. B. Burkholder, R. R. Friedl, D. M. Golden, R. E. Huie, C. E. Kolb, M. J. Kurylo, G. K. Moortgat, V. L. Orkin, and P. H. Wine. Chemical Kinetics and Photochemical Data for Use in Atmospheric Studies, Evaluation No. 17. *JPL Publication, Jet Propulsion Laboratory, Pasadena*, 10-66:1–12, 2011. URL `http://jpldataeval.jpl.nasa.gov`.

M. J. Schwartz, A. Lambert, G. L. Manney, W. G. Read, N. J. Livesey, L. Froidevaux, C. O. Ao, P. F. Bernath, C. D. Boone, R. E. Cofield, W. H. Daffer, B. J. Drouin, E. J. Fetzer, R. A. Fuller, R. F. Jarnot, J. H. Jiang, Y. B. Jiang, B. W. Knosp, K. Krueger, J.-L. F. Li, M. G. Mlynczak, S. Pawson, I. Russell, J. M., M. L. Santee, W. V. Snyder, P. C. Stek, R. P. Thurstans, A. M. Tompkins, P. A.

Wagner, K. A. Walker, J. W. Waters, and D. L. Wu. Validation of the Aura Microwave Limb Sounder temperature and geopotential height measurements. *J. Geophys. Res.*, 113(D15):D15S11, May 2008. doi: 10.1029/2007JD008783.

K. Semendjaev and I. Bronstein. *Taschenbuch der Mathematik*. Harri Deutsch, 2005.

C. Y. She and R. P. Lowe. Seasonal temperature variations in the mesopause region at mid-latitude: comparison of lidar and hydroxyl rotational temperatures using WINDII/UARS OH Height profiles. *J. Atmos. Sol. Terr. Phys.*, 60(16):1573–1583, Nov. 1998. doi: dx.doi.org/10.1016/S1364-6826(98)00082-0.

N. N. Shefov. On determining the rotational temperature of the OH bands. *Spektr. Elektrofotom. Radiolokatsionnye Issled. Polyarn. Siyanii Svecheniya*, 5: 5–9, 1961.

M. G. Shepherd, G. Liu, and G. G. Shepherd. Mesospheric semiannual oscillation in temperature and nightglow emission. *J. Atmos. Sol. Terr. Phys.*, 68(3-5): 379–389, Feb. 2006. doi: 10.1016/j.jastp.2005.02.029.

F. Sigernes, N. Shumilov, C. S. Deehr, K. P. Nielsen, T. Svenœ, and O. Havnes. Hydroxyl rotational temperature record from the auroral station in Adventdalen, Svalbard (78°N, 15°E). *J. Geophys. Res.*, 108(A9):1342, Sept. 2003. doi: 10.1029/2001JA009023.

W. Singer, P. Hoffmann, G. Kishore Kumar, N. Mitchell, and V. Matthias. Atmospheric Coupling by Gravity Waves: Climatology of Gravity Wave Activity, Mesospheric Turbulence and Their Relations to Solar Activity. In F.-J. Lübken, editor, *Springer Atmospheric Sciences*, pages 409–427–. Springer Netherlands, 2013. doi: 10.1007/978-94-007-4348-9_22.

M. Sinnhuber, H. Nieder, and N. Wieters. Energetic Particle Precipitation and the Chemistry of the Mesosphere/Lower Thermosphere. *Surv Geophys*, 33(6): 1281–1334, 2012. doi: 10.1007/s10712-012-9201-3.

D. E. Siskind, L. Coy, and P. Espy. Observations of stratospheric warmings and mesospheric coolings by the TIMED SABER instrument. *Geophys. Res. Lett.*, 32(9):L09804, May 2005. doi: 10.1029/2005GL022399.

G. Sivjee. Airglow hydroxyl emissions. *Planet. Space Sci.*, 40(2-3):235–242, Feb. 1992. doi: 10.1016/0032-0633(92)90061-R.

A. K. Smith. Physics and chemistry of the mesopause region. *J. Atmos. Sol. Terr. Phys.*, 66(10):839–857, July 2004. doi: 10.1016/j.jastp.2004.01.032.

A. K. Smith. Interactions between the lower, middle and upper atmosphere. *Space Sci. Rev.*, 168(1-4):1–21, 2012a. doi: 10.1007/s11214-011-9791-y.

A. K. Smith and D. R. Marsh. Processes that account for the ozone maximum at the mesopause. *J. Geophys. Res.*, 110(D23):D23305, Dec. 2005. doi: 10.1029/2005JD006298.

A. K. Smith, D. R. Marsh, M. G. Mlynczak, and J. C. Mast. Temporal variations of atomic oxygen in the upper mesosphere from SABER. *J. Geophys. Res.*, 115 (D18):D18309, Sept. 2010. doi: 10.1029/2009JD013434.

A. K. Smith, R. R. Garcia, D. R. Marsh, and J. H. Richter. WACCM simulations of the mean circulation and trace species transport in the winter mesosphere. *J. Geophys. Res.*, 116(D20):D20115, Oct. 2011. doi: 10.1029/2011JD016083.

A. K. Smith, V. L. Harvey, M. G. Mlynczak, B. Funke, M. García-Comas, M. Hervig, M. Kaufmann, E. Kyrölä, M. López-Puertas, I. McDade, C. E. Randall, J. M. Russell, P. E. Sheese, M. Shiotani, W. R. Skinner, M. Suzuki, and K. A. Walker. Satellite observations of ozone in the upper mesosphere. *J. Geophys. Res. Atmos.*, 118(11):5803–5821, June 2013. doi: 10.1002/jgrd.50445.

B. Smith. *Fundamentals of Fourier Transform Infrared Spectroscopy.* Taylor & Francis Group, 1995.

S. M. Smith. Seasonal variations in the correlation of mesospheric OH temperature and radiance at midlatitudes. *J. Geophys. Res.*, 117(A10):A10308, Oct. 2012b. doi: 10.1029/2012JA017884.

J. B. Snively, V. P. Pasko, and M. J. Taylor. OH and OI airglow layer modulation by ducted short-period gravity waves: Effects of trapping altitude. *J. Geophys. Res.*, 115(A11):A11311, Nov. 2010. doi: 10.1029/2009JA015236.

J. I. Steinfeld, S. M. Adler-Golden, and J. W. Gallagher. Critical survey of data on the spectroscopy and kinetics of ozone in the mesosphere and thermosphere. *Phys. Chem. Ref. Data*, 16:911–951, 1987. doi: 10.1063/1.555796.

G. R. Swenson and C. S. Gardner. Analytical models for the responses of the mesospheric OH* and Na layers to atmospheric gravity waves. *J. Geophys. Res.*, 103(D6):6271–6294, 1998. doi: 10.1029/97JD02985.

D. W. Tarasick and C. O. Hines. The observable effects of gravity waves on airglow emissions. *Planet. Space Sci.*, 38(9):1105–1119, Sept. 1990. doi: 10.1016/0032-0633(90)90019-M.

D. W. Tarasick and G. G. Shepherd. Effects of Gravity Waves on Complex Airglow Chemistries, 2. OH Emission. *J. Geophys. Res.*, 97(A3):3195–3208, 1992. doi: 10.1029/91JA02580.

D. Turnbull and R. Lowe. New hydroxyl transition probabilities and their importance in airglow studies. *Planet. Space Sci.*, 37(6):723–738, June 1989. doi: 10.1016/0032-0633(89)90042-1.

T. von Clarmann, B. Funke, M. López-Puertas, S. Kellmann, A. Linden, G. P. Stiller, C. H. Jackman, and V. L. Harvey. The solar proton events in 2012 as observed by MIPAS. *Geophys. Res. Lett.*, 40(10):2339–2343, May 2013. doi: 10.1002/grl.50119.

C. von Savigny and O. Lednyts'kyy. On the relationship between atomic oxygen and vertical shifts between OH Meinel bands originating from different vibrational levels. *Geophys. Res. Lett.*, 40:5821–5825, Nov. 2013. doi: 10.1002/2013GL058017.

C. von Savigny, K.-U. Eichmann, C. E. Robert, J. P. Burrows, and M. Weber. Sensitivity of equatorial mesopause temperatures to the 27-day solar cycle. *Geophys. Res. Lett.*, 39(21):L21804, Nov. 2012a. doi: 10.1029/2012GL053563.

C. von Savigny, I. C. McDade, K.-U. Eichmann, and J. P. Burrows. On the dependence of the OH* Meinel emission altitude on vibrational level: SCIAMACHY observations and model simulations. *Atmos. Chem. Phys.*, 12(18):8813–8828, Sept. 2012b. doi: 10.5194/acp-12-8813-2012.

R. L. Walterscheid and G. Schubert. A dynamical-chemical model of tidally driven fluctuations in the OH nightglow. *J. Geophys. Res.*, 92(A8):8775–8780, Aug. 1987. doi: 10.1029/JA092iA08p08775.

R. L. Walterscheid and G. Schubert. Dynamical-Chemical Model of Fluctuations in the OH Airglow Driven by Migrating Tides, Stationary Tides, and Planetary Waves . *J. Geophys. Res.*, 100(A9):17443–17449, 1995. doi: 10.1029/95JA01754.

R. L. Walterscheid, G. Schubert, and J. M. Straus. A dynamical-chemical model of wave-driven fluctuations in the OH nightglow. *J. Geophys. Res.*, 92(A2): 1241–1254, Feb. 1987. doi: 10.1029/JA092iA02p01241.

R. L. Walterscheid, G. G. Sivjee, and R. G. Roble. Mesospheric and lower thermospheric manifestations of a stratospheric warming event over Eureka, Canada (80°N). *Geophys. Res. Lett.*, 27(18):2897–2900, Sept. 2000. doi: 10.1029/2000GL003768.

J. Waters, L. Froidevaux, R. Harwood, R. Jarnot, H. Pickett, W. Read, P. Siegel, R. Cofield, M. Filipiak, D. Flower, J. Holden, G. Lau, N. Livesey, G. Manney, H. Pumphrey, M. Santee, D. Wu, D. Cuddy, R. Lay, M. Loo, V. Perun, M. Schwartz, P. Stek, R. Thurstans, M. Boyles, K. Chandra, M. Chavez, G.-S. Chen, B. Chudasama, R. Dodge, R. Fuller, M. Girard, J. Jiang, Y. Jiang, B. Knosp, R. LaBelle, J. Lam, K. Lee, D. Miller, J. Oswald, N. Patel, D. Pukala, O. Quintero, D. Scaff, W. Van Snyder, M. Tope, P. Wagner, and M. Walch. The Earth observing system microwave limb sounder (EOS MLS) on the aura Satellite. *IEEE Trans. Geosci. Remote Sens.*, 44(5):1075–1092, 2006. doi: 10.1109/TGRS.2006.873771.

J. R. Winick, P. P. Wintersteiner, R. H. Picard, D. Esplin, M. G. Mlynczak, I. Russell, J. M., and L. L. Gordley. Oh layer characteristics during unusual boreal winters of 2004 and 2006. *J. Geophys. Res.*, 114(A2):A02303, Feb. 2009. doi: 10.1029/2008JA013688.

Y.-I. Won, Q. Wu, Y. M. Cho, G. G. Shepherd, T. L. Killeen, P. J. Espy, Y. Kim, and B. Solheim. Polar cap observations of mesospheric and lower thermospheric 4-hour waves in temperature. *Geophys. Res. Lett.*, 30(7):1377, Apr. 2003. doi: 10.1029/2002GL016364.

J. Xu, A. K. Smith, G. Jiang, H. Gao, Y. Wei, M. G. Mlynczak, and J. M. Russell. Strong longitudinal variations in the OH nightglow. *Geophys. Res. Lett.*, 37(21): L21801, Nov. 2010. URL doi:10.1029/2010GL043972.

J. Xu, H. Gao, A. K. Smith, and Y. Zhu. Using TIMED/SABER nightglow observations to investigate hydroxyl emission mechanisms in the mesopause region. *J. Geophys. Res.*, 117(D2):D02301, Jan. 2012. doi: 10.1029/2011JD016342.

J.-H. Yee, G. Crowley, R. G. Roble, W. R. Skinner, M. D. Burrage, and P. B. Hays. Global simulations and observations of $O^1(S)$, $O_2(^1\Sigma)$ and OH mesospheric nightglow emissions. *J. Geophys. Res.*, 102(A9):19949–19968, Sept. 1997. doi: 10.1029/96JA01833.

C. Zülicke and E. Becker. The structure of the mesosphere during sudden stratospheric warmings in a global circulation model. *J. Geophys. Res. Atmos.*, 118 (5):2255–2271, Mar. 2013. doi: 10.1002/jgrd.50219.

Acknowledgements

I would like to express my special appreciation and thanks to Prof. Dr. Justus Notholt for supervising and supporting my PhD studies. I experienced an excellent and vital support to my research in the frame of his working group and I would particularly like to thank Dr. Mathias Palm for his cooperative work and support to my PhD studies. In addition, I would also like to cordially thank Prof. Dr. Christian von Savigny for his encouraging support to the model study of this work. I am very grateful for their discussions on my research and for providing me plenty of leeway for ideas and initiative.

I would like to express my gratitude to the helpful discussions outside of the institute. In this respect, I have to mention in particular Anne K. Smith, NCAR, Boulder, for her SD-WACCM4 related support, Peter Knieling, University of Wuppertal, and Prof. Dr. Patrick J. Espy, NTNU Trondheim, for their suggestions to our measurements and sharing their experience. In general, I very much appreciated the NDMC meetings, which had an important impact on my PhD studies by providing an excellent platform for related discussions. I therefore like to deeply thank the NDMC organisers for their efforts and the beneficial impact of the NDMC meetings on my PhD studies.

With regard to the conducted measurements in Ny-Ålesund, I would like to thank the station engineers for their extensive support in taking care of the measurements. In addition, I would particularly like to thank Tine Weinzierl, IUP, Bremen, for her technical support and maintenance of the spectrometer.

I also have to thank Birgit Teuchert, Sabine Packeiser, and Peter Grupe for their administrative and IT related support.

I very much enjoyed the working atmosphere at the working group of Prof. Dr. Justus Notholt and I would like to thank my colleagues for the pleasant working experience and the helpful discussions, but also for the cheerful moments during and after work. I would like to say many thanks to my office mates, Denise Müller, Christof Petri, and Christoph Hoffmann for strongly contributing to my pleasant working experience. Moreover, I am grateful to Christoph Hoffman for establishing the link to the SD-WACCM4 data and the contact to Anne K. Smith. Furthermore, I thank Dr. Holger Winkler for his assistance in the provided Fortran tool for the theoretical OH* emission line calculations and Matthias Buschmann for his helping hands during our common research stay in Ny-Ålesund in 2012. I would also like to thank Dr. Nicholas Deutscher and my former colleague Dr. Sabrina Melchionna for proofreading parts of this thesis.

Finally, I would like to express my deepest thanks to my parents, Hannelore and Jürgen, and Marjatta for being very supportive and encouraging to me during my PhD studies. I deeply appreciate their patience and encouragement during this demanding time. In particular, I am very pleased about Marjatta's dedicated support and sending a million :-* to you.

Financial support

This project was funded by the German Research Foundation (Deutsche Forschungsgemeinschaft, DFG) with the project PA 1714/4-2. Further financial support for the participation at the European Geosciences Union General Assembly meetings in 2011 and 2012 and the NDMC meetings in 2011,2012, and 2014 was granted by the "Zentrale Forschungsförderung" (ZF) of the University of Bremen. My participation at the NSERC CREATE summer school, 2013 in Alliston, Canada, was funded by the ZF and the Postgraduate International Programme in Physics and Electrical Engineering (pip) of the University of Bremen.

Corrections

p.7, line 19: replaced sentence "[...] radiative cooling mechanism is provided by CO_2. This is because the rate of collisional quenching of these species with ambient air decreases due to the decrease in mesospheric air density with altitude, hence, the probability of radiative deexcitation of these species increases" → "[...] radiative cooling mechanism is provided by CO_2, which is largely driven by transfer of energy due to collisions with atomic oxygen [Beig et al., 2003]."

p.11, line 16: "inverse square of density" → "inverse square root of density"

p.16, line 10: fixed swapped states "$O(^1D_2) \rightarrow O(^1S_0)$" → "$O(^1S_0) \rightarrow O(^1D_2)$"

p.29, Eq. (3.1) and Eq. (3.2): fixed swapped differentials $dx \longleftrightarrow d\sigma$

p.39, Eq. (3.19): $\frac{2\pi c\sigma^2}{\exp(\frac{\sigma}{k_B T})-1} \rightarrow \frac{2\pi c\sigma^2}{\exp(\frac{hc\sigma}{k_B T})-1}$

p.67, Fig. 4.6: "solar elevation $\leq 7°$" → "solar elevation $\leq -7°$"

p.118, Fig. 5.5: inserted correct panel (g)

Erklärung gem. §7, Abs. 2 der Promotionsordnung - Stand 25.04.2012

Ich erkläre hiermit, dass ich:

1. die Arbeit ohne unerlaubte fremde Hilfe angefertigt habe,
2. keine anderen als die von mir angegebenen Quellen und Hilfsmittel benutzt habe und
3. die den benutzten Werken wörtlich oder inhaltlich entnommenen Stellen als solche kenntlich gemacht habe.

Bremen, 22.12.2014
Stefan Kowalewski